

# **Development of Methods for the Characterization of Damage in Sheet Molding Compounds by using In-Situ Computed Tomography**

Zur Erlangung des akademischen Grades eines  
**Doktors der Ingenieurwissenschaften (Dr.-Ing.)**  
von der KIT-Fakultät für Maschinenbau des  
Karlsruher Instituts für Technologie (KIT)

angenommene  
**Dissertation**  
von

Ludwig Schöttl, M.Sc.

Tag der mündlichen Prüfung:	24. September 2021
Referent:	Prof. Dr.-Ing. Peter Elsner
Korreferent:	Associate Prof. Dr. Kaan Inal
Korreferent:	Prof. Dr.-Ing. Kay André Weidenmann





---

"It is not knowledge, but the act of learning, not possession but the act of getting there, which grants the greatest enjoyment."

(Carl Friedrich Gauss, letter to Bolyai on September 2, 1808 [1])



# Kurzfassung

Diskontinuierlich faserverstärkte Polymere, wie Sheet Molding Compounds (SMC) werden häufig in modernen Automobileichtbaukonstruktionen eingesetzt. SMC-Werkstoffsysteme zeichnen sich durch eine gute Umformbarkeit und hohe spezifische mechanische Eigenschaften aus. Des Weiteren erfüllen sie die geforderte Prozesszykluszeit für die Fertigung von Automobilkomponenten. Die mechanischen Eigenschaften auf der makroskopischen Betrachtungsebene und das Schädigungsverhalten von SMC werden maßgeblich durch die Mikrostruktur und insbesondere durch die Anordnung der Fasern beeinflusst. Folglich ist die Berücksichtigung der Mikrostruktur bei der Auslegung und Lebensdauervorhersage von Bauteilen aus SMC unerlässlich.

Moderne Mikro-Computertomographie-Systeme ( $\mu$ CT) erzeugen zerstörungsfrei volumetrische Bilder von Mikrostrukturen. Durch die Kombination von mechanischer Prüfung und  $\mu$ CT-Messung mittels in-situ Experimenten wird sowohl die Mikrostruktur, als auch die Rissausbreitung der untersuchten Probe dreidimensional beobachtet. Ein wesentlicher Aspekt dieser Arbeit ist es, die Mikrostruktur und das Schädigungsverhalten auf der gleichen Betrachtungsebene mittels  $\mu$ CT-Aufnahmen zu analysieren. Die gewonnenen Daten werden genutzt, um den Zusammenhang zwischen der Mikrostruktur und dem Schädigungsverhalten zu untersuchen.

Zur Charakterisierung der Mikrostruktur, wird in dieser Dissertation eine Methode zur Analyse von SMC-Mikrostrukturen mit Hilfe von volumetrischen Bildern vorgestellt. Zentrales Merkmal dieser Methode ist die Ausnutzung

der charakteristischen SMC-Faserbündel. Das führt dazu, dass die notwendige Bildauflösung im Vergleich zur Untersuchung von Einzelfasern vergrößert wird. Diese Eigenschaft ermöglicht es, größere und repräsentative SMC-Mikrostrukturen zu untersuchen. Die SMC-Faserbündel werden iterativ mit Hilfe eines probabilistischen Ansatzes verfolgt, der es ermöglicht, Faserbündel auch in Bereichen zuverlässig zu identifizieren, in denen andere Faserbündel kreuzen.

Das Kernthema dieser Dissertation ist die Charakterisierung von Schädigungen mittels in-situ  $\mu$ CT-Versuchen. Es werden verschiedene Methoden zur Segmentierung von Rissen in volumetrischen Bildern unter Verwendung von Grauwert-Histogrammen, künstlicher Intelligenz und digitaler Volumenkorrelation vorgestellt. Die Fähigkeiten dieser Methoden werden miteinander verglichen und mit Bezug auf die Genauigkeit der segmentierten Risse, praktische Einschränkungen und Anwendbarkeit diskutiert. Anschließend werden Bildverarbeitungsmethoden zur Analyse und Quantifizierung der Schädigung hinsichtlich Rissvolumendichte, räumliche Orientierungsverteilung und Schädigungsmechanismen vorgestellt. Aus den gewonnenen Daten lässt sich umfassend der Zustand und die Entwicklung der Schädigung bewerten.

Abschließend werden die vorgestellten Methoden angewandt, um die Mikrostruktur sowie das Schädigungsverhalten von mehreren repräsentativen SMC-Proben mit unterschiedlichen Mikrostrukturen zu charakterisieren. Als Ergebnis wird der Zusammenhang zwischen der Mikrostruktur und dem Schädigungsverhalten untersucht und diskutiert.

# Abstract

Discontinuous fiber-reinforced polymers such as sheet molding compounds (SMC) are frequently applied in modern automotive lightweight designs. SMC material systems show a good formability, high specific mechanical properties and fulfill the mandatory short process cycle times for automotive manufacturing processes. The macroscopic mechanical properties and damage behavior of SMC is significantly affected by the microstructure and the fiber arrangement in particular. As a consequence, it is essential to take the microstructure into account for lifetime predictions and designs of SMC components.

Modern micro-computed tomography systems ( $\mu$ CT) acquire detailed volumetric images of microstructures in a nondestructive way. Through combining mechanical testing and  $\mu$ CT scanning via in-situ experiments, the microstructure as well as the damage propagation is observed three-dimensionally and comprehensively. An essential aspect of this doctoral thesis is to analyze both, microstructure and damage behavior on the same scale level. The obtained data are used to investigate the relationship between microstructure and damage propagation.

This doctoral thesis introduces an image processing method to analyze SMC microstructures by means of volumetric images. Key feature of this method is to utilize the fiber bundle structure, which is typical for SMC. This increases the required image resolution compared to single fiber analysis, which allows large and representative SMC microstructure volumes to be investigated. The SMC fiber bundles are identified iteratively by means of a probabilistic tracking approach, that enables to reliably identify fiber bundles even in regions where other fibers bundles cross.

Furthermore, the fundamental subject of this doctoral thesis is the characterization of damage on the microstructural level by means of in-situ  $\mu$ CT testing. Several methods to segment cracks within volumetric images by using gray-value histograms, artificial intelligence and digital volume correlation are introduced. The capabilities of those methods are compared and discussed in terms of crack segmentation accuracy, limitations and applicability. Subsequently, image processing methods to analyze and quantify the damage state regarding crack volume, crack orientation distribution and damage mechanism are presented. By means of the obtained crack characterization data, it is possible to comprehensively evaluate the damage state and propagation. Finally, the introduced methods are applied in order to characterize the microstructure as well as the damage behavior of SMC samples with different microstructures. As a result, the relationship between microstructure and damage behavior is examined and discussed.

# Acknowledgment

This doctoral thesis and the scientific work therein were originated during the period from April 2018 to July 2021 at the Institute for Applied Materials (IAM-WK), Karlsruhe Institute of Technology (KIT). The research documented in this doctoral thesis has been funded by the German Research Foundation (DFG) within the International Research Training Group "Integrated engineering of continuous-discontinuous long fiber reinforced polymer structures" (GRK 2078). The support by the German Research Foundation (DFG) is gratefully acknowledged.

First, I would like to thank Peter Elsner, Kaan Inal and Kay André Weidenmann for the supervision and the valuable input to finalize my doctoral thesis. In particular, I would like to acknowledge the scientific guidance and helpful discussions over the past years.

Furthermore, I gratefully appreciate the scientific discussions and excellent support by Wilfried Liebig, all colleagues at the Institute for Applied Materials (IAM-WK) and the International Research Training Group (IRTG). Many thanks especially to Pascal Pinter for his qualified advices and for providing his fiber orientation analysis code. A special thank also goes to my office colleague Miriam Bartkowiak for the productive and highly enjoyable atmosphere.

Moreover, I gratefully acknowledge the support of my assistant students Philipp Kolb, Izzettin Sönmez and Maike Rees, who have helped me a lot with many different and interdisciplinary topics over the past years.

Further thanks go to the technicians and administration of the Institute for Applied Materials (IAM-WK) for their support in various problems.

Many thanks to all the colleagues at the University of Waterloo for the warm welcome and great time in Canada. I would especially like to thank them for their scientific support in the field of artificial intelligence and machine learning during my research stays.

Moreover, I would like to thank Volume Graphics GmbH for their cooperation on digital volume correlation and for providing the corresponding software module.

The deep learning work in this doctoral thesis was performed on the computational resource bwUniCluster funded by the Ministry of Science, Research and the Arts Baden-Wuerttemberg and the Universities of the State of Baden-Wuerttemberg, Germany, within the framework program bwHPC.

Karlsruhe, July 2021

*Ludwig Schöttl*



Dedicated to my sister Theresa, my parents and grandparents.



# Contents

<b>1</b>	<b>Introduction</b>	<b>1</b>
1.1	Motivation	2
1.2	Objectives of the Doctoral Thesis	6
1.3	Outline of the Doctoral Thesis	7
<b>2</b>	<b>State-of-the-Art</b>	<b>9</b>
2.1	Continuum Mechanics	10
2.1.1	Kinematics	10
2.1.2	Homogenization	11
2.2	Damage Behavior of Fiber-Reinforced Composites	15
2.2.1	Principles	15
2.2.2	Damage Modeling	16
2.2.3	Fatigue	17
2.2.4	Fracture Properties	19
2.2.5	Crack Orientation Tensor	22
2.3	Micro-Computed Tomography	24
2.3.1	X-ray Attenuation	25
2.3.2	Geometry and Magnification	27
2.3.3	Reconstruction	28
2.3.4	Volumetric Images	29
2.3.5	In-situ $\mu$ CT Testing	29
2.4	Image Processing	32
2.4.1	Convolutional Filter	33
2.4.2	Threshold Segmentation	35

2.4.3	Seed-Region-Growth Segmentation . . . . .	36
2.4.4	Closing Operation . . . . .	37
2.5	Microstructure of Fiber-Reinforced Polymers . . . . .	38
2.5.1	Fiber Orientation Principles . . . . .	39
2.5.2	Fiber Orientation Measurement . . . . .	40
2.5.3	Single Fiber Tracking . . . . .	41
2.5.4	Fiber Bundle Tracking . . . . .	42
2.5.5	Mapping of Microstructure Properties . . . . .	44
2.6	Digital Volume Correlation . . . . .	45
2.6.1	Principles . . . . .	45
2.6.2	Deformation Measurement . . . . .	46
2.7	Artificial Intelligence . . . . .	48
2.7.1	Principles . . . . .	48
2.7.2	Artificial Neural Networks . . . . .	49
2.7.3	Convolutional Neural Networks . . . . .	53
2.8	Damage Segmentation . . . . .	59
2.8.1	Threshold Segmentation . . . . .	60
2.8.2	Digital Volume Correlation . . . . .	61
2.8.3	Convolutional Neural Networks . . . . .	63
<b>3</b>	<b>Sheet Molding Compounds . . . . .</b>	<b>67</b>
3.1	Manufacturing of SMC . . . . .	68
3.1.1	Semi-finished SMC . . . . .	68
3.1.2	Compression Molding . . . . .	68
3.1.3	SMC Components . . . . .	69
3.1.4	SMC Charge Configuration . . . . .	70
3.1.5	Weld Line Formation . . . . .	73
3.2	Microstructure and Mechanical Characteristics of SMC . . . . .	74
3.2.1	Microstructure . . . . .	74
3.2.2	Mechanical Properties . . . . .	76
3.2.3	Damage Mechanisms . . . . .	80

3.2.4 Material Modeling . . . . .	88
<b>4 Methods . . . . .</b>	<b>91</b>
4.1 Microstructure Characterization . . . . .	92
4.1.1 Fiber Orientation . . . . .	92
4.1.2 Fiber Bundle Tracking . . . . .	95
4.1.3 Fiber Bundle Curvature . . . . .	104
4.2 Damage Segmentation . . . . .	106
4.2.1 Seed-Region-Growth Segmentation . . . . .	106
4.2.2 Digital Volume Correlation . . . . .	108
4.2.3 Convolutional Neural Network . . . . .	110
4.3 Damage Characterization . . . . .	115
4.3.1 Experimental Crack Normal Vector . . . . .	115
4.3.2 Crack Orientation Tensor . . . . .	117
4.3.3 Crack Volume Fraction . . . . .	119
4.3.4 Damage Classification . . . . .	120
<b>5 Experimental . . . . .</b>	<b>125</b>
5.1 Micro-Computed Tomography System . . . . .	126
5.2 In-situ $\mu$ CT Testing Stage . . . . .	127
5.3 Cyclic Tensile Load Protocol . . . . .	129
5.4 Specimen Geometries . . . . .	130
5.5 Fractography . . . . .	131
<b>6 Results . . . . .</b>	<b>133</b>
6.1 Microstructure Characterization . . . . .	134
6.1.1 Fiber Orientation . . . . .	134
6.1.2 Fibers Highly Oriented in Load Direction . . . . .	135
6.1.3 Fibers Highly Oriented Diagonal to the Load Direction . . . . .	136
6.1.4 Fibers Highly Oriented Perpendicular to the Load Direction . . . . .	137
6.1.5 Fibers Randomly Oriented . . . . .	138

6.1.6	Quantification of the Fiber Orientation State . . . . .	139
6.1.7	Fiber Bundle Tracking . . . . .	141
6.1.8	Fiber Bundle Curvature . . . . .	142
6.2	Experimental Damage Investigation . . . . .	144
6.2.1	Fibers Highly Oriented in Load Direction . . . . .	144
6.2.2	Fibers Highly Oriented Diagonal to the Load Direction .	146
6.2.3	Fibers Highly Oriented Perpendicular to the Load Direction	148
6.2.4	Fibers Randomly Oriented . . . . .	151
6.3	Damage Segmentation . . . . .	154
6.3.1	Seed-Region-Growth Segmentation . . . . .	154
6.3.2	Digital Volume Correlation . . . . .	157
6.3.3	Convolutional Neural Network . . . . .	161
6.4	Damage Characterization . . . . .	164
6.4.1	Crack Orientation Tensor . . . . .	164
6.4.2	Crack Volume Fraction . . . . .	167
6.4.3	Damage Classification . . . . .	169
6.5	Fractography . . . . .	171
6.5.1	Fibers Highly Oriented in Load Direction . . . . .	171
6.5.2	Fibers Randomly Oriented . . . . .	173
6.5.3	Fibers Highly Oriented Perpendicular to the Load Direction	175
<b>7</b>	<b>Discussion . . . . .</b>	<b>179</b>
7.1	Microstructure Characterization . . . . .	180
7.1.1	Fiber Orientation . . . . .	180
7.1.2	Fiber Bundle Tracking . . . . .	181
7.1.3	Fiber Bundle Curvature . . . . .	182
7.2	Experimental Damage Investigation . . . . .	183
7.3	Damage Segmentation . . . . .	186
7.3.1	Seed-Region-Growth Segmentation . . . . .	186
7.3.2	Digital Volume Correlation . . . . .	187
7.3.3	Convolutional Neural Network . . . . .	191

---

7.4 Damage Characterization . . . . .	192
7.4.1 Crack Orientation Tensor . . . . .	193
7.4.2 Crack Volume Fraction . . . . .	196
7.4.3 Damage Classification . . . . .	199
7.5 Fractography . . . . .	200
7.6 Damage Mechanisms of SMC . . . . .	202
<b>8 Summary and Conclusions . . . . .</b>	<b>209</b>
8.1 Microstructure Characterization . . . . .	210
8.2 Experimental Damage Investigation . . . . .	211
8.3 Damage Segmentation . . . . .	212
8.4 Damage Characterization . . . . .	214
8.5 Fractography . . . . .	215
8.6 Damage Mechanisms of SMC . . . . .	215
<b>Author's Publications . . . . .</b>	<b>217</b>
<b>Supervised student thesis . . . . .</b>	<b>221</b>
<b>Bibliography . . . . .</b>	<b>223</b>
<b>List of Figures . . . . .</b>	<b>259</b>
<b>List of Tables . . . . .</b>	<b>277</b>
<b>Symbols and Abbreviations . . . . .</b>	<b>281</b>
<b>A Appendix . . . . .</b>	<b>285</b>





# 1 Introduction

The introduction section below presents the motivation and outline of this doctoral thesis. Moreover, the objectives and scientific cooperations performed together with other research areas within the context of the International Research Training Group (IRTG) GRK 2078 are presented.

## Contents

---

<b>1.1 Motivation . . . . .</b>	<b>2</b>
<b>1.2 Objectives of the Doctoral Thesis . . . . .</b>	<b>6</b>
<b>1.3 Outline of the Doctoral Thesis . . . . .</b>	<b>7</b>

---

## 1.1 Motivation

One of the biggest challenges of the 21st century is fighting global warming. A major emitter of greenhouse gases is the transport sector including automotive, train and aviation, as shown in Figure 1.1. Consequently, reducing greenhouse gas emissions, such as CO<sub>2</sub> is a key motivation for reducing fuel consumption of automotive cars. In recent years, legal regulations for CO<sub>2</sub> car emission became stricter. It is the goal of the European Union to achieve a fleet-wide average emission for new cars of 95 g CO<sub>2</sub> per km from 2021 onwards [2]. Lightweight materials and designs play an essential part to fulfill these legal regulation goals. By reducing the vehicle mass by 100 kg, 0.3 – 0.5 l fuel per 100 km and 0.85 – 1.4 kg CO<sub>2</sub> per 100 km will be saved according to Mayyas et al. [3]. For this reason, new lightweight material systems that meet the necessary requirements in terms of mechanical properties, mass production criteria and total costs are required in order to reduce the overall vehicle mass.

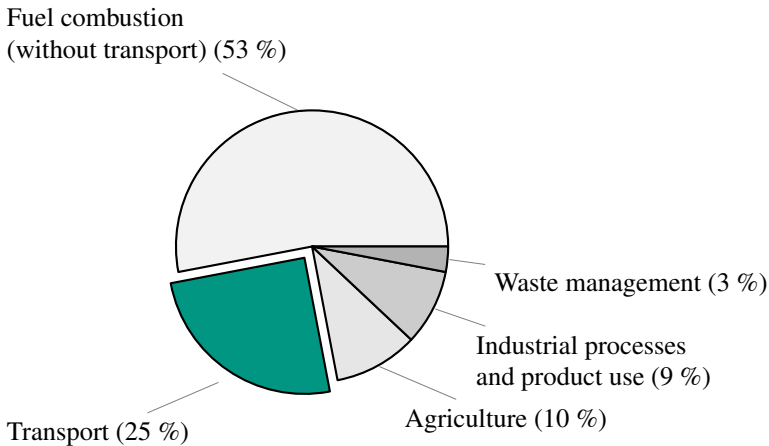


Figure 1.1: Greenhouse gas emission breakdown by the source sectors in the EU-27 2018 (data by European Environment Agency [4]). 25 % of greenhouse gases are emitted by the transport sector including international aviation.

Composite systems are becoming increasingly important for applications in the transportation industry by combining the properties of several raw materials. Designing new composite material systems enables to adjust the material properties in order to meet various requirements. Especially, fiber-reinforced polymers gained enormous relevance through reinforcing light polymer matrices by stiff and strong fibers [5]. Due to low costs and good specific mechanical properties glass fiber-reinforced polymers (GFRP) are applied in many different application fields, as shown in Figure 1.2.

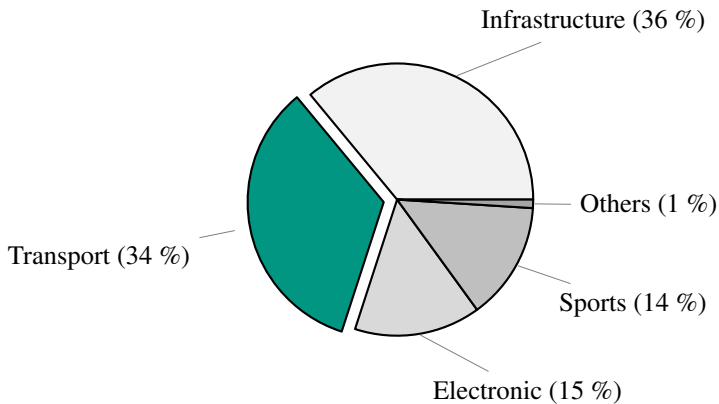


Figure 1.2: GFRP shares of the European market by application area in 2019 (data by Witten and Mathes [6]). The two main application areas for GFRP are infrastructure and transport.

Thermoplastic and thermoset polymer matrices can be reinforced by discontinuous and continuous fibers. This doctoral thesis focuses on the investigation of sheet molding compounds (SMC), which usually consist of a thermoset matrix reinforced by discontinuous fibers. SMC meets both lightweight and mass production criteria [7]. As a result, SMC is frequently applied in the automotive mass production industry. Figure 1.3 shows the production volume of SMC, other manufacturing processes and semi-finished components for GFRP in Europe.

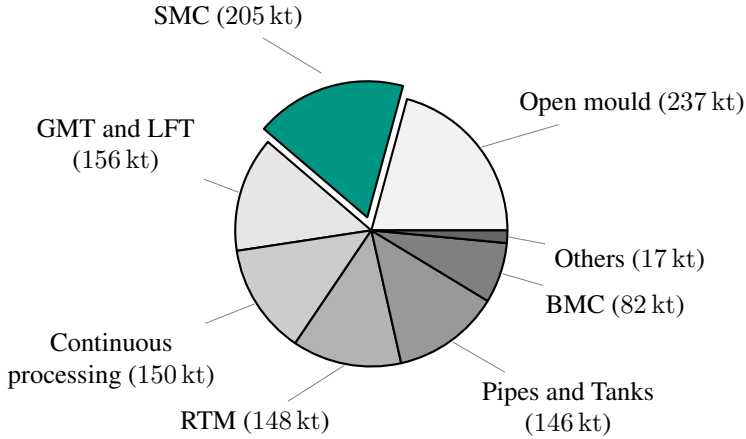


Figure 1.3: GFRP production volumes in Europe according to the manufacturing processes and semi-finished components in 2019 (data by Witten and Mathes [6]). The production fraction of SMC in 2019 is 18 %. Long fiber-reinforced thermoplastics (LFT), glass-mat reinforced thermoplastics (GMT), resin transfer molding (RTM) and bulk molding compounds (BMC).

There is a strong relationship between the manufacturing process, the microstructure and the mechanical properties for composites in general and fiber-reinforced polymers in particular, as illustrated in Figure 1.4. The fiber architecture on the microstructural level significantly affects the mechanical properties on the macroscopic scale. Especially, the anisotropic nature of the mechanical properties and the occurrence of various and complex damage mechanisms is decisive. As a result, it is essential to take the microstructure into account during the design process and for prediction of the mechanical properties. Novel numerical simulation models enable the increasingly accurate prediction of the manufacturing process and mechanical properties. Furthermore, the microstructure and damage behavior of fiber-reinforced polymers is being investigated in a more detailed way through the development of new characterization methods.

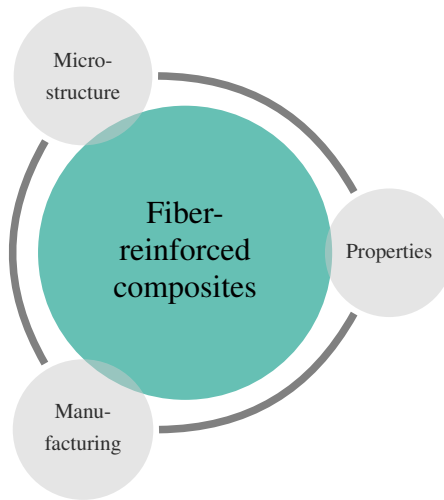


Figure 1.4: Schematic interaction between manufacturing, microstructure and properties. Consideration of the three aspects for fiber-reinforced polymers from a materials science perspective.

The goal is to fully exploit the lightweight construction potential of fiber-reinforced polymers by gaining knowledge and insight about the mechanical behavior of the examined material. This requires extensive microstructure investigations and material characterization, which in turn enable new process and structure simulation models.

## 1.2 Objectives of the Doctoral Thesis

During the last decades, micro-computed tomography ( $\mu$ CT) became one of the most important nondestructive testing methods in material science [8]. Modern  $\mu$ CT systems acquire detailed volumetric images of microstructures and by means of image processing methods microstructure properties are quantified. One objective of this doctoral thesis is the development of methods to characterize microstructures of SMC by using  $\mu$ CT technique. Especially, the characteristic fiber bundle arrangement within SMC microstructures is investigated and analyzed.

In practice, predicting the lifetime and fracture limits of materials is essential for the design process and to push the lightweight potential to the limit. As a consequence of the heterogeneous microstructure and the combination of several material systems, within fiber-reinforced polymers different damage modes occur. Through combining mechanical testing and  $\mu$ CT scanning, volumetric images of microstructures at different stages of the damage process are acquired in-situ. In order to examine and investigate the damage evolution of SMC in-situ  $\mu$ CT tests are carried out. As a result, the SMC damage evolution is observed through volumetric image series. Objective of this doctoral thesis is to develop a suitable in-situ  $\mu$ CT setup and image processing methods to characterize the damaged microstructure. Since the thermoset matrix shows brittle material behavior, the research in this work focuses on analyzing microstructural cracks. Furthermore, microstructure damage characterization methods that apply image segmentation, digital volume correlation and artificial neural networks techniques are introduced.

Cooperations between the research areas are a key aspect of the International Research Training Group (IRTG). Especially, the data transfer between microstructure characterization, process simulation and structure simulation gained increasing importance by providing input data and validation results, as

shown in Figure 1.5. Another object of this doctoral thesis is to develop mapping strategies to transfer microstructure data and utilize them in numerical simulation models.

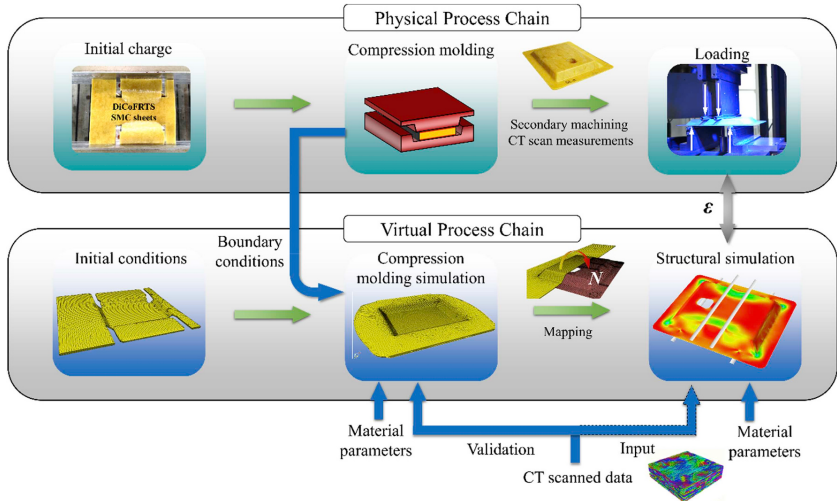


Figure 1.5: Illustration of the virtual process chain and the cooperations between the research areas within the IRTG (figure by Görthofer et al. [9, 10]\*).

## 1.3 Outline of the Doctoral Thesis

This doctoral thesis first provides an overview of the state-of-the-art in chapter 2 regarding the addressed topics and research areas. Fundamentals and relevant publications dealing with fiber-reinforced polymers, microstructure characterization,  $\mu$ CT technique, image processing, digital volume correlation, artificial intelligence and damage characterization are presented.

\* Own publication(s)

Subsequently, chapter 3 introduces the investigated SMC material system. Here, the relationship between the manufacturing process, microstructure and mechanical properties of SMC are presented. Common aspects and approaches on fiber-reinforced polymers introduced in chapter 2 are focused and applied on SMC in general, and the investigated SMC material system in particular. General assumption and classification regarding SMC are presented, which are fundamental for the developed and introduced methods in this doctoral thesis. A central part of this work is the development and application of methods in order to characterize the fiber architecture of SMC and to examine the damage behavior on the microstructural level based on  $\mu$ CT data. The developed and applied image processing methods are introduced in chapter 4.

Chapter 5 presents the experimental equipment used and mechanical testing methods. Here, the  $\mu$ CT system, the experimental in-situ stage and test protocols are introduced in detail.

The obtained results by using in-situ  $\mu$ CT testing, microstructure characterization and damage analysis are presented in chapter 6. These three parts will be combined by experimentally investigating SMC samples by means of in-situ  $\mu$ CT experiments and analyzing them with respect to microstructure and damage behavior.

In chapter 7 the introduced methods are compared with each other and the results are discussed in context of state-of-the-art references. The obtained observations and insights are further discussed with reference to the relationship between microstructure and damage of SMC. Finally, the content of this doctoral thesis is summarized and concluded in chapter 8.



## 2 State-of-the-Art

This chapter provides an overview of the current research state regarding the objectives of this doctoral thesis. Topics including continuum mechanics, computer tomography technique, image processing, artificial neural networks and mechanical behavior of fiber-reinforced polymers in general are presented. Fundamental aspects that form the basis for the developed methods and determined results in this work are introduced.

### Contents

---

<b>2.1 Continuum Mechanics . . . . .</b>	<b>10</b>
<b>2.2 Damage Behavior of Fiber-Reinforced Composites . . . . .</b>	<b>15</b>
<b>2.3 Micro-Computed Tomography . . . . .</b>	<b>24</b>
<b>2.4 Image Processing . . . . .</b>	<b>32</b>
<b>2.5 Microstructure of Fiber-Reinforced Polymers . . . . .</b>	<b>38</b>
<b>2.6 Digital Volume Correlation . . . . .</b>	<b>45</b>
<b>2.7 Artificial Intelligence . . . . .</b>	<b>48</b>
<b>2.8 Damage Segmentation . . . . .</b>	<b>59</b>

---

## 2.1 Continuum Mechanics

This doctoral thesis deals, among other, with the relationship between microstructure and mechanical behavior; and the cooperation between numerical modeling and material characterization. For this purpose, an overview of continuum mechanics with respect to fiber-reinforced composites is given. Section 2.1.1 introduces fundamentals of continuum kinematics, which are especially relevant for the applied correlation methods in context of this work. Subsequently, in Section 2.1.2 state-of-the-art homogenization approaches for fiber-reinforced composites are presented.

### 2.1.1 Kinematics

The position of any material point  $P$  within the reference configuration  $\Omega_0$  at time  $t = t_0$  is determined by the position vector  $\mathbf{X}$ , as shown in Figure 2.1. At time  $t \geq t_0$ , the position vector  $\mathbf{x}$  of any material point  $P$  is given by

$$\mathbf{x} = \chi(\mathbf{X}, t) \quad (2.1)$$

The displacement  $\mathbf{u}(\mathbf{X}, t)$  is introduced as the difference between the reference position and the position at  $t$

$$\mathbf{u}(\mathbf{X}, t) = \mathbf{x}(\mathbf{X}, t) - \mathbf{X}. \quad (2.2)$$

The displacement gradient is defined by

$$\mathbf{H}(\mathbf{X}, t) = \frac{\partial \mathbf{u}(\mathbf{X}, t)}{\partial \mathbf{X}}. \quad (2.3)$$

Assuming only small deformation, the infinitesimal strain tensor is introduced by

$$\boldsymbol{\varepsilon}(\mathbf{X}, t) = \text{sym}(\mathbf{H}(\mathbf{X}, t)) = \frac{1}{2}(\mathbf{H}(\mathbf{X}, t) + \mathbf{H}(\mathbf{X}, t)^T). \quad (2.4)$$

Figure 2.1 schematically illustrates the notation and relationship between reference and deformed state regarding continuum mechanics.

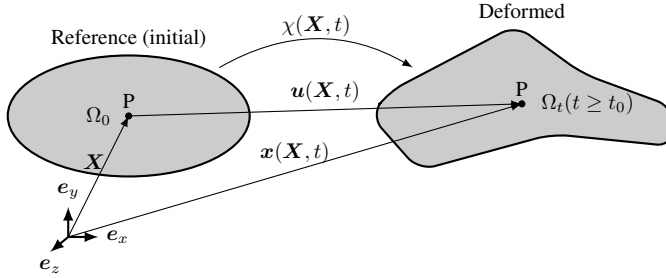


Figure 2.1: Fundamentals of continuum kinematics.

## 2.1.2 Homogenization

In general, the (local) microscopic stress  $\boldsymbol{\sigma}(\mathbf{x})$  and strain  $\boldsymbol{\varepsilon}(\mathbf{x})$  within a heterogeneous microstructure is also heterogeneously distributed. Considering a representative volume element (RVE) the effective stress

$$\bar{\boldsymbol{\sigma}} = \langle \boldsymbol{\sigma}(\mathbf{x}) \rangle = \int_V \boldsymbol{\sigma}(\mathbf{x}) dV \quad (2.5)$$

and effective strain

$$\bar{\boldsymbol{\varepsilon}} = \langle \boldsymbol{\varepsilon}(\mathbf{x}) \rangle = \int_V \boldsymbol{\varepsilon}(\mathbf{x}) dV \quad (2.6)$$

are given by using the volume average  $\langle \cdot \rangle$  over the representative volume  $V$ . In case of linear elastic deformation, the relation between the effective stress  $\bar{\boldsymbol{\sigma}}$  and effective strain  $\bar{\boldsymbol{\varepsilon}}$  is described by the generalized Hooke's law, the local stiffness tensor  $\mathbb{C}(\mathbf{x})$  and the effective stiffness tensor  $\bar{\mathbb{C}}$

$$\bar{\boldsymbol{\sigma}} = \bar{\mathbb{C}}[\bar{\boldsymbol{\varepsilon}}] = \langle \mathbb{C}(\mathbf{x})[\boldsymbol{\varepsilon}(\mathbf{x})] \rangle. \quad (2.7)$$

Defining the compliance tensor  $\mathbb{S} = \mathbb{C}^{-1}$  as the inverse stiffness tensor

$$\bar{\varepsilon} = \bar{\mathbb{S}}[\bar{\sigma}] = \langle \mathbb{S}(\mathbf{x})[\sigma(\mathbf{x})] \rangle. \quad (2.8)$$

The relation between the local and effective strain and stress tensor is given by the localization tensors  $\mathbb{A}$  and  $\mathbb{B}$ , respectively.

$$\varepsilon(\mathbf{x}) = \mathbb{A}(\mathbf{x})[\bar{\varepsilon}] \quad (2.9)$$

$$\sigma(\mathbf{x}) = \mathbb{B}(\mathbf{x})[\bar{\sigma}] \quad (2.10)$$

For the localization tensors it holds that

$$\langle \mathbb{A}(\mathbf{x}) \rangle = \mathbb{I}^S \text{ and } \langle \mathbb{B}(\mathbf{x}) \rangle = \mathbb{I}^S. \quad (2.11)$$

Assuming a composite of several phases  $\alpha$  with homogeneous stiffness properties  $\mathbb{C}_\alpha$  and  $\phi_\alpha = V_\alpha/V$  the volume fraction, the effective stiffness tensor is determined by

$$\bar{\mathbb{C}} = \langle \mathbb{C}(\mathbf{x})\mathbb{A}(\mathbf{x}) \rangle = \sum_{\alpha} \phi_{\alpha} \mathbb{C}_{\alpha} \mathbb{A}_{\alpha}. \quad (2.12)$$

Introducing one phase as the matrix material  $(\cdot)_M$  and considering a fiber-reinforced composite, where all embedded fibers have the same stiffness property  $\mathbb{C}_F$  the effective composite stiffness is given by

$$\bar{\mathbb{C}} = \mathbb{C}_M + \sum_i \phi_i (\mathbb{C}_F - \mathbb{C}_M) \mathbb{A}_i \quad (2.13)$$

$$= \mathbb{C}_M + (\mathbb{C}_F - \mathbb{C}_M) \langle \mathbb{A} \rangle_F, \quad (2.14)$$

where  $\langle \cdot \rangle_F$  is the arithmetic volume average operator over all fibers. The homogenization approach according to Voigt [11] assumes, that the microscopic strain  $\varepsilon(\mathbf{x})$  is equal for all phases of the composite. Consequently, the strain localization tensor  $\mathbb{A}$  becomes the fourth order symmetric identity tensor  $\mathbb{I}^S$ .

As a result, the homogenization scheme according to Voigt [11] is determined by

$$\bar{\mathbb{C}} = \mathbb{C}_M + \phi_F(\mathbb{C}_F - \mathbb{C}_M). \quad (2.15)$$

Another homogenization scheme by Reuss [12] is given by the assumption, that the microscopic stress  $\boldsymbol{\sigma}(\mathbf{x})$  is equal for all phases of the composite. Subsequently, the stress localization tensor  $\mathbb{B}$  becomes  $\mathbb{I}^S$  and the homogenized compliance results in

$$\bar{\mathbb{S}} = \mathbb{S}_M + \phi_F(\mathbb{S}_F - \mathbb{S}_M). \quad (2.16)$$

The homogenized stiffness tensor according to Reuss [12] is determined by

$$\bar{\mathbb{C}} = \bar{\mathbb{S}}^{-1} = \left( \mathbb{C}_M^{-1} + \phi_F(\mathbb{C}_F^{-1} - \mathbb{C}_M^{-1}) \right)^{-1}. \quad (2.17)$$

Considering isotropic elastic properties of both matrix and fiber, the material behaviors are described by Young's modulus  $E_M$  and  $E_F$  and transverse contraction  $\nu_M$  and  $\nu_F$ . Assuming uniaxial tensile load, the effective Young's modulus  $\bar{E}$  is determined as shown in Figure 2.2. In this case, the Voigt and Reuss model corresponds to a unidirectional fiber-reinforced composite with uniaxial load transversal and orthogonal to the fiber orientation, respectively. The homogenization approaches of Voigt [11] and Reuss [12] take the fiber volume fraction into account, but not the microstructure architecture in detail. In contrast, the homogenization scheme by the authors Mori and Tanaka [13] assumes an appropriate RVE and takes the estimated microstructure into account for homogenization. The authors Eshelby and Peierls [14, 15] introduced the micromechanical solution for a single elastic ellipsoid-shaped inclusion within an elastic infinite large matrix. Among other things, this analytical solution is the basis for many homogenization approaches for short fiber-reinforced

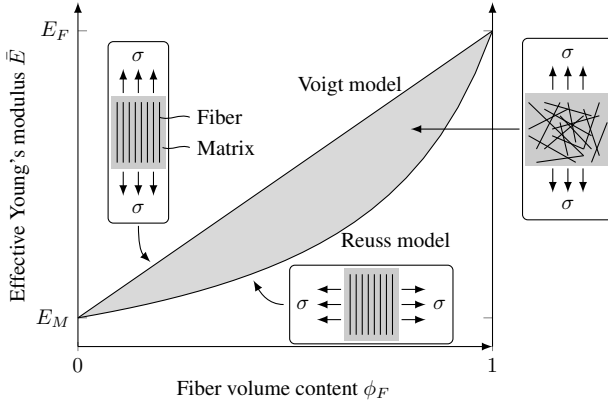


Figure 2.2: The Voigt and Reuss homogenization approaches and the effect of the fiber volume fraction  $\phi_F$  on the effective Young's modulus  $\bar{E}$ .

composites. An overview of continuum micromechanics and fundamental homogenization approaches is provided by the author Zaoui [16], including the approaches by Hill [17, 18], Hashin and Shtrikman [19].

A review of state-of-the-art multi-scale methods for composites is provided by Kanouté et al. [20]. Specific prediction models for SMC on multiple scale levels were developed in the first generation of the IRTG graduate program by several authors [21–24].

Although all homogenization approaches consider different microstructure assumptions, they all require suitable microstructure characterization data. Consequently, detailed microstructure data are essential for reliable mechanical prediction models.

## 2.2 Damage Behavior of Fiber-Reinforced Composites

As a result of the complex microstructure of fiber-reinforced composites, several damage mechanisms occur on the microstructural level. An overview of the damage and fracture mechanisms of fiber-reinforced composites is provided in this section.

### 2.2.1 Principles

In practice, the fracture and failure of components can result in catastrophic consequences. The understanding of the damage and fracture behavior of materials is essential to predict the lifetime of material systems under load and design components that meet the necessary requirements.

Since fiber-reinforced composites are highly heterogeneous, different failure modes occur on the microstructural level. The understanding of initiation, propagation and interaction of those failure modes is essential to reliably predict the failure behavior of fiber-reinforced composites. As a result of the heterogeneous microstructure, fiber-reinforced composites combine not only the elastic properties but also the failure behavior of the individual components. This includes the failure mechanisms of fiber and matrix as well as those of the interface in between. Figure 2.3 schematically illustrates typical damage mechanisms of short fiber-reinforced composites, including (a) failure of the fiber-matrix interface and subsequently, debonding of the fibers from the matrix, (b) breakage of the fiber filaments and (c) crack propagation within the matrix [25].

The way, in which the fiber architecture is structured, significantly affects the damaging process and the fracture modes that occur. Consequently, there are both similar and different damage mechanisms in various fiber-reinforced polymers, such as short fiber-reinforced plastics, discontinuous fiber-reinforced

SMC and continuous fiber-reinforced laminates. Puck and Schürmann [26], Greenhalgh [27], Talreja and Singh [28] examined and discussed the formation and influence of several damage and failure mechanisms within different fiber-reinforced composites.

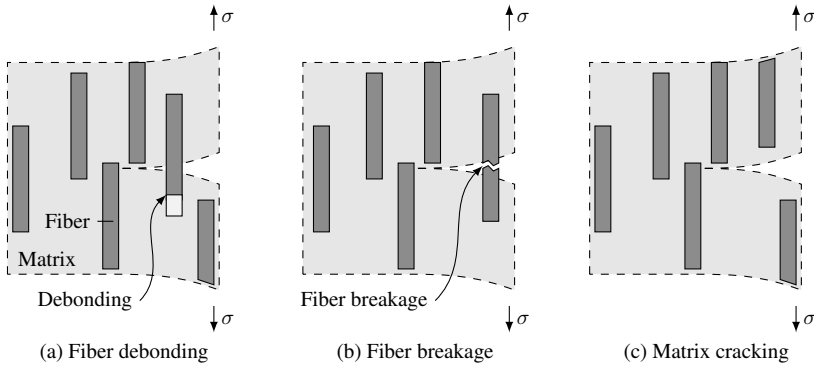


Figure 2.3: Typical failure modes of (short) fiber-reinforced composites. In (a) failing of the fiber-matrix interface and resulting fiber debonding, (b) fracture of fibers under tensile stress and (c) crack propagation through matrix material.

## 2.2.2 Damage Modeling

Early failure models are addressed to unidirectional and later multi-axial fiber-reinforced laminates, since here the fiber architecture is periodical and easy to describe by using mathematics. Inspired by the von Mises yield criterion for metals [29, 30], several failure models based on maximum stress, maximum strain, distortion energy [31] and polynomial functions of stress components [32] are presented. The heterogeneous microstructure of fiber-reinforced composites causes several ways of the composites to fail. Instead of combining all these kinds of failure modes into one criterion, the author Hashin [33] introduced four failure criteria with respect to tensile and compression load for fibers and matrix, respectively.



Over the years, a wide variety of failure criteria has been proposed. According to Talreja and Singh [28], there is no single failure theory that seems to capture all complexities of composite failure.

### 2.2.3 Fatigue

In practice, fatigue is the main failure mechanism for composite structures under cyclic loading. Applying cyclic loading generally leads to progressive damage accumulation, which results in the degradation of macroscopic mechanical properties, such as stiffness reduction [34]. The authors Talreja and Watt [35, 36] investigated the fatigue damage behavior of unidirectional fiber-reinforced composites. The fatigue life diagram in Figure 2.4 illustrates the different damage modes with respect to the applied load and number of load cycles. The experimental study on unidirectional carbon fiber-reinforced epoxy by Curtis [37] shows a good agreement with the fatigue life diagram by Talreja and Watt [35, 36].

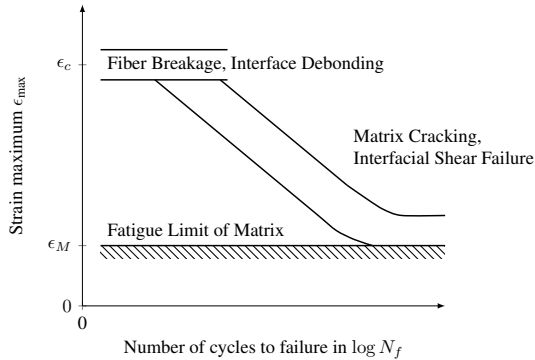


Figure 2.4: Schematic fatigue-life diagram for unidirectional fiber-reinforced composites with tensile load parallel to the fiber orientation, where  $\epsilon_c$  is the composite fracture strain and  $\epsilon_M$  the fatigue limit of the matrix (re-illustration, original figure by Talreja and Watt [35]).

The authors Reifsnider et al. [38] characterized the fatigue life of fiber-reinforced composite laminates by three different stages. The first stage is characterized by forming numerous transverse cracks within the matrix and consequently, a rapid stiffness reduction of the composites. The second stage is proportionally the largest part of the fatigue life. Here, the stiffness is only slightly reduced, which is caused by delamination and matrix cracking. At the end of the second stage, no further cracks are formed and a transition from many microscopic cracks to the formation of a single macroscopic crack takes place. Finally in the third stage, the macroscopic crack propagates followed by fracture. The stiffness degradation and three damage stages are schematically illustrated in Figure 2.5 (a). According to the studies of Hahn and Kim [39] as well as Reifsnider et al. [38], the authors Friedrich et al. [40] and Schulte [41] examined coinciding fatigue life stages of composite laminates.

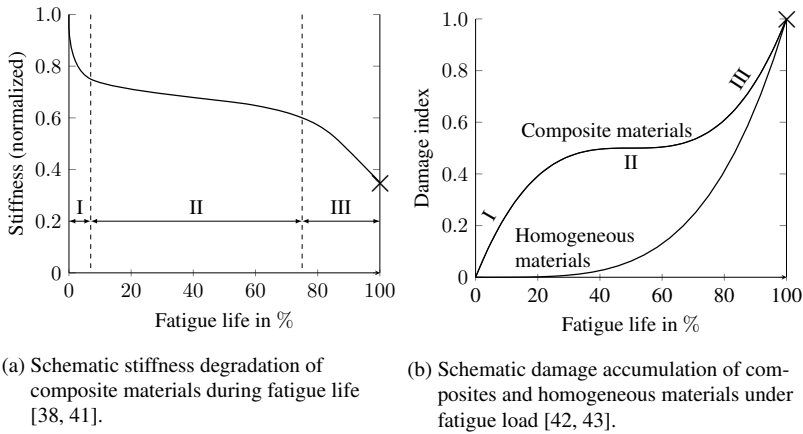


Figure 2.5: Classification of fatigue life by three stages in which different damage mechanisms occur for fiber-reinforced composites. In I) multiple crack formation, II) transition to single macroscopic crack propagation and III) final fracture (re-illustrations, original figures by Schulte [41], Mao and Mahadevan [43]).

By adapting the partition into three damage stages, the authors Mao and Mahadevan [43] introduced a general fatigue damage model, that covers the complex damaging behavior for composites. The fatigue damage progress and the three damage stages of composite material according to the authors Mao and Mahadevan [43] are schematically illustrated in Figure 2.5 (b). The author Stinchcomb [42] investigated the fatigue damage accumulation of composite laminates and introduced a consistent damage accumulation process.

## 2.2.4 Fracture Properties

Besides knowing the elastic properties, for designing and applying fiber-reinforced composites it is important to predict and adjust the effective fracture properties. Since damage is initiated on the microscopic level, the fracture properties of fiber-reinforced composites are significantly influenced by the microstructure. One of the main tasks of fibers is reinforcing the mechanical properties, including the fracture properties. In contrast to the elastic properties, certain criteria have to be met in order to increase the effective fracture properties of the composite.

### Critical Fiber Length

The matrix material encloses the fibers, protects them and transfers the applied forces into the fibers through the interface. In case of fibers, longer than the critical fiber length  $L_{\text{crit}}$ , the shear stress transferred through the interface exceeds the fiber strength [44–46]. As a consequence, the necessary energy to debond fiber and matrix is higher than for fiber breakage. Assuming a cylindrical fiber cross section, constant fiber tensile strength and interface shear strength, the critical fiber length  $L_{\text{crit}}$  is determined by

$$L_{\text{crit}} = \frac{d_F \sigma_{F,\text{max}}}{4\tau_{FM,\text{max}}}, \quad (2.18)$$

with the fiber diameter  $d_F$ , fiber tensile strength  $\sigma_{F,\max}$  and interface shear strength between fiber and matrix  $\tau_{FM,\max}$ .

### Critical Fiber Volume Content

In contrast to the formation of a single crack in homogeneous materials, various damage mechanisms occur in fiber-reinforced composites. These damage mechanisms are decisively affected by the mechanical properties of the individual components and the fiber volume content of the fiber-reinforced composites. According to Cooper [47] by meeting the listed assumptions below:

- Linear elastic deformation of fiber and matrix until fracture (brittle behavior)
- Uniform strength of all fibers over the entire length
- Equal strain of matrix and fiber (no debonding)
- The fiber tensile strength is higher than or equal to the matrix tensile strength ( $\sigma_{F,\max} \geq \sigma_{M,\max}$ )
- The matrix elongation at break is less than or equal to the fiber elongation at break ( $\epsilon_{M,\max} \leq \epsilon_{F,\max}$ )

single crack formation and multiple matrix cracking is separated by the introduced critical fiber volume  $\phi_{\text{crit}}$ . These assumptions apply specifically to glass fiber-reinforced thermoset composites, since here the matrix elongation at break is usually smaller, compared to those of the fibers [48]. In the case of low fiber volume content, the matrix material mainly determines the composite strength. When the maximum strain of the matrix is locally exceeded, cracking of the matrix material occurs. Caused by the low fiber volume content, the intact residual fiber structure cannot bear the applied load. As a consequence, the crack propagation is not constrained and the entire composite structure fails, due to the single crack formation. One important property in this case is the

applied fiber stress at matrix failure  $\sigma_F(\epsilon_{M,\max}) = \hat{\sigma}_F$ , as shown in Figure 2.6 (a). The effective composite strength is expressed by

$$\bar{\sigma}_{\max} = \sigma_{M,\max}(1 - \phi_F) + \hat{\sigma}_F \phi_F. \quad (2.19)$$

If the fiber volume content is high and the fiber architecture is sufficiently strong, the matrix fails first and gradually. Due to the strength of the intact fiber architecture, complete failure of the composite is prevented. After the first matrix crack initiation, further increasing the applied load causes the maximum matrix strain to be exceeded at several locations in the composite. As a result, additional cracks are formed and multiple cracking of the matrix occurs. According to Cooper [47] in this case the composite strength is determined solely by the still intact fiber structure by

$$\bar{\sigma}_{\max} = \sigma_{F,\max} \phi_F. \quad (2.20)$$

Introducing the critical fiber volume content  $\phi_{\text{crit}}$  as the transition between single and multiple cracking, as shown in Figure 2.6 (b).

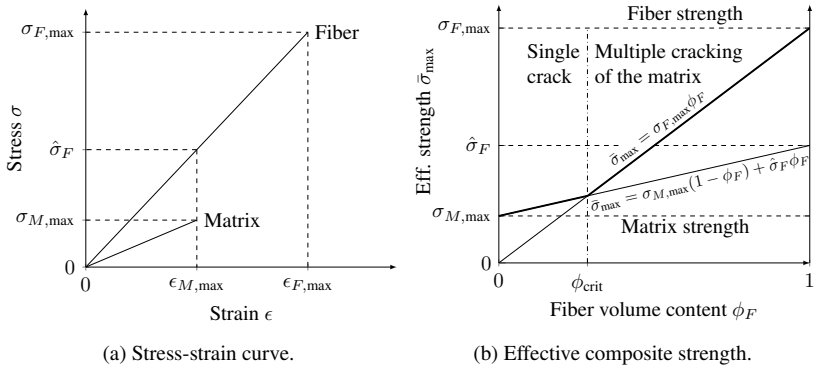


Figure 2.6: Effective composite strength  $\bar{\sigma}_{\max}$  with respect to the fiber volume content  $\phi_F$ . Impact of the fiber volume content  $\phi_F$  on the damage mechanism and the critical fiber volume content  $\phi_{\text{crit}}$ .

As presented and discussed by Cooper [47], Figure 2.7 illustrates schematically the mechanical behavior of the composites with respect to fiber volume contents below and above the critical fiber volume content. The stress-strain curve of multiple matrix cracking is characterized by a yield point, at which the maximum matrix strain is reached and initial damage occurs [47].

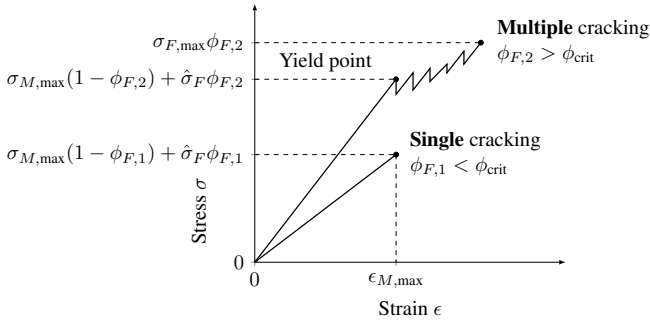


Figure 2.7: Schematic illustration of the stress-strain curve for composites with fiber volume content above and below the critical one, according to Cooper [47]. Impact of the fiber volume content on the formation of single or multiple cracks (re-illustration, original figure by Cooper [47]).

## 2.2.5 Crack Orientation Tensor

In general, fiber-reinforced polymers show anisotropic mechanical properties and the combination of fiber and matrix leads to the appearance of several damage modes. As a result, damaging generally also occurs in an anisotropic way.

In the contribution of Kachanov [49–52], Lubarda and Krajcinovic [53], the crack density distribution  $\rho(\mathbf{g})$  is used to describe the anisotropic damage. The crack orientation is represented by its normal vector  $\mathbf{g}$ , as shown in Figure 2.8.

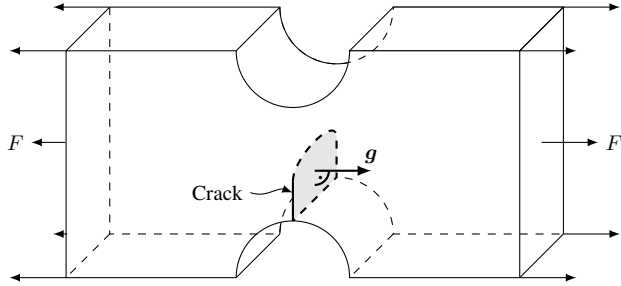


Figure 2.8: Introducing the crack orientation based on the crack normal vector  $\mathbf{g}$ .

The total crack density  $\rho_0$

$$\rho_0 = \oint \rho(\mathbf{g}) \, d\mathbf{g} \quad (2.21)$$

is determined by integration over all directions  $\mathbf{g}$ . Introducing the second-order crack density tensor  $\mathbf{P}$ , the crack density distribution  $\rho(\mathbf{g})$  can be approximated by

$$\rho(\mathbf{g}) = \mathbf{P} \cdot (\mathbf{g} \otimes \mathbf{g}), \quad (2.22)$$

Based on the symmetric second-order crack orientation tensor  $\mathbf{D}$

$$\mathbf{D} = \oint \rho(\mathbf{g}) \mathbf{g} \otimes \mathbf{g} \, d\mathbf{g}, \quad (2.23)$$

the second-order crack density tensor can be substituted by

$$\mathbf{P} = \frac{15}{8\pi} \left( \mathbf{D} - \frac{\rho_0}{5} \mathbf{I} \right), \quad (2.24)$$

where  $\mathbf{I}$  is the second-order identity tensor [53]. Subsequently, based on the crack orientation tensor  $\mathbf{D}$  the crack density distribution is approximately given by

$$\rho(\mathbf{g}) = \frac{15}{8\pi} \mathbf{D}[\mathbf{g} \otimes \mathbf{g}] - \frac{3\rho_0}{8\pi}. \quad (2.25)$$

This means that the anisotropic part of  $\mathbf{P}$  and  $\rho$  is represented entirely by the crack orientation tensor  $\mathbf{D}$ . The presented tensor calculations are introduced in the contribution of Lubarda and Krajcinovic [53]. Furthermore, the crack density tensor and distribution is applied to the experimental data by Hallbauer et al. [54] on microcrack orientation and density in quartzite specimen. The results demonstrate how experimental data are used to evaluate the crack orientation distribution by means of the tensor formulations.

## 2.3 Micro-Computed Tomography

Developed by Cormack and Hounsfield the X-ray computed tomography system [55] was introduced in 1972. For their invention, Cormack and Hounsfield received the Nobel Prize in Physiology or Medicine in 1979 [56].

In recent years, the development of modern Micro-Computed Tomography systems ( $\mu$ CT) enables the ability to image internal structures in even more detailed manner. As a result,  $\mu$ CT imaging became an important method for nondestructive characterization in material science. Especially for the investigation of composite microstructures.

This section provides an overview of X-ray tomography principles, the setup of computed tomography systems and the reconstruction of volumetric images.



### 2.3.1 X-ray Attenuation

During the  $\mu$ CT scanning process the analyzed object is screened by a X-ray beam. The Lambert-Beer-Law

$$I(L, \mu) = I_0 \exp \left( - \int_0^L \mu(x) dx \right), \quad (2.26)$$

describes the intensity degradation of waves while transmitting an object [8, 57, 58].  $I_0$  is the initial intensity,  $I$  the intensity after transmission,  $L$  the transmission length and  $\mu(x)$  the linear attenuation coefficient, as illustrated in Figure 2.9.

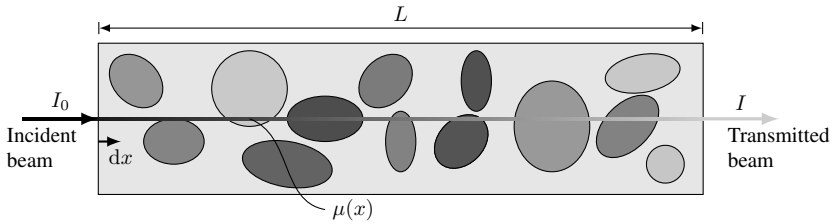


Figure 2.9: Illustration of the Lambert-Beer-Law of decreasing beam intensity and the linear attenuation coefficient  $\mu$ .

The linear attenuation coefficient  $\mu$

$$\mu = \mu_s + \alpha \quad (2.27)$$

is the effective combination of the scattering coefficient  $\mu_s$  and the absorption coefficient  $\alpha$  [58]. The attenuation coefficient is affected by three major properties. The photon energy of the incident beam (beam-specific), the atomic number and the mass density  $\rho$  of the transmitted material (material-specific). The mass density invariant aspect is given by the mass attenuation coefficient  $\mu_m$

$$\mu_m = \frac{\mu}{\rho}. \quad (2.28)$$

The average photon energy of typical X-ray CT systems is 60 keV, according to Low [59]. Table 2.1 summarizes the mass attenuation coefficient of some selected elements and compounds at 60 keV photon energy.

Table 2.1: Mass attenuation coefficients  $\mu_m$  of elements and compounds (data on quartz by Han et al. [60] and the other data by Hubbell and Seltzer [61])

Material	Atomic number	Mass attenuation in $\text{cm}^2\text{g}^{-1}$	Photon energy in keV
Hydrogen	1	$3.260e-01$	60.0
Carbon, Graphite	6	$1.753e-01$	60.0
Aluminum	13	$2.778e-01$	60.0
Silicon	14	$3.207e-01$	60.0
Air (dry, near sea level)		$1.875e-01$	60.0
Glass, Borosilicate		$2.417e-01$	60.0
Glass, Lead		$3.843e-01$	60.0
Quartz ( $\text{SiO}_2$ )		$2.600e-01$	59.5
Bakelite		$1.866e-01$	60.0
Polyethylene (PE)		$1.970e-01$	60.0
Polystyrene (PS)		$1.870e-01$	60.0

In general, the effective mass attenuation  $\bar{\mu}_m$  of compounds is determined by

$$\bar{\mu}_m = \sum_i w_i \mu_{m,i}, \quad (2.29)$$

where  $w_i$  is the weight fraction and  $\mu_{m,i}$  the mass attenuation coefficient of the component  $i$  [59].

### 2.3.2 Geometry and Magnification

The principle  $\mu$ CT system setup consists of a X-ray tube, a detector and a manipulator, as shown in Figure 2.10. The scanned object is incrementally screened from various angles over  $360^\circ$ . The initial and transmitted beam intensity is measured by using the tube controller, calibration data and the detector. As a result, spatial information of the linear attenuation coefficient inside the object are acquired.

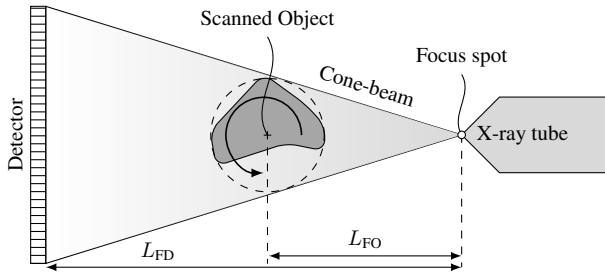


Figure 2.10: General cone-beam computed tomography setup.

Goal of the  $\mu$ CT scanning process is determining a volumetric image of the screened object. Volumetric images are composed of discrete volume elements called voxels, where the voxel size is used as a measure for the image resolution. The voxel size of the resulting volumetric image  $\Delta L_{\text{voxel}}$  is adjusted by the detector pixel pitch  $\Delta L_{\text{Detector}}$  and the geometrical magnification by

$$\Delta L_{\text{voxel}} = \underbrace{\frac{L_{\text{FO}}}{L_{\text{FD}}}}_{\text{geometrical magnification}} \Delta L_{\text{Detector}}. \quad (2.30)$$

By placing the scanned object closer to the X-ray tube, the voxel size  $\Delta L_{\text{voxel}}$  is minimized and high-resolution volumetric images are acquired. However, in this case also the scanned volume is reduced. The geometrical link between the voxel size and the scanned volume is illustrated in Figure 2.11 schematically.

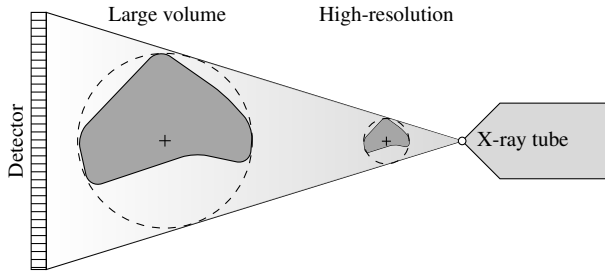


Figure 2.11: Conflict between voxel size and scanned volume of the cone-beam computed tomography setup.

### 2.3.3 Reconstruction

The  $\mu$ CT system screens the analyzed objects from several angles by the X-ray beam and the detector acquires two-dimensional projections of the transmitted beam intensity. Task of the reconstruction process is the determination of a gray-value volumetric image based on the acquired projections. The inverse problem can be solved by algebraic or statistical reconstruction methods. The authors Herman and Sameer [62] present several algebraic and statistical reconstruction approaches for various applications. Since the algebraic methods are computational expensive, usually statistical reconstruction methods are applied. The authors Feldkamp et al. [63] introduced a fundamental reconstruction approach for cone-beam  $\mu$ CT systems. The filtered backprojection method is commonly used in most reconstruction applications. Figure 2.12 illustrates schematically how the volume data are reconstructed based on projections acquired by various angles. The authors Geyer et al. [64] provide an overview of modern state-of-the-art iterative reconstruction methods.

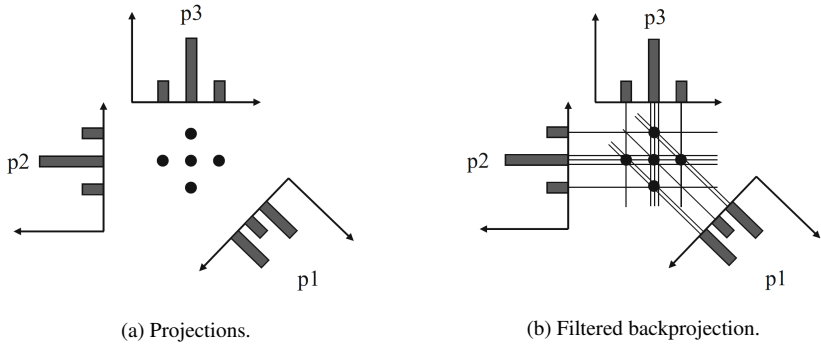


Figure 2.12: The filtered backprojection reconstruction process (figures by Carmignato et al. [8]).

### 2.3.4 Volumetric Images

The  $\mu$ CT scanning and reconstruction process acquires gray-value volumetric images  $g(x, y, z)$ , which represent the spatial distribution of the linear attenuation coefficient. The shape of voxels is usually cuboid. In case of isotropic voxel size ( $\Delta L_x = \Delta L_y = \Delta L_z$ ), the voxels are cube shaped. Besides scalar values, also vectorial quantities can be assigned to voxels, as shown in Figure 2.13. Moreover, two-dimensional cross section images can be extracted from the volumetric images.

### 2.3.5 In-situ $\mu$ CT Testing

Modern  $\mu$ CT systems offer the opportunity to acquire detailed volumetric images of microstructures in a non-destructive way. Additionally, by combining mechanical testing and  $\mu$ CT scanning, the examined microstructures are scanned in-situ while load is applied. As a result, in-situ  $\mu$ CT setups enable to generate volumetric images of the analyzed microstructure through the entire damage process.

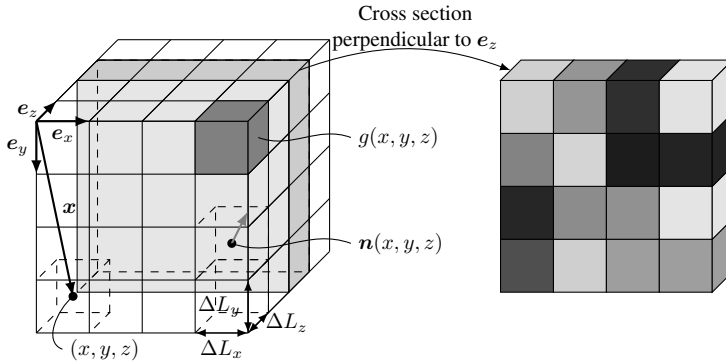


Figure 2.13: Properties of volumetric images, like gray-values  $g$  (scalar), fiber orientations  $\mathbf{n}$  (vector) and two-dimensional cross section image.

In Figure 2.14 different ex-situ and in-situ imaging strategies are illustrated. Since laboratory X-ray  $\mu$ CT scans take several minutes to hours to complete, the temporal resolution is limited and only ex-situ or interrupted in-situ experiments are carried out. In contrast to laboratory  $\mu$ CT systems, the temporal resolution of scans performed by using synchrotron radiation-based  $\mu$ CT system (SRCT) are significantly higher from 0.05 s to 5 min per scan [65]. As a result, SRCT enables continuous streaming of uninterrupted mechanical tests, as shown in Figure 2.14 (d). The experimental part of this doctoral thesis focuses on interrupted in-situ testing by using laboratory  $\mu$ CT systems.

The characterization of microstructural damage properties, such as crack length and crack density is essential to enable novel fracture prediction models for composites [53, 66–70]. Goal of in-situ  $\mu$ CT testing is the detailed characterization of internal structures while applying external load. As a result, in-situ  $\mu$ CT testing provides valuable data of the damage propagation of composites on the microstructural level [71].

A study of different  $\mu$ CT scanning strategies was carried out by the authors Yu et al. [72], in order to explore the optimum method to image fatigue damage in glass fiber woven composites. Here, the size and contrast of the cracks must be

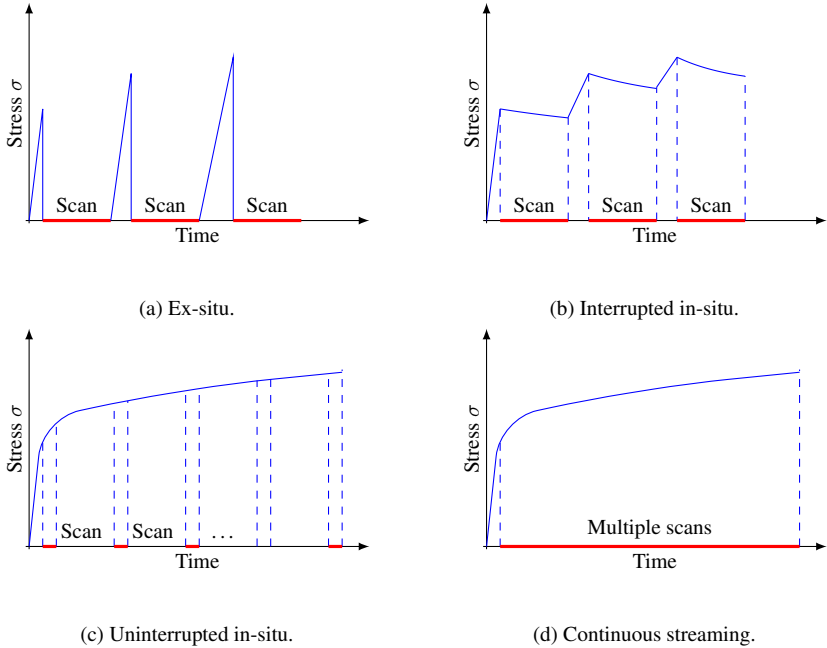


Figure 2.14: Classification of different ex-situ and in-situ imaging strategies. Schematic illustration of the test protocols and stress curves, where the load is applied displacement controlled (re-illustration, original figures by Garcea et al. [65]).

sufficiently high to reliably observe and analyze cracks. When the specimen is unloaded during ex-situ tests, the transverse cracks in the inside of the damaged specimen close. The authors Yu et al. [72] figured out, that both increasing the spatial resolution and scanning while applying load increases the detectability of cracks.

Through performing in-situ and ex-situ tests under cyclic load the different damaging stages of fatigue life are observed and characterized [73–76]. The authors Böhm et al. [77] performed and compared both ex-situ and in-situ  $\mu$ CT tests on carbon fiber-reinforced polymers (CFRP). The study shows that quantitative damage indicators including crack length, density and delamination area

are significantly different when scanned under applied load. Consequently, the authors recommend in-situ  $\mu$ CT testing in case of microstructural damage characterization.

The SRCT imaging techniques enable generating high-resolution volumetric images with a voxel size down to  $0.7\text{ }\mu\text{m}$  in a short time [78]. In-situ tests on carbon fiber-reinforced composites under quasi-static and fatigue load cases by using SRCT were carried out by several authors [78–82]. Goal of the investigation is analyzing the initiation, nucleation and propagation of different failure modes. The authors Cosmi and Bernasconi [83] investigated the different stages of fatigue life of short glass fiber-reinforced polyamide by means of interrupted in-situ SRCT. Through high-resolution volumetric images with a voxel size of  $2\text{ }\mu\text{m}$  the micro-void density along the fatigue life is characterized. The authors Garcia et al. [65, 84–87] investigated the fatigue damage mechanism of carbon fiber-reinforced polymer laminates by using both synchrotron and laboratory  $\mu$ CT systems. Although, SRCT acquire higher-resolution images than the laboratory  $\mu$ CT, the scan volume still limits the study to small samples [65]. Furthermore, laboratory  $\mu$ CT systems are much more available than those using synchrotron radiation.

Performing mechanical tests inside  $\mu$ CT systems leads to limited installation space and test performance. Especially in terms of fatigue testing were commercial in-situ setups are not available, the performance of in-situ  $\mu$ CT setups is limited compared to those of regular laboratory setups.

## 2.4 Image Processing

In addition to the development of  $\mu$ CT systems, the importance of image processing methods for evaluation of the acquired data increased in recent years. By enabling high-resolution  $\mu$ CT scans and subsequently, the observation of microstructures in an even more detailed manner, novel image processing



methods in different research fields and applications for the effective analysis are developed. The goal of image processing methods applied in material science is commonly the extraction and characterization of microstructure features, while facing the challenge of image noise and bad contrast.

In this doctoral thesis, the introduced image processing methods are focused on volumetric images acquired by  $\mu$ CT scanning. Although volumetric images are analyzed, image processing approaches developed for two-dimensional images are adopted and applied. This section provides an overview of fundamental image processing methods.

### 2.4.1 Convolutional Filter

An effective way to process images is given by convolutional filters. In general, the convolution of images is applied through convolving the input image  $g$  with the filter function  $f$  by

$$(g * f)(\mathbf{x}) = \int_{-\infty}^{\infty} f(\mathbf{x}')g(\mathbf{x} - \mathbf{x}') d\mathbf{x}'. \quad (2.31)$$

Since the volumetric images are build up by discrete voxels discrete filter masks are applied. The discrete image convolution for three-dimensional images is given by

$$g_f(x, y, z) = \sum_{x'} \sum_{y'} \sum_{z'} f(x', y', z')g(x - x', y - y', z - z') \quad (2.32)$$

and for two-dimensional images by

$$g_f(x, y) = \sum_{x'} \sum_{y'} f(x', y')g(x - x', y - y'), \quad (2.33)$$

with the input image  $g$ , the discrete filter mask  $f$  and the modified image  $g_f$ . The application of convolution filters to two-dimensional images is schematically illustrated in Figure 2.15.

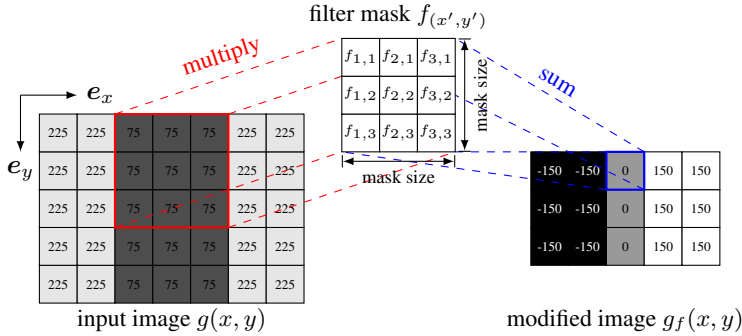


Figure 2.15: Illustrating the application of convolutional filters on two-dimensional images. Filter mask  $f_{(x',y')}$  according to Equation 2.35. By applying the filter mask with a mask size of three, the input image size is reduced by two in both dimensions, since the filter mask cannot be applied to the image edges (no image extension).

Common image processing tools that are applied through image convolution are the Gaussian smoothing and the image gradient. The three-dimensional Gaussian filter mask is given by

$$f_{\sigma}(x', y', z') = \frac{1}{(\sqrt{2\pi}\sigma)^3} e^{-\frac{x'^2 + y'^2 + z'^2}{2\sigma^2}} \quad (2.34)$$

and the two-dimensional image gradient filter mask in  $e_x$ -direction with a mask size of three by

$$f_x(x', y') = \begin{bmatrix} -1 & 0 & 1 \\ -1 & 0 & 1 \\ -1 & 0 & 1 \end{bmatrix}. \quad (2.35)$$

The image gradient filter  $f_x$  in Equation 2.35 corresponds to the filter mask applied in Figure 2.15.

## 2.4.2 Threshold Segmentation

Gray-value threshold segmentation approaches are suitable for applications in which the gray-values can be directly assigned to individual distinguished objects [8]. The basic approach of gray-value thresholding is given by subdividing the gray-value histogram by means of the threshold values  $k$ , as shown in Figure 2.16. Subsequently, all voxels are then assigned to the corresponding object based on their gray-value.

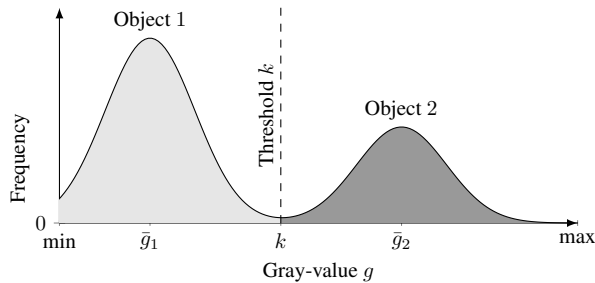


Figure 2.16: Illustration of the simple gray-value thresholding principles for segmenting two objects (Schematic gray-value histogram).

The threshold  $k$  is either defined manually or determined by using a threshold method, that takes particular aspects of the gray-value histogram into account. A frequently applied method to determine thresholds in many different applications is introduced by the authors Otsu et al. [88, 89]. The authors Pinter et al. [90, 91] compared different threshold methods in order to separate fibers and matrix in composites. As a result, the authors revealed that the moment-preserving threshold introduced by the author Tsai [92] works best in terms of separating fiber and matrix of GFRP composites.

The authors Fredo et al. [93], analyzed the damage effect of impact load on glass fiber-reinforced polymer composite laminates. Based on  $\mu$ CT scanning of the damaged samples and by means of simple gray-value thresholding (i.a. Otsu [88]) the damaged areas are segmented within the volumetric images.

Based on the determined segmentation data, perimeter, eccentricity and ratio of the damage regions are measured and studied by the authors.

### 2.4.3 Seed-Region-Growth Segmentation

Besides, simple gray-value thresholding there is a wide range of advanced segmentation approaches for various applications. Simple thresholding only involves the voxels gray-value; however, advanced segmentation approaches take further aspects, such as the relationship of adjacent voxels into account. Consequently, there is a wide range of segmentation approaches which meet the criteria of various applications. Especially, in medical science regarding the segmentation of specific parts of the human skull [94, 95].

The authors Adams and Bischof [96] presented a frequently applied Seed-Region-Growing (SRG) segmentation approach. The approach is based on two gray-value thresholds, as illustrated in Figure 2.17. In the beginning, seed regions are defined by simple gray-value thresholding  $k_{\text{seed}}$ . Subsequently, adjacent voxels, which meet the second threshold criteria  $k_{\text{growth}}$  are iteratively added to the regions. The SRG segmentation process completes, when no more adjacent voxels are added.

Figure 2.17 shows the SRG segmentation process including the initial image, defined seeds and finally segmented region. In (a) the initial image, in (b) the seed voxels and in (c) the iterative region growing result are illustrated. The SRG method segments contiguous objects where voxels with a high gray-value above  $k_{\text{growth}}$  or without neighboring bond to the growing region(s) are not segmented, as shown in Figure 2.17 (c). As a result, individually segmented voxels outside the grown region are usually avoided.

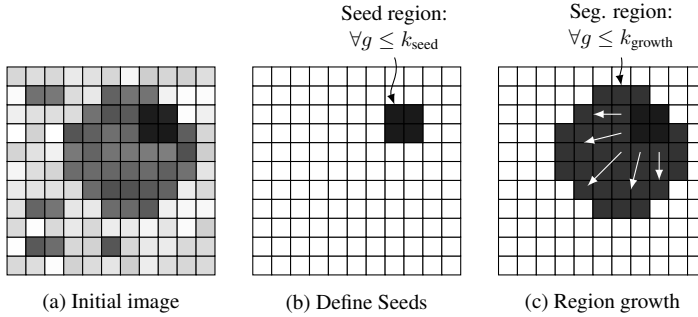


Figure 2.17: Illustrating the segmentation process of the Seed-Region-Growing (SRG) method.

(a) shows an exemplary input image and in (b) the seed voxels are defined by a strict threshold  $k_{seed}$ . Subsequently, the region is expanded iteratively by using the second threshold  $k_{growth}$  in (c).

## 2.4.4 Closing Operation

When analyzing image data, noise is always an aspect that has to be considered. Image noise and artifacts can cause individual voxels to be incorrectly assigned during the object segmentation process. Especially in case of salt-and-pepper-noise, where the gray-value of individual voxels is significantly higher or lower than those of the surrounding voxels. As a consequence, after segmentation the image data is further processed in order to achieve a better overall result. By applying morphological closing operations, voxel errors within segmented objects can be eliminated [97, 98].

The images in Figure 2.18 demonstrate the capability of the closing operation to reduce binary voxel errors. Here, two exemplary binary images in (a) are modified by adding salt-and-pepper-noise (33 %-noise) in (b) which is then eliminated by applying the closing operation in (c). Afterwards only minor artifacts remain compared with the original images.

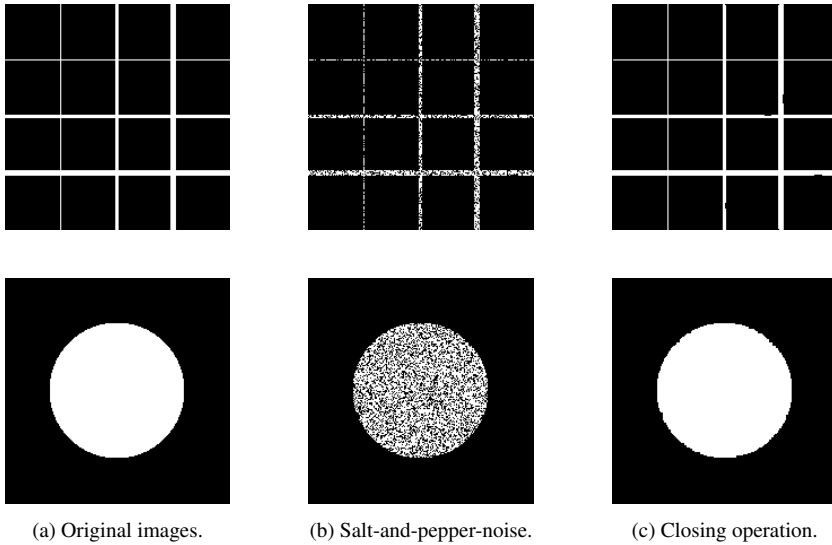


Figure 2.18: Eliminating binary errors by using morphological closing operation. Two binary images with a grid and a circle are shown in (a). In (b) salt-and-pepper-noise is added to the original images (33 %-noise) and (c) shows the closing operator result (background in black and segmented object in white).

## 2.5 Microstructure of Fiber-Reinforced Polymers

The effective macroscopic mechanical properties are a result of the combination of fiber and matrix on the microscopic level. The mechanical properties of the polymer matrix are usually considered isotropic, whereas the fiber architecture can be highly anisotropic and combines several aspects, such as fiber volume fraction, orientation and length distribution.

### 2.5.1 Fiber Orientation Principles

The microstructure of fiber-reinforced polymers significantly affects the mechanical properties. One essential aspect is the fiber orientation. In general, the fiber orientation is quantified by using the fiber orientation distribution  $\psi(\mathbf{p})$ . The distribution function  $\psi(\mathbf{p})$  returns a proportion value of fibers aligned in the related direction of unit vector  $\mathbf{p}$ . The fiber orientation distribution must be symmetric in terms of

$$\psi(-\mathbf{p}) = \psi(\mathbf{p}) \quad (2.36)$$

and normalized by

$$\oint \psi(\mathbf{p}) \, d\mathbf{p} = 1. \quad (2.37)$$

The fiber orientation distribution provides a closed and explicit description of the fiber orientation state [99]. Since the fiber orientation is difficult to parametrize, a convenient description is required. Motivated by the Fourier series expansion the authors Advani and Tucker [99] introduced an alternative formulation based on tensors. The  $n$ -order fiber orientation tensor is introduced by the  $n$ -th dyadic product of the unit vector  $\mathbf{p}$  multiplied with the fiber orientation distribution and the integration over all spatial directions. The exact formulation of the Fourier series includes a large number of  $n$ -order fiber orientation tensors, is complex and usually not necessary. Consequently, in most applications, such as prediction of mechanical behavior and prediction of the fiber orientation through process simulation (Gupta and Wang [100]), using the second-order (and fourth-order) fiber orientation tensor in Equation 2.38 is sufficient.

$$\mathbf{N} = \oint \mathbf{p} \otimes \mathbf{p} \psi(\mathbf{p}) \, d\mathbf{p}. \quad (2.38)$$

Since in practice the distribution function  $\psi(\mathbf{p})$  is usually not available, the author Ken-Ichi [101] introduced an empirical formulation based on  $N$  detected

fiber orientations  $\mathbf{n}_i$ . The empirical second-order fiber orientation tensor is determined by

$$\mathbf{N} = \frac{1}{N} \sum_{i=1}^N \mathbf{n}_i \otimes \mathbf{n}_i. \quad (2.39)$$

Based on the empirical second-order fiber orientation tensor  $\mathbf{N}$ , a smoothed distribution function  $\psi$  is calculated by

$$\psi(\mathbf{p}) \approx \frac{1}{4\pi} + \frac{15}{8\pi} \mathbf{B} \mathbf{F}(\mathbf{p}), \quad (2.40)$$

where  $\mathbf{B} = \mathbf{N} - \frac{1}{3}\mathbf{I}$ ,  $\mathbf{F}(\mathbf{p}) = \mathbf{p} \otimes \mathbf{p} - \frac{1}{3}\mathbf{I}$  and  $\mathbf{I}$  represents the identity tensor (Advani and Tucker [99]). The second-order fiber orientation tensor is symmetrical

$$\mathbf{N} = \mathbf{N}^T \quad (2.41)$$

and as a consequence of the normalization condition ( $\|\mathbf{n}_i\| = 1, \forall i = 1 \dots N$ ), the first principal invariant of  $\mathbf{N}$  is normalized by

$$\text{tr}(\mathbf{N}) = 1. \quad (2.42)$$

## 2.5.2 Fiber Orientation Measurement

The fiber orientation state is essential for predicting the mechanical properties of fiber-reinforced composites. In Section 2.1.2 various homogenization approaches are introduced. All approaches require accurate and reliable fiber orientation data.

The author Kau [102] introduced an image processing method to measure the fiber orientation on the surface of molded sheet molding compound plates based on optical photography. In order to increase the resolution and the measurement accuracy, the authors Gupta and Wang [100] extracted samples at different locations of short fiber-reinforced composite plates. The plates were



manufactured by injection molding and the acquired data are used for the validation of simulation models. The authors Jackson et al. [103] applied and validated the model established by Folgar and Tucker [104] for compression molding of short fiber-reinforced composites by adopting the particle-tracking scheme published by Givler et al. [105].

Modern  $\mu$ CT systems become an essential measurement tool in material characterization, enabling the non-destructive and three-dimensional observation of microstructures. The authors Schladitz et al. [106] used volumetric images acquired through  $\mu$ CT scanning and an anisotropic Gaussian filter to determine the fiber orientation of sheet molding compounds. An alternative method is introduced by Pinter et al. [107]. The authors make use of the structure tensor, presented by Krause et al. [108] in order to measure the local fiber orientation on the voxel level. Here, the local fiber orientations are determined without the need to segment the individual fibers.

By using X-ray scatter dark field tomography and attenuation-based  $\mu$ CT the authors Hanneschläger et al. [109] analyzed the microstructure of glass fiber-reinforced polymer parts manufactured by injection molding. The authors Hanneschläger et al. examined the fiber orientation at different locations along the mold flow including weld lines.

### 2.5.3 Single Fiber Tracking

Section 2.5.2 provides an overview of volumetric image processing methods for determining fiber orientation without the need to segment individual fibers. Besides the fiber orientation, the fiber length distribution and further the fiber aspect ratio are essential microstructure aspects that have to be considered while predicting the mold flow and the mechanical behavior. Especially, for short fiber-reinforced composites that are manufactured by using injection molding the fiber length distribution is a highly relevant microstructure aspect. In order to characterize the fiber length distribution through  $\mu$ CT scanning, the

individual fibers have to be segmented within the acquired volumetric images. To reliably segment the individual fibers, high-resolution images are necessary. In general, volumetric images with a voxel size of at least three to six times smaller than the fiber diameter are required [110–113].

The authors Hessman et al. [111], Pinter et al. [110], Maertens et al. [114]\*, Glöckner et al. [115], Teßmann et al. [116], Kastner et al. [112] and Salaberger et al. [113, 117] introduced and applied different approaches to reliably track individual fibers based on the circular voting filter, segmentation, skeletonization and Monte-Carlo algorithm.

## 2.5.4 Fiber Bundle Tracking

The fiber architecture of sheet molding compounds is distinguished by fibers arranged as fiber bundles. The authors Meyer et al. [118]\*, introduced a direct bundle simulation model, in order to predict the fiber bundle arrangement through process simulation. The model is validated by using  $\mu$ CT scans, characterized fiber bundle curvature and fiber orientation data.

Another fiber bundle based micromechanism deformation model is presented by the authors Guiraud et al. [119]. In addition to pull-out experiments, the microstructure is characterized by  $\mu$ CT scanning. Using the image processing method, introduced by Le et al. [120] fiber bundles are manually segmented and the orientation, bending, thickness, width and cross section area is measured. Since in this study fiber bundles are assumed to be straight, they are described by their orientation vector. The authors Guiraud et al. [119] used both, high-resolution volumetric images with a voxel size of  $3.2\,\mu\text{m}$  acquired by synchrotron  $\mu$ CT and volumetric images with a voxel size of  $15.6\,\mu\text{m}$  acquired by laboratory  $\mu$ CT.

Additionally to  $\mu$ CT scanning, the authors Dumont et al. [121] utilized the transparent polymethylmethacrylate (PMMA) matrix, in order to optically observe the in-plane deformation before and after mold flow deformation. In the

publications of Dumont et al. [121] and Le et al. [120] the voxel size of the applied volumetric images is  $7.5\text{ }\mu\text{m}$ .

Besides material science,  $\mu\text{CT}$  scanning and image processing is a key diagnostic method in medical science. In order to investigate the connections within the human brain, bundle tracking methods are applied. The authors Mori and van Zijl [122] provide an overview of different bundle tracking methods. A second-order probabilistic integration approach is presented by the authors Tournier et al. [123, 124]. The approach tracks along the stepwise most probable path. As a result, the connections within the human brain are reliably tracked, facing the challenge of crossing connections.

The authors Song et al. [125] analyzed the fiber orientation within initial charges and compression molded parts of long fiber-reinforced thermoplastics (LFT). The results show that the fiber orientation determined based on the fiber bundles is similar to those of the individual fibers.

By adapting the tracking methods based on Hessian matrix and eigenvalue analysis of the authors Bassier et al. [126] and Mori et al. [122, 127] from the field of medical science, the authors Bhattacharya et al. [128] tracked and analyzed fiber bundles within carbon fiber woven fabrics. Similar to the work by Bhattacharya et al. [128], the author Straumit et al. [129] utilizes that the fiber bundles in woven composites are structured and arranged in an orderly way. Here, fiber bundles are segmented from the surrounding matrix by means of the structure tensor and a voxel-based representative volume element of the periodic microstructure is determined.

### 2.5.5 Mapping of Microstructure Properties

The data management and transfer between different research fields is a key goal in today's material science. For instance, the data transfer of macroscopic mechanical properties and microstructure data between the research fields of characterization and simulation is important to develop and apply new material systems. Besides the interdisciplinary transfer between research fields, it is also important to pass data over multi-scale levels. Especially in case of numerical prediction models of fiber-reinforced composites, where the microstructure fundamentally affects the macroscopic mechanical properties. For the transfer of process simulation results of different process steps to the next step, the multi-physics mapping scheme MpCCI was developed at the Fraunhofer Institute for Algorithms and Scientific Computing [130].

The input of microstructure data, such as fiber orientation tensors are important for state-of-the-art material prediction models. Novel numerical models predict the mechanical behavior of fiber-reinforced polymers in a more detailed manner. However, in order to increase the prediction accuracy more detailed microstructure data are necessary.

Based on the fiber orientation method presented by Pinter et al. [107], the authors Schöttl et al. [131]\* introduced methods to segment individual layers of unidirectional fiber-reinforced laminates. As a result, the fiber orientations are analyzed and mapped individual for each laminate layer. The mapping scheme is described and applied as part of this doctoral thesis in chapter 4 and chapter 6. The obtained fiber orientation data of the individual laminate layers are then used to validate process simulation models [132]. Furthermore, the mapping scheme is used as part of a virtual process chain, in order to provide fiber orientation data for the validation of compression molding simulation on the one hand and input data for structural simulation on the other [9, 10].

## 2.6 Digital Volume Correlation

Surface digital image correlation (DIC) is well established, both for flat surfaces by using a single camera and curved surfaces with a stereo camera system. By applying a speckle pattern on the specimen surface, the DIC determines displacement field data of the observed surfaces. Adapting the DIC fundamental principles to volumetric images, digital volume correlation (DVC) enables three-dimensional displacement measurement within microstructures [133, 134]. One of the first applications of DVC to  $\mu$ CT data was published by the authors Bay et al. [133], in which the deformation of bones was studied.

### 2.6.1 Principles

Image correlation techniques have been developed to measure displacement fields in a non-contacting way based on image data acquired by single camera, stereo camera or  $\mu$ CT systems. The measured displacement field data are essential in many fields of solid mechanics, such as food science [135], medical science [136], geo-mechanics [137] and material science [138]. An overview of the DIC and DVC techniques developments is provided by the publications of the authors Sutton et al. [139–142]. Emerging from DIC, the development of DVC techniques is related to those of modern  $\mu$ CT systems and in-situ testing. Through in-situ  $\mu$ CT scanning, volumetric images of the initial and deformed state of the same samples are acquired. An introduction into in-situ techniques is provided in Section 2.3.5.

Using DIC displacement measurement technique, a speckle pattern is usually applied on the observed surface, in order to track the movement. Analyzing homogeneous materials, the displacement cannot be determined by using DVC and  $\mu$ CT scanning since there is no traceable microstructure. To overcome this issue, the authors Germaneau et al. [138] added small dense copper particles

to silicon and unsaturated polyurethane resin, in order to improve the local X-ray contrast. Although, the volume fraction of the particles between 1.0 % and 0.2 % is low, there is still an impact on the mechanical properties. Moreover, the local high density difference between the copper particles and the resin lead to artifacts within the acquired volumetric images. Analyzing fiber-reinforced polymer  $\mu$ CT scans, the highly heterogeneous microstructure provides high-contrast volumetric images and functions as an intrinsic speckle pattern. Consequently, no additional tracing particles have to be added here [143].

## 2.6.2 Deformation Measurement

To apply DVC, an initial volumetric image  $g_0$  of the undeformed object and a current image  $g_t$  of the deformed object are acquired. The DVC technique is based on the assumption, that by applying the correct displacement field  $\mathbf{u}$  on the initial volumetric image  $g_0$  the current image  $g_t$  is determined by

$$g_0(\mathbf{u}) \cong g_t. \quad (2.43)$$

Figure 2.19 schematically shows the DVC process. Due to the deformation, the material point P within the object is shifted. The initial and current position of point P is given by the vectors  $\mathbf{X}$  and  $\mathbf{x}$ , respectively.

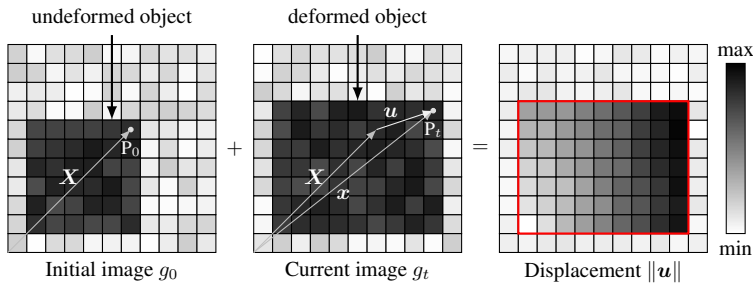


Figure 2.19: Digital volume correlation principles illustrated schematically on artificial data.

The displacement field  $\mathbf{u}$  is parametrized by assuming either rigid transformation, affine transformation or local deformation of the object and corresponding interpolation functions. Subsequently, the displacement field is described by a set of parameters. The correct displacement field is determined by iteratively optimizing these parameters, until the Equation 2.43 is sufficiently fulfilled. The global correlation coefficient  $C$

$$C = \int_V \|g_0(\mathbf{u}) - g_t\| \, d\mathbf{v} \quad (2.44)$$

quantifies the loss score of the optimization loop.

Solving the DVC optimization problem is computational expensive. Especially, for large volumetric images and complex deformation cases. Consequently, multi-threading and efficient implementation are important to apply DVC in an acceptable run time. The authors Klein et al. [144] and Shamonin et al. [145] provide the efficient open-source DVC toolbox Elastix. In addition to open source code, DVC methods are also available in commercial  $\mu$ CT data processing software tools. For instance, the  $\mu$ CT-data analyzing softwares by Thermo Fisher Scientific (Amira-Avizo) [146], LaVision (StrainMaster) [147] and Volume Graphics (VGSTUDIO MAX 3.4) [148] provide DVC modules. Besides the application in material science in terms of characterization, DVC methods are used together with microstructure simulation models. The three-dimensional deformation of polypropylene solid foam by means of  $\mu$ CT and DVC is analyzed by the authors Roux et al. [149]. The three-dimensional deformation is determined by using an approach, which combines the DVC technique and finite element method (FEM). The authors apply an introduced basis function from FEM (C8P1 elements) as a basic displacement function for the DVC. Subsequently, continuum mechanical aspects are considered and the results from DVC measurement and FEM calculation are coherently compared [150–152].

## 2.7 Artificial Intelligence

In this section fundamental methods of artificial intelligence in terms of image processing are introduced. Section 2.7.1 provides a brief historical review and introduces the fundamental idea behind artificial intelligence. In Section 2.7.2 the basic applications of artificial neural networks (ANN) are presented. Convolutional neural networks (CNN) adapt ANN for the use of image processing based on convolutional filter masks. Lastly, an overview on CNN functions is provided in Section 2.7.3.

### 2.7.1 Principles

One of the key figures of modern computational science is Turing [153] for introducing basic concepts of today's computational intelligence and science in general. In 1943, the foundations of modern ANN were laid by the authors McCulloch and Pitts [154] for the first fundamental modeling of biological neurons based on logical operators and later in 1949 by the author Hebb [155] through linking single neurons and building up an ANN. The 1956 research workshop organized by McCarthy et al. [156] is widely regarded as the birth of modern artificial intelligence. Driven by the computer hardware development in the last decades, ANN gained increasing importance and found various applications, among others, in the research fields of medical science [157], transportation [158] and banking [159], as shown in Figure 2.20.

Regarding artificial intelligence, this doctoral thesis focuses on supervised machine learning concepts. ANN are powerful methods for data processing inspired by natural neural networks. In contrast to classical data processing methods, no rules are previously defined, but determined by training using input data and associated ground truth, as illustrated in Figure 2.21. As a result, ANN and CNN are appropriate for the use in application cases with sufficient training data and repeating patterns.



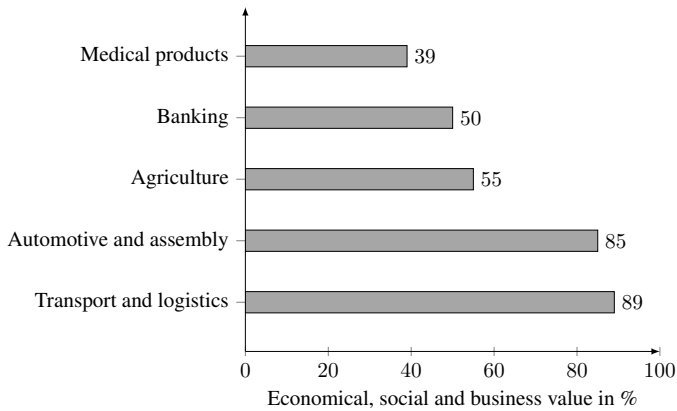


Figure 2.20: Incremental value from artificial intelligence usage in selected sectors 2018 (data by Chui et al. [158, 159]).

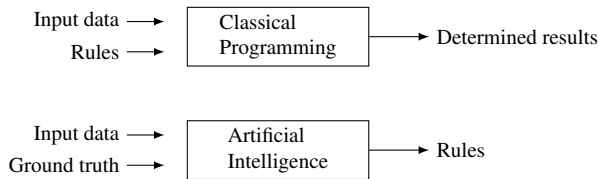


Figure 2.21: Contrast between classical programming and artificial neural network paradigm (re-illustration, original image by Chollet [160]).

## 2.7.2 Artificial Neural Networks

Inspired by biological neural networks, ANN are build up of a large number of neurons, as shown in Figure 2.22. The input data of each neuron is processed using non-linear activation functions  $f$ . The communication between the neurons is modeled by weighting factors  $w$ .

In general, the neurons within an ANN are structured by layers as shown in Figure 2.23. The first layer receives the input data and is called input layer. The last layer is the output layer and returns the predicted results. The layers

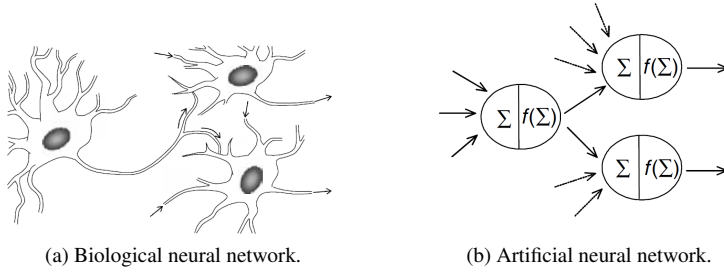


Figure 2.22: Connection and communication between (a) biological and (b) artificial neural networks (figures by Samarasinghe [161]).

between input and output layer are called hidden layers and represent the actual network. The combination of neurons, activation function and connection structure is called the architecture of the ANN.

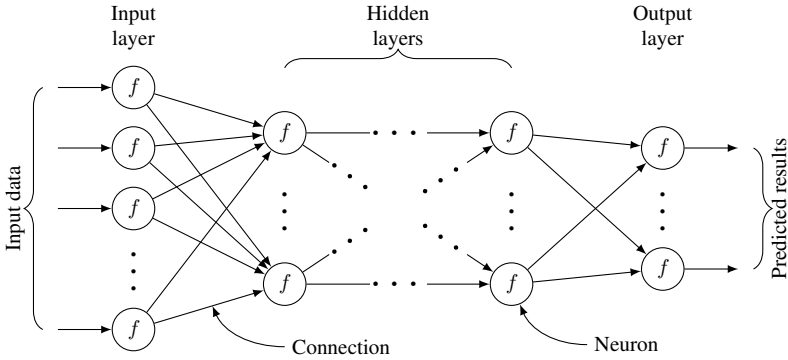


Figure 2.23: Interaction of the input data, neurons, connections, the layer-wise structure and the predicted results of artificial neural network.

The output signal  $b_j$  of a neuron  $j$  is determined by multiplying the output signals  $a_i$  of the previous neurons  $i$  with the weighting factors  $w_i$ ,  $i = 1, \dots, N$  of the connection, summing up and applying the activation function  $f_j$  by

$$b_j = f_j(z_j), \text{ with } z_j = \sum_{i=1}^N w_i a_i, \quad (2.45)$$

and illustrated in Figure 2.24. The function of the whole ANN is the result of the interaction of all neurons.

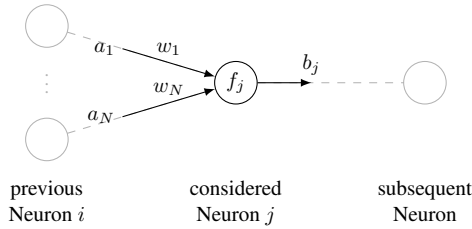


Figure 2.24: Data processing and activation function  $f$  of a single neuron  $j$  within an artificial neural network.

Frequently applied activation functions are the sigmoid and rectified linear unit (ReLU) function listed in Equation 2.46 and Equation 2.47, respectively [162].

Sigmoid: 
$$f(z) = \frac{1}{1 + e^{-z}} \quad (2.46)$$

Rectified Linear Unit (ReLU): 
$$f(z) = \begin{cases} 0, & \text{if } z < 0. \\ z, & \text{if } z \geq 0. \end{cases} \quad (2.47)$$

In addition to the sigmoid and the ReLU function, the softmax function is an activation function which is designed for the usage within the output layer of classification applications. By applying the softmax function

$$\text{Softmax: } f_j(z_1, \dots, z_N) = \frac{e_j^z}{\sum_{i=1}^N e^{z_i}} \quad (2.48)$$

the sum of the  $N$  output signals is normalized.

The architectures of ANN are universally applicable for many different tasks. In order to complete the ANN model and use it for a specific application, the weighting factors  $w_i$  must be determined. This is the goal of the training process, in which the optimal weighting factors for a specific application are determined based on a training data set, including input data and corresponding ground truth. The weighting factors are determined by iterative optimization, as shown in Figure 2.25.

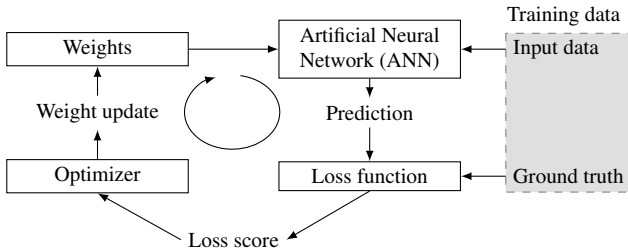


Figure 2.25: Determination of weight factors by using the training data set and iterative optimization (re-illustration, original figures by Chollet [160]).

Task of the loss function is to return a steady loss score, which represents the current training status. An appropriate set of weighing factors is found when the loss score is sufficiently small. A commonly used loss function is the cross entropy given by

$$\text{Cross-Entropy } (M > 2): \quad \text{loss} = - \sum_{i=1}^M y_i \log(p_i), \quad (2.49)$$

where the prediction probability  $p$  is the proportion of correctly predicted results and  $y$  the training data fraction of the  $M$ -number classes. In case of a binary classification task ( $M = 2$ ) the binary cross entropy is determined accordingly by

$$\text{Binary Cross-Entropy: } \text{loss} = -y \log(p) - (1 - y) \log(1 - p). \quad (2.50)$$

### 2.7.3 Convolutional Neural Networks

In recent time CNN gaining increasing applicability to image processing, due to the ability of efficient image pattern recognition. Similar to ANN, CNN are adapted for image processing tasks. By training the parameters of convolutional filter masks, introduced in Section 2.4.1, CNN are designed for pattern classification, detection and segmentation within images. Once the architecture is set up and the filter parameters of the CNN are properly trained, predictions are performed in an efficient manner. These aspects make CNN suitable for analyzing large image data, such as volumetric images.

Similar to ANN, CNN are build up of convolutional filters structured by layers. By connecting several convolutional filter layers in series, patterns are recognized hierarchically. The process is schematically illustrated in Figure 2.26. Since convolutional filters are applied, features are recognized within the examined image in a transversal invariant way [160]. This means, that features and patterns are recognized equally all over the image, regardless of where they are located.

Besides convolutional filter layers, additional layers with specific functions are installed in CNN architectures. Max pooling and mean pooling layers return the maximum and mean value within the specified filter mask, respectively. The task of the two types of pooling layers is to extract the most significant filter response and reducing the image data.

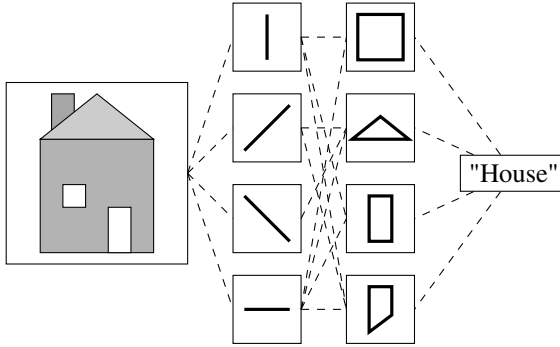


Figure 2.26: Schematic illustration of the principle approach for pattern recognition based in convolution neural networks (new-illustration, original illustration by Chollet [160]).

Dropout layers are another layer type that is frequently applied in CNN architectures [163, 164]. During training, the dropout layer set the output value of random neurons to zero. The proportion of omitted neurons is selected by the dropout value, which is usually between 0.2 and 0.5. As a result, dropout layers reduce over-fitting effects and increase the regularization of the CNN model [160, 163–165].

Based on convolutional filter, pooling and dropout layers, many different CNN architectures can be built. The basic structure of CNN allows them to be trained and used for the recognition of different image patterns. For this reason, standardized architectures are used in many different applications. One of the first CNN architectures for image classification is presented by the authors LeCun et al. [166, 167]. In practice, CNN are usually combined with ANN to interpret the extracted features. One of the first CNN with such architectures are presented by the authors Krizhevsky et al. [168], Simonyan and Zisserman [169] and He et al. [170].

As shown in Figure 2.27, the VGG architecture named after the Visual Geometry Group at the University of Oxford and introduced by Simonyan and Zisserman [169] consists of two parts. The first part is a CNN, build up of

convolutional filter and max pooling layers. Task of the CNN part is to extract features and patterns from the analyzed image. The second part is a fully connected ANN, which evaluates the extracted features and classifies the recognized objects.

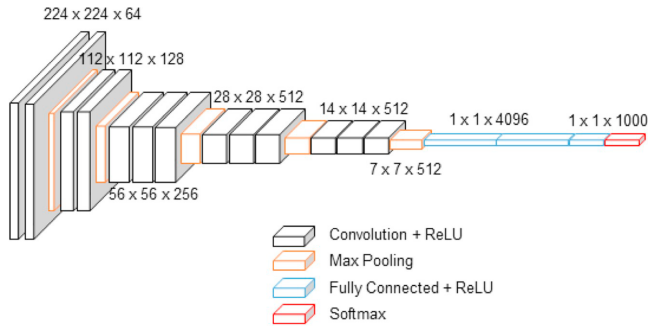


Figure 2.27: The VGG16 architecture for pattern detection and classification by Simonyan and Zisserman [169] (illustration by Dung and Anh [171]).

A typical task of CNN models such as the VGG16 architecture in Figure 2.28 is the classification of imaged objects. Output of such CNN models are single class labels, as shown in Figure 2.26 and Figure 2.28 (a). Furthermore, in many applications the output should also include the location of specific objects. Additional to classification, there are CNN for detection and segmentation tasks, where the location of specific objects is determined. Figure 2.28 illustrates the different outputs between classification, detection and segmentation. In case of detection tasks, a rough object localization is indicated by using bounding boxes, as shown in Figure 2.28 (b). CNN for segmentation tasks indicate the location of the searched objects in the most exact way, by segmenting the objects pixel-wise and returning a binary image of the same size as the input image for each class (see Figure 2.28 (c)).

Similar to classification, there are standardized and frequently applied CNN architectures for object segmentation applications. The U-Net architecture presented by Ronneberger et al. [172] is based on the work of Cirosan et al. [173]

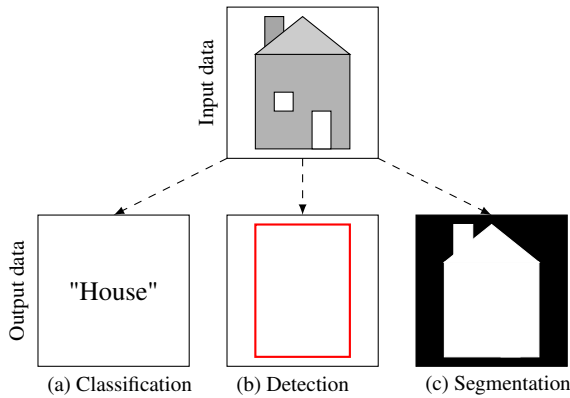


Figure 2.28: The difference between the classification, detection and segmentation tasks of CNN. For classification in (a) the output is a single class label. In (b) the detected object is located by bounding boxes (red) and (c) the object is segmented pixel-wise (white pixels).

and is a frequently used CNN architecture, which segments objects pixel-wise. Figure 2.29 illustrates the standardized U-Net architecture. In the first half of the U-Net architecture on the left, features of the input image are extracted progressively. Subsequently, the second part expands the acquired information and generates the segmented output image. The key aspect of the U-Net architecture is that the extracted features are passed on several abstraction levels and the avoidance of a bottleneck, which enables the precise segmentation of even small objects.

The pixel-wise object segmentation is a binary classification for each pixel. The results of the pixel-wise segmentation make it possible to extend the evaluation metrics of CNN. The segmented object is described as positive and the background as negative. Correctly segmented pixels are described as true and incorrect pixels as false. As a result, there are four different cases for each predicted pixel, that are summarized in Table 2.2: true positive (TP), true negative (TN), false positive (FP) and false negative (FN).



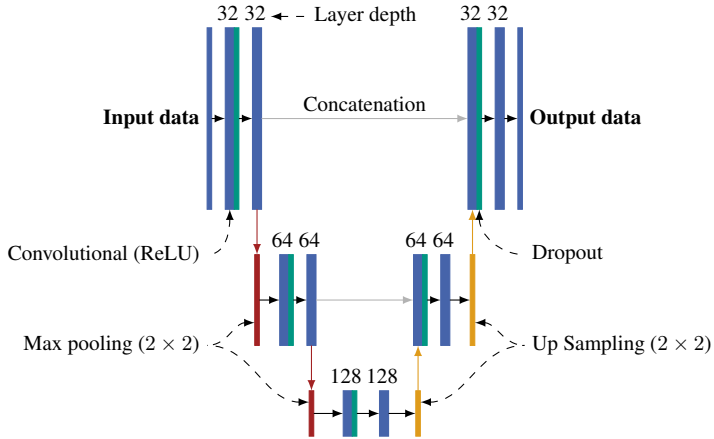


Figure 2.29: The U-Net architecture for object segmentation tasks by Ronneberger et al. [172].

Table 2.2: Detailed categorization of the pixel-wise object segmentation results.

Ground Truth \ Predicted Results	Object	Background
	TP	FN
Object	TP	FN
Background	FP	TN

To monitor and evaluate the capability of trained ANN and CNN models, the accuracy metric is introduced by the ration between the number of correct predictions and the total number of predictions

$$\text{Accuracy} = \frac{\text{TP} + \text{TN}}{\text{TP} + \text{TN} + \text{FN} + \text{FP}}. \quad (2.51)$$

In addition to the accuracy for general tasks in Equation 2.51, further metrics to quantify the segmentation results are introduced [174, 175]. The precision value in Equation 2.52 determines the proportion of the segmented pixels,

which are actually correct and the recall value in Equation 2.53 the proportion of positive pixels, which are identified correctly.

$$\text{Precision} = \frac{TP}{TP + FP} \quad (2.52)$$

$$\text{Recall} = \frac{TP}{TP + FN} \quad (2.53)$$

Overall, the precision metric evaluates the overestimation and the recall value the underestimation of the segmented objects. This issue is illustrated in Figure 2.30.

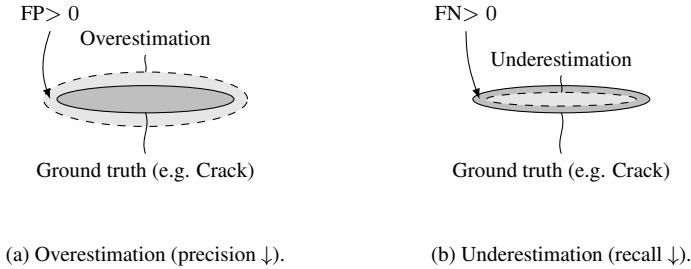


Figure 2.30: Monitoring and quantifying over- and underestimation of the segmented objects by means of precision and recall metrics.

To fully evaluate the capability of a trained model, both the precision and recall have to be examined. However, there is a contradiction between the precision and recall metrics. Combining precision and recall, the F-measure in Equation 2.54 by Chinchor [176] is balanced between those two by

$$\text{F-measure} = \frac{2 \cdot \text{Recall} \cdot \text{Precision}}{\text{Recall} + \text{Precision}}. \quad (2.54)$$

## 2.8 Damage Segmentation

The characterization and classification of occurring damages is a key aspect in material science through all investigated material systems. In case of fiber-reinforced polymers under fatigue load, the initiation and propagation of cracks usually leads to the final fracture of components. Subsequently, the characterization and modeling of the initiation and propagation cracks within brittle material systems is important to predict the fatigue life [28, 177].

The authors Paris and Erdogan [178] presented a fundamental power law relationship for crack propagation based on stress intensity factors. In the contribution of Owen and Bishop [179, 180] crack growth test under cyclic tensile load on polyester-reinforced chopped glass fiber mats were carried out. The crack length was measured by using a clip gauge between two clamped knife edges. In addition, the measured specimen compliance and crack length are linked and the crack propagation power law by Paris and Erdogan [178] is applied.

There is a wide range of non-destructive testing methods for different material systems and applications. The authors La Saponara and Elhajjar [181] provide an overview on experimental methods to examine microscopic damage in fiber-reinforced polymers. The most common non-destructive testing methods for evaluation of cracks are ultrasonic inspection, acoustic emission, thermography and  $\mu$ CT scanning [182]. In comparison to other non-destructive characterization methods,  $\mu$ CT offers the opportunity to acquire detailed volumetric images of the investigated microstructures. The contribution of Maire and Withers [143] provides an overview of the possible applications of  $\mu$ CT from acquisition techniques, conventional threshold segmentation to DVC in various research fields. In this doctoral thesis, microscopic damage is characterized by means of  $\mu$ CT scanning. Subsequently, the introduced methods focus on the characterization of cracks within digital volumetric images.

## 2.8.1 Threshold Segmentation

When it comes to conventional segmentation of objects in digital images, thresholding methods are widely used image processing techniques [183]. The threshold values are selected either manually, automatically or by using standardized threshold methods [88, 92].

Since the microstructure of fiber-reinforced polymers is highly heterogeneous, it is difficult to segment features such as cracks and voids. The author Yu et al. [72] compared different thresholding techniques and evaluated the capability to segment cracks within  $\mu$ CT volumetric images of composites. In general, segmentation of features in gray-scale volume images requires sufficient gray-scale contrast between the features and the surrounding background. The author Yu et al. [72] introduced the contrast value  $\Delta C_{\text{crack}}$  regarding cracks within composites by

$$\Delta C_{\text{crack}} = \frac{\|\bar{g}_{\text{crack}} - \bar{g}_{\text{composite}}\|}{\bar{g}_{\text{composite}}}, \quad (2.55)$$

where  $\bar{g}_{\text{crack}}$  is the mean gray-value of the crack and  $\bar{g}_{\text{composite}}$  of the surrounding composite. In case of poor contrast, the mean gray-value of the crack is equal to the surrounding composite ( $\bar{g}_{\text{crack}} = \bar{g}_{\text{composite}}$ ), which results in a contrast value of  $\Delta C_{\text{crack}} = 0$ . The best case for segmentation is given, when the mean gray-value of the crack is much smaller (or higher) than those of the surrounding composite ( $\bar{g}_{\text{crack}} \ll \bar{g}_{\text{composite}}$ ). In this case the contrast value would be close to one ( $\Delta C_{\text{crack}} \rightarrow 1$ ).

The authors Wright et al. [78] investigated the damage mechanisms of unidirectional carbon fiber-reinforced epoxy laminate. Ex-situ tests of notched specimens are carried out in order to observe damaging at the notch tip. Through synchrotron tomography scanning, ultra-high resolution volumetric images with a isotropic voxel size down to  $0.7 \mu\text{m}$  are acquired. By using gray-value thresholding technique the damaged regions are segmented and manually classified.

The authors Yu et al. [72, 75, 76, 184] carried out fatigue in-situ  $\mu$ CT tests on woven glass fiber reinforced composite. The voxel size of the acquired volumetric images was  $11.8\ \mu\text{m}$ . Cracks are segmented by using gray-value thresholding and are subsequently classified. In addition, contrast agent and staining procedure were applied to detect cracks more easily. In Figure 2.31 different types of cracks are segmented, classified and colored according to their type. Observed damage mechanisms are resin cracking, transverse cracks, binder/binder (B/B), weft/binder (W/B), binder/resin (B/R) and weft/resin (W/R) interface failure. The different cracks are classified based on their orientation and local neighboring microstructure.

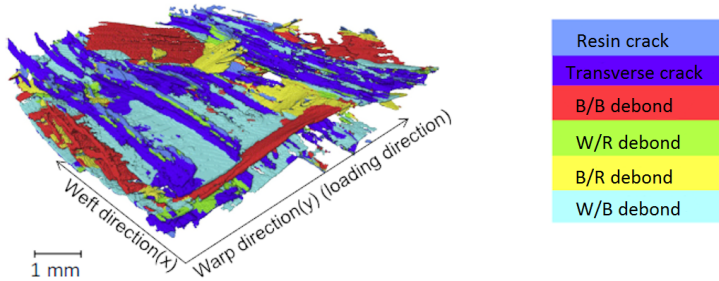


Figure 2.31: Segmentation and classification of different type of cracks within woven glass fiber reinforced composite (figure by Yu et al. [76]).

Besides fiber-reinforced polymers and material science, also in different research domains fracture processes and damage mechanisms are examined based on  $\mu$ CT scanning and threshold segmentation. For instance, the crack propagation within various types of stone material are investigated by means of  $\mu$ CT scanning and threshold segmentation in the field of geology [185, 186].

## 2.8.2 Digital Volume Correlation

DIC method tools for determining displacement fields on surfaces by using single or stereo camera systems are well established. Based on the measured

displacement field data, the strain field and other features can be derived. As introduced in Section 2.6, DVC methods adapt the fundamental principles of DIC to volumetric images acquired by  $\mu$ CT scanning.

Today, DVC methods are available in many software tools [144–148]. In general, DVC is appropriate for  $\mu$ CT volumetric images where sufficient gray-value contrast is intrinsically given by the examined microstructure. In materials science, this applies to material systems with highly heterogeneous microstructure, such as fiber-reinforced composites and homogeneous materials with isolated particles or precipitates [143].

An important application of DVC is the characterization of cracks within microstructures. The restricted nature of solid deformations and the compatibility of kinematic hypotheses lead to the fact that cracks result in an ambiguity and singularity of the displacement field. The authors Wang et al. [82, 187] and Agyei et al. [188] examined the three-dimensional strain distribution and damage mechanisms within carbon fiber-reinforced polymers, foam structures and short glass fiber-reinforced polymers by means of in-situ SRCT imaging and full-field DVC methods. Agyei et al. [188] detected crack regions through thresholding the DVC results.

In the contribution of Rannou et al. [189] a multi-scale crack detection method by means of DVC is introduced. The authors carried out synchrotron in-situ tests on nodular graphite cast iron. The average nodular graphite diameter is  $50\mu\text{m}$  and acts as natural markers for the DVC. Figure 2.32 shows in (a) the synchrotron tomography image under maximum load, in (b) the displacement field obtained by DVC and in (c) the determined crack surface. In addition, the stress intensity factors at the crack tip are calculated by combining DVC and FEM methods. Other fatigue synchrotron in-situ studies dealing with nodular graphite cast iron and DVC were carried out by Limodin et al. [151] and Réthoré et al. [152]. In addition, an extended DVC approach combining DVC fundamentals and finite-element elements is introduced [150]. As a result, the displacement field close to the crack tip was measured and compared to results of finite element method simulation.

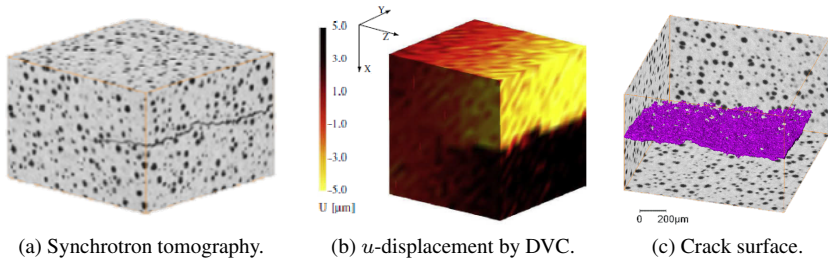


Figure 2.32: Synchrotron tomography in-situ testing on nodular graphite cast iron. (a) Tomography image of the occurred crack, (b)  $u$ -displacement field vertical to the crack surface by DVC and (c) the determined crack surface by correlation residual field thresholding (figures by Rannou et al. [189]).

### 2.8.3 Convolutional Neural Networks

Due to their diverse applicability, high accuracy, and efficient use, CNN, as presented in Section 2.7.3, are well suited for the analysis of image data. Especially for feature extraction, CNN are increasingly used alongside conventional image processing methods, such as thresholding techniques.

The visual inspection of concrete surfaces for cracks are important to quantify the health status of buildings, road pavements and civil structures. In recent decades, crack detection based on computer vision techniques in combination with autonomous image acquisition has been extensively investigated in many areas of civil engineering. The ability of CNN to reliably detect repetitive patterns, such as cracks, lead to an increasingly important role of CNN in this application field.

A widely used application is the periodic monitoring and evaluation of concrete structures. The authors Dung and Anh [171], Jiang and Zhang [190], Cha et al. [191], Feng et al. [175] and Yang et al. [192] presented CNN methods for the defect classification, detection and segmentation on surface of concrete structures in civil engineering, such as buildings, dams and bridges.

Additional to buildings, real-time crack inspection is a critical task for the periodic maintenance of concrete and asphalt road pavements. The application of vision-based automated crack detection methods using CNN are a reliable and time-saving way. Various vision-based CNN methods are proposed in the contribution of Pauly et al. [193], Dung and Anh [171], Fan et al. [194] and Zhang et al. [195, 196].

The inspection of high-security components is time-consuming and requires a high degree of accuracy to comply with the necessary safety regulations. A CNN based method to inspect nuclear power plant components was introduced by the authors Chen et al. [197]. The CNN method deals with crack detection of metallic surfaces, whereby the cracks must be distinguished from weld seams, scratches and grinding marks. The CNN task, image size, number of training data and achieved accuracy of introduced applications are listed in Table 2.3. Figure 2.33 shows the output of exemplary CNN for (a) crack classification, (b) detection and (c) segmentation tasks. In addition, the achieved metrics of the crack segmentation tasks are listed in Table 2.4.

Besides crack recognition within civil structures based on optical photography, the authors Bang et al. [198] used thermography imaging and CNN to detect cracks within composite structures.

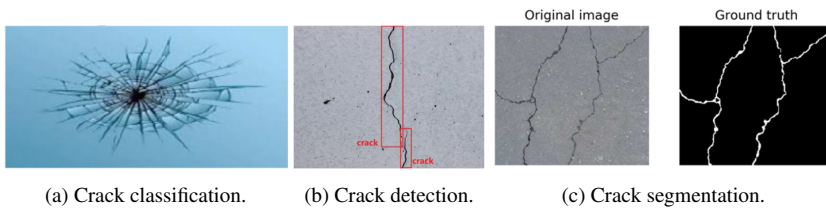


Figure 2.33: Comparing the results and output of crack classification, detection and segmentation by using CNN for safety and inspection tasks. In (a) crack classification by Kouze-hgar et al. [199], in (b) crack detection by Jiang and Zhang [190] and in (c) crack segmentation by Yang et al. [192].



Table 2.3: Summary of presented crack classification, detection and segmentation models in civil engineering. Image size, number of training data and achieved accuracy.

Task	Image size	Training data sets	Accuracy	Reference
Class.	$480 \times 240 \text{ px}^2$	3104	89.67 %	Kouzehgar et al. [199]
Class.	$99 \times 99 \text{ px}^2$	40000	91.30 %	Pauly et al. [193]
Class.	$227 \times 227 \text{ px}^2$	32000	99.90 %	Dung and Anh [171]
Class.	$227 \times 227 \text{ px}^2$	30000	99.92 %	Fan et al. [194]
Det.	$640 \times 480 \text{ px}^2$	1030	94.48 %	Jiang and Zhang [190]
Det.	$256 \times 256 \text{ px}^2$	32000	98.22 %	Cha et al. [191]
Det.	$120 \times 120 \text{ px}^2$	296804	98.30 %	Chen et al. [197]
Segm.	$227 \times 227 \text{ px}^2$	400	89.30 %	Dung and Anh [171]
Segm.	$256 \times 256 \text{ px}^2$	1800	$\approx 90$ %	Zhang et al. [195]
Segm.	$1024 \times 512 \text{ px}^2$	2500	$\approx 90$ %	Zhang et al. [196]
Segm.	$512 \times 512 \text{ px}^2$	35100	$\approx 90$ %	Zou et al. [200]
Segm.	$608 \times 608 \text{ px}^2$	404	97.27 %	Feng et al. [175]
Segm.	$224 \times 224 \text{ px}^2$	800	97.96 %	Yang et al. [192]

Table 2.4: Additional information of the achieved performance precision, recall and F-measure metrics of different crack segmentation models in civil engineering.

Task	Precision	Recall	F-measure	Reference
Segm.	89.30 %	-	89.30 %	Dung and Anh [171]
Segm.	90.13 %	87.63 %	88.86 %	Zhang et al. [195]
Segm.	89.91 %	91.84 %	89.62 %	Zhang et al. [196]
Segm.	-	-	90.95 %	Zou et al. [200]
Segm.	80.45 %	80.31 %	79.16 %	Feng et al. [175]
Segm.	81.73 %	78.97 %	79.95 %	Yang et al. [192]



# 3 Sheet Molding Compounds

The investigations and developed methods in this doctoral thesis focus on the characterization of SMC. In this chapter SMC material systems in general and the investigated SMC material system in particular are introduced. First the manufacturing process of SMC is presented and subsequently, impact of process parameters and especially the initial charge configuration on the SMC microstructure are introduced. These aspects together with the description of the SMC microstructure from different scale levels are fundamental for the microstructure characterization methods in this work.

Furthermore, the mechanical behavior with respect to the manufacturing process, SMC composition and applied load cases are presented. The analytical state-of-the-art approaches in Section 2.2.4 are applied to the investigated SMC material system in order to estimate the expected damage behavior. Overall, these aspects are essential for the developed damage characterization methods and the obtained insights in this doctoral thesis. These chapters represent a transitional step from the general state-of-the-art introduction to the developed methods and obtained results in this work.

## Contents

---

3.1 Manufacturing of SMC . . . . .	68
3.2 Microstructure and Mechanical Characteristics of SMC	74

---

## **3.1 Manufacturing of SMC**

The manufacturing process of SMC is basically subdivided in two parts: manufacturing of the semi-finished SMC and subsequently, the compression molding process. Important parameters to adjust the SMC manufacturing process are the charge configuration and the SMC composition. Those aspects and the manufacturing process itself are introduced in this section.

### **3.1.1 Semi-finished SMC**

SMC material systems combine good specific mechanical properties, low costs and fast manufacturing cycle times [201]. In the automotive industry a low process time is mandatory due to the high production rhythm. SMC material systems meet both, lightweight and mass production criteria, which makes SMC components highly relevant for automotive applications [7].

Figure 3.1 shows schematically the semi-finished SMC manufacturing process. First, continuous fiber rovings are chopped into fiber bundles with a specific length of typically 25.4 mm (1 inch). The chopped fiber bundles drop randomly oriented onto a resin coated carrier foil and are then covered by another resin coated carrier foil. By going through the impregnation zone, the fiber bundles are infiltrated by the resin. Afterwards, the semi-finished SMC rolls are stored for maturation. During the maturation process the resin viscosity increases by three to four orders [201].

### **3.1.2 Compression Molding**

In order to produce the finished SMC components, the matured SMC is cut and weight out into specified charge patches. The cold SMC charges are then placed into a preheated mold form, as shown in Figure 3.2. By using compression molding technology, the SMC are formed into the final geometry followed

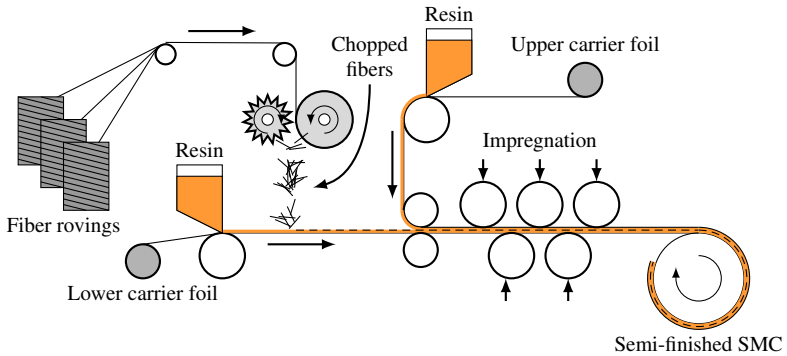


Figure 3.1: Manufacturing process of semi-finished SMC.

by curing of the resin matrix at approximately  $150\text{ }^{\circ}\text{C}$  and  $2500\text{ kN}$ . The SMC components in this doctoral thesis are manufactured at Fraunhofer Institute for Chemical Technology (ICT) in Pfinztal, Germany by using a press of Dieffenbacher GmbH (Eppingen, Germany) under the leadership of Sergej Ilinzeer.

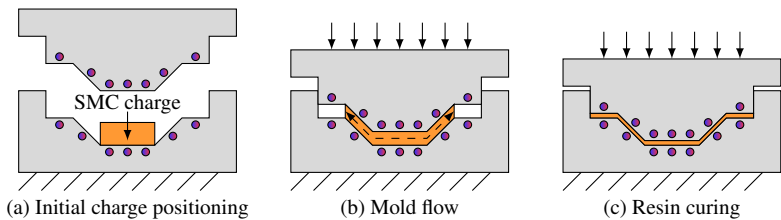


Figure 3.2: The SMC compression molding process of generic geometries. In (a) placing the semi-finished SMC initial charge, (b) compression molding and (c) finally, curing of the resin.

### 3.1.3 SMC Components

In this doctoral thesis a SMC material system is analyzed, which consists of an unsaturated polyester polyurethane hybrid (UPPH) resin reinforced by glass

fibers. As stated in Section 3.1.2, the investigated SMC material was manufactured entirely at the Fraunhofer ICT in Pfinztal, Germany. Detailed informations of the SMC composition are listed in Table 3.1. The SMC composition was developed at the Fraunhofer ICT under the leadership of David Bücheler [202].

Table 3.1: Components of the examined glass fiber-reinforced UPPH SMC.

Component	Trade name	Supplier	Content
UPPH resin	Daron ZW 14141	Aliancys	100 parts
Release agent, Flowaid	BYK 9085	BYK	2 parts
Deaeration aid	BYK A-530	BYK	0.5 parts
Inhibitor	pBQ	Fraunhofer ICT	0.3 parts
Peroxide	Trignox 117	Akzonobel	1 parts
Thickener, Isocyanate	Lupranat M20R	BASF	24.2 parts
Glass-fiber	Multistar 272 4800 80	Johns Manville	41 wt. %

### 3.1.4 SMC Charge Configuration

One important parameter to adjust the SMC component during the manufacturing process is the charge configuration. The initial position and coverage of the SMC charge affect the mold flow behavior during the compression molding process. For instance, a small charge coverage results in a long flow path during compression molding which leads to a highly oriented fiber distribution due to the orientation of the fibers during the mold flow. In contrast, large or full charge coverage result in a more planar isotropic fiber distribution. This phenomena and different charge coverages are schematically illustrated in Figure 3.3.

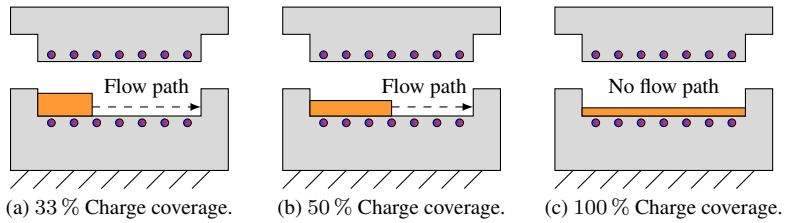


Figure 3.3: Different initial charge configurations and flow paths. In (a) long flow path, (b) medium flow path and (c) no significant flow path due to full charge coverage

The author Motaghi and Hrymak [203] analyzed the effect of 30 % and 62 % SMC charge coverage on the microstructure during compression molding. It was figured out that in case of 62 % charge coverage there is no significant change of the fiber orientation between the initial charge and final component due to the relatively short flow path. In contrast, there is a significantly higher alignment of the fiber bundles along the mold filling direction (MFD) in case of the 30 % charge coverage.

In the contribution by Jackson et al. [103] SMC mold filling experiments are carried out, where the initial charges cover between 33 % and 100 % of the final area. The authors Chen and Tucker [204] studied the effect of fiber volume content, charge coverage and fiber orientation of glass fiber-reinforced thermoset polyester SMC on the mechanical properties. The influence of the charge coverage on the fiber orientation of the molded plates is determined by using radiography. The fiber volume fraction of maximum and minimum fiber orientation listed in Table 3.2 represent the peak and low points of the respective fiber orientation distribution, as illustrated in Figure 3.4. As a consequence, high fiber volume fraction values of the maximum fiber orientation indicate a high anisotropic fiber distribution. Both, the results of Chen and Tucker [204] in Table 3.2 for 33 % initial charge coverage and those of Gandhi et al. [205] in Figure 3.4 reveal a corresponding fiber volume fraction of about 21 vol.% for the maximum fiber orientation.

Table 3.2: Effect of the charge coverage on the fiber orientation distribution of glass fiber-reinforced polyester SMC. The data are manually extracted from the contribution of Chen and Tucker [204].

Charge coverage	Fiber volume fraction of the <b>maximum</b> fiber orientation	Fiber volume fraction of the <b>minimum</b> fiber orientation
100 %	8 vol. %	2 vol. %
67 %	12 vol. %	2 vol. %
50 %	19 vol. %	2 vol. %
33 %	21 vol. %	1 vol. %

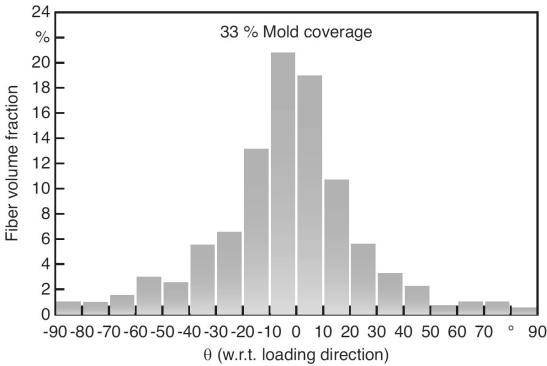


Figure 3.4: The fiber orientation distribution histogram of SMC plate with an initial mold coverage of 33 %. Fiber volume fraction of the most dominate fiber orientation is approximately 21 vol. % (figure by Gandhi et al. [205]).

Overall, the measured fiber orientation histograms in the contributions of Jackson et al. [103] and Chen and Tucker [204] both show an increasing level of fiber alignment along the MFD as a result of decreasing the charge coverage. Those results reveal that the initial charge coverage has a major impact on the SMC microstructure and the fiber orientation in particular. These insights are important for adjusting, characterization and comprehending the examined



SMC microstructure in this doctoral thesis. By adjusting the initial charge coverage different fiber orientation states are generated, which are then characterized in terms of the microstructure and damage behavior.

### 3.1.5 Weld Line Formation

In practice, as a result of the charge configuration or the component geometry two or more mold flow fronts can meet during the mold filling process. Subsequently, weld lines occur as a consequence of these clashing mold flow fronts. In general, the microstructure and mechanical properties of weld lines are a weak point and it is common to try to avoid them or to position them in a suitable location. Although attempts are made to avoid weld lines, they cannot always be avoided in practice. In particular, for the manufacturing of complex geometries where melt flow separation occurs. Figure 3.5 illustrates schematically how weld lines take place in a common geometry, as a result of the initial charge placement. In this doctoral thesis, microstructure in and around a weld line is analyzed in order to examine the locally changing microstructure. The examined SMC component with a weld line was manufactured by Lucas Bretz at the Institute of Production Science (wbk), Karlsruhe Institute of Technology (KIT).

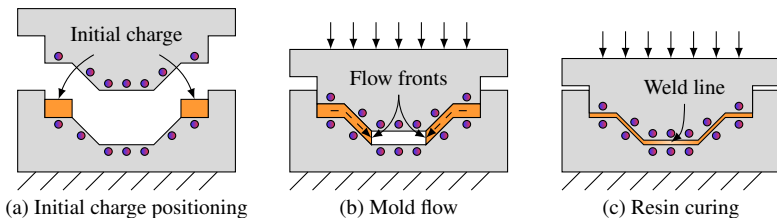


Figure 3.5: The SMC compression molding process. In (a) placing two semi-finished SMC initial charges, (b) compression molding and (c) weld line formation.

## 3.2 Microstructure and Mechanical Characteristics of SMC

There is a strong relationship between the manufacturing process, microstructure and mechanical properties for fiber-reinforced polymers and SMC in particular. In this section the characteristics of SMC microstructures are introduced from several scale perspectives. Furthermore, the damage behavior of SMC with respect to the microstructure and load case is presented. Finally, numerical prediction models for SMC material systems to predict the mechanical and damage behavior are introduced.

### 3.2.1 Microstructure

The SMC microstructure is distinguished from that of other fiber-reinforced composites. Figure 3.6 illustrates and compares the principle microstructures of unidirectional laminates, SMC material and injection molded short fiber-reinforced polymers. A characteristic aspect of the SMC microstructure is the fact that the copped fiber rovings are still intact within the final component. Figure 3.7 shows representative  $\mu$ CT cross sections of typical SMC microstructures and the characteristic fiber bundle architecture.

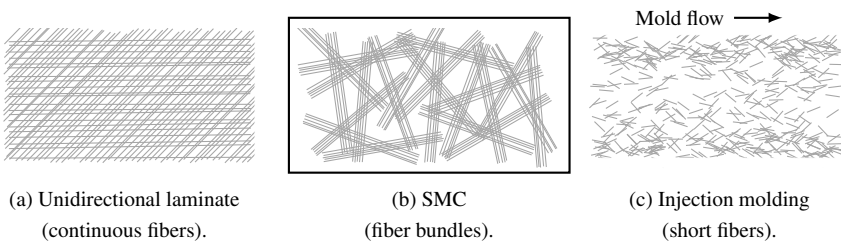


Figure 3.6: Principle microstructure of unidirectional laminates, SMC with random oriented chopped fiber bundles and short-fiber reinforced polymer injection molding.

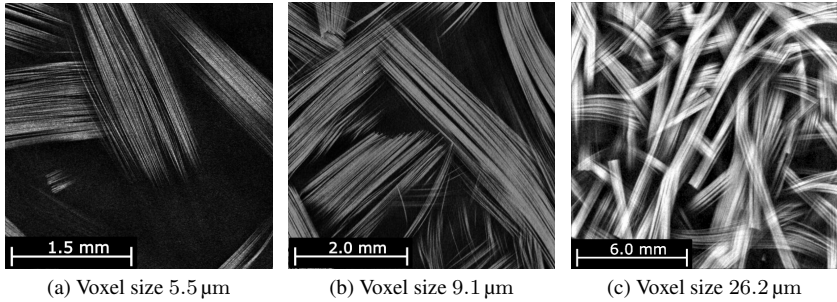


Figure 3.7: The SMC characteristic fiber bundle arrangement on the microstructural level. Fiber bundles in white and the surrounding matrix in black.  $\mu\text{CT}$  cross section acquired at different scale levels.

The SMC microstructure is taken into account on different scale levels from micro to macro by characterization methods and numerical simulation models. According to the considered scale level different aspects of the SMC microstructure are characterized or modeled. In this work the SMC microstructure is classified by using micro-, meso- and macroscopic scale perspectives, as shown in Figure 3.8. On the microscopic level the fiber architecture of SMC is characterized by individual filaments, on the mesoscopic level by fiber bundles and on the macro scale the SMC material is considered as a composite structure.

In case of image based experimental microstructure studies, there is usually a conflict between the image resolution and the size of the examined microstructure. In Section 2.3 this conflict for the investigation by means of cone-beam  $\mu\text{CT}$  scanning is presented. The classification scheme in Figure 3.8 clarifies on which scale level which characterization method can be used with respect to  $\mu\text{CT}$  scanning. In this doctoral thesis, SMC microstructures are examined from a meso- and macro-scale perspective.

When characterizing microstructures, it is important to be able to estimate which microstructure volume is representative for the studied material system. The authors Sabiston et al. [206] analyzed the SMC microstructure with respect

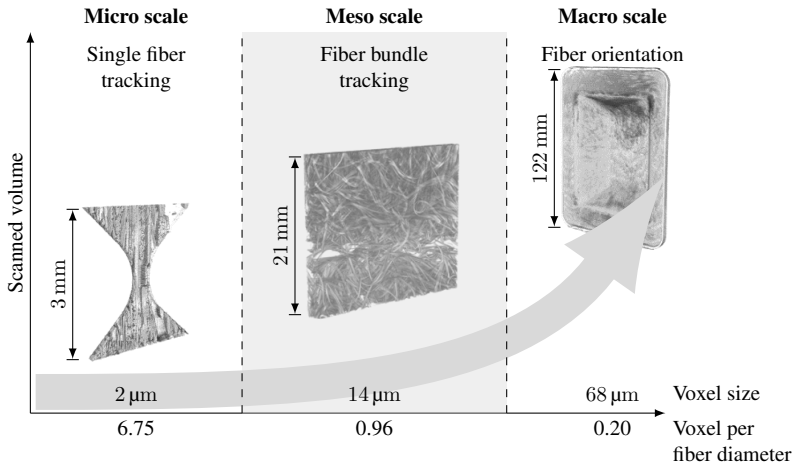


Figure 3.8: Classifying the SMC microstructure by different scale levels. Illustrating the conflict between voxel size and scanned volume with respect to laboratory  $\mu$ CT scanning based on three exemplary SMC specimens. Using different characterization methods on respective scale levels. Referenced glass fiber diameter of  $13.5\ \mu\text{m}$ .

to the second-order fiber orientation tensor. The objective of the study was to analyze the fiber orientation distribution and identify a minimum control volume size for which the second-order fiber orientation tensor is representative. In case of the studied SMC plates, the authors found out that the fiber orientation tensor becomes approximately constant for a cubic control volume with an edge length of about 5 mm. Based on this result, representative volume elements and control volumes are selected in this work.

### 3.2.2 Mechanical Properties

The effect of several aspects, such as the fiber volume content and charge coverage on the mechanical properties are presented in this section. Figure 3.9 illustrates typical tensile load-elongation curves of SMC with respect to different fiber weight contents of 30 wt.%, 50 wt.% and 65 wt.%. Initially, SMC

materials show a linear-elastic behavior. The subsequent onset of non-linearity indicates damage initiation [207]. The transition between those two stages of the stress-strain curve is characteristic for SMC and is called knee or yield point. Figure 3.9 shows that with increasing fiber weight content the knee point is less pronounced.

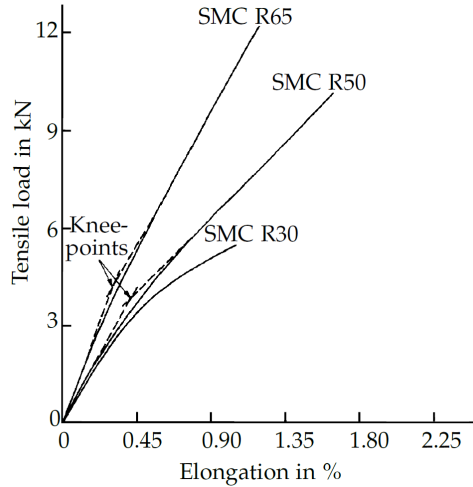


Figure 3.9: Illustrating the effect of the fiber content on the mechanical behavior. Typical stress-strain curves of SMC with different fiber volume content between 30 wt.% and 65 wt.% (figure by Chaturvedi et al. [208]).

As introduced in Section 3.1.4 there is an impact of the SMC charge coverage on the fiber orientation distribution. Consequently, also the mechanical properties are affected by the charge coverage. Figure 3.10 shows the stress-strain curves of SMC with different charge coverages between 33 % and 100 %. The study reveals that with decreasing charge coverage the mechanical properties including Young's modulus and tensile strength increase along the MFD and decrease perpendicular to it. Overall, an anisotropy of the fiber orientation distribution caused by small charge coverage also leads to anisotropic mechanical properties.

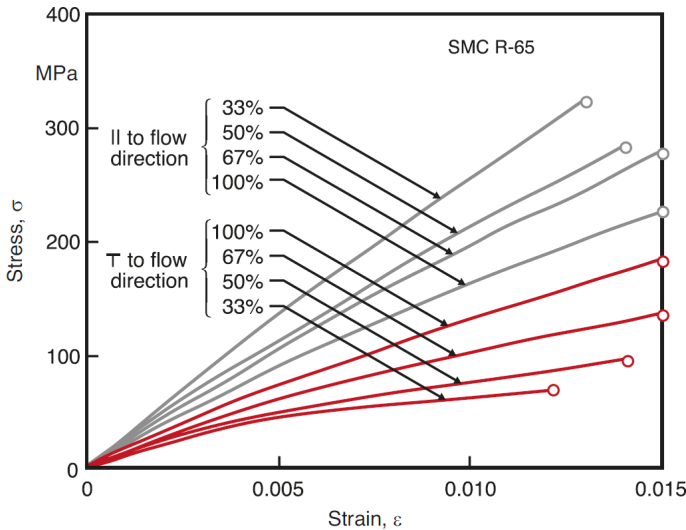


Figure 3.10: Typical stress-strain curves of SMC regarding the charge coverage between 33 % and 100 %, along and perpendicular to the MFD. The stress-strain curves illustrate the increasing anisotropic mechanical behavior as a result of decreasing charge coverage. Fiber weight content of the examined SMC is 65 wt. % (figure by Gandhi et al. [205]).

The mechanical properties of the investigated matrix, fibers and SMC material system were comprehensively characterized in previous contributions. In Table 3.3 and Table 3.4 the mechanical properties of the UPPH matrix and glass fiber are listed, respectively. The corresponding referenced measurements in Table 3.3 on the UPPH matrix were conducted by Miriam Bartkowiak at the Institute for Applied Materials (IAM-WK). The effective mechanical properties of the investigated SMC material system in this doctoral thesis are given in Table 3.5.

Table 3.3: Mechanical properties of the UPPH matrix. Tensile strength and failure strain of the UPPH matrix were characterized by Miriam Bartkowiak at the IAM-WK.

Property	Unit	Quantity	Reference
Young's modulus	GPa	3.45	Trauth [209]
Tensile strength	MPa	46	Bartkowiak
Failure strain	%	1.4	Bartkowiak
Mass density	g/cm <sup>3</sup>	1.15	Schwab [210]

Table 3.4: Mechanical properties of the glass fibers.

Property	Unit	Quantity	Reference
Young's modulus	GPa	82.6	Hüther et al. [211]
Tensile strength	GPa	2.0	Hull and Clyne [48]
Failure strain	%	2.6	Hull and Clyne [48]
Fiber diameter	μm	13.5	Görthofer et al. [9]*
Fiber length	mm	25.4	Görthofer et al. [9]*
Mass density	g/cm <sup>3</sup>	2.60	Meyer et al. [118]*

Table 3.5: Mechanical properties of the UPPH glass fiber reinforced SMC.

Property	Unit	Quantity	Reference
Young's modulus	GPa	9.3–13.2	Trauth [209]
Tensile strength	MPa	84–183	Trauth [209]
Failure strain	%	1.2–1.7	Trauth [209]
Fiber mass content	wt.%	41	Trauth [209]
Fibers per bundle	—	200	MultiStar 272 [212]
Mass density	g/cm <sup>3</sup>	1.90	Görthofer et al. [9]*
Interface strength	MPa	60–70	Rohrmüller et al. [213, 214]

### 3.2.3 Damage Mechanisms

The composition and microstructure significantly affect the damage and failure behavior of composites. In fiber-reinforced composites, the mechanical properties of fiber and matrix, as well as the interaction and fiber-matrix interface are essential aspects.

In case of glass fiber-reinforced thermoset composites the elongation at break of the matrix is typically less than that of the fibers, which is also the case for the examined SMC material system in this doctoral thesis, as shown in Table 3.3 and Table 3.4. The proportion of strength and elongation at breakage between matrix and fiber of the examined SMC material is illustrated in Figure 3.11 (a).

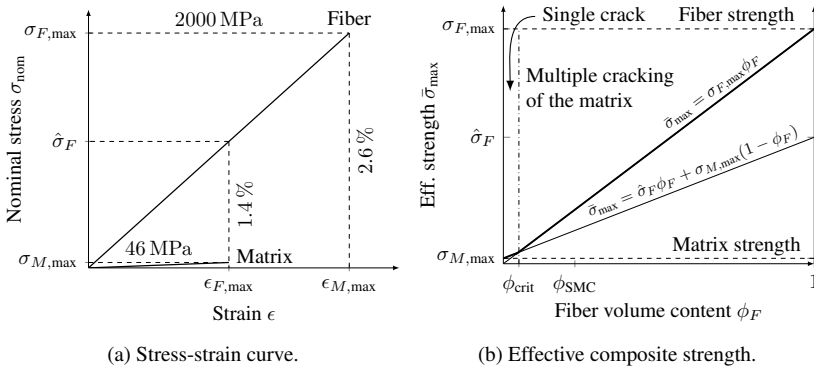


Figure 3.11: Effective composite strength  $\bar{\sigma}_{max}$ , the effect of the fiber volume content  $\phi_F$  and the critical fiber volume content  $\phi_{crit}$  of the examined SMC material according to von Bernstorff and Ehrenstein [215]. The curves are generated based on the data in Table 3.4 and Table 3.3.

As introduced in Section 2.2.4, the microstructure and fiber volume content in particular affect the damage behavior of SMC. The authors von Bernstorff and Ehrenstein [215] adapted the model by Cooper [47] to SMC material and studied how the combination of mechanical properties leads to the formation of multiple matrix cracks instead of a single one. Figure 3.11 (b) illustrates



the effective composite strength as a function of the fiber volume content  $\phi_F$  based on the model by Cooper [47]. According to the study by von Bernstorff and Ehrenstein [215], in case the fiber volume content  $\phi_F$  exceeds the critical fiber volume content  $\phi_{\text{crit}}$  a transition from single to multiple matrix cracking occurs. As a consequence, the fiber volume content determines whether single or multiple cracking tends to occur in composite materials. Figure 3.12 shows the principle stress-strain curve of those two fracture cases. According to Cooper [47] and illustrated in Figure 2.7, the stress-strain curve of multiple cracking is characterized by a yield point.

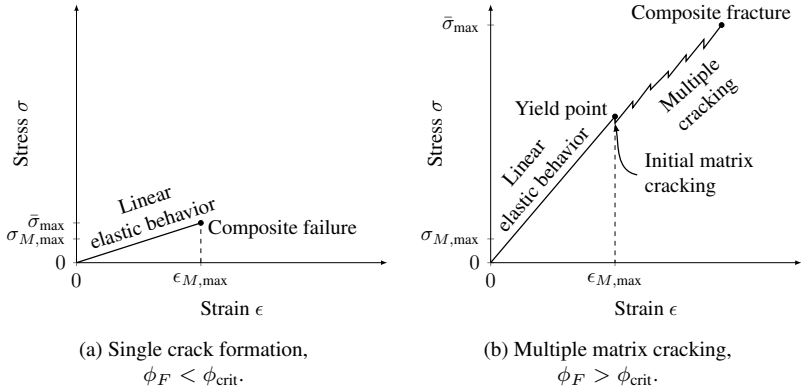


Figure 3.12: Schematic stress-strain curves of fiber-reinforced composites where (a) single crack formation and (b) multiple matrix cracking occurs with respect to the fiber volume content  $\phi_F$  [47, 207, 215].

Based on the material properties in Table 3.3 and Table 3.4, the fiber volume content  $\phi_{\text{SMC}}$  of the investigated SMC material system is above the critical one, as shown in Figure 3.11 (b). In general, the fiber volume content of SMC material systems is well above the critical fiber volume content, as indicated by the characteristic yield or knee point for SMC in Figure 3.9 [207, 208].

Due to the brittle matrix material and glass fibers, the assumptions and model of Cooper [47] can be used to predict the effective strength and damage behavior of SMC, as discussed by von Bernstorff and Ehrenstein [215]. However,

the fiber architecture and orientation of SMC in particular are not taken into account here. Cooper [47] generally assumes a unidirectional orientation of fibers in tensile load direction, which is only in limited agreement with the SMC microstructure.

As introduced in Section 2.2.3, the authors Reifsnider et al. [38] characterized the fatigue life of fiber-reinforced composite laminates and revealed three different stages of damaging. As demonstrated by von Bernstorff and Ehrenstein [215], the fatigue and damage process of fiber-reinforced composite laminates investigated by Reifsnider et al. [38] occurs in a similar way in SMC. In addition, the authors showed that there is a maximum crack density for fiber-reinforced composites, which is typical for the material system, but independent of the load history [38, 215]. In particular, it is regardless of whether quasi-static or fatigue load is applied. Motivated by the direct correlation between crack density and stiffness [215], the authors Reifsnider et al. [38] introduced a stiffness based fatigue failure criterion.

The complexity of (discontinuous) fiber-reinforced composite microstructures leads to the presence of different damage mechanisms [25]. A characteristic aspect of the SMC microstructure is the fiber bundle arrangement, as shown in Figure 3.7. As a consequence of this fiber bundle structure, additional and modified failure modes can occur in SMC. In Figure 3.13 (a) matrix cracking and (c) fiber bundle fracture in the context of SMC are illustrated. An additional failure mode of SMC is the pseudo-delamination, as illustrated in Figure 3.13 (b). This failure mode causes internal propagation of matrix cracks and matrix-fiber interface failure along the fiber bundles. Pseudo-delamination of fiber bundle is commonly compared to delamination of unidirectional fiber-reinforced laminates [216]. Figure 3.14 shows  $\mu$ CT image cross sections, where in (a) matrix cracking, (b) pseudo-delamination and (c) fiber bundle fracture is observed. In Figure 3.15 the crack formations and damage mechanisms in SMC are illustrated three-dimensionally. Similar to short fiber-reinforced composites, in practice SMC failure modes usually do not occur separately but rather mixed.

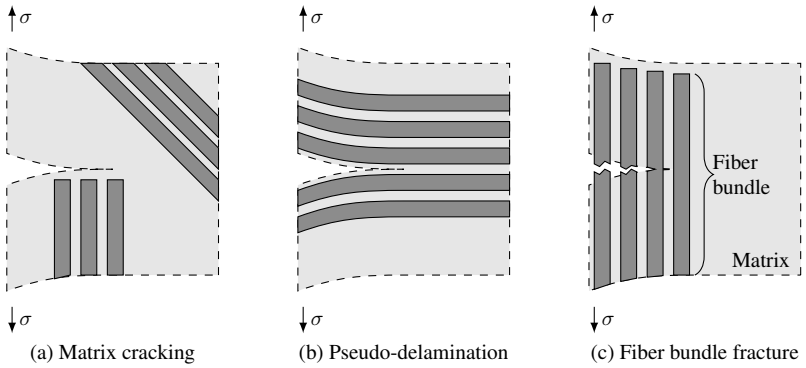


Figure 3.13: Typical failure modes of SMC. In (a) cracking of the matrix, (b) crack propagation along the fiber bundle and (c) fiber bundle breakage under tensile stress.

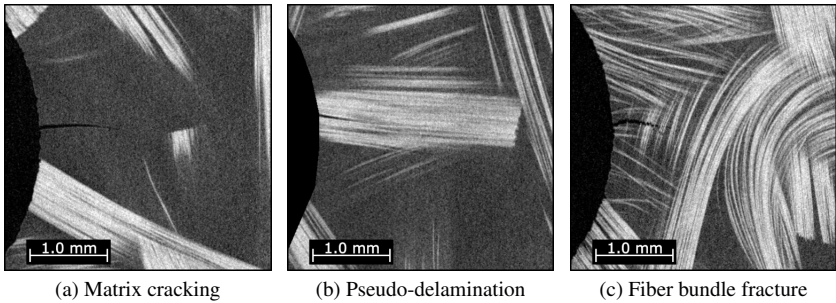


Figure 3.14:  $\mu$ CT image cross sections of typical SMC failure modes. In (a) Cracking of the matrix, (b) crack propagation along the fiber bundle and (c) fiber bundle breakage under tensile stress (voxel size of  $6.8\ \mu\text{m}$ ).

The damage mechanisms of SMC under fatigue load were examined by the authors Wang et al. [217–220]. The experimental results reveal that the damage mechanisms occurred predominantly in various forms of microscopic cracks, such as cracks within the matrix, debonding at the fiber-matrix interface, and cracks at the fiber end. In addition, the authors found out that fiber bundle breakage, which frequently occurs in continuous fiber composites [180, 221], was only slightly observed in fatigue failure of SMC material here.

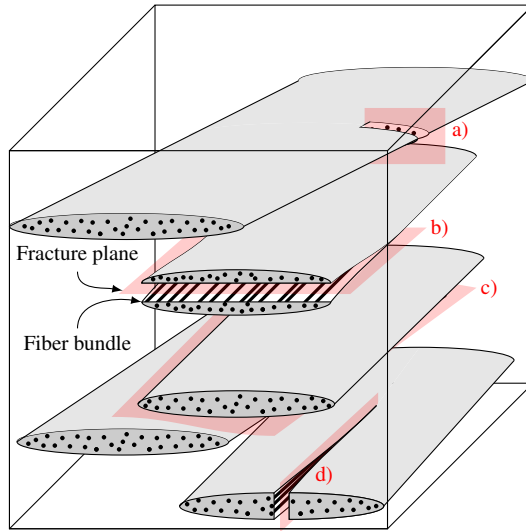


Figure 3.15: 3D illustration of the characteristic failure modes of SMC. At a) fiber bundle fracture perpendicular to the bundle orientation, b) horizontal intra-bundle pseudo-delamination, c) inter-bundle fracture of the matrix and d) vertical intra-bundle pseudo-delamination.

Meraghni et al. [222, 223] classified the damage mechanisms by two dominant types: matrix damage and interface damage. The first type A describes the failure of the matrix and includes matrix cracking and pseudo-delamination. Damage type B regrades the interfacial failure and mostly refers to fiber pull-out. In addition to Wang et al. [217], pseudo-delamination is introduced as another damage mechanism. The fracture or breakage of fiber bundles is not considered by the authors damage classification scheme, since this mechanism only appears during the final stage of the damage process [222, 223]. The SMC classification scheme by Meraghni et al. [222, 223] is discussed and confirmed by several authors and the basis of various modeling approaches [21, 207, 224, 225].

Although different failure mechanisms occur under quasi-static and alternating stresses, according to von Bernstorff and Ehrenstein [215] the formation of multiple cracks is responsible for fatigue. The results of Meraghni et al. [222, 223] show that the content and geometry of those (micro-) cracks affect the macroscopic stiffness, but the effective composite stiffness is more sensitive to the crack content than to the geometry. In general, the formation of cracks is directionally dependent. Consequently, the mechanical properties of SMC becomes more anisotropic as the damage process progresses and furthermore, this effect is enhanced when the SMC material is already anisotropic in the beginning.

The authors Shirinbayan et al. [226–229] characterized the mechanical behavior of SMC considering isotropic and anisotropic microstructures. As part of the research, the damage mechanisms of SMC with randomly and highly oriented fibers in and perpendicular to the load direction are examined. The results show that in case of SMC microstructures with highly oriented fiber in load direction (HO-0°) fiber breakage and pseudo-delamination are the predominate damage mechanisms [226]. In contrast, the fiber-matrix interface debonding predominantly promotes damaging, when the fibers are highly oriented perpendicularly to the load direction (HO-90°). Here, high normal stresses occur on the fibers oriented 90° to the load direction, which results in the formation and propagation of cracks perpendicular to the tensile direction. According to results of Shirinbayan et al. [226], damage in SMC with randomly oriented fibers (RO) is initiated at the interface of fibers, which are oriented perpendicular to the load direction. Subsequently, damage and in particular cracks propagate further along similar oriented fiber interfaces.

The contribution and experimental investigation of Shirinbayan et al. [228] establish that the fatigue life is strongly affected by the microstructure and especially the fiber orientation distribution. However, for SMC with highly transverse oriented fibers (HO-90°) the fatigue life is not significantly affected compared to that of SMC with randomly oriented fibers (RO), since the matrix material is relevant here.

Although thermoset matrix and glass fibers tend to brittle failure behavior SMC composites reveal visco-damage effects [48]. As examined by Shirinbayan et al. [226–228] and Jendli et al. [230] the viscous nature of SMC damage refers mostly to fiber-matrix interface damaging. This phenomenon is either least or most significant for fibers oriented transversely or longitudinally to the tensile load direction, respectively, since the interfaces here are mostly subjected to normal or shear stress. Consequently, this leads to an anisotropic visco-damage aspect of the fiber-matrix interface.

The damage mechanisms of different SMC configurations have been studied and modeled by several authors. Depending on the load case and the SMC composition, different damage mechanisms were found out to be predominant. The listing in Table 3.6 establishes that most authors examined that matrix cracking is the predominant failure mechanism under cyclic fatigue loading. Moreover, there is a trend to fiber related failure modes with higher fiber content. In contrast, the reference results reveal that SMC fails under quasi-static load due to interfacial and debonding failure precedes matrix cracking. Especially, in case of SMC with higher fiber content. Overall, apart of the applied load case the fiber content clearly corresponds with the dominant damage mechanisms. Although it has to be considered that some of the examined SMC material systems in Table 3.6 are filled with hollow glass spheres [229], calcium carbonate ( $\text{CaCO}_3$ ) and other filler material, the results provide a comprehensive overview on damage mechanisms in SMC.

Table 3.6: Summary of the predominant damage mechanisms in SMC considering the load case and fiber content, which have been studied by several authors. The examined SMC composites consist of diverse matrix systems, which are reinforced by chopped glass fiber bundles. Matrix Cracking = MC, Pseudo-Delamination = PD, Fiber Pull-Out = PO and Fiber Breakage = FB. Damage mechanisms indicated by parentheses (×) are not explicitly identified by the authors as predominant mechanisms but are relevant nonetheless.

Fiber content	Load case	Damage mechanisms				Reference
		MC	PD	PO	FB	
25 wt.%	Quasi-static	×				[231]
26 wt.%	Quasi-static	×	×			[207]
14 – 31 vol.%	Quasi-static	(×)	×			[216]
23 – 50 vol.%	Quasi-static	×	(×)	×		[21]
50 vol.%	Quasi-static	×	×	(×)		[222]
50 vol.%	Quasi-static	×	×	(×)		[223]
30 wt.%	Quasi-static	(×)	×	×		[229]
50 wt.%	Quasi-static	×	×	×		[227]
50 wt.%	High strain rate	(×)	×	×	×	[226]
50 wt.%	Quasi-static			×	×	[231]
50 – 65 wt.%	Quasi-static		×	×		[221]
30 – 65 wt.%	Quasi-static			×		[208]
25 wt.%	Fatigue	×				[231]
30 wt.%	Fatigue	×				[215]
30 wt.%	Fatigue	×	×			[232]
42 wt.%	Fatigue	(×)	×			[224]
50 wt.%	Fatigue	×	×		×	[231]
50 wt.%	Fatigue	×	×	×		[217]
50 wt.%	Fatigue	×	×	×		[219]
50 wt.%	Fatigue	×	×	×		[228]
25 – 65 wt.%	Fatigue	×	×			[221]

### 3.2.4 Material Modeling

Since the heterogeneous microstructure of fiber-reinforced polymers leads to the appearance of complex deformation behavior and several damage mechanisms, elaborate mathematical models are necessary for reliable predictions. The authors Kabelka et al. [216] introduced an overview of different models to predict the elastic properties, damaging process and failure criteria. One fundamental assumption made for the prediction of SMC is the approximation to consider and model each fiber bundle as unidirectional laminate layer [216]. This assumption enables to adapt prediction models for unidirectional fiber-reinforced polymer laminates to SMC. The authors Chen and Tucker [204] presented a model for predicting the mechanical properties of discontinuous fiber reinforced polymers including SMC by adapting the laminate analogy. Since there are different damage mechanisms for unidirectional laminates and discontinuous fiber reinforced composites, a suitable damage function is applied.

In addition to quasi-static load, the fatigue behavior of SMC is characterized comprehensively by the author Wang et al. [218, 219]. Furthermore, a power-law based multi-scale homogenization model for fatigue damage growth in SMC under cyclic load is established. Here, the three-dimensional elliptical crack theory for anisotropic material behavior considering probabilistically distributed microcracks is an essential aspect [220].

Focusing on the elastic deformation of SMC, the author Sabiston et al. [233] introduced a two-step Mori Tanaka homogenization scheme to predict the elastic deformation considering misaligned fiber composites. Furthermore, the necessary number of fiber orientation data from  $\mu$ CT scanning required for a reliable prediction is evaluated.

Mori-Tanaka schemes and various interface failure criterion for the damage prediction of SMC are established by the authors von Bernstorff and Ehrenstein [215], Fitoussi et al. [234], Meraghni and Benzeggagh [222] and



Ben Cheikh Larbi et al. [224]. Here, the (predominate) damage mechanisms are considered individually by the homogenization scheme.

The SMC material and the mechanical properties are modeled by the projects of the IRTG across several scale levels. On the mesoscopic level mean- and full-field approaches are used by Kehrner et al. [23, 24, 235, 236] to predict the thermoelastic and thermal expansion. Furthermore, Görthofer et al. [237] discretized the SMC microstructure based on homogenized fiber bundles and matrix material and modeled the elastic mechanical properties by using Fourier transform methods. The SMC microstructures are obtained by improving the multi-scale stochastic fiber bundle microstructure model of the authors Chen et al. [238]. On the macroscopic scale, the authors Schemmann et al. [21, 22, 239] introduced a Mori-Tanaka homogenization scheme and damage prediction model for SMC. Instead of concerning individual fiber bundles, on the macro scale the SMC microstructure is taken into account by fiber orientation tensors obtained from  $\mu$ CT scans [107],[131]\*.



# 4    **Methods**

This chapter represents a key element of this doctoral thesis. Based on state-of-the-art methods and considering the investigated SMC material system, in this chapter image processing methods are introduced to characterize and analyze both, the microstructure and the damage state of SMC specimens by means of  $\mu$ CT scanning. First, the microstructure characterization methods are introduced. Subsequently, image processing methods to segment cracks and characterize the damage state are presented. The introduced methods in this chapter were developed by the author of this doctoral thesis and mostly refer to the contributions [131, 240–243]\*.

## **Contents**

---

<b>4.1 Microstructure Characterization . . . . .</b>	<b>92</b>
<b>4.2 Damage Segmentation . . . . .</b>	<b>106</b>
<b>4.3 Damage Characterization . . . . .</b>	<b>115</b>

---

## 4.1 Microstructure Characterization

The microstructure of fiber-reinforced polymers fundamentally affects the mechanical properties and further, the nature of damage to the material.  $\mu$ CT scanning and image processing are powerful tools to analyze microstructures in terms of homogeneity [244]\*, fiber orientation [131]\* and fiber bundle structure [240, 242]\*. To study the relationship between microstructure and damage behavior, the microstructures of the examined SMC specimens by means of in-situ  $\mu$ CT are characterized regarding the fiber architecture. The developed and applied microstructure characterization methods are introduced in this section.

### 4.1.1 Fiber Orientation

In this work the orientation of fibers within volumetric images are determined based on the structure tensors established by Krause et al. [108] and the implemented image processing method of Pinter et al. [90, 107]. For visualization of fiber orientations, the planar part of fiber orientation vector is expressed by means of the angle  $\phi$ . As shown in Figure 4.1, the angle  $\phi$  is visualized by adapting the HSV color space with respect to the fiber orientation symmetry ( $\mathbf{n} \hat{=} -\mathbf{n}$ ).

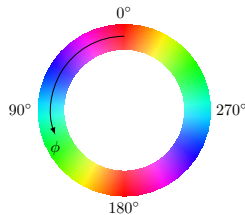


Figure 4.1: Illustration of the planar fiber orientation  $\mathbf{n}$  with respect to the symmetry ( $\mathbf{n} \hat{=} -\mathbf{n}$ ).

An essential part of the IRTG is the collaboration across different research areas and the establishment of a virtual process chain [9, 10, 245]\*. To enable a

virtual process chain for fiber-reinforced polymers, microstructure data must be exchanged between characterization methods and numerical simulation models. Regarding the IRTG virtual process chain, fiber orientation data from the voxel-level of volumetric images are mapped to structured meshes for the use in finite element simulations. From a scale perspective, microstructure data are transferred here from the  $\mu\text{m}$ -scale level of the  $\mu\text{CT}$  scan to the  $\text{mm}$ -scale level of the finite element meshes.

Fundamental approach of the mapping procedure is to describe the local fiber architecture around an analyzed point of the structured mesh and to overcome the difference in scale through cumulating the fiber orientation data by applying the second-order fiber orientation tensor  $\mathbf{N}$ . Introducing the cylindrical reference volumes  $\mathcal{B}$  around the analyzed points with the radius  $R$  and the center axis aligned along the thickness direction  $\mathbf{e}_{z'}$ . Due to the cylindrical shape, the microstructure is equally considered in all spatial directions around the central axis. The thickness normal vector can be predefined in case of planar samples or obtained either by the structured mesh or the fiber orientation data. The alignment of the reference volumes  $\mathcal{B}$  are illustrated schematically in Figure 4.2 (a). Only fiber orientation data within the reference volume  $\mathcal{B}$  are taken into account for mapping of the respective analyzed point. In addition, a weighting factor  $c_i$  is introduced in Equation 4.1 to assign different weights to fiber orientation data  $\mathbf{n}_i$  at different distances  $r$  from the center axis  $\mathbf{e}_{z'}$ . The distribution of the Gaussian weighing function  $c(r)$  is given in Equation 4.2 and illustrated in Figure 4.2 (b).

$$\mathbf{N} = \frac{1}{\sum_{i=1}^N c_i} \sum_{i=1}^N c_i \mathbf{n}_i \otimes \mathbf{n}_i. \quad (4.1)$$

$$c_i = \frac{1}{\sqrt{2\pi\sigma^2}} \exp\left(-\frac{r_i^2}{2\sigma^2}\right), \quad r_i \in [-R, \dots, R] \quad (4.2)$$

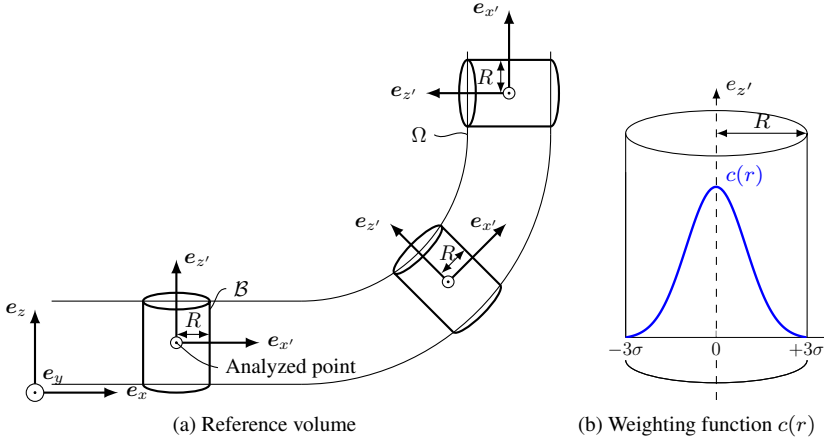


Figure 4.2: In (a) the alignment of the cylindrical reference volumes  $B$  and (b) the shape of the weighting function  $c(r)$  (Gaussian function,  $\sigma = 1/3R$ ) (re-illustration, original figures by Schöttl et al. [131]\*).

When dealing with interdisciplinary virtual process chains, the fiber orientation data obtained by characterization methods have to be processed and transferred to numerical simulation models. By combining structured meshes,  $\mu$ CT fiber orientation data and applying the presented mapping methods, the local fiber orientation distribution at defined mesh points (e.g. mesh nodes or Gaussian points) are mapped and can be taken into account for numerical simulations [9, 10]\*. As a result, microscopic data obtained from  $\mu$ CT data are evaluated and brought to the macro scale. Decisive is the selection of the cylindrical reference volume  $B$  by the radius  $R$  to include a locally representative microstructure for the evaluation. The radius  $R$  should be therefore selected based on the investigated material system and microstructure. According to the investigation by the authors Sabiston et al. [206] the size of the representative microstructure volume elements for SMC are selected to 5 mm and the radius  $R$  to 2.5 mm, respectively.

### 4.1.2 Fiber Bundle Tracking

As introduced in Section 3.2.1, besides the fiber orientation on the macro scale, the microstructure of SMC can also be characterized on the meso scale by means of fiber bundle tracking. A characteristic aspect of the SMC microstructure is that the chopped fiber bundles within the semi-finished SMC do not split up entirely into individual fibers during the compression molding and are still arranged as bundles within final parts. The  $\mu$ CT cross section view of a typical SMC microstructure in Figure 4.3 (a) shows the characteristic fiber bundle arrangement. The presented characterization approach utilizes the fiber bundle structure for analyzing the SMC microstructure and tracks the SMC fiber bundles within volumetric images. In this section, the fiber bundle tracking and clustering methods published by the authors Schöttl et al. [242]\* are introduced in detail.

For analyzing the SMC microstructure, the fiber bundles are classified on two different scale levels. Mesoscopic fiber bundles  $\mathcal{R}$  emerge from the chopped fiber rovings of the manufacturing process and consist of a large number of individual fibers. Fibers within mesoscopic bundles run parallel and are located close together. Exemplary mesoscopic bundles are highlighted in Figure 4.3 (b). Mesoscopic bundles are inhomogeneous and sub-bundles are revealed in Figure 4.3 (a). The substructure of mesoscopic bundles is classified by microscopic bundle  $\mathcal{S}$ . Figure 4.3 (c) highlights exemplary microscopic bundles. In summary, mesoscopic bundles correspond to the chopped fiber bundles, which consist of several microscopic bundles.

As published in the contribution [242]\* a bottom-up approach is applied, in which first microscopic bundles are tracked iteratively by a probabilistic integration method. Subsequently, based on the tracking results a hierarchical agglomerative clustering strategy finally identifies the mesoscopic bundles.

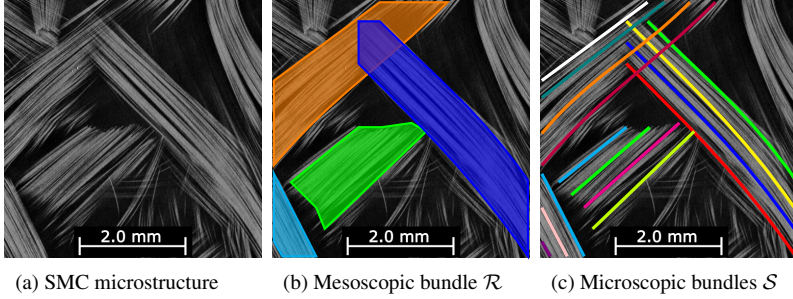


Figure 4.3:  $\mu$ CT cross section of a typical SMC sample. Classification of the SMC microstructure by mesoscopic and microscopic bundles. In (a) an exemplary SMC microstructure, (b) the mesoscopic bundles and (c) the microscopic bundles are marked, respectively. Voxel size is  $9.1 \mu\text{m}$  and glass-fiber diameter  $13.5 \mu\text{m}$  (re-illustration, original figures by Schöttl et al. [242]\*).

## Probabilistic tracking method

Based on the experimental fiber orientation data  $\mathbf{n}(x, y, z)$ , trajectories are determined iteratively by moving along the step-wise highest probabilistic path. Starting at voxel  $\mathbf{x}_i$ , first several potential next iteration step voxels  $\tilde{\mathbf{x}}_j$  are identified by lower radius  $R_1$ , upper radius  $R_2$  and aperture angle  $\theta$ . The potential next iteration step voxels are marked by red circles in Figure 4.4 (a). The paths between  $\mathbf{x}_i$  and the potential next iteration step voxels  $\tilde{\mathbf{x}}_j$  are taken into account by second-order polynomial space curves

$$\mathbf{s}_j(t) = \mathbf{s}_0 + \mathbf{s}_1 t + \mathbf{s}_2 t^2, \quad t = 0 \dots 1, \quad (4.3)$$

defined by the conditions  $\mathbf{s}_j(0) = \mathbf{x}_i$ ,  $\mathbf{s}_j(1) = \tilde{\mathbf{x}}_j$  and  $\mathbf{s}'_j(0) = \mathbf{n}_i$ . The tangent of the curves  $\mathbf{s}_j(t)$  at  $\tilde{\mathbf{x}}_j$  is given by  $\mathbf{s}'_j(1)$ . Based on that,  $\tau_j$  is introduced as the angle between the curve tangent  $\mathbf{s}'_j(1)$  (blue) and the local fiber orientation data  $\tilde{\mathbf{n}}_j$  (red) of the potential next voxel  $\tilde{\mathbf{x}}_j$ , as shown in Figure 4.4 (b).

$$\tau_j = \angle(\tilde{\mathbf{n}}_j, \mathbf{s}'_j(1)) \quad (4.4)$$



Small  $\tau$  indicate a high accordance between the curve  $s(t)$  and the experimental fiber orientation data  $\mathbf{n}$ . Consequently, the voxel  $\tilde{\mathbf{x}}_j$  with the smallest  $\tau_j$  represents the highest probability between the integration step and the fiber orientation data  $\mathbf{n}$ . As illustrated in Figure 4.4 (c), this voxel with the smallest  $\tau_j$  value then becomes the next iteration step voxel  $\mathbf{x}_{i+1}$ . By iterating along the step-wise highest probability, a high global probability of the resulting trajectory is also obtained.

Introducing  $\mathcal{S}$  as the determined trajectory of a tracked microscopic bundle, which contains all iteration step voxels  $\mathbf{x}_i$  and corresponding orientation vectors  $\mathbf{n}_i$ . In order to analyze the whole microstructure, a sufficient large number of trajectories  $\mathcal{S}$  starting at different points  $\mathbf{x}_0$  are tracked. Usually, the number of trajectories is between 6000 and 16000, details will be given later in this chapter.

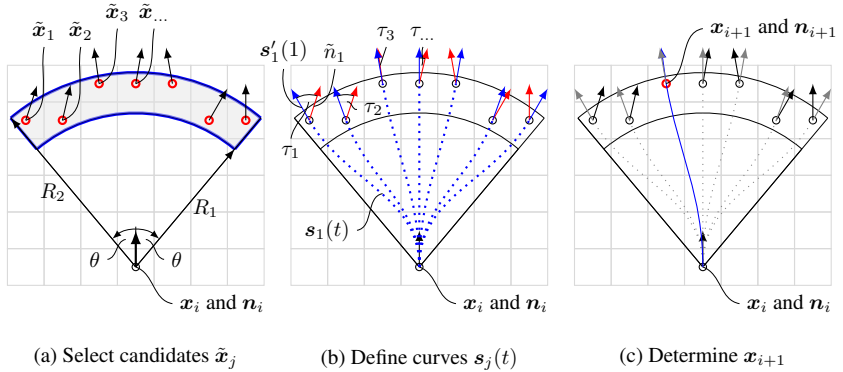


Figure 4.4: Iterative tracking along the path with the highest probability to the experimental fiber orientation data  $\mathbf{n}$  (figure by Schöttl et al. [242]\*).

## Allocation criteria

Subsequently, after determining a large number of microscopic bundle trajectories  $\mathcal{S}$  the mesoscopic bundles have to be further identified. As introduced,

mesoscopic bundles consist of several related microscopic bundles. Through applying clustering methods, the trajectories that belong to the same mesoscopic bundle are merged together and as a result, the mesoscopic bundles are identified. To clarify which microscopic bundle belongs to which mesoscopic bundle two criteria are introduced below.

- **Distance:** Microscopic bundles of the same mesoscopic bundle are located close together and consequently, the distance between those microscopic bundles is small.
- **Orientation:** Microscopic bundles of the same mesoscopic bundle run parallel and consequently, the local orientation difference is small.

Suitable factors to quantify these two criteria and taking them into account for clustering are presented. Trajectory A is given by  $\mathcal{S}_A = \{\mathbf{x}_i : i = 1 \dots m_A\}$  and trajectory B by  $\mathcal{S}_B = \{\mathbf{y}_j : j = 1 \dots m_B\}$ . Introducing  $\tilde{\mathbf{y}}_i$  as the element of  $\mathcal{S}_B$ , with the smallest euclidean distance to  $\mathbf{x}_i$ . Conversely, define  $\tilde{\mathbf{x}}_j \in \mathcal{S}_A$ , with the smallest euclidean distance to  $\mathbf{y}_j$ . Figure 4.5 illustrates schematically the corresponding elements  $\tilde{\mathbf{y}}_i$ ,  $\mathbf{x}_i$ ,  $\tilde{\mathbf{x}}_j$  and  $\mathbf{y}_j$ . The mean distance between two trajectories  $\mathcal{S}_A$  and  $\mathcal{S}_B$  is introduced by

$$\hat{d}_{AB} = \frac{1}{m_A} \sum_{i=1}^{m_A} |\mathbf{x}_i - \tilde{\mathbf{y}}_i| \quad \text{and} \quad \hat{d}_{BA} = \frac{1}{m_B} \sum_{j=1}^{m_B} |\mathbf{y}_j - \tilde{\mathbf{x}}_j|. \quad (4.5)$$

Distance  $\hat{d}_{AB}$  (and  $\hat{d}_{BA}$ ) quantifies the mean distance from trajectory  $\mathcal{S}_A$  to  $\mathcal{S}_B$  (and reverse). However, in general  $m_A \neq m_B$  and consequently,  $\hat{d}_{AB} \neq \hat{d}_{BA}$ . In order to define a symmetric distance value in terms of  $d_{AB} = d_{BA}$ , the distance between two trajectories  $\mathcal{S}_A$  and  $\mathcal{S}_B$  is defined by  $d_{AB} = \min(\hat{d}_{AB}, \hat{d}_{BA})$ .

Additionally, to the spatial distance, also the difference in orientation between two trajectories is taken into account for clustering. To compare the local orientation of two microscopic bundles  $\mathcal{S}_A$  and  $\mathcal{S}_B$ , the trajectories are subdivided

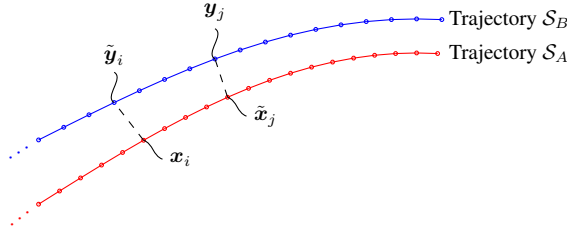


Figure 4.5: The distance between the two trajectories  $\mathcal{S}_A$  and  $\mathcal{S}_B$  (figure by Schöttl et al. [242]\*).

into sections of equal length. Subsequently, determining the second-order orientation tensor  $\mathbf{N}$  according to Equation 2.39 of all sections based on the associate orientation vectors  $\mathbf{n}_i$ . The first eigenvector  $\mathbf{v}_1$  of  $\mathbf{N}$  indicates the principal orientation of the corresponding trajectory section.

The orientation difference of two trajectories  $\mathcal{S}_A$  and  $\mathcal{S}_B$  is determined by pairwise comparison of the sections of both microscopic bundles. The first eigenvectors of the  $n_{AB}$  closest section pairs are compared. In this doctoral thesis and the contribution [242]\*, sections and section pairs are indicated by lowercase  $\alpha$ . The first eigenvectors of section pair  $\alpha$  are labeled by  $\mathbf{v}_\alpha$  and  $\tilde{\mathbf{v}}_\alpha$ , respectively. The difference in orientation of the section pair  $\alpha$  is quantified by the angle  $\phi_\alpha = \angle(\tilde{\mathbf{v}}_\alpha, \mathbf{v}_\alpha)$ , as illustrated in Figure 4.6. The overall orientation

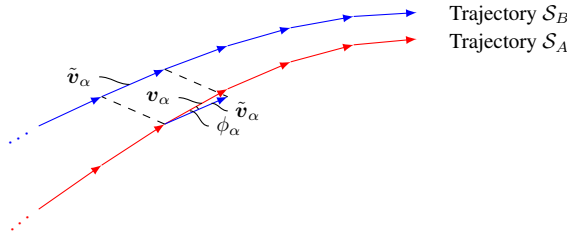


Figure 4.6: The orientation difference  $\phi_\alpha$  of section pair  $\alpha$  (figure by Schöttl et al. [242]\*).

difference between two microscopic bundles  $\mathcal{S}_A$  and  $\mathcal{S}_B$  is then given by the mean angle  $\phi_{AB}$  of the  $n_{AB}$  closest section pairs.

$$\phi_{AB} = \frac{1}{n_{AB}} \sum_{\alpha=1}^{n_{AB}} \phi_{\alpha}. \quad (4.6)$$

## Hierarchical Agglomerative Clustering

Mesoscopic bundles are identified by clustering microscopic bundles based on the introduced criteria. Step-wise close and parallel trajectories are composed to the same cluster. Two clusters  $\mathcal{R}_A$  and  $\mathcal{R}_B$  are compared by the averaged  $\bar{d}_{AB}$  and  $\bar{\phi}_{AB}$  values of all microscopic bundle pairs between both clusters. By taking the average distance  $\bar{d}_{AB}$  and orientation difference  $\bar{\phi}_{AB}$  into account, the similarity value

$$\rho_{AB} = \frac{1}{\lambda_G + \lambda_O} \left( \lambda_O \left( \frac{k_O - \bar{\phi}_{AB}}{k_O} \right) + \lambda_G \left( \frac{k_G - \bar{d}_{AB}}{k_G} \right) \right) \quad (4.7)$$

between two clusters  $\mathcal{R}_A$  and  $\mathcal{R}_B$  is introduced. The average distance  $\bar{d}_{AB}$  and the orientation difference  $\bar{\phi}_{AB}$  are normalized by  $k_G$  and  $k_O$ . By adapting those two weighting factors  $\lambda_G$  and  $\lambda_O$ , the distance and orientation criteria leverages are adjusted. The similarity value  $\rho_{AB}$  ranges from 0 to 1 and specifies the similarity of two clusters. In case of  $\rho_{AB} = 1$ , both clusters  $\mathcal{R}_A$  and  $\mathcal{R}_B$  are identical.

As published in the contribution of Schöttl et al. [242]\*, microscopic bundles are clustered by a state-of-the-art hierarchical agglomerative (bottom - up) clustering approach [246, 247]. In the beginning all trajectories  $\mathcal{S}$  initialize an individual cluster  $\mathcal{R}_i = \{\mathcal{S}_i\}$ , so that there are as many clusters as trajectories. For each clustering step the similarity value  $\rho_{AB}$  of all cluster pairs is determined. The cluster pair with the highest similarity is then merged together. As a result, the number of clusters is reduced by one in each iteration step. The clustering process is stopped when the highest similarity drops below a defined threshold  $k_{\rho}$  or the difference of the highest similarity between two consecutive iteration

steps is below a defined threshold  $\Delta k_\rho$ . Usually, the threshold  $k_\rho$  is selected between 0.85 and 0.95 and  $\Delta k_\rho$  between  $-0.02$  and  $-0.01$ , respectively.

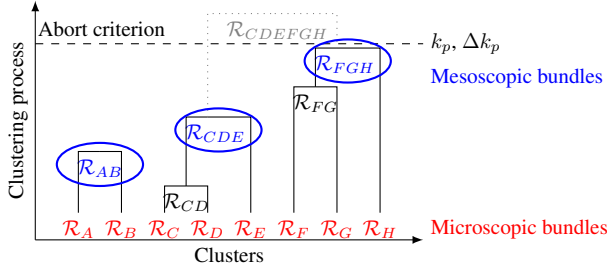


Figure 4.7: Illustration of the hierarchical agglomerative clustering scheme to identify mesoscopic bundles (figure by Schöttl et al. [242]\*).

Figure 4.7 schematically illustrates the hierarchical agglomerative clustering process. Initially each trajectory  $\mathcal{S}_{A...H}$  forms an individual cluster  $\mathcal{R}_{A...H}$ . In this example, the mesoscopic bundles are finally given by the resulting microscopic bundle clusters  $\mathcal{R}_{AB} = \{\mathcal{S}_A, \mathcal{S}_B\}$ ,  $\mathcal{R}_{CDE} = \{\mathcal{S}_C, \mathcal{S}_D, \mathcal{S}_E\}$  and  $\mathcal{R}_{FGH} = \{\mathcal{S}_F, \mathcal{S}_G, \mathcal{S}_H\}$  (cf. ellipses in Figure 4.7).

### Selecting Appropriate Parameters

In order to apply the introduced fiber bundle tracking methods, appropriate parameters have to be selected. The tracking radius  $R_1$  and  $R_2$  should be selected as large as possible to reduce computational time and as small as necessary to enable reliable tracking of even strongly curved fiber bundles. Consequently, efficient and appropriate parameters have to be selected. Instead of defining all parameters independently and individually, Figure 4.8 clarifies the relationship between step length  $S$  and angle  $\theta$ , when tracking along a circular arc with radius  $R$ . In this case, the aperture angle  $\theta$  is determined as a function of  $S$  and  $R$  by

$$\theta = \sin^{-1} \left( \frac{S}{2R} \right). \quad (4.8)$$

For the fiber bundle tracking method the lower radius  $R_1$  and upper radius  $R_2$  should be selected below and above  $S$  with respect to the aperture angle  $\theta$ . As a consequence, the tracking parameters can be selected directly depending on the minimum radius  $R$  that should be able to track.

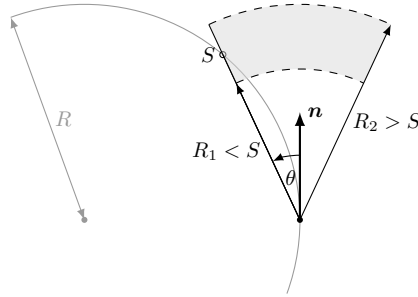


Figure 4.8: Iterative tracking along a circular arc. Linking the tracking radii  $R_1$ ,  $R_2$  and the aperture angle  $\theta$  (figure adapted from Tournier et al. [124]).

In practice, the radius  $R_1$  and  $R_2$  are selected with respect to the fiber bundle geometry including the width and the maximum curvature. Subsequently, the aperture angle  $\theta$  is defined in order to track fiber bundles with a minimum curvature radius of  $R$ . The selected values for  $R_1$ ,  $R_2$  and  $\theta$  were chosen rather conservatively to ensure an accurate result.

Furthermore, the number of starting points is selected based on the specimen size and fiber bundle width. In this work the starting point locations are defined by an equidistant grid. Other options such as a random distribution are available but have not been applied due to reproducibility issues.

Fiber bundles within three different SMC samples with different voxel sizes are tracked and further analyzed. The first two samples were used to validate the tracking method in the contribution of Schöttl et al. [242]\* and the second sample to investigate the fiber bundle curvature within a weld line of a SMC component [118, 240]\*. In Table 4.1 the selected tracking and clustering parameters of the respective samples are listed.

Table 4.1: Selected parameters of the fiber bundle tracking and clustering method [118, 240, 242]\*.

Property	Unit	Sample No. 1	Sample No. 2	Sample No. 3
Voxel size	$\mu\text{m}$	9.1	6.8	17.2
Lower radius $R_1$	Voxel	16	22	12
	mm	0.15	0.15	0.21
Upper radius $R_2$	Voxel	20	26	17
	mm	0.18	0.18	0.29
Aperture angle $\theta$	$^\circ$	6	6	10
Starting point location	-	Equidistant	Equidistant	Equidistant
No. of starting points	-	6032	9240	15876
Weighting factor $\lambda_G$	-	2	2	2
Weighting factor $\lambda_O$	-	1	1	1
Threshold $k_\rho$	-	0.9	0.9	0.9
Threshold $\Delta k_\rho$	-	-0.015	-0.015	-0.015
Application	-	Validation	Validation	Weld line

### Computational Parallelization for Multi-thread Application

For SMC fiber bundle analysis, a large number of microscopic fiber bundles are tracked. The tracking process of large volumetric image data is computational and memory expensive. Subdividing the overall analysis task into small separable tasks enables the parallel processing on several CPUs. The fiber bundle tracking is well suited for parallel processing, since the iterative tracking process at different starting points  $\mathbf{x}_0$  take place independently of each other. For each parallel operation the necessary fiber orientation data  $\mathbf{n}$  must be provided. In order to save memory and to enable running multiple parallel threads, not the entire volumetric data are passed to each thread but only sufficient local data. Figure 4.9 illustrates schematically the local passed volumetric data in the

context of the entire data set. As a result, the memory is used more efficiently and more threads can run in parallel. To ensure that the necessary data are provided to all parallel threads, the cut off radius  $r_{\text{cut}}$  of the spherical sub-volume is selected to be the fiber bundle length of 25.4 mm.

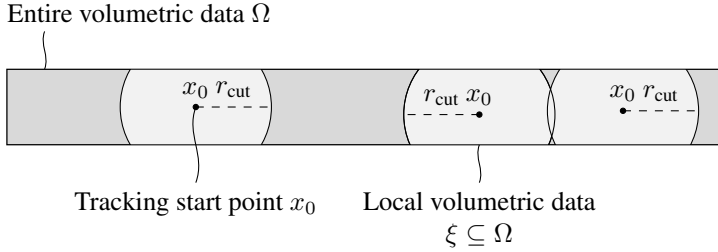


Figure 4.9: Parallelization of the fiber bundle tracking process and dividing the volumetric data into sub-volumes by means of cut off radius  $r_{\text{cut}}$ .

### 4.1.3 Fiber Bundle Curvature

Beyond fiber orientation tensors  $N$  and distribution, further fiber architecture properties can be used to characterize the SMC microstructure. Similar to fiber undulation of woven fabrics, the curvature of SMC fiber bundles affects the mechanical properties. In this doctoral thesis, the fiber bundle curvature is characterized based on the fiber bundles tracking results.

In general, the curvature  $\kappa$  of a space curve or trajectory  $\mathbf{r}(s)$  is given by

$$\kappa(s) = \left\| \frac{d^2 \mathbf{r}(s)}{ds^2} \right\|, \quad (4.9)$$

where  $s$  is the arc length along the curve  $\mathbf{r}(s)$ . Figure 4.10 illustrates the curvature by means of a circular arc. In case the fiber bundle is circular shaped, the curvature  $\kappa$  becomes the radius reciprocal  $1/R$ .



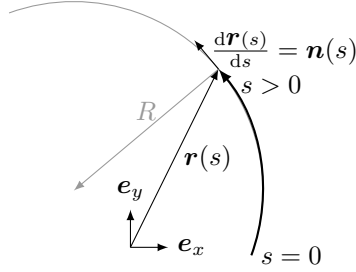


Figure 4.10: Introducing the curvature  $\kappa$  of a space curve  $\mathbf{r}(s)$ .

As published in the contribution [240]\* the fiber bundle curvature is determined based on the fiber bundle tracking data. Since the tangent vector  $\mathbf{n}$  is already determined during the fiber bundle tracking process and

$$\mathbf{n} = \frac{d\mathbf{r}(s)}{ds}, \quad (4.10)$$

the curvature is determined by

$$\kappa(s) = \left\| \frac{d\mathbf{n}(s)}{ds} \right\|. \quad (4.11)$$

The numerical derivation of the local fiber orientation  $\mathbf{n}$  according to the arc length  $s$  was implemented via the midpoint differentiation scheme. Furthermore, to eliminate noise effects, the curvature data are smoothed by applying the median filter along the fiber bundles.

The fiber bundle tracking results and curvature analysis data are applied to characterize the fiber bundle curvature within and around a weld line [240]\*. In addition the obtained curvature distribution data are further used for comparison and validation of a novel fiber bundle process simulation model in the contribution of Meyer et al. [118]\*.

## 4.2 Damage Segmentation

In-situ  $\mu$ CT testing acquires volumetric images of SMC specimen microstructures featuring cracks. In this section three different image processing methods to segment cracks three-dimensionally are introduced. All these methods are based on fundamentally different approaches, including gray-scale neighborhood processing, full-field correlation and artificial intelligence. The performance and applicability of these methods is evaluated and compared in the following chapters.

### 4.2.1 Seed-Region-Growth Segmentation

Image processing methods based on gray-value histogram are well suited to segment objects which are monolithic and thus, associated with a homogeneous gray-value. In case of  $\mu$ CT scanning the gray-values represent the X-ray attenuation and voxels of the same material are indicated by equal gray-values. Although cracks are homogeneous, the gray-value within them will vary due to image noise and  $\mu$ CT artifacts. Because of that image noise and the fact that cracks form slim structures, advanced image processing methods are necessary for accurate crack segmentation.

In this doctoral thesis the Seed-Region-Growth segmentation method (SRG) introduced by Adams and Bischof [96] is applied to segment cracks within  $\mu$ CT volumetric images [241]\*. The aim of the SRG method is to identify interrelated structures by using a growth approach based on two thresholds  $k_{\text{seed}}$  and  $k_{\text{growth}}$ , as introduced in Section 2.4.3. Both thresholds are selected relative to the maximum gray-value, in order to be applied equally to images with different gray-value distributions.

The segmentation process including defining seed, region growing and the final segmented cracks are illustrated in Figure 4.11. For comparison between the SRG method and basic thresholding technique (cf. Section 2.4.2), Figure 4.11 (d) shows the single thresholding result by using the upper threshold

$k_{\text{growth}}$ . To distinguish cracks and background around the specimen, the surface of the specimen is determined by using VGSTUDIO MAX 3.4 by Volume Graphics.

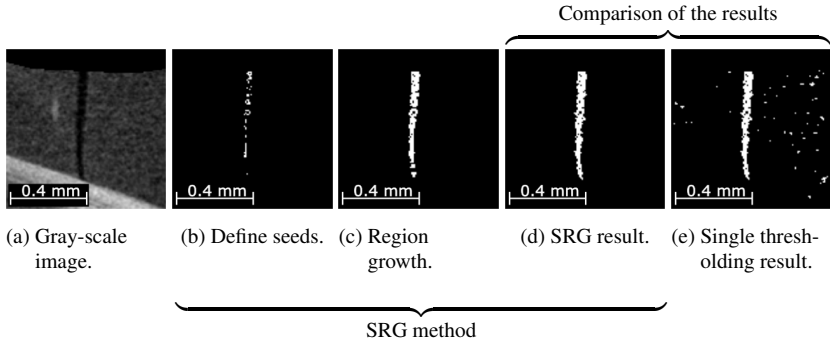


Figure 4.11: In (a) an exemplary gray-scale image and in (b) to (d) the crack segmentation process by means of the SRG method. For comparison the single thresholding result is shown in (e). Background in black and segmented crack in white.

As introduced in Section 2.4.4, the closing-operation eliminates incorrect segmented voxels inside objects by closing inclusions within objects in binary image data. Goal of the closing-operation is to obtain a simple contiguous object by performing a morphological image operation. In order to improve the SRG crack segmentation results, a slight closing operation is applied subsequently. Figure 4.12 shows the process and how incorrect voxels inside the SRG segmented crack are eliminated. In this work the *imclose*-function by MATLAB (R2020b) is applied.

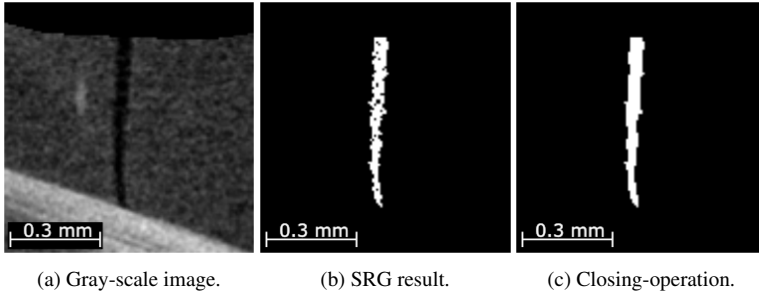


Figure 4.12: Eliminating incorrect segmented voxels by using the closing operation (background in black and segmented crack in white).

## 4.2.2 Digital Volume Correlation

Interrupted in-situ  $\mu$ CT testing acquires volumetric images of the same specimens prior to and after deformation. Based on these volumetric images digital volume correlation (DVC) methods determine the displacement and strain field between the initial and deformed microstructure. According to the fundamental kinematics of continuum mechanics presented in Section 2.1.1, within deformed solids without cracks the function  $\chi$  in Equation 2.1 can clearly assign the initial and deformed state. Yet, cracks lead to an ambiguity of the continuum mechanics kinematic. In regions where cracks occur the DVC cannot clearly correlate the initial and deformed microstructure. This phenomenon is schematically illustrated in Figure 4.13, where the material point  $P$  cannot be clearly associated with either  $P^+$  or  $P^-$  due to the crack formation. This inconsistency leads locally to a bad correlation result and consequently, a high difference volume within the crack region of the DVC result. The larger the crack opening, the greater the phenomenon that occurs and the more distinct is the resulting feature in the DVC data.

This phenomenon is utilized to identify cracks by means of DVC. In this doctoral thesis the DVC method by VGSTUDIO MAX 3.4 is applied. A local

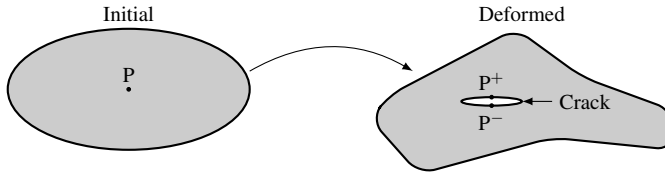


Figure 4.13: Ambiguity and singularity in continuum kinematics due to crack formation.

non-linear transformation is selected, where the displacement field is determined by using third-degree b-spline functions. The DVC result is calculated by the DVC software based on a global DVC optimization approach, as introduced in Section 2.6.

Crack regions within the SMC microstructure are identified by correlating volumetric images of the initial and deformed specimen and subsequently, evaluating the difference volume data. The decisive parameter for the application of DVC methods is the grid size. The control point spacing parameter in Table 4.2 were selected based on performed applications in advance.

Table 4.2: Selected parameters of the digital image correlation analysis.

Property	Quantity
DVC software	VGSTUDIO MAX 3.4
Control point spacing	64 voxels
Type of transformation	Local non-linear
Maximum number of iterations	500
Full-field quantity	Difference volume von Mises strain

### 4.2.3 Convolutional Neural Network

Artificial intelligence approaches and convolutional neural networks (CNN) in particular are well suited to segment objects within image data. In this doctoral thesis CNN models are used to segment cracks within volumetric images acquired by  $\mu$ CT scanning. The fundamental approach is to optimize the weights of series-connected convolution filters, in order to recognize and segment the targeted objects. Training of the CNN requires a sufficient and suitable image database, that consists of input and ground truth images, in which the corresponding cracks are labeled. The training data set is extracted by separated volumetric images, which are not used for the microstructure and crack analysis. First,  $\mu$ CT cross sections are extracted from the volumetric images and cracks are manually labeled. Then, a large number of square image sections are extracted with the corresponding input size for the CNN. This procedure is schematically illustrated in Figure 4.14. A large part of the training data used in this doctoral thesis was generated as part of the master thesis of Sönmez [248]. The volumetric images used for the training process and the damage characterization were strictly separated.

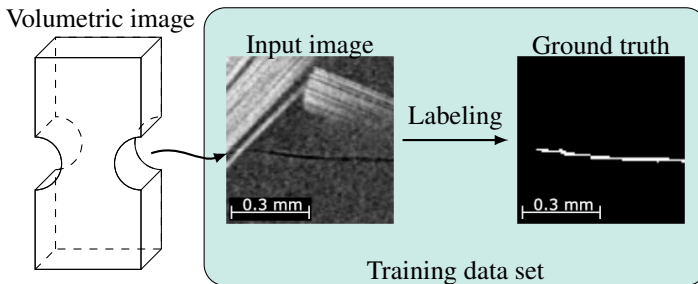


Figure 4.14: Schematic illustration of the process for generating the training data. Acquisition of input images and corresponding ground truth from volumetric images for training of the CNN model. The dimension bars were not part of the input data or ground truth and were added for display only.

In general, the acquisition of training data is highly time consuming and therefore, only a limited number of labeled images are available. To increase the number of training images, image augmentation methods are applied. Here the original images are slightly modified to create artificial new ones. In order to keep the training data set consistent, the input and ground truth data have to be modified equivalently. In this work the training images are augmented by using rotation and flipping. Figure 4.15 illustrates representative input images in the upper row and the corresponding ground truth below. On the left side original images are shown and on the right images which were generated by using image augmentation.

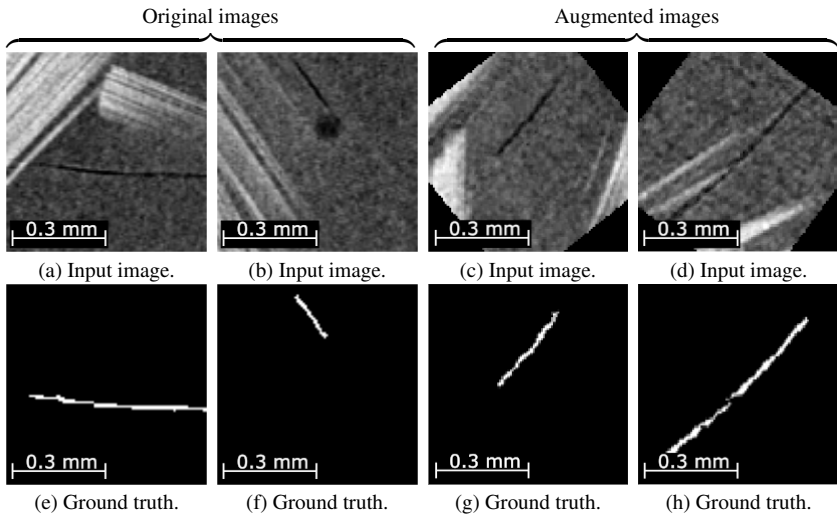


Figure 4.15: In the upper row representative input images and the corresponding ground truth below (background in black and labeled cracks in white). On the left side original images and on the right images, which were modified by using image augmentation. The image size is 96 pixels  $\times$  96 pixels and the voxel size 6.2 – 7.0  $\mu\text{m}$ . The dimension bars were not part of the input data or ground truth and were added for display only.

In this doctoral thesis the U-Net architecture presented by Ronneberger et al. [172] and illustrated in Figure 2.29 is selected as the CNN model. Here, the basic layer structure, activation functions and further details are specified by the U-Net architecture. The model is implemented by using Tensorflow 2.3.1, Keras 2.4.3 and Jupyter Notebook 2.2.8. The U-Net architecture is characterized by the fact that there is no bottleneck regarding the feature transfer and as a result, it can segment even fine structures and objects. As usual for CNN, the U-Net architecture consists of several convolutional filters and can therefore recognize and segment features transversely invariant. Utilizing the acquired training data the U-Net model is trained to segment cracks voxel-wise. The model was trained and evaluated by using the bwUniCluster 2.0 at the Karlsruhe Institute of Technology (KIT). Selected parameters and options of both the U-Net architecture and training processes are listed in Table 4.3.

Table 4.3: Parameters and options of the convolutional neural network and the training process.

Parameter/Option	Quantity/Setting
Architecture	U-Net [172]
Mask size	Convolutional ( $3 \times 3$ ), Max pooling ( $2 \times 2$ )
Activation function	ReLU (cf. Equation 2.47)
Output function	Softmax (cf. Equation 2.48)
Metric	Accuracy, Precision, Recall and F-measure (cf. Equation 2.52)
Loss	Binary Cross-Entropy (cf. Equation 2.50)
Optimizer	Adam [249]
Trainable parameters	465986
Image augmentation	Rotation ( $\leq 180^\circ$ ), Horizontal/Vertical Flip
Input/output image size	96 pixels $\times$ 96 pixels
No. of original images	9926
Data share	Training (70 %), Validation (20 %), Test (10 %)



The CNN model returns a prediction result with values between zero and one, indicating voxel-wise whether a crack or background has been recognized. These prediction values are interpreted as the confidence of the CNN model to have identified either a crack or background. The higher the prediction value, the more confident the CNN model is.

A limitation of fully-connected CNN in general and the U-net in particular, is the fixed and predefined size of the input image. For most CNN models the input images must be square and a multiple of 32. In this work the input image size is selected to be 96 pixels  $\times$  96 pixels. In order to evaluate large-scale volumetric images and with variable sizes, they are subdivided equidistantly into image patches with the predefined size of 96 pixels  $\times$  96 pixels. These image patches are evaluated by the trained CNN and afterwards reassembled to a volumetric data set. As a result, cracks are segmented within large-scale volumetric images with variable size independent of the predefined input image size. Figure 4.16 schematically illustrates this crack segmentation process on volumetric images.

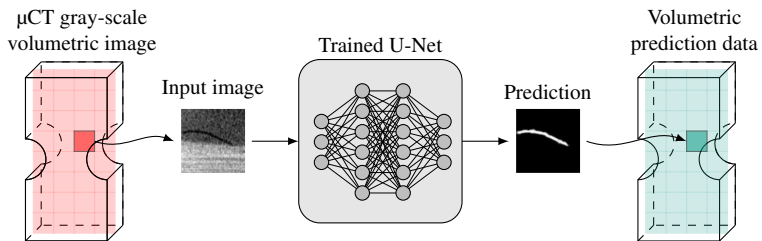


Figure 4.16: Segmenting cracks within volumetric images with variable size by using a trained U-Net model. Extracting image section, crack segmentation by applying the trained U-Net and reassembling of the volumetric prediction data.

The grid by which the image patches are extracted and reassembled can affect the crack segmentation results. For this reason the  $\mu$ CT volumetric images are

evaluated multiple times by using slightly shifted grids. The determined volumetric prediction data by using those different grids are afterwards combined and as a result, grid related effects are eliminated. Figure 4.17 illustrates the application process based on multiple grids. In this doctoral thesis, the  $\mu$ CT volume images are evaluated by a number of five slightly shifted grids.

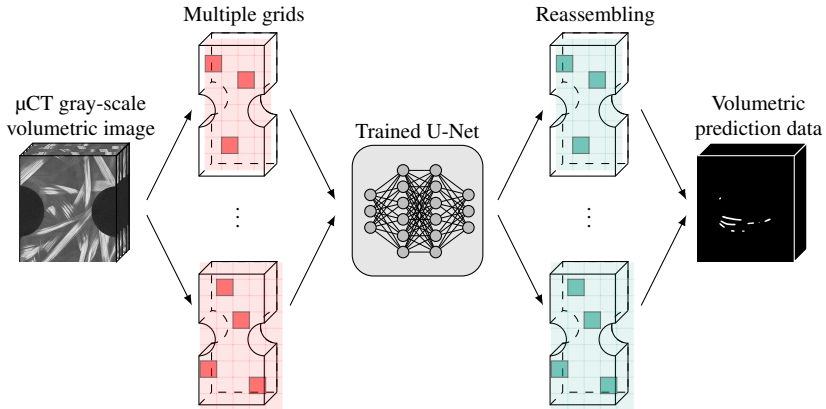


Figure 4.17: Procedure to segment cracks within volumetric images with variable size by using the trained U-Net model. Minimizing discretization effects of the patches by initiating, evaluating and reassembling using multiple slightly shifted grids.

## 4.3 Damage Characterization

The image data of the spatially segmented cracks are used to further examine damage comprehensively. In this section, image processing methods to characterize damage based on the crack segmentation results are presented. The introduced methods in this section mostly refer to the contributions [241, 243]\*.

### 4.3.1 Experimental Crack Normal Vector

To quantify the crack orientation distribution by means of experimental crack segmentation data, first the local orientation of cracks has to be determined. As introduced in Section 2.2.5 and Figure 2.8, the geometry of cracks is assumed to be step-wise planar and the orientation is described by the normal unit vector  $\mathbf{g}$ . In practice, cracks are usually not perfectly planar and consequently, the orientation of a crack cannot be expressed by a single normal vector  $\mathbf{g}$ . However, since the surface of cracks is considered to be step-wise planar and the crack orientation is characterized by a large number of unit vectors  $\mathbf{g}$  normal to the crack surface, as illustrated in Figure 4.18. As a result, the crack geometry is discretized by those experimental crack normal vectors  $\mathbf{g}$ .

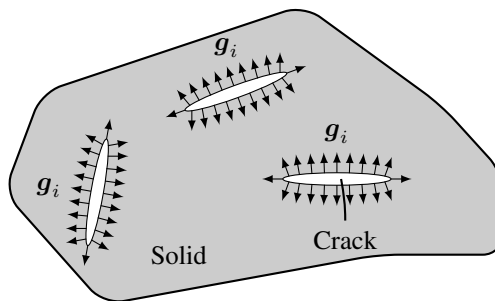


Figure 4.18: Illustration of cracks within a solid and the crack normal unit vectors  $\mathbf{g}$  (figure by Schöttl et al. [243].)

In this doctoral thesis and the contribution [241]\*, cracks are analyzed based on volumetric images acquired through  $\mu$ CT scanning. By applying the introduced segmentation methods in Section 4.2, the cracks are segmented voxel-wise and a binary volumetric image is returned. The unit vectors  $\mathbf{g}$  normal to the crack surface are then determined by using Gaussian blurring and the three-dimensional Gradient filter. First Gaussian blurring is applied to smooth the edges between background and segmented cracks. This is done to reduce the effects of voxel-related discretization. The Gradient filter then determines the vectors normal to the crack surface based on the contrast between background and segmented crack voxels. Subsequently, the crack normal vectors  $\mathbf{g}$  are calculated by normalizing the gradient vectors  $\mathbf{g} = (g_x, g_y, g_z)^T$ , so that  $\|\mathbf{g}\| = 1$ . Through the normalization the contrast gradient aspect is eliminated and the vectors  $\mathbf{g}$  only indicate the crack normal direction. Figure 4.19 illustrates the introduced procedure to determine the crack normal vectors  $\mathbf{g}$  step-by-step based on an exemplary image with a segmented crack. In Figure 4.19 (b) and Figure 4.19 (c) Gaussian blurring and Gradient filter operations are applied one after the other.

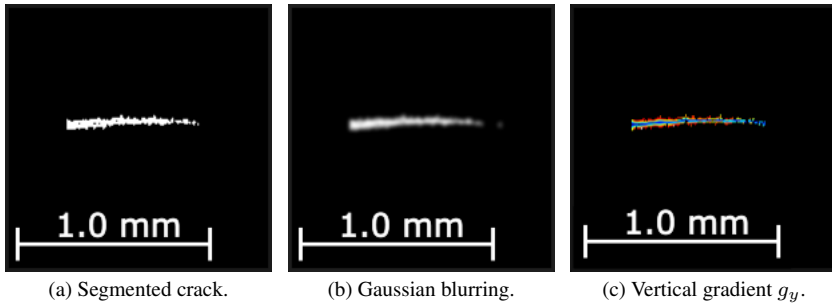


Figure 4.19: Image processing to determine the crack normal orientations. In (a) the voxel-wise segmented crack, (b) the Gaussian blurring result ( $\sigma = 1.5$  voxel) and (c) the gradient in vertical direction (background in back and the crack in white, voxel size of  $6.8 \mu\text{m}$ , re-illustration original figures by Schöttl et al. [243]\*).

### 4.3.2 Crack Orientation Tensor

The authors Lubarda and Krajcinovic [53] introduced the second-order crack orientation tensor  $\mathbf{D}$  in Equation 2.23 to describe anisotropic damaging mathematically. Similar to the work of Ken-Ichi [101] on the fiber orientation tensor, the contribution by Schöttl et al. [243]\* establishes the empirical crack density function  $\rho(\mathbf{g})$  by using  $N$  experimentally determined crack normal unit vectors  $\mathbf{g}_i$  and the discretization

$$\rho(\mathbf{g}) = \frac{1}{N} \sum_{i=1}^N \delta(\|\mathbf{g} - \mathbf{g}_i\|), \quad (4.12)$$

where  $\delta(\cdot)$  is the Dirac delta function. As a consequence and analog to Equation 2.39, the second-order crack orientation tensor  $\mathbf{D}$  is empirically determined by

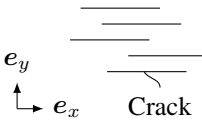
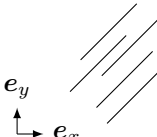
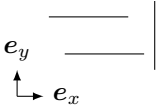
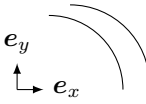
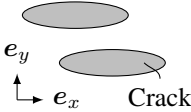
$$\mathbf{D} = \frac{1}{N} \sum_{i=1}^N \mathbf{g}_i \otimes \mathbf{g}_i. \quad (4.13)$$

The trace of the empirical second-order crack orientation tensor  $\mathbf{D}$  is normalized since

$$\text{tr}(\mathbf{D}) = 1 = \rho_0. \quad (4.14)$$

As a result, the total crack density is normalized to 1. The empirical second-order crack orientation tensor  $\mathbf{D}$  describes the anisotropic characteristics of the damage, but due to the normalization ( $\rho_0 = 1$ ) it does not quantify the total damage. Table 4.4 shows exemplary cases of different crack orientations and shapes and the resulting crack orientation tensors  $\mathbf{D}$ .

Table 4.4: Schematic cases of different types, shapes and orientations of cracks and the resulting second-order crack orientation tensors  $\mathbf{D}$ .

Crack orientation	Illustration	Second-order crack orientation tensor $\mathbf{D}$
Cracks normal to $e_y$		$\begin{bmatrix} 0 & 0 & 0 \\ 0 & 1.0 & 0 \\ 0 & 0 & 0 \end{bmatrix}_{\{e_x, e_y, e_z\}}$
Cracks oriented in $45^\circ$ to $e_x$ direction		$\begin{bmatrix} 0.5 & 0.5 & 0 \\ 0.5 & 0.5 & 0 \\ 0 & 0 & 0 \end{bmatrix}_{\{e_x, e_y, e_z\}}$
Cracks normal to $e_x$ and $e_y$		$\begin{bmatrix} 0.5 & 0 & 0 \\ 0 & 0.5 & 0 \\ 0 & 0 & 0 \end{bmatrix}_{\{e_x, e_y, e_z\}}$
Quarter circle formed cracks		$\begin{bmatrix} 0.5 & 0.3 & 0 \\ 0.3 & 0.5 & 0 \\ 0 & 0 & 0 \end{bmatrix}_{\{e_x, e_y, e_z\}}$
Ellipse-shaped cracks (aspect ratio = 4)		$\begin{bmatrix} 0.1 & 0 & 0 \\ 0 & 0.9 & 0 \\ 0 & 0 & 0 \end{bmatrix}_{\{e_x, e_y, e_z\}}$

### 4.3.3 Crack Volume Fraction

As presented, the crack orientation tensor  $\mathbf{D}$  characterizes the spatial damage distribution in terms of anisotropy, but not the total damage state. As a consequence, an additional scalar value must be introduced to describe the damage state. As a supplement to the empirical crack orientation tensor  $\mathbf{D}$ , the crack volume fraction  $\rho_{\text{Crack}}$  is introduced in the contribution of Schöttl et al. [241]\* to quantify the total damage state. The crack volume fraction  $\rho_{\text{Crack}}$  is determined by the ration between the accumulated volume of all cracks  $V_{\text{Crack}}$  and the reference volume  $V_{\text{ref}}$  by

$$\rho_{\text{Crack}} = \frac{V_{\text{Crack}}}{V_{\text{ref}}}. \quad (4.15)$$

The reference volume  $V_{\text{ref}}$  covers the total specimen volume within the  $\mu\text{CT}$  scanned region including the cracks, which means that the reference volume  $V_{\text{ref}}$  is independent of the crack formation state. Figure 4.20 illustrates the accumulated volume of all cracks  $V_{\text{Crack}}$  and the reference volume  $V_{\text{ref}}$  schematically. As a consequence, the crack volume fraction  $\rho_{\text{Crack}}$  takes into account both damage propagation aspects, the growth of cracks and the formation of additional cracks.

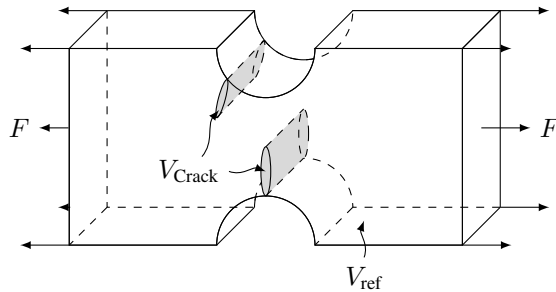


Figure 4.20: Illustration of the accumulated crack volume  $V_{\text{Crack}}$  and the reference volume  $V_{\text{ref}}$ .

### 4.3.4 Damage Classification

Mechanical properties on the macro scale are significantly affected by the formation of cracks on the microscopic level. However, the formation of cracks in fiber-reinforced composites affects the mechanical properties on the macro scale in different ways, depending on whether the cracks damage the matrix, fiber bundles or interface. As shown in Section 2.2 and Section 3.2.3, various damage mechanisms occur within fiber-reinforced composites and SMC, in particular. The individual damage mechanisms proceed differently and also have different effects on the mechanical behavior. As a consequence, the identification and quantification of predominant damage mechanism(s) is essential to understand the damaging process comprehensively.

In this doctoral thesis a method is introduced to classify damage mechanisms which are related to crack formation based on in-situ  $\mu$ CT results. Cracks are segmented by using the presented methods in Section 4.2. Based on the crack segmentation and fiber orientation results (cf. Section 2.5.2), three different damage mechanisms for SMC are investigated and classified:

I Matrix cracking

II Pseudo-delamination

III Fiber bundle fracture

The introduced classification method in this work is inspired by the fundamental crack classification approach presented by Yu et al. [76], in which cracks within woven glass fiber-reinforced composites are classified based on their orientation and neighboring microstructure. To identify the local damage mechanism the surrounding microstructure around the cracks has to be taken into account for the evaluation. Figure 4.21 illustrates schematically a crack along and through fiber bundles, as well as matrix. In order to classify the local damage mechanism at a specific location of this crack, the spherical control



volume  $\mathcal{B}$  with radius  $R$  is introduced. Based on the microstructure within the control volume  $\mathcal{B}$  the corresponding damage mechanisms are evaluated.

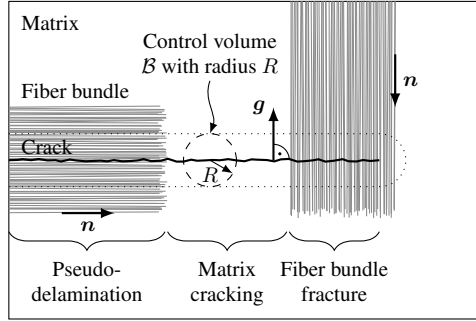


Figure 4.21: Identification of damage mechanisms by taking the surrounding microstructure into account. Classification approach for the damage mechanisms based on the control volume  $\mathcal{B}$  around the crack. The proportions of radius  $R$ , fiber diameter and bundle width are not illustrated realistically.

In practice, damage mechanisms do not occur isolated but rather mixed. For this reason criteria are introduced to identify the mixed nature of the damage mechanisms. Figure 4.22 presents the mathematic classification criteria of the three SMC damage mechanisms matrix cracking, pseudo-delamination and fiber bundle fracture. The damage mechanisms are determined based on the control volume  $\mathcal{B}$  around the crack, including the interaction of crack orientation  $\mathbf{g}_j$  and fiber orientation  $\mathbf{n}_i$  data. The matrix crack fraction  $\rho_{I,j}$  is calculated by the volume fraction of matrix within the control volume  $\mathcal{B}$ . Complementary to this, the other two damage mechanisms are divided depending on whether the crack is oriented parallel or perpendicular to fibers within  $\mathcal{B}$ . Here it should be noted that the crack orientation  $\mathbf{g}_j$  is normal to the crack plane.

The pseudo-delamination criterion includes the delamination within one (intra) and between two fiber bundles (inter). All three damage criteria are normalized in the way that their sum is one ( $\rho_{I,j} + \rho_{II,j} + \rho_{III,j} = 1$ ). By applying the damage classification method the fraction of the three individual damage

mechanisms are quantified. Together with the crack volume fraction and the crack orientation analysis, the damage characterization methods presented in this doctoral thesis make it possible to determine the extent of cracks, the direction in which they are oriented and what aspects of the microstructure they damage.

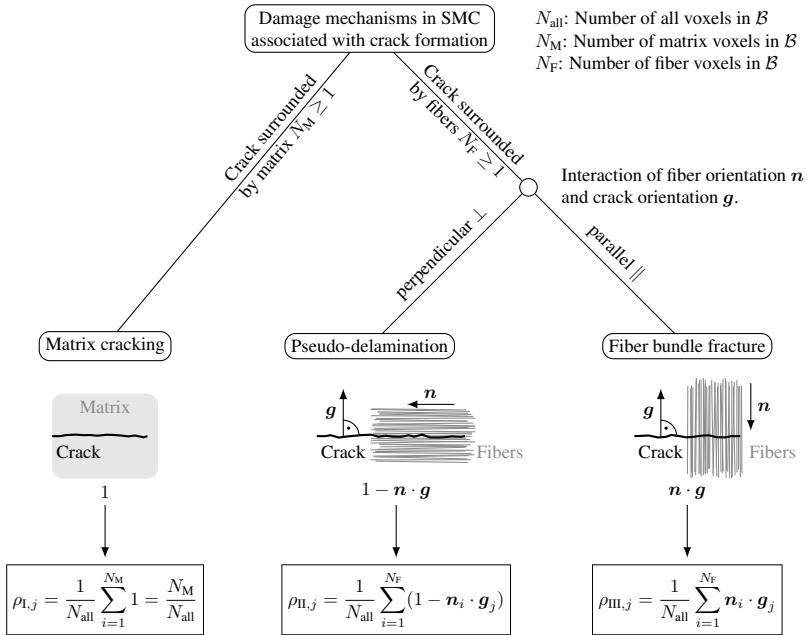


Figure 4.22: Introducing mathematical criteria  $\rho_{I,j}$ ,  $\rho_{II,j}$  and  $\rho_{III,j}$  to quantify the damage mechanisms in SMC that are associated with crack formation. The damage mechanisms are classified for each crack voxel  $j$  individually.

An important aspect while applying the damage classification method is to select an appropriate radius  $R$  of the spherical control volume  $\mathcal{B}$ . The radius  $R$  should be selected appropriately to take a representative microstructure volume around the cracks into account and to make a meaningful statement about the

evaluated damage mechanisms. To adjust the control volume independent by the voxel size of the  $\mu$ CT scan, the radius  $R$  is defined by referring to the fiber diameter. The radius  $R$  is selected to be 20 times the fiber diameter and was adjusted by application in advance.



# 5 Experimental

The key aspect of the experimental investigation in this doctoral thesis is the acquisition of volumetric images by means of  $\mu$ CT scanning and interrupted in-situ testing in order to analyze the damaging behavior on the microstructural level. Details of the used  $\mu$ CT system, in-situ testing stage and analyzed specimens are given in the sections below.

## Contents

---

5.1 Micro-Computed Tomography System . . . . .	126
5.2 In-situ $\mu$ CT Testing Stage . . . . .	127
5.3 Cyclic Tensile Load Protocol . . . . .	129
5.4 Specimen Geometries . . . . .	130
5.5 Fractography . . . . .	131

---

## 5.1 Micro-Computed Tomography System

The  $\mu$ CT measurements in this doctoral thesis were performed on a CT Precision system from XYLON International GmbH (Hamburg, Germany) installed at the Institute for Applied Materials (IAM-WK), Karlsruhe Institute of Technology (KIT). The  $\mu$ CT system can be equipped with either a transmission or a reflection tube head from Comet Group AG (Flamatt, Switzerland). The maximum power of the transmission tube head is 10 W and 200 W of the reflection tube head. Resolution of the detector, edge length and pixel pitch of the flat panel Y.XRD1620 from PerkinElmer Inc. (Waltham, United States) are  $2048 \text{ pixels} \times 2048 \text{ pixels}$ , 409.6 mm and  $200 \mu\text{m}$ , respectively. Before each  $\mu$ CT experiment, the X-ray detector is calibrated by a free-beam measurement. The operation parameters exposure time, current, voltage and frame binning were selected to 500 - 1000 ms, 0.03 - 0.25 mA, 130 - 150 kV and 2, respectively.

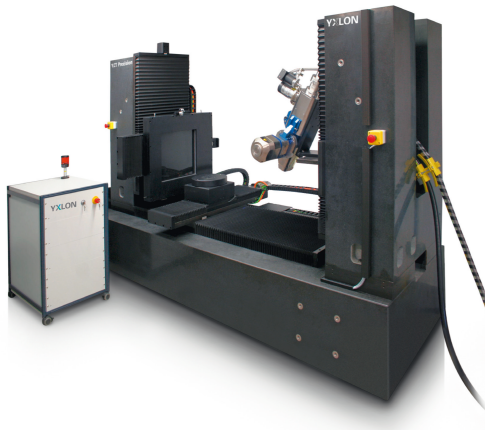


Figure 5.1: XYLON CT Precision  $\mu$ CT System [250].

## 5.2 In-situ $\mu$ CT Testing Stage

In-situ  $\mu$ CT testing is an experimental method in material science, which combines mechanical testing and  $\mu$ CT scanning. The principle in-situ  $\mu$ CT setup and the fundamental process, where a specimen under mechanical load is screened by  $\mu$ CT scanning is illustrated in Figure 5.2. The acquired volumetric images offer a three-dimensional view into microstructure of the specimen while damage takes place. In this work interrupted in-situ  $\mu$ CT tests are carried out. As a result, volumetric images of the examined specimens at selected damage stages are acquired.

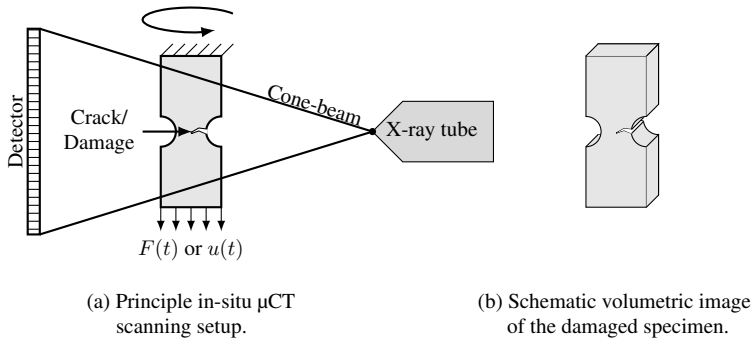


Figure 5.2: Illustrating the principle in-situ  $\mu$ CT testing setup. Combining  $\mu$ CT scanning and in-situ tensile testing in order to acquire volumetric images of damaged microstructures.

The in-situ  $\mu$ CT testing stage used in this doctoral thesis is shown in Figure 5.3. It was designed at the Institute for Applied Materials (IAM-WK) [251–254],[241, 243]\*. The lean design of the load frame made of a CFRP tube enables to place the testing stage close to the focus spot and thus, acquire high-resolution volumetric images with high contrast. Figure 5.4 shows the clamping situation inside the load frame. Material with high mass density, such as metals highly absorb X-ray and can negatively affect the  $\mu$ CT scan. Although the clampings are made of steel, those are not located inside the cone-beam

area, as illustrated in Figure 5.4 (a) and consequently, do not affect the  $\mu$ CT scanning process. The maximum traverse speed and load of the in-situ  $\mu$ CT load stage are  $2.4 \text{ mm min}^{-1}$  and  $5 \text{ kN}$ , respectively.

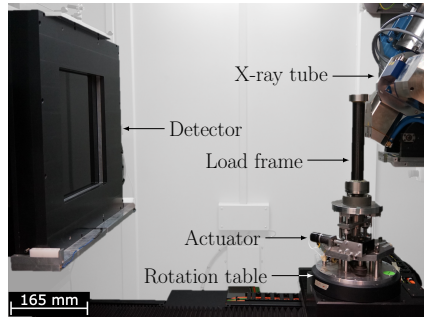
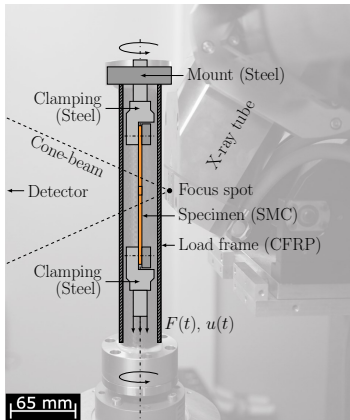
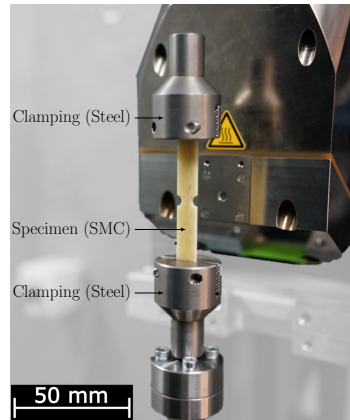


Figure 5.3: The  $\mu$ CT system including detector, rotation table and X-ray tube. Furthermore, the mechanical setup to conduct in-situ tensile tests, which consists of a CFRP load frame where the specimen is clamped inside (figure by Schöttl et al. [241]\*).



(a) Cross section of the setup.



(b) Specimen clamping.

Figure 5.4: Illustration of the  $\mu$ CT system and the in-situ testing setup. In (a) the cross section of the in-situ setup and (b) the clamped SMC specimen without the load frame (figures by Schöttl et al. [241]\*).



## 5.3 Cyclic Tensile Load Protocol

In practice, cyclical load is a common use case. The in-situ  $\mu$ CT tests in this work are carried out by applying cyclic tensile load. To investigate the crack propagation in detail by means of interrupted  $\mu$ CT scanning the damage is introduced step-wise in a controlled manner by using cyclic load increase tests. The mechanical tensile tests are carried out displacement controlled. Figure 5.5 (a) illustrates the in-situ  $\mu$ CT protocol using cyclic load, where the displacement amplitude is constant and the mean displacement is increased in each load step. In the beginning an initial  $\mu$ CT scan of the specimen is acquired. Subsequently, after each load step a  $\mu$ CT scan is performed at the upper displacement amplitude  $u_{\text{scan}} = u_m + \Delta u$ , where  $u_m$  is the mean displacement and  $\Delta u$  the displacement amplitude. As a result, volumetric images of the microstructure with maximum crack opening are acquired.

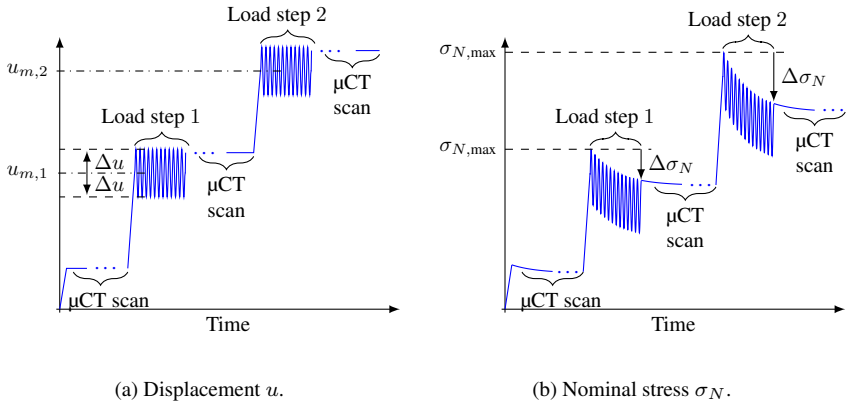


Figure 5.5: Illustration of the (a) displacement and (b) nominal stress along the interrupted in-situ  $\mu$ CT test applying cyclic tensile load which is increased by each load step.

A cyclic load step takes about 30 min to complete. In order to avoid specimen moving during the scan and acquire sharp projections, 5 min are waited between the load step end and the beginning of the  $\mu$ CT scan. Acquiring the  $\mu$ CT

projections over  $360^\circ$  takes 80 min. All  $\mu$ CT scans of the same sample are performed with the same scan parameters. Figure 5.5 (b) illustrates schematically the measured nominal stress signal. Important quantities are the maximum nominal stress  $\sigma_{N,\max}$  and the drop of the nominal stress  $\Delta\sigma_N$  for each load step.

## 5.4 Specimen Geometries

The investigated specimens are extracted by water jet cutting from plates of  $800\text{ mm} \times 250\text{ mm}$  and  $800\text{ mm} \times 150\text{ mm}$ . The plates are between 1.5 mm and 2.0 mm thick.

As introduced in Section 3.1.4, the initial charge coverage and mold flow process affect the fiber alignment of the microstructure. SMC samples with initial charge coverage between 25 % and 50 % and plate orientations of  $0^\circ$ ,  $45^\circ$  and  $90^\circ$  with respect to the mold filling direction (MFD) are analyzed, as shown in Figure 5.6. The geometry of the examined SMC samples by means of in-situ  $\mu$ CT testing is illustrated in Figure 5.7. The notched geometry was developed to force a stress concentration here and study the microstructural damage in detail by focusing the  $\mu$ CT scanning on the notched region. Similar geometries for in-situ  $\mu$ CT testing have been studied in several contributions [84, 85, 255].

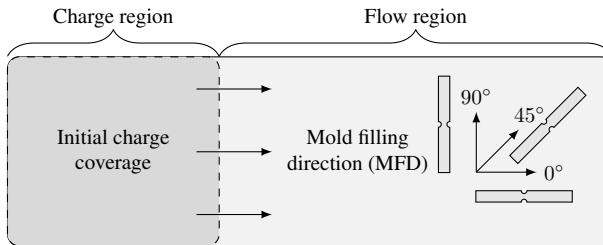


Figure 5.6: Plate orientation of the extracted SMC samples in  $0^\circ$ ,  $45^\circ$  and  $90^\circ$  to the MFD. Illustration of the initial charge coverage, flow region and MFD.

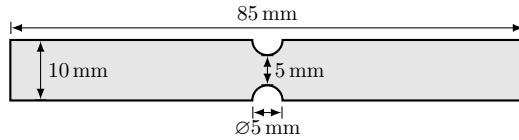


Figure 5.7: Illustration of the double semi-circle notched sample geometry, which is used for in-situ  $\mu$ CT tests. Sample thickness  $t = 1.5 - 2.0$  mm (figure by Schöttl et al. [241]\*).

## 5.5 Fractography

In addition to the in-situ  $\mu$ CT measurements, the fracture surfaces of the tested SMC samples are examined by using scanning electron microscopy (SEM). The SEM images in this doctoral thesis were acquired by using an EVO 50 SEM system by Carl Zeiss AG (Oberkochen, Germany) at the Institute for Applied Materials (IAM-WK). Before scanning the SMC specimens, a layer of gold was sputtered on the fracture surfaces. The operation parameters of the SEM including the working distance and accelerating voltage were selected to 8.0 - 10.5 mm and 10.0 kV, respectively. The SEM images were acquired with the support of Jonas Hüther.



# 6 Results

Chapter 4 and chapter 5 introduce the developed methods as well as the experimental applications. The obtained results in terms of microstructure and damage characterization are presented comprehensively in this chapter. Goal of this doctoral thesis is to investigate the relationship between microstructure and damage behavior by means of  $\mu$ CT technique. Consequently, the results on microstructure and damage characterization are brought together. First, the SMC microstructure of the in-situ  $\mu$ CT specimens is characterized, among others, and their damage behavior is then investigated further.

## Contents

---

<b>6.1 Microstructure Characterization . . . . .</b>	<b>134</b>
<b>6.2 Experimental Damage Investigation . . . . .</b>	<b>144</b>
<b>6.3 Damage Segmentation . . . . .</b>	<b>154</b>
<b>6.4 Damage Characterization . . . . .</b>	<b>164</b>
<b>6.5 Fractography . . . . .</b>	<b>171</b>

---

## 6.1 Microstructure Characterization

In this section the results in terms of microstructure characterization are presented. The fiber architectures of the in-situ  $\mu$ CT specimens are examined regarding the fiber orientation distribution. Furthermore, the fiber bundles of SMC microstructures are analyzed and the curvature distribution within a weld line is characterized.

### 6.1.1 Fiber Orientation

The presented microstructure characterization methods in Section 4.1 are applied to analyze the SMC microstructure in terms of the fiber orientation distribution. In following sections the microstructure characterization results of the in-situ  $\mu$ CT specimens with the geometry in Figure 5.7 are presented. Four SMC specimens with different microstructures are examined in detail. The microstructures of the specimens are characterized by the fact that the fiber orientation distributions are:

- Highly oriented in  $0^\circ$  (HO- $0^\circ$ )
- Highly oriented in  $45^\circ$  (HO- $45^\circ$ )
- Highly oriented in  $90^\circ$  (HO- $90^\circ$ )
- Randomly oriented (RO)

with respect to the tensile load direction ( $\hat{=}$   $0^\circ$ ).

## 6.1.2 Fibers Highly Oriented in Load Direction

Presenting the microstructure data of a specimen with  $0^\circ$  plate orientation. Figure 6.1 shows a representative  $\mu$ CT cross section and the corresponding fiber orientations visualized by HSV color space. The fiber orientation histogram and the orientation tensors  $\mathbf{N}$  are illustrated in Figure 6.2. The results reveal that the fibers are highly oriented along the tensile load direction (HO- $0^\circ$ ).

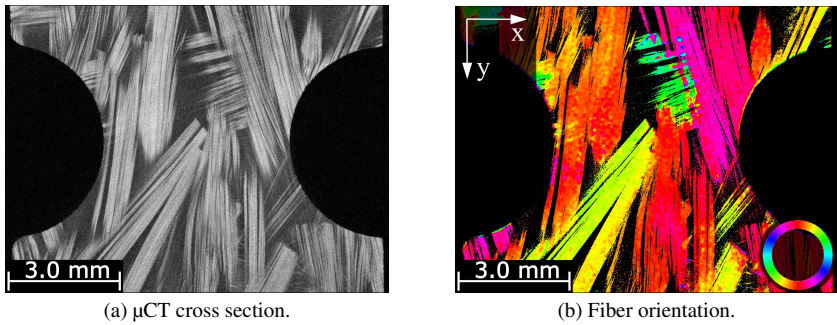


Figure 6.1: Characterizing the microstructure of the HO- $0^\circ$  specimen. In (a) a gray-value  $\mu$ CT cross section and (b) the fiber orientation visualized by HSV color map.

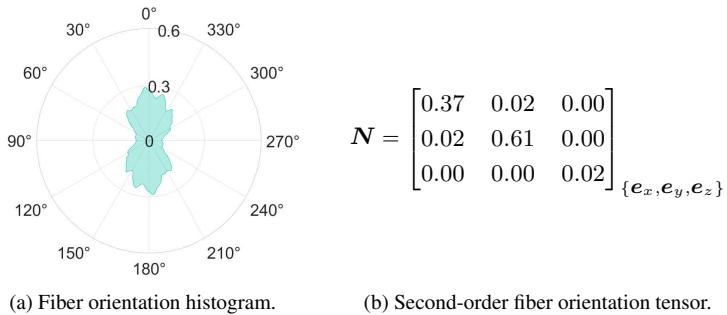


Figure 6.2: In (a) the fiber orientation histogram of the entire specimen and (b) the empirical second-order orientation tensor  $\mathbf{N}$  of the HO- $0^\circ$  specimen. Load direction  $\hat{=}$   $0^\circ$ .

### 6.1.3 Fibers Highly Oriented Diagonal to the Load Direction

Figure 6.3 illustrates a representative  $\mu$ CT cross section of the SMC in-situ specimens with  $45^\circ$  plate orientation and the corresponding fiber orientations. In addition, the fiber orientation histogram and second-order fiber orientation tensors  $\mathbf{N}$  are shown in Figure 6.4. The fiber orientation histogram in Figure 6.4 shows that the fibers are highly oriented at  $45^\circ$  (HO- $45^\circ$ ).

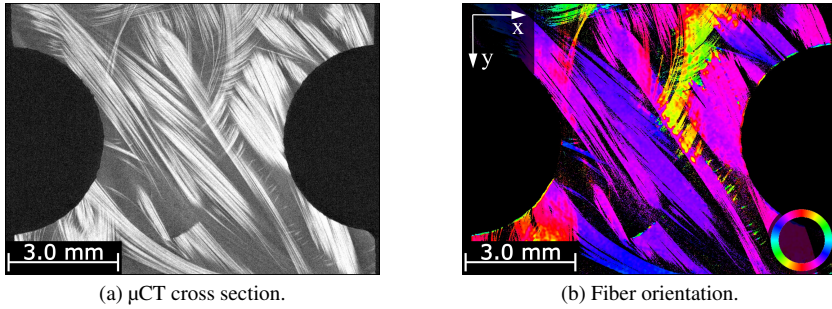


Figure 6.3: Characterizing the microstructure of the HO- $45^\circ$  specimen. In (a) a gray-value  $\mu$ CT cross section and (b) the fiber orientation visualized by HSV color map.

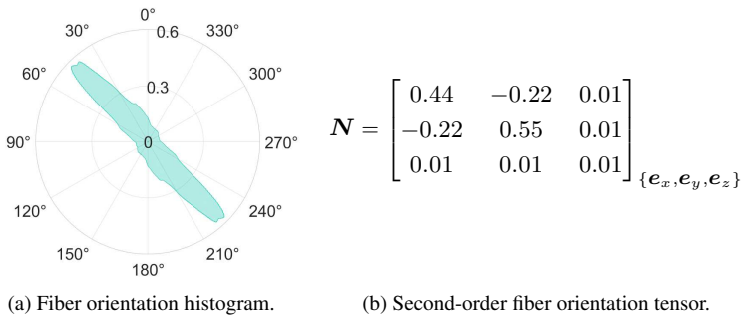


Figure 6.4: In (a) the fiber orientation histogram of the entire specimen and (b) the empirical second-order orientation tensor  $\mathbf{N}$  of the HO- $45^\circ$  specimen. Load direction  $\hat{=}$   $0^\circ$ .



### 6.1.4 Fibers Highly Oriented Perpendicular to the Load Direction

In Figure 6.5 a representative  $\mu$ CT cross section and the corresponding fiber orientations are illustrated of a specimen with  $90^\circ$  plate orientation. Figure 6.6 shows the determined fiber orientation histogram and fiber orientation tensor  $\mathbf{N}$ . The results in Figure 6.5 (b) and Figure 6.6 (a) both reveal that the principal fiber orientation is aligned perpendicular to the load direction (HO- $90^\circ$ ).

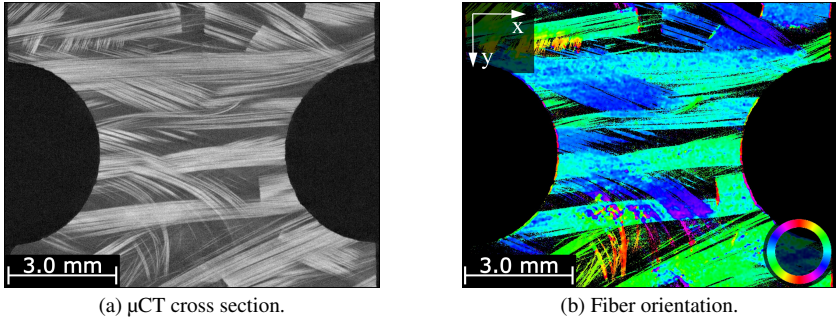


Figure 6.5: Characterizing the microstructure of the HO- $90^\circ$  specimen. In (a) a gray-value  $\mu$ CT cross section and (b) the fiber orientation visualized by HSV color map.

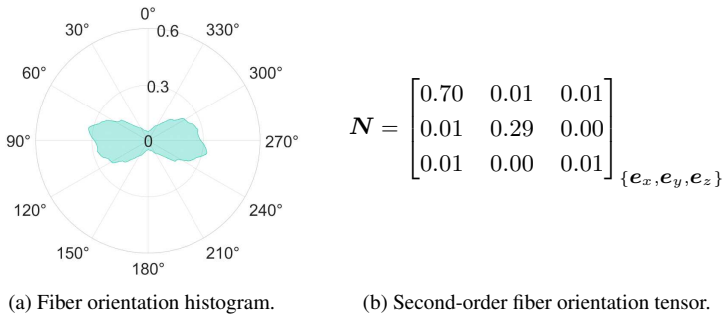


Figure 6.6: In (a) the fiber orientation histogram of the entire specimen and (b) the empirical second-order orientation tensor  $\mathbf{N}$  of the HO- $90^\circ$  specimen. Load direction  $\hat{=}$   $0^\circ$ .

### 6.1.5 Fibers Randomly Oriented

Although the specimen in Figure 6.7 was extracted from a plate with 25 % charge coverage, the fiber orientation data in Figure 6.8 reveal that there is no principal fiber orientation and the fibers are randomly oriented (RO). As a consequence, the fiber orientation state in this SMC specimen is referred to as approximately planar isotropic.

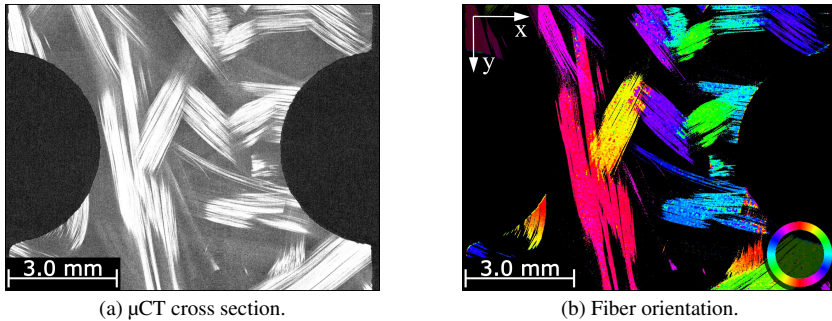


Figure 6.7: Characterizing the microstructure of the RO specimen. In (a) a gray-value  $\mu$ CT cross section and (b) the fiber orientation visualized by HSV color map.

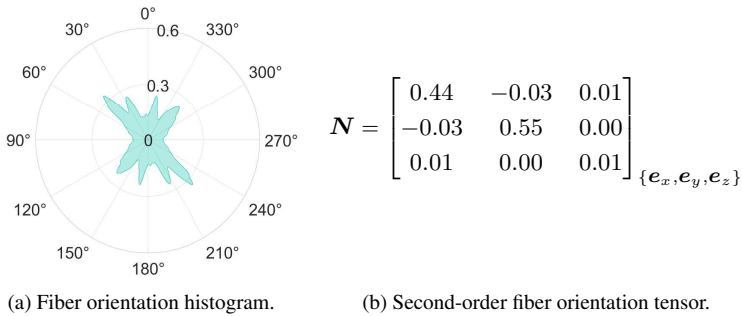


Figure 6.8: In (a) the fiber orientation histogram of the entire specimen and (b) the empirical second-order orientation tensor  $\mathbf{N}$  of the RO specimen. Load direction  $\hat{=}$   $0^\circ$ .

### 6.1.6 Quantification of the Fiber Orientation State

The fiber orientation state of the examined SMC specimens is illustrated in Figure 6.9 based on the corresponding eigenvalues  $\lambda_i$  of the second-order fiber orientation tensor  $\mathbf{N}$  and the visualization scheme according to Cintra and Tucker [256]. In this case the fiber orientation state is completely described by (any) two eigenvalues of  $\mathbf{N}$ , since  $\lambda_1 + \lambda_2 + \lambda_3 = 1$  and  $1 \geq \lambda_1 \geq \lambda_2 \geq \lambda_3 \geq 0$ . Figure 6.9 shows that  $\lambda_3$  is marginal for all four specimens, since the eigenvalues are located near the ideal planar orientation state. Consequently, there are planar fiber orientation states in all four SMC microstructures.

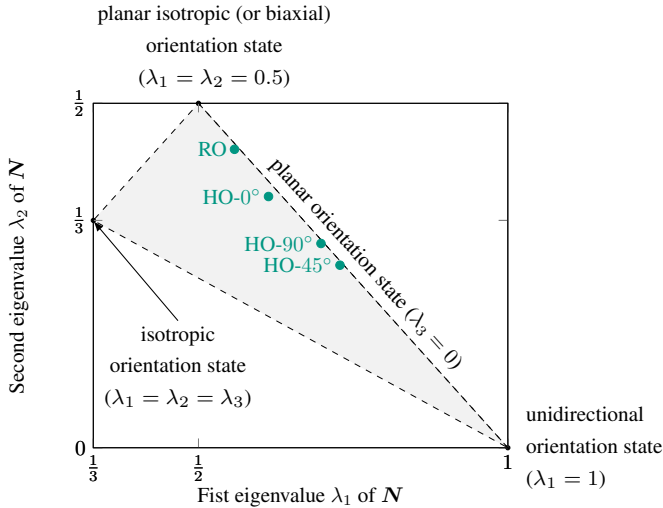


Figure 6.9: Illustrating the fiber orientation state of the four examined SMC specimens for in-situ  $\mu$ CT testing according to the scheme by Cintra and Tucker [256].

In addition to the illustration in Figure 6.9 and the respective fiber orientation histograms, the anisotropy of the fiber orientation distribution is quantified by

using the coherence  $c_w$  of the second-order fiber orientation tensor  $\mathbf{N}$ . According to Jähne [257], the coherence  $c_w$  is determined based on the first two eigenvalues  $\lambda_{1,2}$  of  $\mathbf{N}$  by

$$c_w = \frac{\lambda_1 - \lambda_2}{\lambda_1 + \lambda_2}. \quad (6.1)$$

In case of a planar isotropic (or biaxial) fiber orientation distribution,  $\lambda_1$  is equal to  $\lambda_2$  and as a result, the coherence  $c_w$  becomes zero. If the first eigenvalue  $\lambda_1$  is one, all fibers are oriented in the same direction (ideal unidirectional fiber orientation distribution) and the coherence  $c_w$  becomes one. Table 6.1 lists the charge coverage, coherence and plate orientation of the examined specimens. For the specimens with a distinctive fiber orientation, the principal fiber orientation is determined based on the maximum of the respective fiber orientation histogram.

Table 6.1: Summary of microstructure properties. Charge coverage, coherence, plate orientation and principal fiber orientation of the examined SMC specimens.

Label	Charge coverage	Coherence $c_w$ of $\mathbf{N}$	Plate orient.	Principal fiber orient.
HO-0°	50 vol. %	0.25	0°	4.0°
HO-45°	25 vol. %	0.47	45°	45.4°
HO-90°	50 vol. %	0.40	90°	78.5°
RO	25 vol. %	0.13	45°	planar isotropic

As consistently quantified by the coherence  $c_w$  in Table 6.1, the illustration in Figure 6.9 and the fiber orientation histogram in Figure 6.8, the fibers within the RO-specimens are oriented nearly planar isotropically. The fibers of the SMC specimens HO-0°, HO-45° and HO-90° are significantly more aligned, with the HO-45° specimen having the highest degree of fiber alignment.

### 6.1.7 Fiber Bundle Tracking

By applying the fiber bundle tracking and clustering methods, which are presented in Section 2.5.4, the SMC fiber bundle structure is analyzed. The corresponding results of the contribution by Schöttl et al. [242]\* are presented in this section. The fiber bundles within two different SMC specimens are tracked and clustered. Figure 6.10 (a) shows the gray-scale  $\mu$ CT volumetric image and Figure 6.10 (b) the identified fiber bundles, respectively. Trajectories of the same fiber bundle are indicated by uniform colors. To visualize the identified fiber bundle with a good contrast, the respective color of the fiber bundles is selected randomly. In Figure 6.11 the fiber bundle tracking results of another SMC specimen are illustrated. The identified fiber bundles within the marked region in Figure 6.11 (b) are shown more detailed in Figure 6.12.

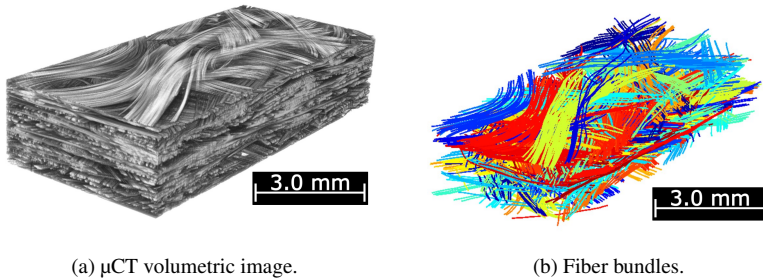


Figure 6.10: The (a) gray-value volumetric image acquired by  $\mu$ CT scanning and (b) the visualized tracked and clustered fiber bundles (figures by Schöttl et al. [242]\*). Sample No. 1 in Table 4.1.

The comparisons between the gray-scale  $\mu$ CT volumetric images in Figure 6.10 (a) and Figure 6.11 (a) and the visualized fiber bundles in Figure 6.10 (b) and Figure 6.11 (b) reveal that the corresponding fiber bundles have been identified accordingly by using the introduced fiber bundle tracking method. The fiber bundle tracking results of both SMC samples were used to validate and discuss the fiber bundle tracking method in the contribution [242]\*.

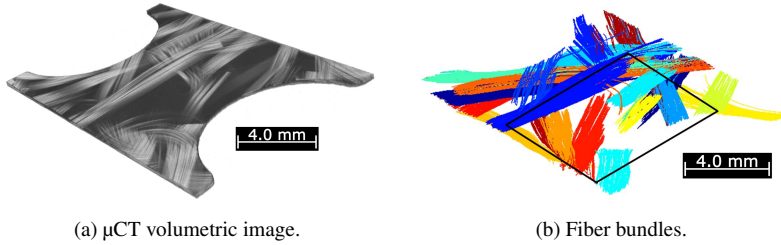


Figure 6.11: Tracked and clustered fiber bundles within the in-situ  $\mu$ CT specimen HO-0°. In (a) the gray-value  $\mu$ CT volumetric image and (b) the visualized fiber bundles (figures by Schöttl et al. [242]\*). Sample No. 2 in Table 4.1.



Figure 6.12: Close-up of the tracked and clustered fiber bundles within the marked region in Figure 6.11 (b) (figure by Schöttl et al. [242]\*).

## 6.1.8 Fiber Bundle Curvature

The characterization results on fiber bundle curvature published in the contribution [118, 240]\* are summarized in this section. As introduced in Section 3.1.5, a weld line can be formed during the SMC molding filling process as a result of clashing mold fronts. In this doctoral thesis the fiber bundle curvature around and inside a weld line formation is investigated. Figure 6.13 (a) shows a representative  $\mu$ CT cross section of the examined weld line. The tracked fiber bundles are illustrated in Figure 6.13 (b) and the determined fiber bundle curvature in Figure 6.13 (c). A statistical analysis of the mean and maximum curvature orthogonal to the weld line is given in Figure 6.14.

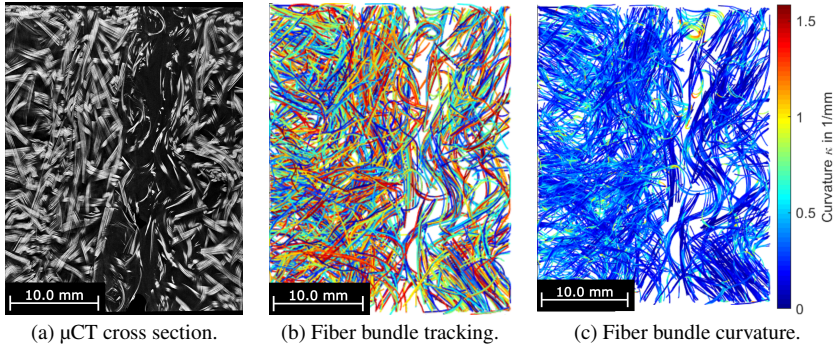


Figure 6.13: Analyzing the SMC fiber bundle within a weld line region. In (a) the  $\mu$ CT cross section, (b) the tracked fiber bundles and (c) the fiber bundle curvature (figures by Schöttl et al. [240]\*). Sample No. 3 in Table 4.1.

Both, Figure 6.13 (c) and Figure 6.14 reveal that there are local curvature peaks within the weld line region. Although the mean curvature distribution shows only a slight peak within the weld line, the maximum curvature shows a significant increase in this area. It can be concluded that only a few fiber bundles within the weld bundle are strongly curved. This is also confirmed by Figure 6.13 (c).

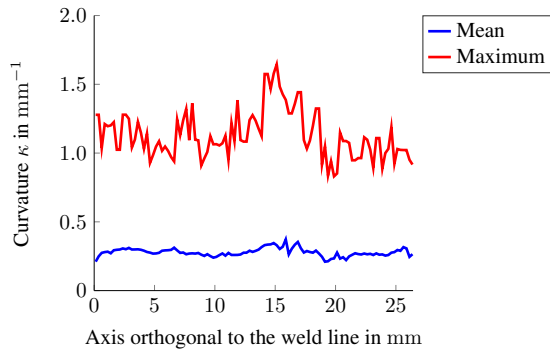


Figure 6.14: The mean and maximum curvature distribution orthogonal to the examined SMC weld line (data by Schöttl et al. [240]\*).

## 6.2 Experimental Damage Investigation

The details and results of the experimental in-situ  $\mu$ CT tests are given in this section. Four SMC specimens with different microstructures are examined. The test procedures are adapted accordingly to the specimen's plate orientation and microstructure.

### 6.2.1 Fibers Highly Oriented in Load Direction

Table 6.2 lists details of the performed in-situ  $\mu$ CT tests on a specimen extracted with a plate orientation of  $0^\circ$  to the MFD. As a consequence, the fiber bundles within the specimen are highly oriented in load direction (HO- $0^\circ$ ), as shown in Figure 6.2 (a). The maximal stress  $\sigma_{N,\max}$  and stress relaxation  $\Delta\sigma_N$  in each load step indicate the propagating damage process during the in-situ  $\mu$ CT test. The displacement  $u$  and nominal stress  $\sigma_N$  curves along the tests are illustrated in Figure 6.15.

Table 6.2: Selected load step parameters of the respective in-situ  $\mu$ CT test examining the HO- $0^\circ$  specimen. Furthermore, the measured nominal stress maximum  $\sigma_{N,\max}$  and drop  $\Delta\sigma_N$  of each load step (data by Schöttl et al. [241]\*).

Parameters		Load step					Fracture
		Initial	1	2	3	4	
$u_m$	mm	-	1.1	1.4	1.7	2.0	-
$\Delta u$	mm	-	$\pm 0.1$	$\pm 0.1$	$\pm 0.1$	$\pm 0.1$	-
$N$	-	-	100	100	100	100	-
$f$	Hz	-	0.067	0.067	0.067	0.067	-
$\sigma_{N,\max}$	MPa	19.4	160.5	192.7	209.8	227.9	231.7
$\Delta\sigma_N$	MPa	-	-17.9	-29.8	-32.7	-39.0	-



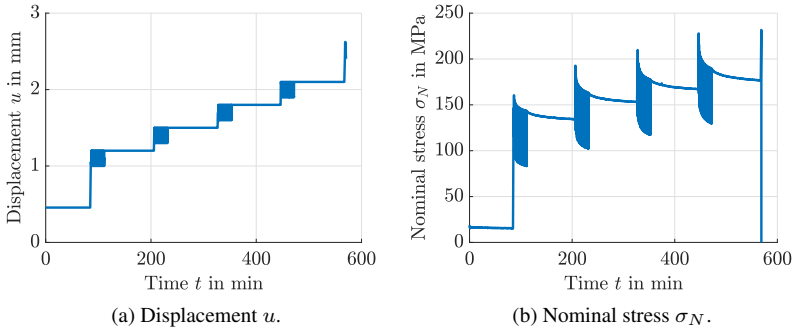


Figure 6.15: Four cyclic load steps are carried out. Initially and after each load step the specimen is screened by means of  $\mu$ CT scanning. In (a) the displacement  $u$  and (b) the nominal stress  $\sigma_N$  curves along the in-situ test process are plotted (figure by Schöttl et al. [241]\*).

The crack initiation and propagation within the HO-0° specimen is illustrated by means of representative  $\mu$ CT cross sections. Figure 6.16 (a) presents the schematic location of the  $\mu$ CT cross section in Figure 6.16 (b), where the initial microstructure is shown. Furthermore, detailed  $\mu$ CT cross section views of the marked region in Figure 6.16 (b) are given in Figure 6.16 (c) to (f) for the respective load steps. In the first load step a single crack is initiated, which propagates during the second and third load step.

As shown in Figure 6.16 (f) in the fourth load step additional cracks are initiated. The nominal stress data  $\sigma_{N,\max}$  in Table 6.2 indicates, the HO-0° specimen fails immediately after the fourth load step. As a consequence, the  $\mu$ CT cross section in Figure 6.16 (f) shows the damaged SMC microstructure just before fracture.

This shows a damage development from a single crack to the formation of multiple cracks in the progressive damage state. Furthermore, the  $\mu$ CT cross sections in Figure 6.16 (c) to (f) of the corresponding load steps reveal that cracks mainly occur in the matrix here.

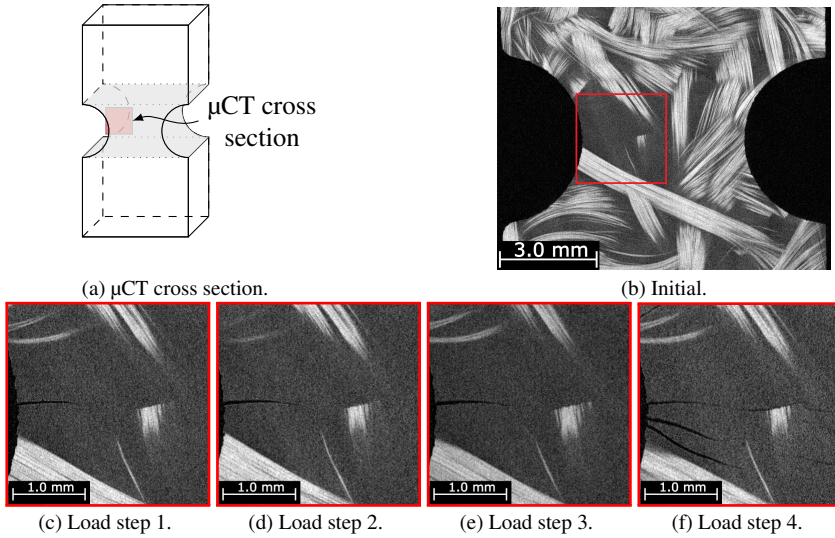


Figure 6.16: The SMC damage evolution within the  $\mu$ CT cross section. In (b) the initial and (c) to (f) the enlarged SMC microstructure after the respective load steps (figures by Schöttl et al. [241]\*).

## 6.2.2 Fibers Highly Oriented Diagonal to the Load Direction

The in-situ  $\mu$ CT test results of the SMC specimen which was extracted with a  $45^\circ$  plate orientation are presented in this section. As shown by Figure 6.8, the fibers are mostly oriented in  $45^\circ$  to the load direction (HO- $45^\circ$ ). Detailed parameters of the in-situ  $\mu$ CT test are given in Table 6.3. The displacement  $u$  and nominal stress curves  $\sigma_N$  along the in-situ  $\mu$ CT test are illustrated in Figure 6.17.

Although five load steps are performed in total, damage is only observed within the last two. Representative  $\mu$ CT cross section views of these two load steps are given in Figure 6.18. As shown in Figure 6.18 (a), during the fourth load step a single crack is initiated close to the plate surface, which propagates during the

fifth load step and leads to fracture of the specimen. Both  $\mu$ CT cross sections in Figure 6.18 (b) and (c) show the damaged microstructure after the fifth load step at different locations within the specimen.

Table 6.3: Selected load step parameters of the respective in-situ  $\mu$ CT test examining the HO-45° specimen. Furthermore, the measured nominal stress maximum  $\sigma_{N,\max}$  and drop  $\Delta\sigma_N$  of each load step.

Parameters			Load step					Fracture
			Initial	1	2	3	4	
$u_m$	mm	-	0.60	0.75	0.90	1.05	1.20	-
$\Delta u$	mm	-	$\pm 0.05$	$\pm 0.05$	$\pm 0.05$	$\pm 0.05$	$\pm 0.05$	-
$N$	-	-	100	100	100	100	100	-
$f$	Hz	-	0.2	0.2	0.2	0.2	0.2	-
$\sigma_{N,\max}$	MPa	8.2	70.0	92.2	112.2	130.3	142.6	152.5
$\Delta\sigma_N$	MPa	-	-2.7	-1.9	-3.1	-6.3	-10.5	-

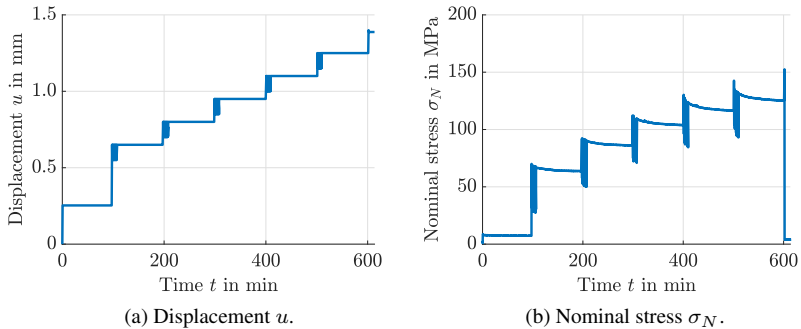


Figure 6.17: Five cyclic load steps are carried out. Initially and after each load step the specimen is screened by means of  $\mu$ CT scanning. In (a) the displacement  $u$  and (b) the nominal stress  $\sigma_N$  curves along the in-situ test process are plotted.

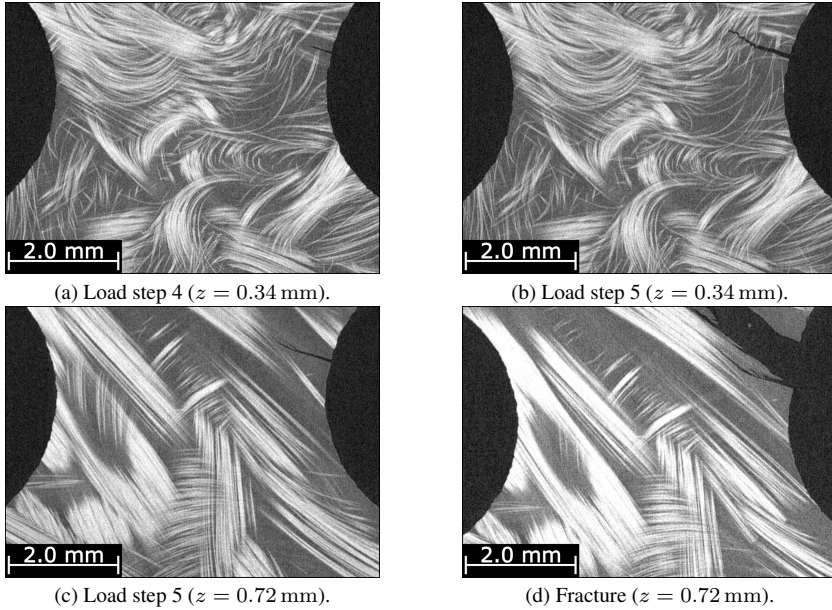


Figure 6.18:  $\mu$ CT cross sections of the damaged SMC microstructure with highly diagonally oriented fiber bundles. The crack in (a) is initiated during the fourth load step close to the surface. During the fifth load step the crack propagates in length (b) and width (c). In (d) the fractured microstructure.

### 6.2.3 Fibers Highly Oriented Perpendicular to the Load Direction

As given in Figure 6.6, the fibers within the analyzed sample in this section are highly oriented at  $90^\circ$  to the load direction (HO- $90^\circ$ ). The in-situ  $\mu$ CT test protocol is adjusted accordingly for the HO- $90^\circ$  samples. Appropriate parameters for the in-situ  $\mu$ CT test are shown in Table 6.4. In contrast to the  $\mu$ CT test on the other samples, here the displacement amplitude  $\Delta u$  and number of cycles per load step  $N$  are selected to be rather small, since a significantly lower strength is expected. The displacement and nominal stress data along the in-situ  $\mu$ CT

test are illustrated in Figure 6.19. The sample fracture at a maximum nominal stress of 91.9 MPa. Figure 6.20 shows corresponding  $\mu$ CT cross sections of all three load steps. The  $\mu$ CT cross sections in Figure 6.20 (a) to (c) reveal that there is no crack initiation and propagation observed by the  $\mu$ CT scanning within these three load steps. The specimen fails close after the third load step, whereby pseudo-delamination occurred at and close to the fracture surface, as shown in Figure 6.20 (d). Although Figure 6.20 (c) shows the microstructure close before fracture, no cracks are observed here.

Table 6.4: Selected load step parameters of the respective in-situ  $\mu$ CT test examining the HO-90° specimen. Furthermore, the measured nominal stress maximum  $\sigma_{N,\max}$  and drop  $\Delta\sigma_N$  of each load step.

Parameters		Load step				Fracture
		Initial	1	2	3	
$u_m$	mm	-	0.4	0.5	0.6	-
$\Delta u$	mm	-	$\pm 0.05$	$\pm 0.05$	$\pm 0.05$	-
$N$	-	-	75	75	75	-
$f$	Hz	-	0.2	0.2	0.2	-
$\sigma_{N,\max}$	MPa	9.9	40.5	59.6	77.1	91.9
$\Delta\sigma_N$	MPa	-	0.0	-0.5	-0.4	-

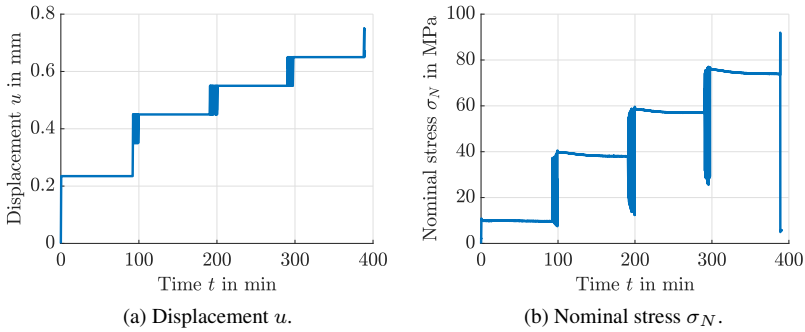


Figure 6.19: Three cyclic load steps are carried out. Initially and after each load step the specimen is screened by means of  $\mu$ CT scanning. In (a) the displacement  $u$  and (b) the nominal stress  $\sigma_N$  curves along the in-situ test process are plotted.

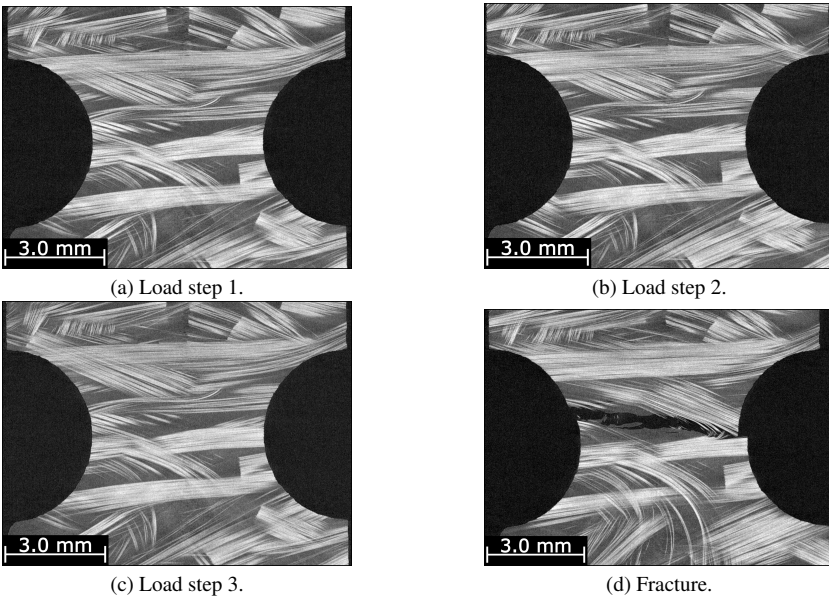


Figure 6.20: In (a) to (d) representative  $\mu$ CT cross sections. No cracks are observed during the three load steps. The HO-90° specimen fractures right after the third load step.

## 6.2.4 Fibers Randomly Oriented

In addition to samples in which the fiber bundles are highly oriented, also a SMC specimen with a random or planar isotropic fiber distribution is examined, as shown in Figure 6.8. The selected parameters of the in-situ  $\mu$ CT test are listed in Table 6.5. Similar to the HO samples, the test parameters are adapted accordingly to the microstructure in order to examine the damage in detail. The sample with randomly oriented fibers (RO) fractured at a maximum nominal stress of 170.5 MPa. Figure 6.22 (a) to (d) show representative  $\mu$ CT cross sections of the four load steps. The  $\mu$ CT cross sections reveal where crack initiation and propagation on the microstructural level occurs. In the upper left area, there is a cavity, which already existed at the beginning of the test, as shown in Figure 6.23 (a). The  $\mu$ CT cross section in load step three and four show a crack is initiated at the tip of this cavity.

Table 6.5: Selected load step parameters of the respective in-situ  $\mu$ CT test examining the RO specimen. Furthermore, the measured nominal stress maximum  $\sigma_{N,\max}$  and drop  $\Delta\sigma_N$  of each load step.

Parameters		Load step					Fracture
		Initial	1	2	3	4	
$u_m$	mm	-	0.7	0.9	1.1	1.3	1.5
$\Delta u$	mm	-	$\pm 0.1$	$\pm 0.1$	$\pm 0.1$	$\pm 0.1$	$\pm 0.1$
$N$	-	-	75	75	75	75	75
$f$	Hz	-	0.1	0.1	0.1	0.1	0.1
$\sigma_{N,\max}$	MPa	17.3	69.3	100.5	127.8	151.9	170.5
$\Delta\sigma_N$	MPa	-	-3.0	-4.8	-5.6	-8.6	-8.8

Together with the crack at the cavity tip, another crack is formed in the lower left region of Figure 6.22 (c) during the third load step. Furthermore, during the fourth load step here additional cracks are formed, as illustrated in Figure 6.22 (d). The cracks run through almost the entire RO specimen, whereby they occur to be matrix cracks and fiber bundles do not fracture. During the fourth load step, no significant crack propagation of the crack at the cavity tip is observed in Figure 6.22 (d).

The RO specimen fails while scanning after the fifth load step and in addition to the  $\mu$ CT cross sections in Figure 6.22, Figure 6.23 (b) shows the microstructure after fracture. The  $\mu$ CT cross section illustrates that the final fracture occurred close to the notch center. Figure 6.23 (b) reveals that the cracks in the lower left region lead finally to the failure of the RO specimen and not the cavity or the crack at the cavity tip in the upper left region.

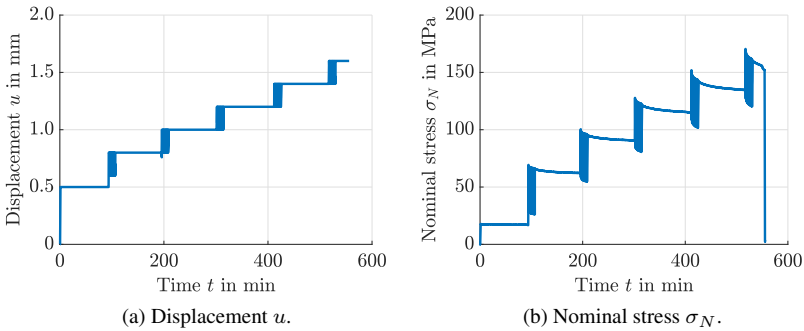


Figure 6.21: Five load steps are carried out. Initially and after each load step the specimen is screened by means of  $\mu$ CT scanning. In (a) the displacement  $u$  and (b) the nominal stress  $\sigma_N$  curves through the in-situ test process are plotted.



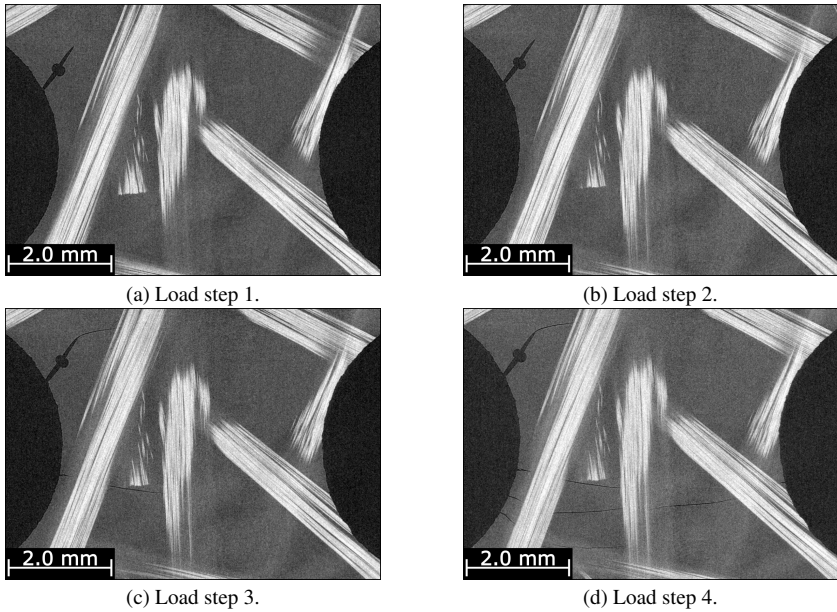


Figure 6.22: The damage propagation within the RO specimen. In (a) to (d) the SMC microstructure after the respective load steps. The  $\mu$ CT cross section reveal the crack initiation and propagation within the microstructure, in particular at the tip of a cavity.

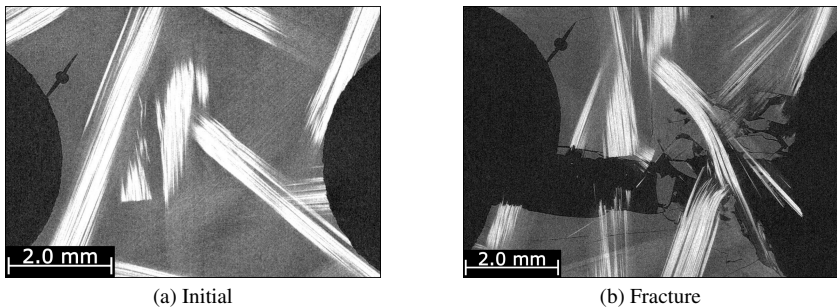


Figure 6.23:  $\mu$ CT cross section of the (a) initial and (b) fractured RO sample, in which fiber bundle breakage, pull-out and matrix fragmentation occurred.

## 6.3 Damage Segmentation

In this work several methods to segment crack regions within volumetric images are introduced. The results of those image processing methods are presented in this section. The content of this section refers mainly to the publications of Schöttl et al. [241, 243]\*.

### 6.3.1 Seed-Region-Growth Segmentation

For a reliable segmentation of objects like cracks a sufficient contrast between the cracks and the surrounding material is necessary [65, 72]. In case of  $\mu$ CT scanning and SMC, the X-ray attenuation of the glass fibers, UPPH matrix and cracks are decisive. In a first approximation the attenuation of glass fibers, UPPH matrix and cracks (or air) are determined based on the mass attenuation values in Table 2.1 and the mass densities in Table 3.3 and Table 3.4, respectively.

Mass attenuation properties of glass fibers and UPPH matrix are not available in the data base of Hubbell and Seltzer [61] and others. Since silicon dioxide ( $\text{SiO}_2$ ) is the main component of e-glass fibers [48], for a simple estimation the mass attenuation of e-glass is assumed to be equal to that of quartz. Due to similar chemical composition, the mass attenuation values of various polymers in Table 2.1 are about the same. For this reason and the similar chemical thermoset structure, the X-ray mass attenuation of the UPPH matrix is approximated by those of Bakelite.

The in-situ  $\mu$ CT test are carried out in a laboratory environment. It is assumed that the gray-value of cracks is estimated by the X-ray attenuation value of dry air at laboratory conditions. Based on that assumption the X-ray attenuation quantities of the respective components are calculated by

$$\mu_{\text{Glass fiber}} = \rho_{\text{Glass fiber}} \cdot \mu_{m,\text{Quartz}} = 0.68 \text{ 1/cm}, \quad (6.2)$$

$$\mu_{\text{UPPH}} = \rho_{\text{UPPH}} \cdot \mu_{m,\text{Bakelite}} = 0.22 \text{ 1/cm}, \quad (6.3)$$

$$\mu_{\text{Crack}} = \rho_{\text{Air}} \cdot \mu_{m,\text{Air}} = 0.23 \cdot 10^{-3} \text{ 1/cm}, \quad (6.4)$$

with the properties introduced in Table 2.1, Table 3.3 and Table 3.4:

$\mu_{m,\text{Quartz}}$	$= 0.26 \text{ cm}^2/\text{g}$	– Quartz mass attenuation
$\mu_{m,\text{Bakelite}}$	$= 0.19 \text{ cm}^2/\text{g}$	– Bakelite mass attenuation
$\mu_{m,\text{Air}}$	$= 0.19 \text{ cm}^2/\text{g}$	– Air mass attenuation (dry, sea level)
$\rho_{\text{Glass-fiber}}$	$= 2.60 \text{ g/cm}^3$	– Glass-fiber mass density
$\rho_{\text{UPPH}}$	$= 1.15 \text{ g/cm}^3$	– UPPH mass density
$\rho_{\text{Air}}$	$= 1.20 \cdot 10^{-3} \text{ g/cm}^3$	– Air mass density (dry, sea level, 20 °C)

The results reveal that the estimated X-ray attenuation of UPPH is approximately  $10^3$ -times higher than those of cracks or air. Furthermore, glass fibers have a X-ray attenuation that is approximately three-times higher than those of the UPPH matrix. As a result, there is a clear contrast in  $\mu\text{CT}$  scans between cracks and the surrounding SMC material, as well as between the UPPH matrix and the glass fibers.

Cracks within the volumetric images are segmented by using the SRG segmentation method by Adams and Bischof [96] introduced in Section 4.2. Representative results are presented here. In the upper row of Figure 6.24  $\mu\text{CT}$  cross sections of cracks within the HO-0° specimen are shown (c.f. Figure 6.16 (c) to (f)). The segmented cracks by means of the SRG method are illustrated correspondingly in the lower row. Here, black indicates the background and white the segmented cracks. In addition to these cross sections, the segmented cracks are three-dimensionally visualized in Figure 6.25.

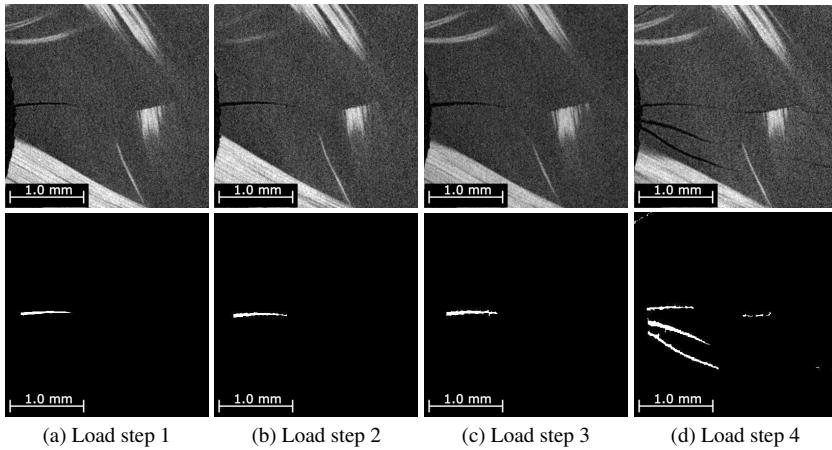


Figure 6.24: Crack segmentation by means of the SRG method. In the upper row gray-scale  $\mu$ CT cross sections of the HO-0° specimen and below the corresponding binary images, in which the cracks are segmented (white) (data by Schöttl et al. [241]\*).

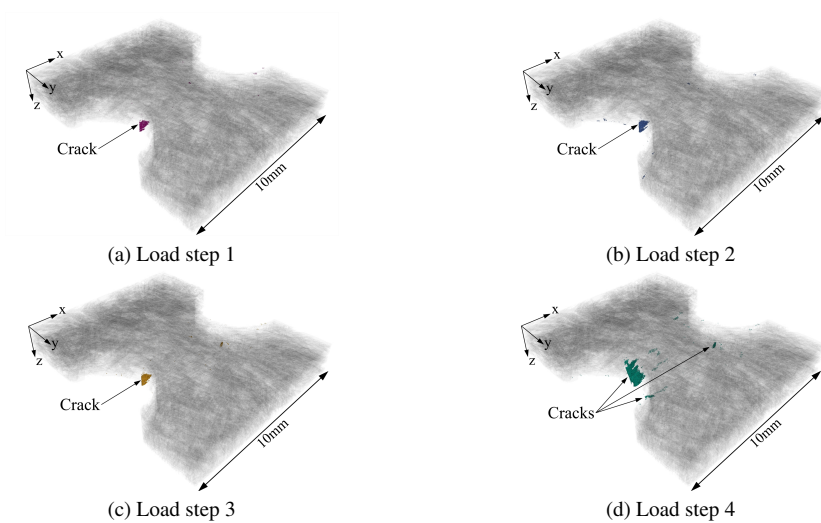


Figure 6.25: 3D-visualization of the segmented cracks together with the microstructure (transparent) for all four load steps of the HO-0° specimen (figures by Schöttl et al. [243]\*).

### 6.3.2 Digital Volume Correlation

Through applying the DVC technique and providing volumetric images of the initial and deformed specimen, the displacement and deformation field on the microstructural level between these two states are determined. In this doctoral thesis the DVC method provided by VGSTUDIO MAX 3.4 from Volume Graphics is used. The SMC specimen with highly oriented fibers diagonal to the tensile load direction ( $HO-45^\circ$ ) in Figure 6.18 is studied through DVC and the results are presented in this section. Here, the initially acquired volumetric image and those after the fifth load step of the in-situ  $\mu$ CT test are correlated. Figure 6.26 shows representative  $\mu$ CT cross sections of the corresponding initial and deformed microstructures. Large absolute values of the difference volume indicate a local loss of correlation. This is mainly due to ambiguity and singularity phenomena of the displacement field, which are caused by the formation of cracks, as introduced in Section 4.2.2.

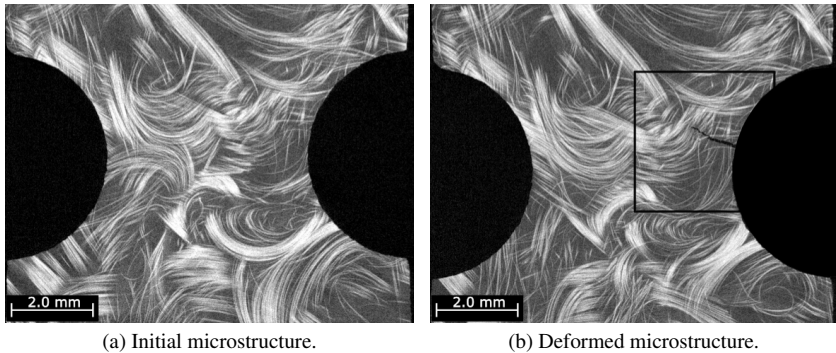


Figure 6.26: Required input data for DVC including volumetric images of the initial and deformed specimen. Corresponding gray-scale  $\mu$ CT cross section of the (a) initial and (b) deformed microstructure. Formation of a crack with a large crack opening.

Figure 6.27 illustrates the  $\mu$ CT cross section and DVC results inside the marked region in Figure 6.26 (b), where a single crack with a large crack opening is formed. The DVC method indicates cracks not directly from the volumetric

image data but indirectly based on the difference volume data. The DVC results are referred to the deformed microstructure and high difference volume values indicate the formation and location of cracks. As a consequence, the comparison of the cracked microstructure in Figure 6.27 (a) and the difference volume data in Figure 6.27 (b) reveal, that high absolute difference volume values occur at the crack formation.

From the DVC data not only cracks can be identified but also the strain fields can be analyzed. In addition to the identification of crack regions also the strain field around those cracks is analyzed by means of the DVC method. Introducing the von Mises strain  $\epsilon_{vM}$  as a scalar equivalent strain quantity by

$$\epsilon_{vM} = \frac{2}{3} \sqrt{\frac{(\epsilon_{xx} - \epsilon_{yy})^2 + (\epsilon_{yy} - \epsilon_{zz})^2 + (\epsilon_{zz} - \epsilon_{xx})^2 + 6(\epsilon_{xy}^2 + \epsilon_{yz}^2 + \epsilon_{zx}^2)}{2}}, \quad (6.5)$$

where  $\epsilon_{ij}$  with  $i, j = \{x, y, z\}$  are the entries of the strain tensor  $\epsilon$ . Figure 6.27 (c) illustrates the von Mises strain field around the crack. Here, close to the crack the local von Mises strain values are high and decrease with increasing distance. The measured von Mises strain values inside the cracks is a DVC artifact, since no strain is applied to any solid here.

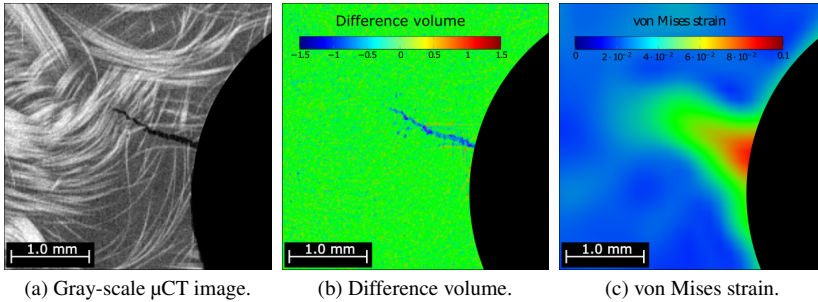


Figure 6.27: Illustration of the DVC results inside the marked region in Figure 6.26 (b). Identifying the crack by means of the difference volume in (b) and illustrating the von Mises strain field around the crack in (c).

In addition, the crack in Figure 6.27 with a large crack opening, also different crack formation phenomena are examined further. Figure 6.28 shows the  $\mu$ CT cross section and DVC results, where a crack within a fiber bundle is formed. Although, the crack opening is rather small here, the difference volume data in Figure 6.28 (b) reveal a significant contrast. Since the crack opening is small, also the resulting impact on the von Mises strain field around crack in Figure 6.28 (c) is rather marginal, but clearly visible.

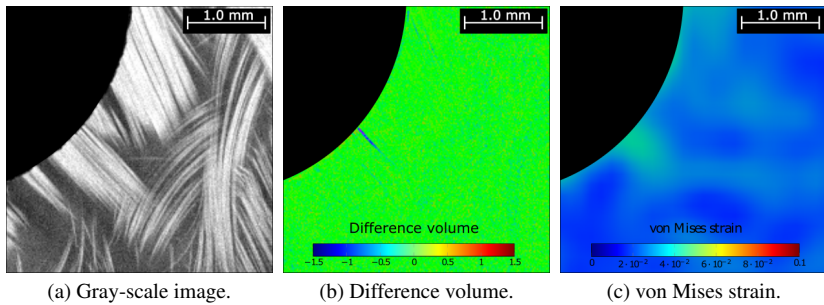


Figure 6.28: Examining a single crack inside a fiber bundle. In (a) the  $\mu$ CT cross section, (b) difference volume and (c) von Mises strain field determined by means of DVC.

Furthermore, a crack that is mainly embedded within the matrix material is analyzed by means of DVC in Figure 6.29. Here the crack opening and length are large compared to the crack in Figure 6.28. However, the difference volume contrast between the crack and the surrounding in Figure 6.29 (b) is rather poor due to the less distinctive fiber architecture pattern around the crack which is required for precisely applying the DVC method.

Figure 6.29 (c) illustrates the determined von Mises strain field around the matrix crack with respect to the DVC resolution. Around the crack a von Mises equivalent strain value between 4 % to 6 % of the surrounding matrix is reached. Here, the DVC resolution with regard to the control point spacing must be taken into account.

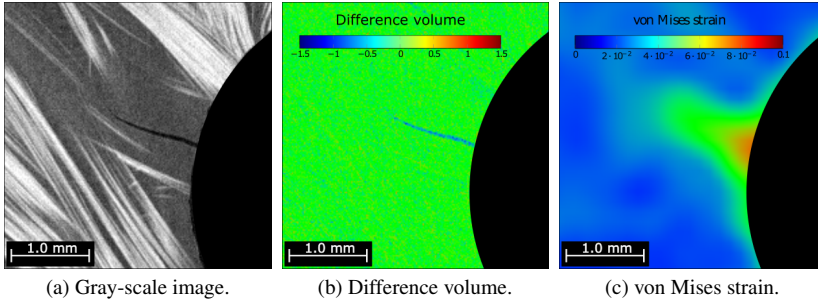


Figure 6.29: Illustration of a matrix crack in (a) and the corresponding DVC results regarding the difference volume in (b) and von Mises strain field around the crack in (c).

In addition to the cross section views, the segmented cracks by means of the DVC methods are also visualized three-dimensionally in Figure 6.30. Here, the cracks are segmented based on a absolute difference volume threshold of 0.9. Since the difference volume depends directly on the volumetric image gray-values and consequently, on the examined material system and  $\mu$ CT scanning process a general selection is not appropriate and should be selected individually for further applications.

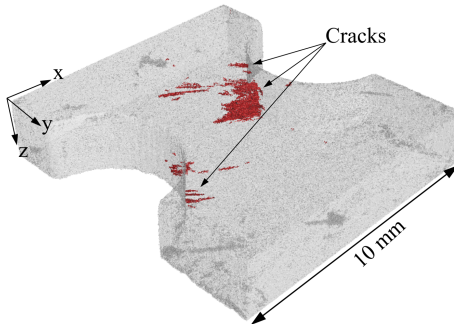


Figure 6.30: 3D-visualization of the indicated cracks within the HO-45° specimen after the fifth load step by using the DVC method. Cracks are segmented by selecting an absolute difference volume threshold of 0.9.



### 6.3.3 Convolutional Neural Network

In order to apply a CNN model, the architecture has to be properly trained in the first place. In this work, the trainable parameters of the U-Net architecture are optimized, as introduced in Figure 2.25. Details of the training process and the U-Net architecture are given in Table 4.3. Based on training and validation data sets the performance of the U-Net architecture is monitored during the training process in Figure 6.31. The crack segmentation capability of the trained U-Net model is evaluated by different metrics. Table 6.6 lists the finally achieved accuracy, precision, recall and F-measure metrics. The recall values are higher than those of the precision which indicates slight over estimation of the segmented cracks. Overall, the metric values show a good performance of the trained U-Net model.

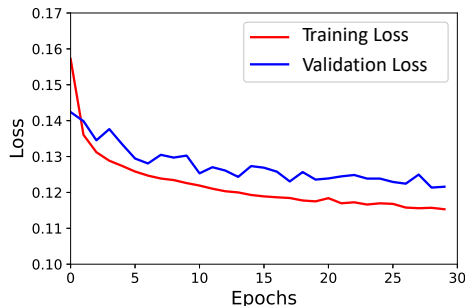


Figure 6.31: Monitoring the training progress of the U-Net architecture by means of the loss value. Loss value distribution of the training and validation data set.

After the U-Net architecture is properly trained as shown by the training and validation data set in Table 6.6, the capability of the U-Net model is evaluated based on the separate test data set. Two exemplary input images, corresponding ground truth and predictions by the U-Net are shown in Figure 6.32. The returned prediction images are further binarized in order to segment cracks and background.

Table 6.6: Evaluating the trained U-Net performance by different metrics and data sets.

Metric	Training	Validation	Testing
Accuracy	92.70 %	98.30 %	98.68 %
Precision	86.35 %	86.08 %	86.31 %
Recall	99.23 %	98.99 %	99.14 %
F-Measure	92.34 %	92.08 %	92.28 %

Segmenting cracks within the large-scale volumetric images of the RO specimen acquired after the fourth load step (c.f. Figure 6.22). Figure 6.33 (a) illustrates a representative  $\mu$ CT cross section view and (b) the corresponding U-Net prediction results. Here, cracks are indicated in white and background in black. Comparing both images in Figure 6.33 demonstrates the good performance of the U-Net model to segment cracks.

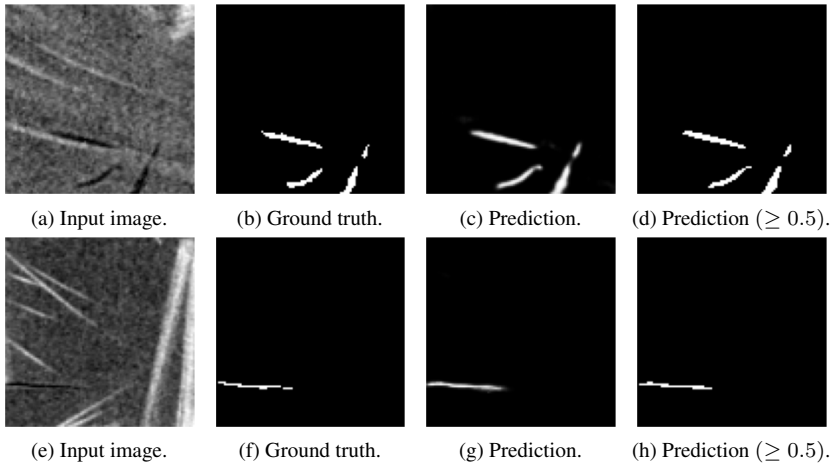


Figure 6.32: Testing the trained U-Net Model. Exemplary input images, ground truth, prediction and binary prediction (background in black and labeled cracks in white). The image size is 96 pixels  $\times$  96 pixels and the voxel size 6.1 – 7.0  $\mu$ m.

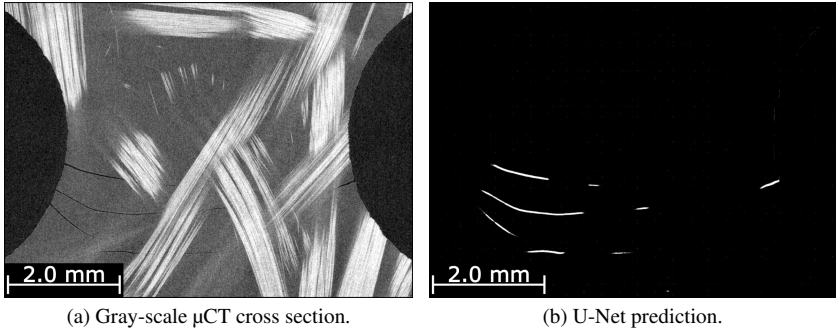


Figure 6.33: Segmenting cracks within a large-scale volumetric image by means of the trained U-Net model. In (a) an exemplary  $\mu$ CT cross section and in (b) the crack prediction result by the U-Net model, where cracks are indicated by white and background in black. The volumetric image was obtained after the fourth load step of the RO specimen, presented in Figure 6.22.

In addition to Figure 6.33, the segmented cracks are visualized spatially for the load steps four of specimen RO in Figure 6.34. The segmented cracks are shown in green together with the microstructure, which is illustrated transparently and provides a spatial impression of formed cracks.

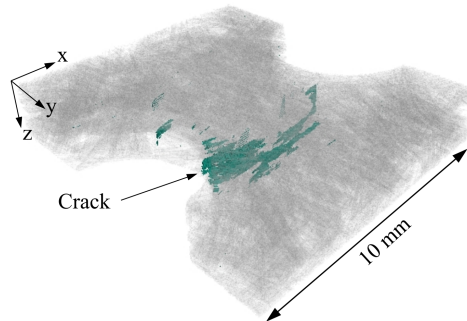


Figure 6.34: 3D-visualization of the segmented cracks within the RO specimen after the fourth load step by means of the U-Net model.

## 6.4 Damage Characterization

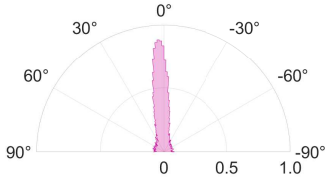
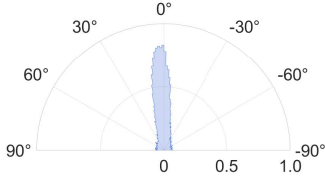
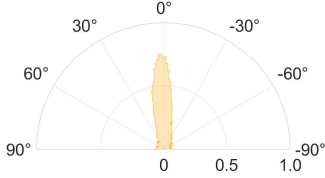
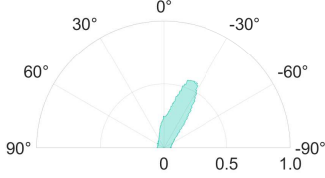
The obtained crack segmentation data in Section 6.3 are further processed by applying the methods described in Section 4.2, in order to examine the cracked microstructure in detail. Different methods and approaches to characterize and quantify various aspects of damage are introduced in Section 4.3. The determined results of the respective damage characterization methods are introduced in this section. The presented results mainly refer to the contributions by Schöttl et al. [241, 243]\*.

### 6.4.1 Crack Orientation Tensor

In composite materials with heterogeneous microstructure, cracks usually occur in irregular patterns. To characterize the damage anisotropy, the local crack normal vectors  $\mathbf{g}$  are determined by using the introduced image processing method from Section 4.3.1. Based on the obtained crack orientation data the empirical crack orientation tensor  $\mathbf{D}$  in Equation 4.13 is then calculated to describe the crack orientation distribution compactly.

Based on the crack segmentation results in Figure 6.24, the spatial crack orientation of the SMC specimen with a HO-0° microstructure is examined. Table 6.7 lists the resulting crack orientation histograms and crack orientation tensors  $\mathbf{D}$  of all four load steps, respectively. The crack orientation histograms reveal there is a similar crack orientation distribution for the first to third load step, where the majority of crack normal vectors are oriented along the tensile load direction. Accordingly, the crack orientation tensor  $\mathbf{D}$  of the corresponding three load levels are also similar and the largest entry is  $D_{yy}$ , where  $\mathbf{e}_y$  marks the tensile load direction. Close before fracture of the HO-0° specimen in the fourth load step, the principal crack orientation changes approximately by 30°, as shown by the crack orientation histogram. This change is also indicated accordingly by the respective crack orientation tensor  $\mathbf{D}$ .

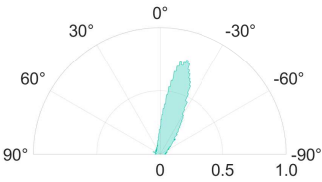
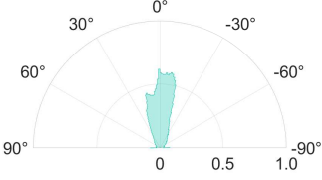
Table 6.7: Characterizing the spatial damage anisotropy of the in-situ  $\mu$ CT tested HO-0° specimen in Figure 6.16. Crack orientation histogram and crack orientation tensor  $\mathbf{D}$  of the respective load steps (data by Schöttl et al. [243]\*).

Load step	Crack orientation histogram tensile load direction $\hat{=}$ 0°	Crack orientation tensor $\mathbf{D}$ in $\{e_x, e_y, e_z\}$
1		$\begin{bmatrix} 0.10 & -0.05 & 0.00 \\ -0.05 & 0.81 & -0.01 \\ 0.00 & -0.01 & 0.09 \end{bmatrix}$
2		$\begin{bmatrix} 0.10 & -0.02 & 0.01 \\ -0.02 & 0.80 & -0.01 \\ 0.01 & -0.01 & 0.10 \end{bmatrix}$
3		$\begin{bmatrix} 0.10 & -0.02 & 0.00 \\ -0.02 & 0.82 & -0.01 \\ 0.00 & -0.01 & 0.08 \end{bmatrix}$
4		$\begin{bmatrix} 0.17 & 0.20 & 0.07 \\ 0.20 & 0.64 & 0.16 \\ 0.07 & 0.16 & 0.19 \end{bmatrix}$

Additionally to the HO-0° specimen, the crack orientation distribution of the HO-45° and RO specimens during the final load step are characterized. Table 6.8 presents the crack orientation histograms and the crack orientation tensors  $\mathbf{D}$ , respectively. In case of the HO-45° specimen the results reveal a similar crack orientation distribution of those in the HO-0° specimen during the final load step. As a consequence, the entries of the crack orientation tensors  $\mathbf{D}$  are similar as well.

In contrast to the HO-0° and HO-45° specimens, the RO specimen shows a wider crack orientation distribution, where the majority of cracks are oriented within about  $\pm 20^\circ$  to the tensile direction. Accordingly,  $D_{yy}$  is the largest entry of the crack orientation tensor  $\mathbf{D}$ , with  $\mathbf{e}_y$  marking the tensile direction.

Table 6.8: Analyzing the spatial damage anisotropy of the HO-45° and RO specimens during the final load step of in-situ  $\mu$ CT test. Crack orientation histogram and crack orientation tensor  $\mathbf{D}$ , respectively.

Specimen	Crack orientation histogram tensile load direction $\hat{=}$ 0°	Crack orientation tensor $\mathbf{D}$ in $\{\mathbf{e}_x, \mathbf{e}_y, \mathbf{e}_z\}$
HO-45°		$\begin{bmatrix} 0.16 & 0.19 & 0.00 \\ 0.19 & 0.68 & 0.02 \\ 0.00 & 0.02 & 0.16 \end{bmatrix}$
RO		$\begin{bmatrix} 0.07 & -0.01 & 0.01 \\ -0.01 & 0.81 & 0.01 \\ 0.01 & 0.01 & 0.12 \end{bmatrix}$

## 6.4.2 Crack Volume Fraction

In addition to the crack orientation distribution, the crack volume fraction  $\rho_{\text{Crack}}$  introduced in Section 4.3.3 quantifies the total damage propagation along the in-situ  $\mu\text{CT}$  test. The crack volume fraction results in this doctoral thesis are determined based on the crack segmentation results obtained by the SRG method. In order to investigate the relationship between microstructure and damage behavior, the crack volume fraction distributions of the SMC specimens with RO, HO-0° and HO-45° are examined. Since no cracks were observed and segmented within the HO-90° specimen by the in-situ  $\mu\text{CT}$  test, no crack volume data could be evaluated.

Figure 6.35 (a) illustrates the crack volume fraction  $\rho_{\text{Crack}}$  initial and after all respective load steps. In addition, the crack volume fraction data are normalized in the way that  $\rho_{\text{Crack, Initial}} = 0$  to eliminate initial artifacts. In Figure 6.35 (b) the normalized crack volume fraction data are shown accordingly.

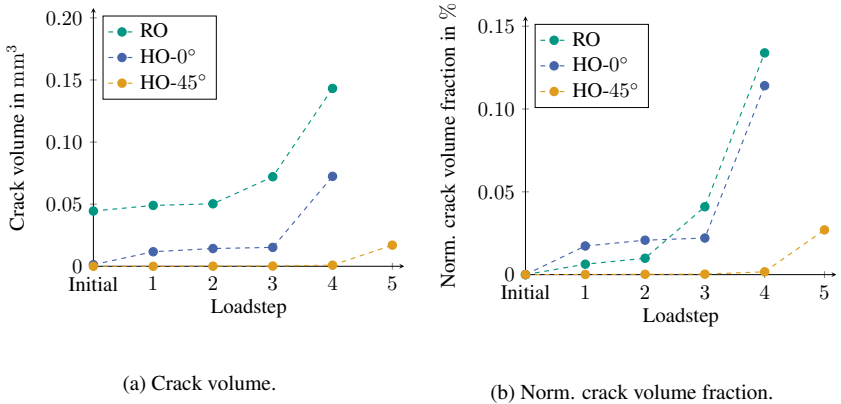


Figure 6.35: Measuring the crack and damage accumulation. In (a) the crack volume and (b) the normalized crack volume fraction distribution  $\rho_{\text{Crack}}$  initial and after all respective load steps.

In case of the RO and HO-0° specimens, initially in the first load steps the normalized crack volume fraction increases evenly and subsequently, in the last load step it rises sharply. The crack volume data in Figure 6.35 (a) reveal that there are cavities within the RO sample, which lead to an off-set of the crack volume data. This off-set is eliminated by the normalization in Figure 6.35 (b). In contrast to those two samples, the HO-45° specimen shows a different damage behavior. Here, the crack volume fraction is initially smaller and only increases during the final load step. However, the crack volume here is still significantly lower than that of the other two specimens. Since the specimen failed immediately after the last load step, the crack volume fraction quantifies the total damage state close before fracture.

The in-situ  $\mu$ CT test is performed displacement controlled and individual protocols are applied for the examined samples. To investigate the relationship between applied stress and damage development, Figure 6.36 shows the normalized crack volume data together with the maximum nominal stress of the respective load steps. Here, a consistent linear increase of the normalized crack volume for the RO and HO-0° samples is revealed.

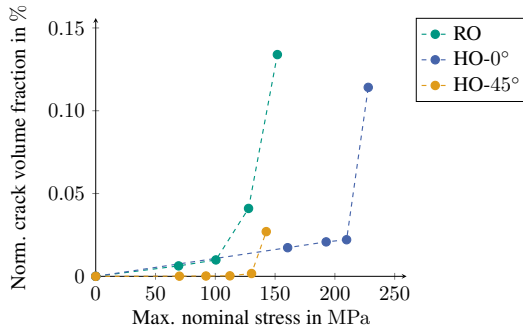


Figure 6.36: Crack volume fraction  $\rho_{\text{Crack}}$  over maximum nominal stress  $\sigma_{N,\text{max}}$  of the respective load steps. Comparison between SMC specimens with different microstructures.



### 6.4.3 Damage Classification

Similar to the previous damage characterization, the method to classify and quantify the damage mechanisms introduced in Section 4.3.4 is applied to the in-situ  $\mu$ CT results in Section 6.2. The method combines crack and microstructure analysis data to determine the damage nature. As input for the damage classification method fiber orientation data  $\mathbf{n}$ , crack segmentation results and crack orientation data  $\mathbf{g}$  are required.

In this doctoral thesis, the proportion by volume of matrix cracking, pseudo-delamination and fiber breakage are examined for three SMC samples with different microstructures, where the fibers are HO-0°, HO-45° and RO with respect to the tensile load direction. The HO-90° specimen was not analyzed since here no cracks are observed and segment within the acquired volumetric images.

Table 6.9 lists the quantified damage mechanism proportions during the final load step of the in-situ  $\mu$ CT procedure for three samples. The resulting data show that the damage mechanisms occur similarly in all three specimens and that matrix cracking is the dominant case. Pseudo-delamination and fiber breakage occur to an equal degree of insignificance.

Table 6.9: Quantifying the damage mechanisms for three SMC samples with HO-0°, HO-45° and RO microstructures. The damage mechanism fractions are quantified for the respective samples during the final in-situ  $\mu$ CT load step.

	Damage mechanism fractions		
	Matrix cracking	Pseudo-delamination	Fiber breakage
	$\rho_I$	$\rho_{II}$	$\rho_{III}$
HO-0°	92.3 %	4.0 %	3.7 %
HO-45°	90.8 %	3.8 %	5.4 %
RO	94.1 %	2.0 %	3.9 %

Furthermore, the change of the damage mechanism fractions within the HO-0° specimen is investigated over the course of the in-situ  $\mu$ CT test. Figure 6.37 (a) shows the proportion of the three damage mechanisms for all respective load steps. The results reveal that there is only a slight change of the damage mechanism fractions and that matrix crack is predominate from crack initiation until fracture. Figure 6.37 (a) illustrates the proportion of the three damage classes to each other regarding all load steps individually but not in the context of total damage propagation through the entire in-situ  $\mu$ CT test. In order to visualize the three damage mechanism fractions together with the total damage state, the damage mechanism distributions in Figure 6.37 (b) are scaled by the nominal crack volume fraction distribution in Figure 6.35 (b). The curves show the increasing impact of matrix cracks on the damage behavior along the load steps.

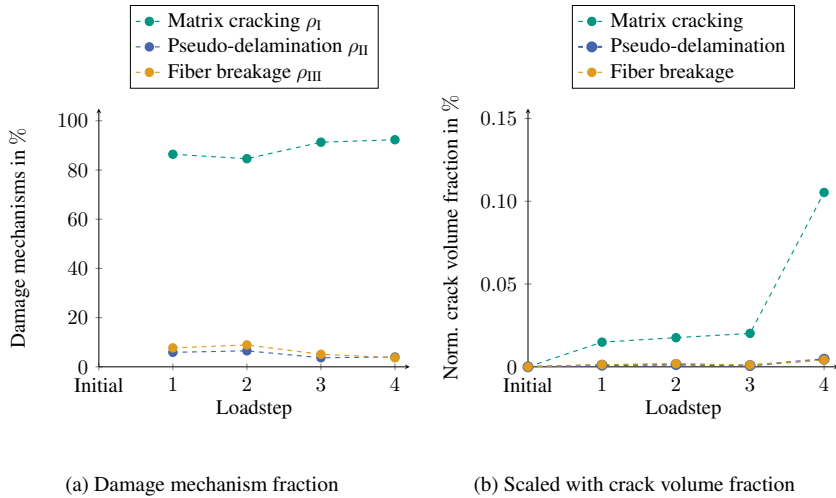


Figure 6.37: Propagation and development of the damage mechanisms during the in-situ  $\mu$ CT test. Examining the proportion of matrix cracking, pseudo-delamination and fiber breakage within the SMC sample with HO-0° microstructure.

## 6.5 Fractography

Supplementary to the in-situ  $\mu$ CT measurements and the damage characterization methods, the fracture surfaces of the corresponding SMC specimens are examined by using SEM. Due to the different microstructures of the analyzed samples, various failure phenomena are examined at the fracture surface. In this section, the fracture surfaces of representative specimens and sections are examined. Details and operation parameters of the SEM measurements are presented in Section 5.5.

### 6.5.1 Fibers Highly Oriented in Load Direction

Overviews and detailed images of selected regions for both fracture surfaces are acquired by means of SEM. Figure 6.38 presents SEM images of both fracture surfaces of the HO-0° specimen. Two locations are marked where at location 1) fiber bundle breakage and at location 2) fiber bundle pull-out occurred. Detailed SEM images of the broken fiber bundle at region 1) are illustrated in Figure 6.39. The enlarged SEM images are marked accordingly by colored frames. An even more detailed view of the location marked in Figure 6.39 (a) is given in Figure 6.40. The SEM images show broken and partially pulled out fiber filaments. Around the broken fiber bundle, there is a smooth fracture surface of the matrix.

Additionally to fiber bundle breakage, fiber bundle pull-out occurred at location 2) marked in Figure 6.38. Corresponding close-up SEM images of both fracture surfaces are given in Figure 6.41. Figure 6.41 (a) shows the remaining matrix gap and Figure 6.41 (b) the pulled-out fiber bundle.

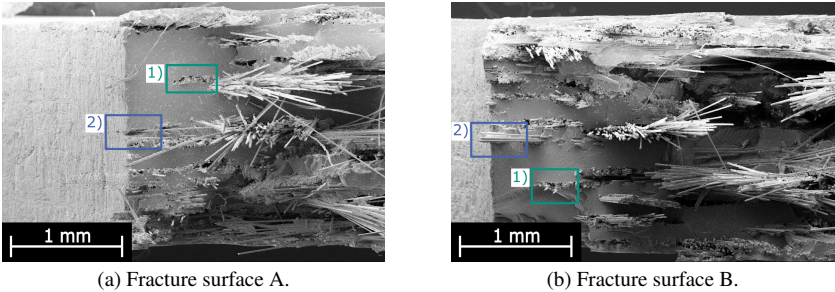


Figure 6.38: Overview of the both fracture surfaces of the HO-0° specimen. Two locations are marked were at 1) fiber bundle breakage and at 2) fiber bundle pull-out is observed.

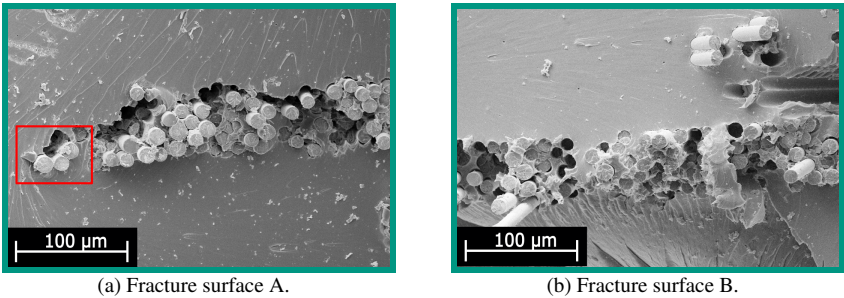


Figure 6.39: Close-up of the region 1) in Figure 6.38 (a) and (b) of the HO-0° specimen. The SEM images in (a) and (b) show broken and partially pulled-out fibers.

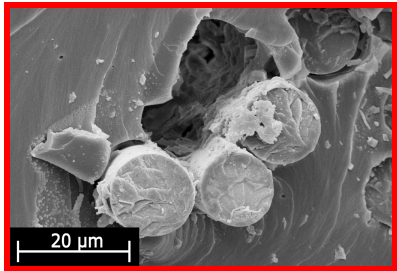


Figure 6.40: Fracture surface A of the HO-0° specimen. Close-up of the marked region in Figure 6.39 (a). The SEM image shows broken and slightly pulled-out fiber filaments.

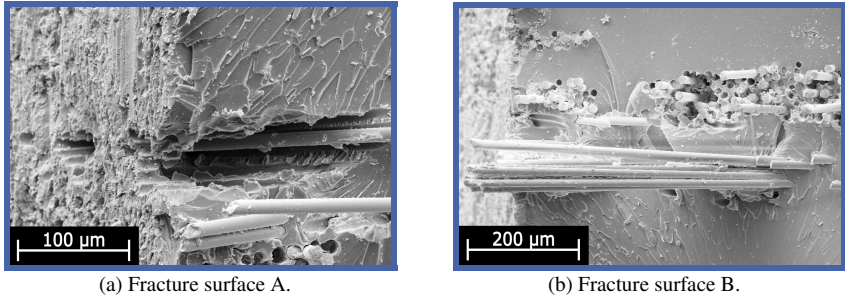


Figure 6.41: Detailed SEM images of the pulled-out fiber bundle at location 2) in Figure 6.40.

The SEM image (a) shows the remaining matrix material and (b) the pulled-out fiber bundle on the fracture surface of the HO-0° specimen.

### 6.5.2 Fibers Randomly Oriented

The fracture surfaces of the failed RO specimen in Figure 6.23 (b) are analyzed in this section. The SEM images in Figure 6.42 illustrate both fracture surfaces. Here, two regions are highlighted, which are examined in detail. The first region 1) reveals a pulled-out fiber bundle and the corresponding matrix gap. Detailed SEM images of that region are presented in Figure 6.43. In Figure 6.42 a second region 2) where fiber bundle breakage occurred is analyzed. Figure 6.44 shows the fractured fiber bundle and remaining fibers. In both SEM images a smooth and clean matrix fracture surface around the broken fiber bundle is revealed. In addition, the marked regions in Figure 6.44 are investigated in more detailed. Close-up SEM images of those regions are shown in Figure 6.45. Figure 6.45 (a) shows fractured and partially pulled-out fibers. A matrix fragment with periodic groove pattern is observed in Figure 6.45 (b).

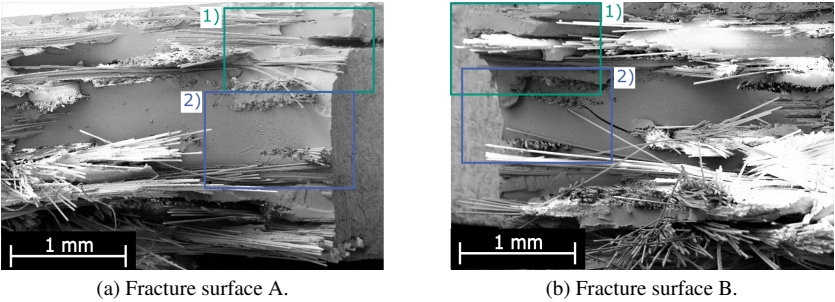


Figure 6.42: Overview of both fracture surfaces A and B. Two highlighted regions of the RO specimen are examined in detail.

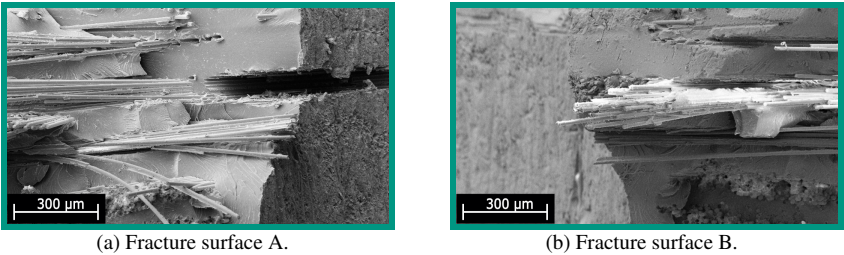


Figure 6.43: Pulled out fiber bundle and remaining matrix gap. Close-up SEM images of the marked regions in Figure 6.42 at location 1) of the RO specimen.

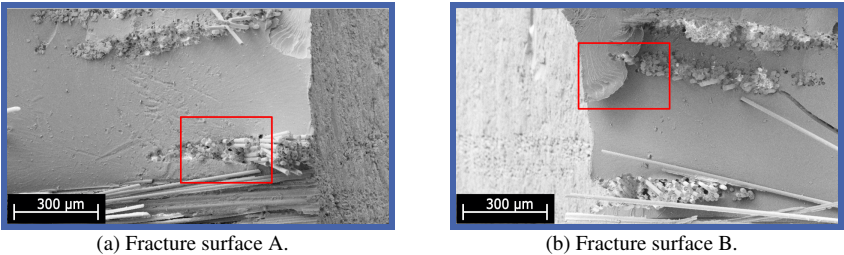


Figure 6.44: Close-up SEM images of fiber bundle breakage and matrix fragments within the regions marked in Figure 6.42 at location 2) of the RO specimen.

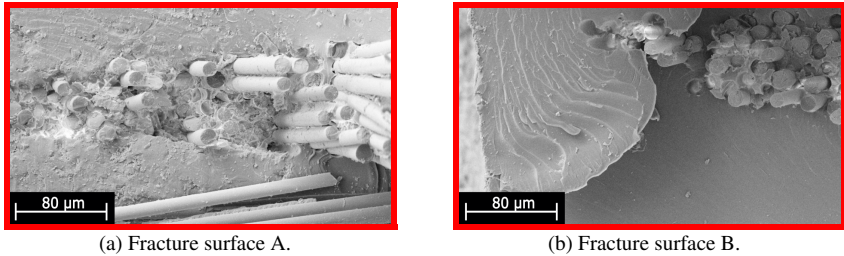


Figure 6.45: Fiber bundle breakage and matrix fragments. Close-up SEM images of the marked regions in Figure 6.44 of the RO specimen.

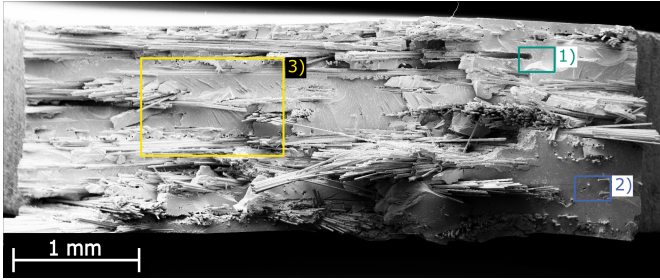
### 6.5.3 Fibers Highly Oriented Perpendicular to the Load Direction

Examining the fracture surfaces of the SMC sample with HO-90° microstructure. Figure 6.46 presents overview SEM images of both fracture surfaces. Three matching regions that are highlighted by red boxes are investigated in detail.

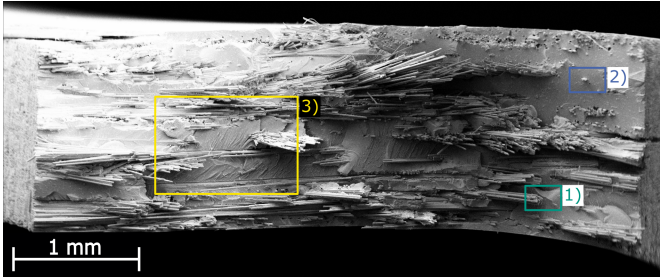
A pulled-out fiber bundle is shown in Figure 6.47 (b) and the corresponding matrix outbreak in Figure 6.47 (a). The smooth and straight surface fragments around the pulled-out fiber bundle are shaped to match.

Figure 6.48 presents the fracture surface regions, where fiber bundle breakage and partially pull-out occurred. Furthermore, the SEM images reveal a smooth and straight fracture surface of the matrix around the fibers.

The SEM images in Figure 6.49 reveal periodic matrix grooves on both fracture surfaces. In addition, pulled-out fiber bundles, that are aligned along the fracture surface and the matching matrix pattern are observed. In Figure 6.50 the marked regions in Figure 6.49 with periodic grooves are observed in more detail. The SEM images show matching matrix fragments with smooth and straight surfaces.

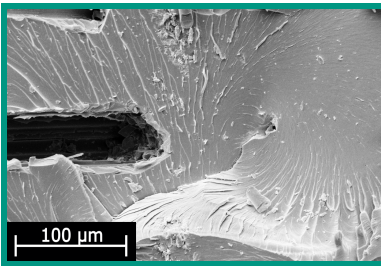


(a) Fracture surface A.

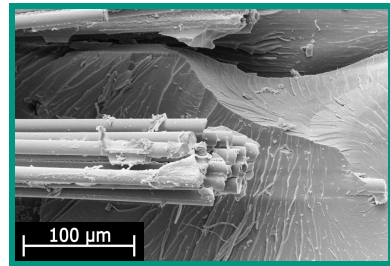


(b) Fracture surface B.

Figure 6.46: Overview of both fracture surfaces A and B. The HO-90° specimen was extracted with a plate orientation of 90°.



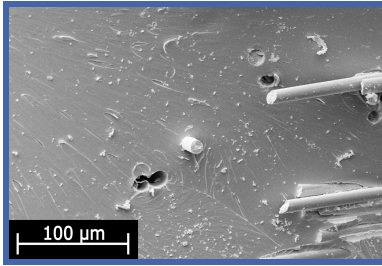
(a) Fracture surface A.



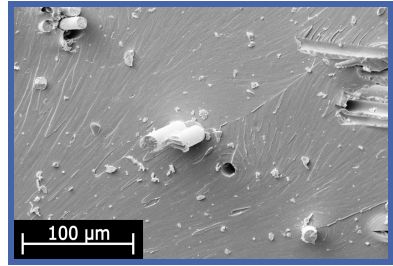
(b) Fracture surface B.

Figure 6.47: Close-up SEM images of a pulled out fiber bundle in Figure 6.46 at location 1), which is aligned along the fracture surface. Furthermore, the SEM image shows matching matrix fracture contours in both fracture surfaces of the HO-90° specimen.



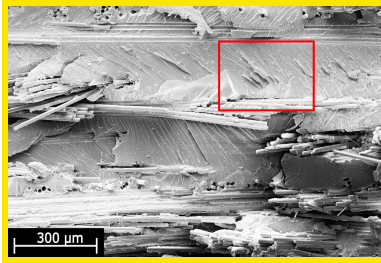


(a) Fracture surface A.

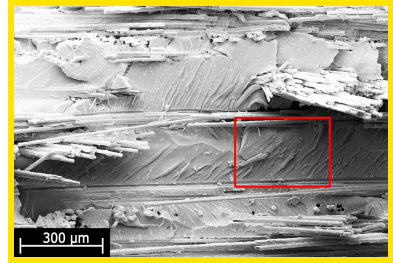


(b) Fracture surface B.

Figure 6.48: Close-up SEM images of partial pulled out and broken fibers. The fibers are embedded by a matrix region with a smooth fracture surface. The region of the close-up SEM images is illustrated in Figure 6.46 at location 2) of the HO-90° specimen.

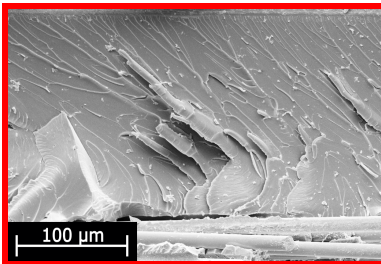


(a) Fracture surface A.

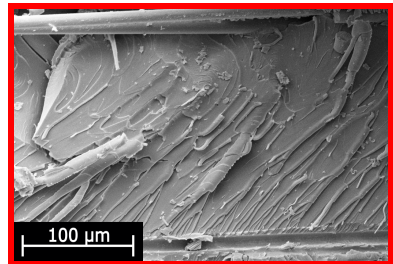


(b) Fracture surface B.

Figure 6.49: Close-up SEM images of the HO-90° specimen at marked regions in Figure 6.46 at location 3) show the matrix fracture surfaces with periodic grooves.



(a) Fracture surface A.



(b) Fracture surface B.

Figure 6.50: Detailed SEM images of the marked regions in Figure 6.49. The SEM images show periodic the groove pattern in detail. On the left side, the SEM images reveal matching matrix fragments on both fracture surfaces of the HO-90° specimen.



# 7    Discussion

This section summarizes and links the methods and results presented in this doctoral thesis. Furthermore, the obtained scientific insights are discussed in context of state-of-the-art literature.

## Contents

---

<b>7.1 Microstructure Characterization . . . . .</b>	<b>180</b>
<b>7.2 Experimental Damage Investigation . . . . .</b>	<b>183</b>
<b>7.3 Damage Segmentation . . . . .</b>	<b>186</b>
<b>7.4 Damage Characterization . . . . .</b>	<b>192</b>
<b>7.5 Fractography . . . . .</b>	<b>200</b>
<b>7.6 Damage Mechanisms of SMC . . . . .</b>	<b>202</b>

---

## 7.1 Microstructure Characterization

In general, the microstructure of fiber-reinforced composites significantly affects the mechanical behavior on the micro and macro scale. When characterizing fiber-reinforced composites taking the microstructure into account is essential for a comprehensive understanding of the mechanical behavior. The developed characterization methods and obtained results in this work are discussed in this chapter with context to state-to-the-art.

### 7.1.1 Fiber Orientation

State-of-the-art image processing methods for analyzing the fiber architecture of fiber-reinforced polymers based on  $\mu$ CT scans have been published by several authors [106–108, 110]. In this doctoral thesis the image processing method by Pinter et al. [107] is applied. Central feature of this method is the use of the structure tensor introduced by Krause et al. [108] to determine the local orientation of fibers. The method is validated and discussed in the contributions by Pinter et al. [90, 91, 107].

The fiber orientation states of the SMC samples which were further examined by means of in-situ  $\mu$ CT testing are characterized in Section 6.1. As illustrated by the visualization scheme according to Cintra and Tucker [256] in Figure 6.9, there are planar fiber orientation states in all specimens, which was to be expected since all these specimens were cut from compression molded SMC plate material.

The samples were extracted with different plate orientations regarding the MFD. As shown by the fiber orientation histograms in Figure 6.2, Figure 6.4 and Figure 6.6, the fibers within these three samples are highly oriented according to the MFD (HO-0°, HO-45° and HO-90°). Consequently, the corresponding coherence value of these specimens in Table 6.1 is higher compared to that of the specimen with randomly oriented (RO) fibers. Where the HO-0° specimen has the lowest coherence value and hence, the lowest degree of

fiber alignment of these three HO specimens. Furthermore, the principal fiber orientations in Table 6.1 which are determined based on the fiber orientation histogram maximum show a good agreement with the MFD.

The fibers within the RO sample are randomly oriented as illustrated by the fiber orientation histogram in Figure 6.8. Although this sample was extracted from a SMC plate with 25 % charge coverage, the fiber distribution is considered to be planar isotropic. In addition to the fiber orientation histogram in Figure 6.8, this assumption is confirmed by the low coherence value in Table 6.1.

As revealed by Chen and Tucker [204] as well as Jackson et al. [103] decreasing charge coverage leads to increasing fiber orientation alignment. A consistent trend is observed for the SMC samples studied in this work, where the HO-45° specimen shows the most aligned fiber orientation state with the smallest charge coverage of 25 %; however, the RO specimen is an exception here. All four SMC specimens were extracted from the flow region of the respective SMC plates.

## 7.1.2 Fiber Bundle Tracking

The presented fiber bundle tracking method in Section 4.1.2 is also validated and discussed in the contribution of Schöttl et al. [242]\*. Key aspect of the fiber bundle tracking approach is the iterative proceeding along the step-wise highest probability. The tracking method adapts the fundamental approach by Tournier et al. [123, 124] from medical to material science.

In the contribution of Pinter et al. [110], individual fiber filaments are identified by using the circular voting filter and  $\mu$ CT scanning. Here, the voxel size of the volumetric images is 3  $\mu$ m. As a consequence of the high image resolution, which is required for the single fiber tracking, the overall examined sample size is limited, as illustrated in Figure 2.11. Through applying the presented method, fiber bundles instead of fiber filaments are tracked and consequently,

$\mu$ CT scans with a voxel size up to  $9.05\text{ }\mu\text{m}$  can be used. As a result, the  $\mu$ CT related conflict between image resolution and size of the studied microstructure is reduced.

Besides SMC, there is a wide range of fiber-reinforced composites where fibers are arranged as bundles or rovings. The authors Straumit et al. [129] and Bhattacharya et al. [128] tracked and analyzed the carbon fiber bundles in woven composites. Here both authors make use of the fact, that fiber bundles within woven composites are arranged in a structured way. Moreover, as a result of the periodically arranged microstructure, the number of fiber bundles within a periodic cell can be calculated and utilized for clustering.

As introduced in Section 3.1.1, fiber bundles are chopped and randomly oriented during the manufacturing process of the semi-finished SMC. For this reason, the fibers within SMC materials are arranged as fiber bundles, but the orientation and arrangement are to some extent randomly determined, as illustrated in Figure 3.7. Although the fiber bundles in this work are tracked using a similar method introduced by the authors Mori et al. [122, 127] and applied by Bhattacharya et al. [128], the clustering process of fiber bundles is decidedly more complex compared with woven composites, due to the randomly oriented microstructure of SMC. Furthermore, the SMC microstructure is generally non-periodic, making periodic assumptions for woven composites inapplicable here.

### **7.1.3 Fiber Bundle Curvature**

In this doctoral thesis the curvature of fiber bundles in and around a weld line formation are characterized based on the method introduced in Section 4.1.3. The method and results on fiber bundle curvature are presented and discussed previously in the contribution by Schöttl et al. [240]\*.

The fiber bundle curvature is determined and analyzed based on the fiber bundle tracking results illustrated in Figure 6.13 (b). Figure 6.14 shows the curvature distribution along the examined weld line. In the weld line region, the maximum curvature reaches a peak value of  $1.65 \text{ mm}^{-1}$ , with only a minimal increase of the mean curvature. From these curvature data and Figure 6.13 (c), it can be concluded that only a few fiber bundles were strongly curved within the weld line. This is confirmed by the local fiber bundle curvature results in Figure 6.13 (c), where most of the fiber bundles show a local curvature below  $0.75 \text{ mm}^{-1}$  and there are only a limited number of strongly curved fiber bundles with a local curvature above  $1.25 \text{ mm}^{-1}$ . Furthermore, Figure 6.13 (c) illustrates that all these strongly curved fiber bundles are located within the weld line.

The obtained data on the fiber bundle curvature are utilized in the contribution of Meyer et al. [118]\* to validate a process simulation model, that directly predicts the fiber bundle deformation through the compression molding process. Both results of the fiber bundle tracking and process simulation show a good agreement in terms of the fiber bundle curvature.

The evaluation of fiber bundle curvature in this work demonstrates the applicability of the fiber bundle tracking method in order to analyze SMC microstructures. Furthermore, it is shown that both local and statistical analysis of the curvature data can be performed.

## 7.2 Experimental Damage Investigation

Central element of the experimental damage investigation in this work is the in-situ  $\mu\text{CT}$  testing. The lean design of the load frame in Figure 5.3 enables to place the mechanical testing setup close to the focus point of the  $\mu\text{CT}$  scanner. As a consequence, high-resolution volumetric images of the SMC microstructures are acquired. The presented  $\mu\text{CT}$  cross sections in Section 6.2 show the

scanned microstructures in a sharp and high-contrast way. Furthermore, cracks are clearly visible with respect to the image resolution.

The examined samples are mechanically tested by displacement controlled tensile load. Figure 5.5 illustrates the mechanical test protocol. Since a cyclic tensile load is applied during the load steps, damage is introduced in a controlled manner. Initially and after each load step the displacement is fixed and high-resolution volumetric images of the examined specimen microstructure are acquired. According to Garcea et al. [65] the carried out in-situ  $\mu$ CT tests in this doctoral thesis are classified as an interrupted in-situ imaging procedure, as shown in Figure 2.14 (b).

In order to investigate the correlation between microstructure and damage behavior, SMC samples with different microstructure are examined. Samples with different SMC fiber architectures are generated by adjusting the initial charge coverages and the extraction angles with respect to the MFD. To conclusively characterize the microstructure anisotropy induced by the mold filling process, according to Chaturvedi et al. [208] specimens with  $45^\circ$  (or  $-45^\circ$ ) to the MFD are analyzed along with  $0^\circ$  and  $90^\circ$  specimens. Together with specimens in which the fibers are randomly or planar-isotropic oriented, the impact of the SMC microstructure on the damage behavior is examined comprehensively. The parameters of the respective in-situ  $\mu$ CT experiments are selected appropriately for each SMC specimen in order to examine the microstructure damage behavior in detail. The obtained image data are then analyzed further by the introduced image processing methods.

The nominal stress curves in Section 6.2 show, that during the load steps there is a drop of the nominal stress quantified by the  $\Delta\sigma_N$  value. In case of the HO- $0^\circ$ , HO- $45^\circ$  and RO specimens the nominal stress drop increases with each load step. Especially for the HO- $0^\circ$  specimen, where cracks are already initiated in the first load step, as shown in Figure 6.16. In contrast, there are only marginal nominal stress drops of the HO- $90^\circ$  specimen, as listed in Table 6.4, with no cracks observed in these load steps either.



The specimen geometry in Figure 5.7 was designed to observe damage initiation and propagation on the microstructural level by means of in-situ  $\mu$ CT testing. As a result of the notched geometry, there is a stress concentration that allows the damage to be examined in detail here by focusing the  $\mu$ CT scans on this notched region. In-situ  $\mu$ CT tests with similar specimen geometries were carried out in several contributions to examine the damage behavior within carbon fiber reinforced laminates during fatigue as well as GFRP under tensile load [84, 85, 255]. The studies demonstrated that the specimen geometry with two circular notches is very well suited for the investigation of damage and crack formations by means of in-situ  $\mu$ CT measurements.

In this work, cyclic displacement controlled load is applied during in-situ  $\mu$ CT test, with the mean displacement increasing in each load step. Comparing the maximum nominal stresses of the respective specimens with the tensile strength of quasi-static tests in Table 7.1, reveals a good agreement and consistent results. The relatively low fiber orientation degree of the HO-0° specimen, as illustrated in Figure 6.9, might present a possible explanation for the different strength properties here. In the work by Trauth [209], the SMC strength was characterized using 9 to 15 rectangular shaped specimens per microstructure case, making these results statistically representative.

Table 7.1: Comparing the maximum nominal stress of the in-situ  $\mu$ CT tested specimens with the quasi-static tensile test results by Trauth [209] on the same SMC material system with an initial charge coverage of 33 %.

Microstructure	Quasi-static [209]	Cyclic load
HO-0°	183 MPa	231.7 MPa
HO-45°	-	152.5 MPa
HO-90°	101 MPa	91.9 MPa
RO	167 MPa	170.5 MPa

In addition, Trauth identified matrix cracking perpendicular to the load direction as the predominate damage mechanism. This observation is in good agreement with the damage characterization results in this work, as presented in Table 6.7 and Section 6.4.3. Furthermore, Trauth examined that matrix cracks were forced to propagate around fiber bundles, with a similar phenomenon observed in Figure 6.22.

## 7.3 Damage Segmentation

To investigate the crack related damage process by  $\mu$ CT scanning it is essential to reliably segment those cracks within the acquired volumetric images. In this doctoral thesis several segmentation methods are presented and applied. Below the individual image processing methods and results are discussed.

### 7.3.1 Seed-Region-Growth Segmentation

$\mu$ CT scans provide volumetric images of samples, with gray-values indicating the local material composition. Objects and features consisting of the homogeneous material can be detected directly by their gray-value [8]. Gray-value histogram based segmentation methods are widely used and applied in many different fields of image processing [88, 89].

In Section 4.2, cracks within volumetric images are segmented by using the seed-region-growing method (SRG) presented by the authors Adams and Bischof [96]. From a  $\mu$ CT perspective, cracks are uniform contiguous structures. The gray-value of cracks is referred to those of air and provides sufficient contrast with the surrounding microstructure, as shown in Section 6.3.1. As a consequence of these properties, the SRG method is ideally suited for segmenting cracks.

Figure 6.24 illustrates gray-value  $\mu$ CT cross sections in the upper row and the corresponding SRG segmented cracks as binary images in the lower row. These results show that the SRG method reliably segments cracks and eliminates disturbing noise outside the crack. Advantage of the SRG method is the reliable segmentation of connected objects. However, voxels within the segmented object can be mismatched. In addition to the contribution by Schöttl et al. [241]\*, the image processing method is improved by adding slightly closing operation, as shown in Figure 4.12. As a result, the combined methods perform both, segmentation of coherent crack structures and elimination of image noise effects inside the segmented cracks.

### 7.3.2 Digital Volume Correlation

DVC is an established image processing method to determine the displacement and deformation field three-dimensionally on the microstructural level. DVC methods are available in many commercial [146–148] and open-source image processing softwares [144, 145]. As discussed by Maire and Withers [143] the full-field data obtained by DVC can be used to identify cracks. Here, the formation of cracks lead to singularities and ambiguities of the displacement field and consequently, local high difference volume results of the DVC. The larger the crack opening, the larger the resulting singularity and difference volume of the DVC.

Several characteristic crack formation regions within the HO-45° specimen are examined in detail by means of the DVC. Figure 6.27 (a) to (c) show a representative  $\mu$ CT cross section and the corresponding DVC results regarding a single crack. The large crack opening here leads to a high-contrast difference volume data and as a result, the crack is clearly identified in Figure 6.27 (b).

The DVC results in this doctoral thesis demonstrate the performance of DVC to identify cracks and are in good agreement with those in the publications of Wang et al. [82, 187] and Agyei et al. [188]. Due to the DVC fundamentals,

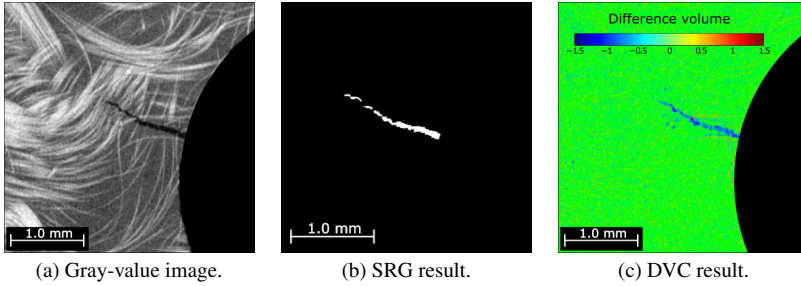


Figure 7.1: Comparing the DVC performance with those of the SRG method regarding the crack segmentation results. In (a) the gray-value image, (b) SRG and (c) DVC the crack segmentation results of an exemplary  $\mu$ CT cross section. In contrast to SRG, cracks are segmented rather smoothed by using the DVC method.

the selected control point spacing, type of transformation and approximation function regarding the displacement and strain field, cracks are not sharply segmented but rather smoothed out compared to SRG results, as illustrated in Figure 7.1. However, this effect depends on the microstructure pattern around the crack which is important for the image correlation. In this work, this smoothing effect occurs only slightly and cracks are identified relatively sharp, as shown in Figure 6.30 and Figure 7.1.

Figure 6.28 (a) shows a crack formed within a fiber bundle which is examined by using DVC in Figure 6.28 (b) and (c). Although the crack opening is small, the DVC is still capable to identify the crack. Figure 7.2 illustrates the corresponding  $\mu$ CT cross sections of the initial and deformed microstructure alongside with the difference volume data. The initial and deformed microstructure are slightly shifted due to the applied load and resulting deformation of the specimen. Even though the crack opening is marginal, the crack is clearly identified in Figure 7.2 (c). Reasons for that are the gray-value contrast between crack and fiber bundle together with the accurate DVC results due to the well-suited microstructure pattern around the crack. In contrast to the DVC, this crack could not be segmented with the SRG method, because the crack

opening is too small and only becomes visible in comparison with the initial volumetric image.

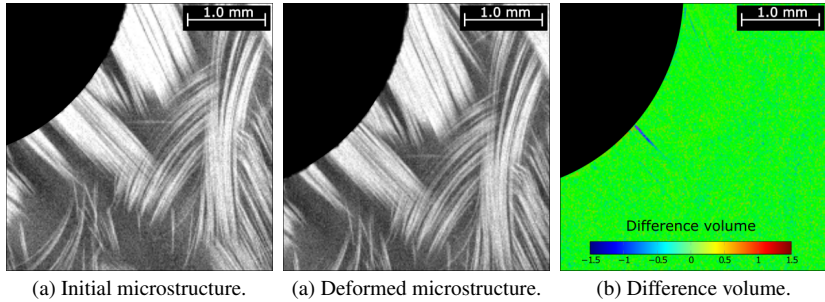


Figure 7.2: Illustrating the (a) initial and (b) deformed microstructure together with the (c) difference volume determined by DVC. Comparison between initial and deformed microstructure demonstrates the capability of the DVC method to identify even the formation of pseudo-delamination crack with marginal crack opening.

A case where a bad correlation pattern leads to poor difference volume contrast is illustrated in Figure 6.29. Although the crack opening in Figure 6.29 (a) is larger than in Figure 6.28 (a), Figure 6.29 (b) reveals a lower difference volume contrast of the crack. Reason here is that the crack is mostly embedded with matrix and consequently, a sufficient correlation pattern is missing here. However, the difference volume contrast is still significant and the crack is clearly identified. Nevertheless, the comparison between Figure 6.28 and Figure 6.29 shows the importance of an appropriate correlation pattern when using DVC methods.

As a summary, crack segmentation by means of DVC requires a highly heterogeneous microstructure to obtain accurate correlation results. Similar to the work of Wang et al. [82] and Agyei et al. [188], in this investigation the fiber-reinforced microstructure works as correlation pattern. The results show that in case of the studied SMC microstructure even cracks with small crack opening can be clearly identified based on the difference volume results.

A restriction of the fundamental DVC approach is that volumetric images of

the initial and deformed microstructure are mandatory. As a result, the application of DVC methods is generally combined with in-situ  $\mu$ CT testing, where both volumetric images are acquired. This restriction limits the applicability of DVC compared to those of SRG and CNN. However, beyond crack segmentation results DVC determines full-field displacement and strain data on the microstructural level. Figure 7.3 illustrates the von Mises strain field around a representative crack formation by a free cut. The shown crack region corresponds to that in Figure 6.29. The von Mises strain field data in Section 6.3.2 reveal that due to the microstructure deformation, as a result of the crack formation, the local von Mises strain values close to the crack are high and decrease with increasing distance.

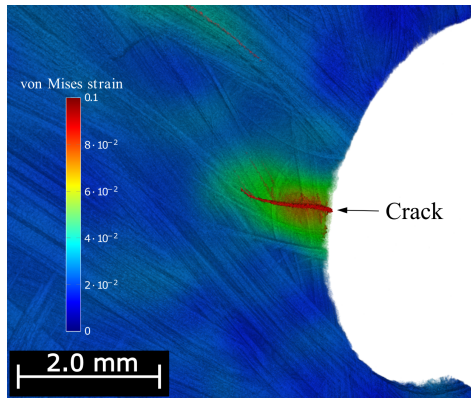


Figure 7.3: Visualizing the von Mises strain field determined by DVC around a matrix crack formation. The crack is segmented according to Figure 6.30 and visualized by a uniform color.

DVC methods require an appropriate microstructure as correlation pattern. Depending on this pattern, displacement and strain fields are determined with according resolution. Since the microstructure and thus, the correlation pattern results directly for a given material system, the DVC resolution is also directly limited by the studied material system. A reference parameter to quantify the

spatial resolution of the DVC strain data is the control point spacing of 64 voxels (or 0.4 mm) [143]. As a consequence, the microstructure strain around cracks with according distance are determined, but not near field strain data close to the crack tip.

Figure 7.3 and Figure 6.29 reveal that a von Mises strain between 4 % to 6 % is applied around the matrix crack formation here. Even though the von Mises strain can only be compared qualitatively with the elongation at break from the tensile test results in Table 3.3, it still shows an exceeding as discussed by von Bernstorff and Ehrenstein [215].

### 7.3.3 Convolutional Neural Network

Several authors previously segmented cracks by means of convolutional neural networks in the field of civil engineering [171, 175, 192, 195, 196, 200]. The summary in Table 2.3 shows that the authors used training data sets ranging from 400 up to 35100 and achieved accuracies between 89.30 % and 97.96 %. The corresponding F-measure quantities in Table 2.4, range from 70.16 % to 90.95 %.

In this doctoral thesis a data set of 9926 input images and ground truth is used to train, validate and test the U-Net architecture by Ronneberger et al. [172]. Parameters and strategy of the training process in Table 4.3 are selected according to previous tests and literature recommendations [162, 192]. As listed in Table 6.6, the trained U-Net model achieves a final accuracy, precision, recall and F-measure of 98.68 %, 86.31 %, 99.14 %, and 92.28 %, respectively. The difference between precision and recall indicates slight overestimation of the segmented cracks, as illustrated in Figure 2.30. Comparison with the summarized literature results in Table 2.3 shows that the introduced CNN method in this work segments cracks with similar exactness. Overall, the metrics and results demonstrate the high capability of the trained U-Net model to reliably segment cracks within volumetric  $\mu$ CT images of SMC.

Comparing the results of the trained CNN model and those of by the SRG segmentation method in Figure 7.4. The first column shows exemplary gray-scale image sections. Second and third column show the corresponding crack segmentation results of the CNN model and SRG method. The results in the first row demonstrate that the CNN model and SRG method both segment cracks accurately.

The images in the second row illustrate the different fundamental approaches of these two methods. The CNN method is trained in order to segment cracks. Accordingly, the pore within Figure 7.4 (d) is not segmented by the CNN model in Figure 7.4 (e). The CNN model distinguishes between pore and crack, although they have the same gray-value. In contrast, the SRG method segments objects based on their gray-value and not their shape. Pores and cracks are associated to the same gray-value and as a result, in Figure 7.4 (f) the SRG method segments both pore and cracks in the same way.

The results in Figure 7.4 reveal the performance and difference of the CNN and SRG segmentation methods. Advantage of the CNN model compared to the SRG method is that only cracks are segmented, which can be used for specific further processing. However, the initial effort for the SRG method is significantly lower compared to those for the CNN approach. Especially the acquisition and labeling of training data is time and data intensive.

## 7.4 Damage Characterization

Quantification and characterization of the damage process is important to understand and predict the mechanical properties and failure behavior of materials. As part of this doctoral thesis the damage stages of SMC are comprehensively analyzed by combining crack orientation and crack volume characterization methods. The discussions in this section refer mostly to those in the contributions of Schöttl et al. [241, 243]\*.



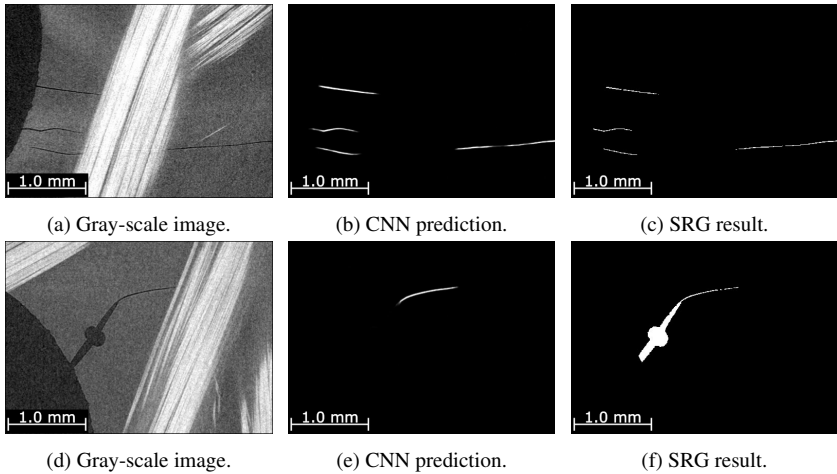


Figure 7.4: Comparing the capability of the trained U-Net model and the SRG method to segment cracks. First row shows gray-scale image sections, second and third row show the corresponding the CNN and SRG results, respectively (crack in white and background in black).

### 7.4.1 Crack Orientation Tensor

Cracks in discontinuous fiber-reinforced composites are formed directionally dependent with respect to the microstructure and load case. In general, the formation of cracks leads to a stiffness reduction in an anisotropic way. Here the stiffness in crack normal direction degrades stronger than the perpendicular one. As a consequence, the macroscopic behavior of SMC becomes even more anisotropic with progressing damage [216].

The study and quantification of the anisotropic nature of damage is essential to comprehensively characterize the damage behavior. In this doctoral thesis the fundamental approach by the authors Kachanov [49–51], Lubarda and Krajcinovic [53] from damage prediction modeling is adapted to evaluate experimental crack data. In Section 4.3.2, crack characterization methods are presented

to study the damage anisotropy. In order to quantify the crack orientation distribution an empirical formulation of the second-order crack orientation tensor  $D$  is applied. As a consequence, similar to the fiber orientation tensor [101] the experimentally obtained crack normal vectors  $g_i$  are statistically summarized by a tensor.

The experimental results of Wang et al. [219] on SMC reveal, that the micro-crack majority is oriented within  $30^\circ$  to the loading direction. Consistent results were also observed by Jendli et al. [230]. Regarding this statement it must be noted that the crack direction in some publications were introduced in a different way compared to this work.

By means of in-situ  $\mu$ CT testing and the presented image processing methods in Section 4.3.2 the crack orientation distribution is evaluated. In this work the crack orientations are examined along the damaging process of a SMC sample with highly oriented fibers in tensile load direction (HO- $0^\circ$ ). The crack orientation histogram results in Table 6.7 reveal, that during the first three load steps the majority of cracks are oriented within  $10^\circ$  to the tensile direction. During the fourth load step, additional cracks are formed and the principal crack orientation is changed by approximately  $30^\circ$ .

In addition to the HO- $0^\circ$  specimen, the crack orientation during the final load step of the HO- $45^\circ$  and RO specimens are analyzed. The results in Table 6.8 reveal that there is a similar crack orientation distribution within the HO- $0^\circ$  and HO- $45^\circ$  specimens during the respective final load step. Furthermore, the RO specimen shows a crack orientation distribution, where the cracks are mostly oriented along the tensile load direction. The crack orientation results of the HO- $45^\circ$  and RO specimens are both in good agreement with the  $\mu$ CT cross sections in Figure 6.18 (c) and Figure 6.23 (d).

In order to model the formation of cracks in state-of-the-art continuum mechanic models, the geometry of the defects has to be simple and known (eg. penny shaped) [49, 50]. In practice, however, the geometry of defects is usually complex and unknown. The evaluation of the crack orientation distribution

in this doctoral thesis demonstrates the capability of the presented method to quantify the damage anisotropy.

The authors Wang et al. [219] studied the orientation of cracks on a SMC material system, which consists of a polyester matrix reinforced by a glass fiber content of 50 wt.%. The authors revealed that in matrix-rich areas nearly all cracks are formed normal to the load direction, as shown in Figure 7.5 (a). The crack density and orientation are examined by optical cross sections and manual evaluation. The crack orientations are quantified by the symmetric off-axis angles  $\theta_{\text{crack}}$  regarding the load direction, where  $\theta_{\text{crack}} \hat{=} -\theta_{\text{crack}}$ . For comparison the crack orientation distribution results in this work are illustrated similarly in Figure 7.5 (b). Here, the orientation distribution of the crack volume fraction in Figure 7.5 (b) is quantitatively compared with those of the crack density results in Figure 7.5 (a). The crack orientation results of the fourth load step are illustrated separately in Table 6.7, since here crack phenomena close to the final fracture are examined, which are not covered by the results of Wang et al. [219].

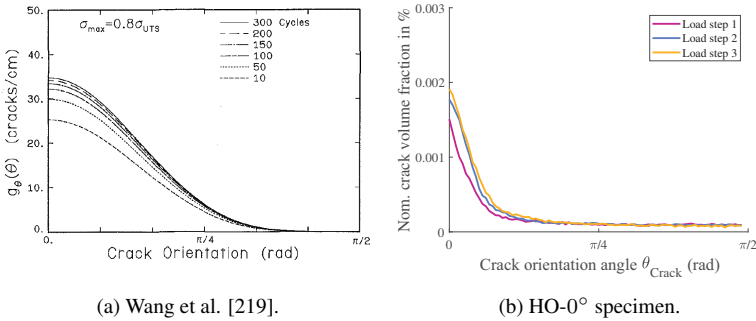


Figure 7.5: Crack orientation distribution with respect to the crack density. Comparing the crack orientation results (a) studied by Wang et al. [219] and (b) characterized in this doctoral thesis (figure in (a) by Wang et al. [219]).

Comparing both results in Figure 7.5 (a) and (b) reveals that there are quantitative similar trends, but a significant wider crack orientation distribution around

the load direction of the results by Wang et al. [219]. A reason for this is the proportion and frequency of matrix cracks, since these preferentially occur normal to the load direction. The studied SMC material by the authors Wang et al. includes a higher fiber content of 50 wt.% compared to those in this work. Consequently, the formation of matrix cracks is proportionally more likely within the investigated SMC material in this doctoral thesis. This is in good agreement with the damage mechanism classification results in Table 6.9, where matrix cracking is identified as the predominate damage mechanism.

## 7.4.2 Crack Volume Fraction

The authors Meraghni and Benzeggagh [222] established that the content and geometry of (micro-)cracks affect the macroscopic stiffness of SMC. However, according to the authors study the macroscopic stiffness reduction is affected more sensitive by the crack content than on their geometry. The authors Reifsnider et al. [38], von Bernstorff and Ehrenstein [215] revealed the existents of a maximum crack density for fiber-reinforced composites, which is characteristic for the material but independent of the load history. This maximum crack density is especially applicable to whether a quasi-static or fatigue load is applied. Crack density and volume fraction are commonly used to quantify the damage state. The authors von Bernstorff and Ehrenstein [215] examined that there is a direct correlation between crack density on the micro scale and stiffness degradation on the macro scale.

In contrast to crack density obtained by cross section preparation and optical microscopy, in this doctoral thesis the crack volume is determined three-dimensionally by means of in-situ  $\mu$ CT testing. Figure 6.35 presents the characterized crack volume and normalized crack volume fraction. The results of three representative specimens are visualized with respect to the microstructure (RO, HO-0°, and HO-45°). Since no cracks are observed within the HO-90° specimen until fracture by means of the in-situ  $\mu$ CT test, no crack volume data

are obtained here. Due to cavities within the RO specimen, as shown in Figure 6.22 the initial crack volume in Figure 6.35 (a) is shifted compared to those of the other samples.

The crack volume distributions of the three analyzed specimen show, that there is a high increase of the crack volume just before final fracture. The normalized crack volume fraction with respect to the maximum nominal stress of the load step are illustrated in Figure 6.36. There is a similar development of the crack density for the RO and HO-0° microstructure. However, the RO specimen failed at a lower tensile stress level. According to several authors [38, 215, 219], the crack density within fiber-reinforced polymers is directly associated with the macroscopic stiffness degradation and overall damage state. The measured normalized crack volume fraction values in Figure 6.36 for SMC show a good agreement with the schematic damage progression for composites materials in Figure 2.5 according to Stinchcomb [42] as well as Mao and Mahadevan [43].

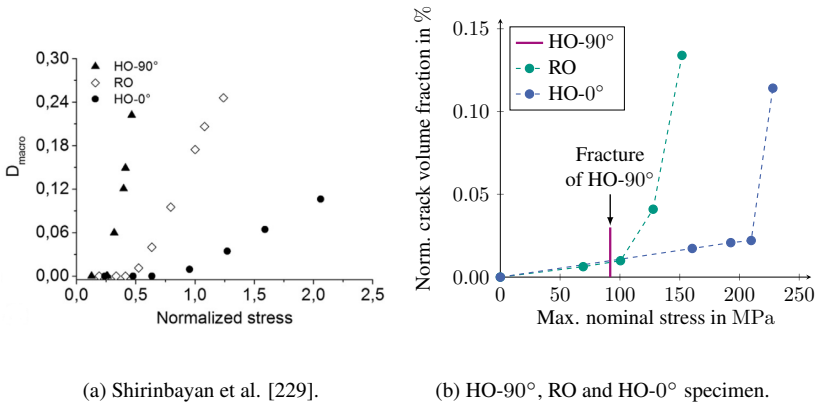


Figure 7.6: Comparing macroscopic damage variable and norm. crack volume fraction. Development of the (a) damage variable and (b) crack volume fraction with respect to the applied stress and the fiber architecture (figure in (a) by Shirinbayan et al. [229]).

The authors Shirinbayan et al. [229] studied the damage development in SMC with respect to different microstructures. The damage is quantified by means of the damage variable  $D_{\text{macro}} = 1 - E_D/E_0$ , where  $E_D$  is the current and  $E_0$  the initial Young's modulus. Figure 7.6 (a) illustrates the damage propagation of the respective SMC specimens. As established by Meraghni and Benzeggagh [222], the macroscopic stiffness reduction strongly correlates to the crack density. The characterization results in this work on the crack volume fraction together with the maximum nominal stress  $\sigma_{N,\text{max}}$  of the respective load steps are shown in Figure 7.6 (b). Since no cracks were observed before the rupture fracture of the HO-90° specimen, here no crack volume values are determined. The nominal stress at fracture of the HO-90° specimen is illustrated in Figure 7.6 (b) by a vertical line.

Comparing the damage propagation results in Figure 7.6 reveals similar trends in the corresponding distributions. There is a sharp damage increase for the HO-90° specimen in Figure 7.6 (a), which is in good agreement with the observation in this doctoral thesis. Furthermore, similar trends are observed with respect to the RO and HO-0° SMC microstructures, with an increasing damage of the HO-0° specimen at corresponding higher stress values. Overall, comparing the results on macroscopic damage and crack volume fraction in Figure 7.6 reveals that both results show consistent trends. As a consequence, the introduced and characterized crack volume fraction reliably quantifies the damage state.

Goal of the introduced methods in Section 4.3 is to comprehensively characterize the damage state on the microscopic level. The crack orientation tensor presented in Section 4.3.2, quantifies the damage anisotropy and spatial distribution but not the overall damage state. Complementary, the introduced crack volume fraction supplements this aspect. Together the crack orientation tensor  $\mathbf{D}$  and crack volume fraction  $\rho_{\text{Crack}}$  quantify the damage in a comprehensive way.

### 7.4.3 Damage Classification

From a damage modeling perspective, the authors Meraghni et al. [222, 223] classified damage mechanisms in SMC by two types. Matrix cracking and pseudo-delamination are associated to type A and fiber pull-out to type B. Furthermore, several authors examined the damage behavior of SMC and identified different predominate damage mechanisms, as shown in Table 3.6. The four main types of SMC damage referred to in literature are matrix cracking, pseudo-delamination, fiber pull-out and fiber breakage.

In this work a classification method is introduced to identify the predominate SMC damage mechanism(s) based on in-situ  $\mu$ CT acquired volumetric images. Criteria based on crack orientation, neighboring microstructure and fiber orientation are presented for matrix cracking, pseudo-delamination and fiber bundle breakage. In contrast to the study by Wright et al. [78], in which damage is classified manually, the introduced mathematical criteria allow cracks to be classified automatically, deterministically, and reproducibly.

In addition to the three considered damage mechanisms, fiber pull-out is mentioned by several authors as another damage mechanism [21, 208, 226, 231]. Fiber pull-out is mainly caused by shear stress induced failure of the interface, which leads to a shear deformation and slipping of fiber and matrix. As a consequence, there is no significant crack opening between fiber and matrix, which could be observed by  $\mu$ CT scanning. Because of this reason, shear stress induced fiber pull-out is not observed and considered by the presented characterization method. Since the actual fiber length is above of the critical, fiber breakage occurs preferentially before fiber pull-out. This subject is discussed in detail in the section below. Interface failure due to normal stresses between fiber and matrix, which leads to crack opening at the interface is associated to pseudo-delamination by the introduced classification scheme.

The introduced and applied method in this doctoral thesis is inspired by the crack classification approach of Yu et al. [76]. However, in contrast to the classification scheme by the authors Yu et al., in addition to crack orientation and

adjacent microstructure also the orientations of neighboring fibers are taken into account. As a result, longitudinal and transverse cracks within fiber bundles are classified separately.

The damage mechanisms of SMC samples with different microstructure as well as along the in-situ  $\mu$ CT load steps are examined. The results in Table 6.9 and Figure 6.37 reveal that matrix cracking ( $> 90\%$ ) is by volume the predominate damage mechanism of the examined SMC material system. In contrast the proportion of pseudo-delamination and fiber breakage are both marginal (both  $< 6\%$ ). There are only minor differences between the samples with different microstructures. Comparison with Figure 6.16, Figure 6.18 and Figure 6.22 shows that these results, which indicate dominant matrix cracking, are plausible. The examined SMC material system contains a fiber content of 41 wt.%. Summarized results by several authors in Table 3.6 show that for SMC with similar fiber content matrix cracking and pseudo-delamination are the predominate damage mechanisms.

## 7.5 Fractography

The author Greenhalgh [27] examined the fracture surface of unidirectional fiber laminates. The author stated that river lines and scraps are important features for diagnosing the crack propagation based on fractography. Due to the difference in stiffness between fiber and matrix together with the resulting stress intensities, the river lines mainly occur at the matrix surface near or between fibers [258]. The crack propagation direction can be determined by the direction in which the river lines converge. Scraps mark the boundary between two converging crack which are initiated on slightly different planes [27]. The occurrence of scarps on the fracture surfaces consequently indicates that multiple cracks have been formed. River lines and scraps mainly occur during (pseudo-)delamination.



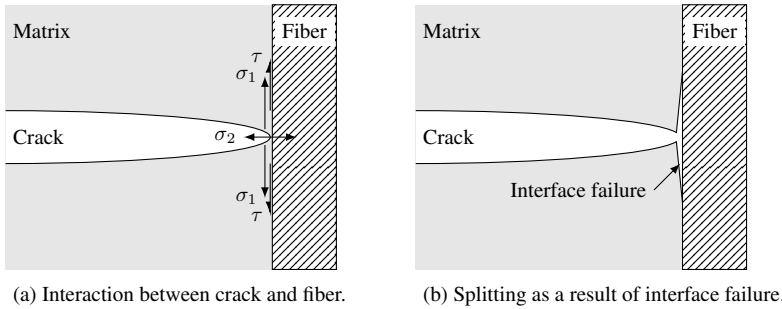


Figure 7.7: The Cook-Gordon mechanism of longitudinal splitting. Introducing shear stress parallel to the interface by means of tension crack propagation towards a longitudinal fiber (re-illustration, original figures by Greenhalgh [27] and Cook et al. [259]).

The authors Cook et al. [259] studied the mechanics of cracks within unidirectional fiber-reinforced laminates and the interaction of matrix cracks and fibers. They demonstrate how tensional cracks introduce shear stress at the fiber-matrix interface by propagating towards a longitudinal fiber, as illustrated in Figure 7.7. If the introduced shear stress exceeds the interface strength, the interface fails close to the crack tip and local fiber debonding occurs. Regarding longitudinal splitting by the Cook-Gordon mechanism, Greenhalgh [27] established that the poor fiber-matrix interface of GFRP leads to extensive longitudinal splitting and subsequently, predominately fiber debonding before fiber breakage occurs. This results in a high degree of fiber brooming on the fracture surface, as shown in Figure 7.8 (a). In contrast, Figure 7.8 (b) shows a fracture surface where brittle tension failure with limited splitting occurred.

The fracture surface in Figure 6.38 (HO-0°), Figure 6.42 (RO) and Figure 6.46 (HO-90°) reveal extensive brooming of the fiber bundles. Although there are some fiber bundles which failed in a brittle way (cf. Figure 6.40), the majority of fiber bundles show broom-like failure. According to Greenhalgh [27] and Cook et al. [259], the reason for this is the relatively weak interface between the glass fibers and the matrix. In addition to fiber bundle brooming, the SEM

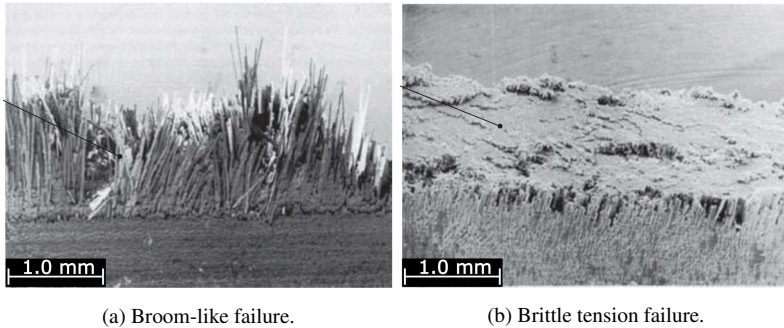


Figure 7.8: Difference between (a) extensive fiber debonding and (b) dominate fiber breakage of GFRP laminate (original figures by Greenhalgh [27]).

images in Figure 6.41 ( $HO-0^\circ$ ) and Figure 6.43 (RO) reveal that entire fiber bundles are pulled out as a whole. Brooming and pull-out of the fiber bundles occurs during the final stage of the damage process [27].

The SEM images in Figure 6.47 and Figure 6.50 (both  $HO-90^\circ$ ) show several river lines, scraps and fiber tracks on the matrix surface in fiber rich regions. These features indicate that several cracks were initiated due to the stress intensities at the fiber surface [27]. Based on this together with the in-situ  $\mu CT$  results in Figure 6.19 and Figure 6.20, it is concluded that multiple matrix cracks occur during the sudden failure of the  $HO-90^\circ$  SMC specimen and pseudo-delamination is the predominant damage mode.

## 7.6 Damage Mechanisms of SMC

In this section, results and insights from damage characterization and fractography are brought together and discussed regarding the damage mechanisms of the investigated SMC material system. In order to design discontinuous

fiber-reinforced composite components, it is important to predict their mechanical behavior as a function of the manufacturing process, microstructure and damage behavior [260]. Since local damage condition affects the mechanical properties of composite structures, the substantial description, characterization and prediction of damage mechanisms are scientifically and industrially imperative. However, the damage mechanisms of discontinuous fiber-reinforced composites occur diversely and in a complex manner. As a consequence, comprehensive experimental investigations are essential to describe them properly. In practice, damage modes often occur simultaneously, which makes predicting the mechanical behavior a difficult task. One of the most significant degradations of the mechanical properties of discontinuous fiber-reinforced composites takes place under cyclic fatigue loading [260, 261].

The critical fiber length determined according to Equation 2.18 and the material properties in Table 3.4 and Table 3.5 is  $112.5\text{ }\mu\text{m}$ . Fiber bundle length of the investigated SMC is  $25.4\text{ mm}$ . Accordingly, fiber fracture should be more likely to occur than fiber pull-out. However, in discontinuous fiber-reinforced composites the assumption that there is equal strain of fiber and matrix is not fulfilled adequately. According to Piggott [262], the fibers are less strained than the matrix which results in shear strain at the fiber-matrix interface. As a result, although the actual fiber length in SMC is much longer than the critical, fiber pull-out is more likely to occur.

Although fiber and matrix individually behave brittle [48, 263], SMC composites show a time-depended damage process. Jendli et al. [230] examined that time and strain-rate dependent loads mostly affect the fiber-matrix interface. According to Jendli et al. [230] and Shirinbayan et al. [226], the viscous nature of microscopic damage in SMC is associated to the development of interface damage and in particular to pseudo-delamination.

According to Cook et al. [259] and Greenhalgh [27], matrix cracking within a fiber-reinforced composite with poor fiber-matrix interface properties can lead

to massive interface failure. The damage mechanisms in various SMC material systems are examined, modeled and discussed by several authors. Table 3.6 summarizes the predominate damage mechanism(s) for SMC regarding the fiber content and monotonic or cyclic load case. The analyzed SMC system has a nominal fiber content of 41 wt.%. In literature, matrix cracking and pseudo-delamination have been identified as the predominate damage mechanisms for similar SMC material systems [215, 224, 232].

The damage mechanisms which occur within the examined SMC samples are observed by in-situ  $\mu$ CT testing and subsequently, analyzed by the classification scheme in Figure 4.22. Section 6.4.3 presents the damage classification results with respect to different SMC microstructures, as well as the propagation of the damage process.

The damage classification results in Figure 6.35 and Table 6.9 reveal that there are only marginal difference between the SMC specimens, although those specimens have different fiber orientation distribution. It is concluded that the fiber architecture does affect the damage behavior, as shown in Section 6.2 but not the predominate damage mechanism in particular. For the SMC specimens, matrix cracking is evaluated to be the predominate damage mechanism, as shown in Figure 7.9.

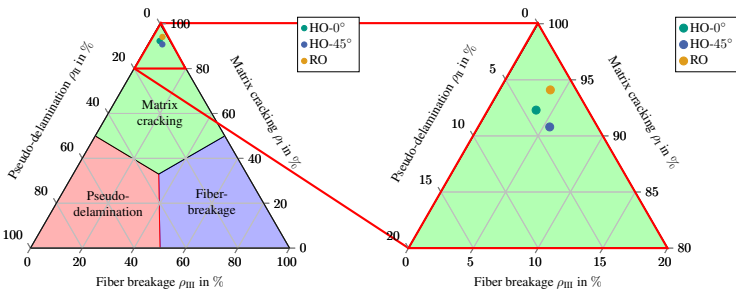


Figure 7.9: Classification of the analyzed damage mechanisms. Visualization of the damage mechanism fractions by a ternary plot and a detailed view of the relevant region. All the SMC specimens investigated exhibit predominant matrix cracking.

In addition to the investigation on the occurring damage mechanisms in different microstructures, the development along the damage process from crack initiation to final fracture is examined in Figure 6.37. The obtained results reveal that volume fractions of the damage mechanisms do not change significantly through the entire damaging process.

Both characterization data in Table 6.9 and Figure 6.37 show that matrix cracking occurs predominately by volume within the investigated SMC material system ( $> 90\%$ ) compared with pseudo-delamination and fiber breakage (both  $< 6\%$ ). These results are consistent with the observations within the  $\mu$ CT cross sections in Section 6.2. In particular, the damaged microstructures in Figure 6.22 and Figure 6.22 establish that cracks occur mainly within the matrix. Although the fraction of fiber bundle breakage is small, it has massive impact on the mechanical behavior on the macroscopic scale, since the stiffness and strength of fibers are significantly higher than those of the matrix.

The authors von Bernstorff and Ehrenstein [215] discussed the occurrence of single and multiple matrix cracking with respect to the fiber volume content. Figure 3.11 (b) illustrates the estimated effective composite strength as a function of the fiber content and the transition between single and multiple matrix cracking. The actual fiber volume content of the examined SMC material is higher than the critical fiber volume content. According to von Bernstorff and Ehrenstein [215] multiple matrix cracking is expected for the studied SMC material. The authors Wang et al. [219] established that fatigue load with high cyclic stress introduces damage with high crack density but short characteristic crack length and fatigue load with low cyclic stress does the opposite. From a volumetric perspective it is concluded that high cyclic loads lead to the formation of a higher number of cracks compared to low cyclic loads. The applied load during the in-situ  $\mu$ CT test in this work is rather associated to high cyclic load. The  $\mu$ CT cross sections in Section 6.2 reveal that in the beginning of the damage process first a single crack initially occurs, which is later followed by further cracks close before fracture. This damage progress is observed especially in case of the SMC microstructures with highly oriented

fibers in tensile load direction (see Figure 6.16) and randomly oriented fibers (see Figure 6.22). Overall, the in-situ  $\mu$ CT observations on SMC in this doctoral thesis are shown to be in good agreement with the studies on SMC by Wang et al. [219], von Bernstorff and Ehrenstein [215].

Figure 7.10 (a) shows exemplary matrix crack formation within the investigated SMC material system and Figure 7.10 (b) illustrates them schematically. Here multiple cracks are formed at different locations. Due to the stress intensity, at (I) a crack has occurred at a cavity tip. Additional matrix cracks are formed at (II), that surpass a fiber bundle at (III) without fiber bundle breakage. This phenomenon is explained by the lower failure strain of the matrix compared to the fiber.

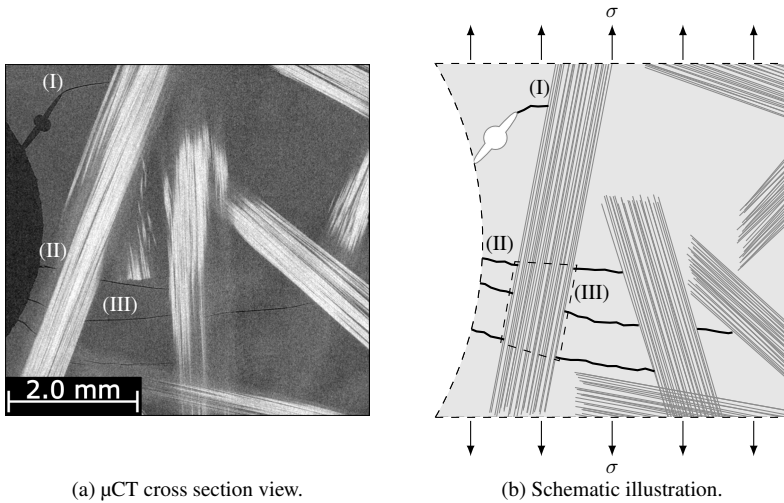


Figure 7.10: Damage mechanisms in SMC with planar randomly oriented fiber bundles (RO) under cyclic load. In (a) an exemplary  $\mu$ CT cross section of the RO sample and (b) illustration of the observed damage phenomena. At (I) crack initiation at a pore tip, (II) crack propagation through the UPPH matrix and (III) bypassing fiber bundles.

During the formation and propagation of cracks in solids, various phenomena can occur which are typical for the respective material. In the work of Naebe et

al. [261] these crack phenomena for composite materials were presented and discussed. The results in this doctoral thesis show that fiber bundle bridging and crack deflection occurs in SMC. The fiber bundle bridging leads to the fact that the composite material becomes macroscopically tougher compared to the pure UPPH matrix and crack propagation in the brittle matrix can be stopped. In this case and as shown in Figure 7.10, fiber bundles do not necessarily bridge the two crack surfaces directly but stabilize the crack by surrounding it.

The authors Shirinbayan et al. [226–229] examined the SMC damage mechanisms with respect to the fiber orientation distribution. According to the authors fatigue life of SMC is strongly affected by the fiber orientation distribution. In this work, a significant difference is observed between the analyzed fiber architectures regarding the damage behavior.

Different damage behavior with respect to the SMC microstructure is examined in this work. As shown by the results from experimental in-situ  $\mu$ CT testing and fractography, SMC with highly oriented fibers perpendicular to the tensile load direction (HO-90°) fail in a sudden manner, where the matrix material appears to be mainly responsible. The  $\mu$ CT cross section in Figure 6.20 (d) reveals that during final fracture additionally to matrix cracking also pseudo-delamination occurred. Matching features, such as river lines, scraps and fiber tracks, that also indicate pseudo-delamination are evident by examining the fracture surface in Figure 6.49.

The SMC samples with HO-0°, RO and HO-45° microstructure show steady damage behavior in descending order, as illustrated in Figure 6.36. Compared with the HO-90° specimen, the mechanical behavior of these samples is mostly associated to the composites properties. In contrast to the results by Shirinbayan et al. [228], the results in this doctoral thesis reveal that the damage behavior and maximum nominal stress of the random oriented (RO) and transverse highly oriented fiber orientation (HO-90°) is significantly distinguished.

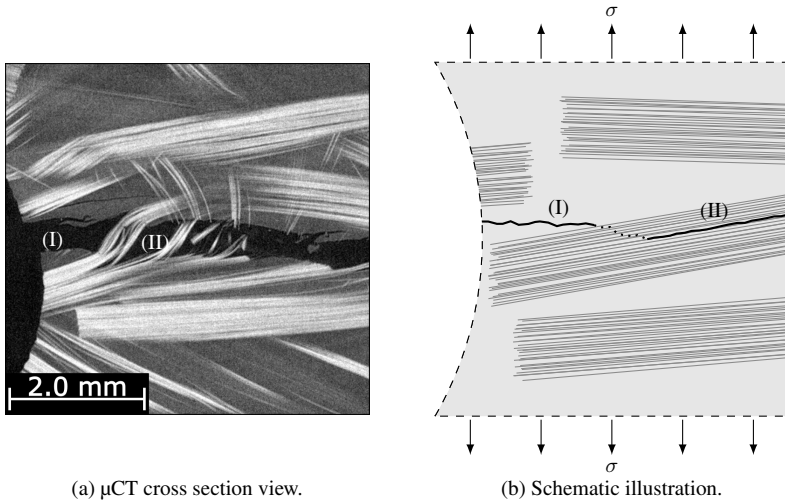


Figure 7.11: Illustration of the observed damage mechanisms in HO-90° SMC. In (a)  $\mu$ CT cross section and in (b) schematic illustration of the crack formation, where predominately matrix cracking and pseudo-delamination occurs.

Figure 7.11 schematically illustrates the crack formation and damage mechanisms with respect to the fiber architecture based on the results in this work. The crack formation within the HO-90° SMC in Figure 7.11 (b) is reconstructed based on the SEM images and fractography. Since massive river lines, scraps and fiber tracks are observed here and due to the fiber architecture, it is concluded that matrix cracking and pseudo-delamination mainly occurred, as observed in Figure 7.11 (a) at (I) and (II).



# 8     Summary and Conclusions

This work covers several aspects regarding the material science investigations on SMC. In this chapter the methods, results and discussion of the microstructural characterization, experimental in-situ  $\mu$ CT investigations and damage characterization are summarized and conclusions are drawn.

## Contents

---

<b>8.1 Microstructure Characterization . . . . .</b>	<b>210</b>
<b>8.2 Experimental Damage Investigation . . . . .</b>	<b>211</b>
<b>8.3 Damage Segmentation . . . . .</b>	<b>212</b>
<b>8.4 Damage Characterization . . . . .</b>	<b>214</b>
<b>8.5 Fractography . . . . .</b>	<b>215</b>
<b>8.6 Damage Mechanisms of SMC . . . . .</b>	<b>215</b>

---

## 8.1 Microstructure Characterization

Cooperations and interactions between different research areas is important in order to combine the respective capabilities and open up new possibilities. For materials science and the International Research Training Group (IRTG) in particular, the transition of data between numerical modeling and characterization, as well as between scale levels is critical. In this doctoral thesis the microstructure of sheet molding compounds (SMC) is characterized by means of micro-computed tomography ( $\mu$ CT) scanning and image processing methods. The acquired fiber orientation data on the microscale level are transferred to macro scale by the introduced mapping scheme. This enables the utilization of the acquired fiber orientation data for the validation of process simulation or as input for mechanical prediction models. Furthermore, the fiber orientation within the SMC samples that are examined through in-situ  $\mu$ CT testing are characterized. This allows a comprehensive investigation of the SMC samples with regard to the microstructure as well as the mechanical behavior.

This doctoral thesis introduces a method to identifying and analyzing fiber bundles within  $\mu$ CT volumetric images of SMC. The introduced method basically consists of two parts. First, microscopic fiber bundles are iteratively tracked by step-wise determining the step-wise highest probabilistic path with respect to the orientation data. Compared to woven fabrics the fiber bundles within SMC are generally randomly oriented and unstructured. The stream-line inspired method meets the requirement to reliably track microscopic fiber bundles even in regions where other fiber bundles cross. To determine the mesoscopic fiber bundles based on the microscopic tracking results, criteria are introduced to quantify distance and orientation between microscopic bundles. Subsequently, those criteria are implemented by an agglomerative hierarchical clustering method and the mesoscopic fiber bundles are determined.

The basic approach of the fiber bundle tracking method utilizes the fiber bundle structure, which is typical for SMC material. Fiber bundles are analyzed instead of individual fibers and as a consequence, the necessary minimum voxel

size of the  $\mu$ CT scan is increased significantly. As a result, larger and more representative SMC microstructure volumes can be examined by means of cone-beam  $\mu$ CT scanning. Compared to state-of-the-art methods, the introduced characterization method is capable to identify and analyze the unstructured and randomly oriented SMC microstructure.

The characterization and prediction of SMC microstructures is essential for designing components and optimizing the manufacturing process. Weld lines occur when two mold fronts clash during the mold filling process, representing a mechanical weak point. Although efforts are made to avoid this, it cannot always be ruled out. Especially for SMC components with complex geometry, weld lines are often unavoidable in practice. The introduced fiber bundle tracking method is used to analyze fiber bundles within and around weld lines. In particular, the fiber bundle curvature distribution through the weld line is examined. Obtained results reveal, that there is a higher curvature of fiber bundles within the weld line than outside. However, only limited number of fiber bundles are strongly bended here.

## **8.2 Experimental Damage Investigation**

Damage investigation of SMC by means of interrupted in-situ  $\mu$ CT is one key aspect of this work. Through combining mechanical in-situ testing and lab-based  $\mu$ CT scanning, volumetric images of an examined microstructure at different damage stages are acquired. Here,  $\mu$ CT scans are performed initially and after each interrupted load step.

Goal of the experimental procedure is to investigate the damage process on the microstructural level. The load is introduced displacement controlled and increased step-wise by each load step. As a consequence, damage is introduced in a controlled manner, which enables to observe crack initiation and propagation through several load steps although the examined SMC material shows brittle behavior.

The in-situ  $\mu$ CT setup has a slim load frame, that allows to place the in-situ  $\mu$ CT setup close to the focus spot in order to acquire high-resolution projections. The load frame is made of carbon fiber-reinforced polymer, which only weakly absorbs X-rays. As a result, high-resolution volumetric images with low image noise are obtained of the damage SMC microstructures. Overall, the applied in-situ  $\mu$ CT setup acquires volumetric images with clear contrast and voxel size between 6 and 7  $\mu\text{m}$ .

## 8.3 Damage Segmentation

Effective and reliable image processing methods are important to analyze microstructures by means of volumetric images. One key aspect of this doctoral thesis is the characterization of microstructural damage regarding the initiation and propagation of cracks. To examine damage features, cracks are segmented reliably in the first place. In this work different segmentation methods including gray-value histogram based seed region growth approach (SRG), convolutional neural networks (CNN) and digital volume correlation (DVC) are presented and applied.

Gray-value histogram image processing techniques are widely used in many fields. The SRG method is designed to reliably segment contiguous objects. The method proves to be robust against image noise. The results show that cracks are segmented reliably and accurately in the  $\mu$ CT volumetric images of SMC. Since the gray-value level of cracks and pores is similar, both phenomena are segmented in the same way by the SRG method.

Methods based on CNN approaches are highly capable to classify, detect and segment objects within image data. The basic concept of CNN is to train a general architecture based on input images and corresponding ground truth data to enable the CNN model to segment specific objects. This doctoral thesis presents a CNN method to segment cracks within  $\mu$ CT volumetric images of SMC. Image data for the training process are obtained by interrupted in-situ

$\mu$ CT testing. In total, a dataset including 9926  $\mu$ CT images and corresponding ground truth labels was acquired. The training images are taken from separate in-situ  $\mu$ CT experiments and are strictly separated from the examined SMC samples.

In this doctoral thesis, the U-Net architecture is selected, implemented and trained by the training dataset. Final accuracy, precision, re-call and F-Measure of 98.68 %, 86.31 %, 99.14 %, and 92.28 % are achieved by the U-Net model, respectively.

The trained CNN model is implemented in a data processing setup to automatically segment cracks within large-scale volumetric images. Here, image patches are extracted equidistant by a grid, analyzed by the trained CNN and re-assembled subsequently. In order to eliminate effects by the grid, the large-scale volumetric images are analyzed by means of several grids and the results are merged together. As a result, cracks within large-scale volumetric images with individual sizes are segmented reliably and efficiently based on the trained CNN model.

Based on volumetric images of the initial and deformed microstructure, the changes can be inferred. Digital volume correlation (DVC) techniques determine the displacement and deformation field three-dimensionally. Here, the highly heterogeneous microstructure is used as a correlation pattern. As part of this work the DVC method by VGSTUDIO MAX 3.4 from Volume Graphics is applied. The formation of cracks leads to ambiguities and singularities of the continuum mechanic, which are used to recognize cracks. The results in this doctoral thesis demonstrate the capability of DVC to identify cracks. Furthermore, besides crack segmentation the DVC are used to analyze the strain field around crack formations.

Due to the complex and heterogeneous microstructure of SMC and fiber-reinforced composites in general, it is difficult to segment and analyze cracks within volumetric images. However, there is a need for reliable and efficient image processing methods to characterize microstructural damage. This work

shows, compares and discusses the ability and capability of the presented crack segmentation methods.

Compared to the CNN method, the SRG not only segments cracks but also pores, since these have a similar gray-value. The DVC approach differs the most from both other methods SRG and CNN. Here, volumetric images of the initial and deformed specimen are mandatory as input. As a result, informations about the displacement and deformation field within the microstructure are obtained, from which the position of cracks can be deduced. The greatest effort is required for the CNN method, since this requires an extensive training dataset to be generated and an architecture to be trained at great expense in the first place. However, if the CNN has been trained properly, it generates the most accurate crack segmentation results.

## **8.4 Damage Characterization**

Cracks and damage on the microstructural level significantly affects the mechanical behavior on the macro scale. Consequently, the characterization of damage is essential to understand and predict the mechanical behavior of material system comprehensively. By utilizing the damage segmentation methods and results, microstructural cracks are characterized in this doctoral thesis. Methods are introduced to further analyze and quantifying crack formations by two different aspects.

The presented crack volume fraction takes the overall crack volume into account and quantifies both propagation of cracks as well as the formation of further cracks. From this data, the overall state of damage can be derived. The results show how the examined SMC damages through the interrupted in-situ  $\mu$ CT test and that this behavior corresponds to that of established characterization results and models.

In general, the mechanical properties of fiber-reinforced composites are anisotropic. Since, damage is usually introduced directionally dependent and consequently, the degree of anisotropy is increased as the damage progresses. State-of-the-art structure models predict the mechanical behavior and take the anisotropic damage development into account. However, they require detailed microstructure characterization data as an input and for the validation.

Methods to characterize the damage anisotropy by means of the crack orientation are presented. The crack orientation distribution is quantified through an empirical formulation of the second-order crack orientation tensor  $D$ . Subsequently, the presented methods are applied and the anisotropic nature of damage is analyzed for the studied SMC material system.

## 8.5 Fractography

In addition to the in-situ  $\mu$ CT tests, the fracture surfaces of studied SMC samples are analyzed by means of scanning electron microscopy (SEM). The analyzed fracture surfaces show massive fiber bundle brooming which indicates matrix cracking and poor interface strength with respect to the Cook-Gordon mechanism. Furthermore, on the fracture surface of the SMC with highly oriented fibers perpendicular to the tensile load direction (HO-90°) a large number of river lines, scraps and fiber tracks are observed. Those features indicate pseudo-delamination and rupture fracture, which is consistent with the observations of the in-situ  $\mu$ CT test.

## 8.6 Damage Mechanisms of SMC

Due to the combination of different materials in composites, not only one damage mechanism occurs but many different ones. Those damage mechanisms

occur in different ways, damage different parts of the microstructure and consequently, do have different impact on the mechanical behavior.

One key aspect of this work is the combination of microstructure and damage characterization methods and data on the same scale level. By merging microstructure data from the fiber orientation analysis and crack data from the in-situ  $\mu$ CT testing and damage characterization, suitable mathematical criteria for the SMC damage mechanisms matrix cracking, pseudo-delamination and fiber bundle breakage are introduced. Based on that damage classification scheme, the fractions of these three damage mechanisms is determined for the SMC samples studied. The results reveal that matrix cracking ( $> 90\%$ ) is the predominate case by volume. However, although the fractions of the other two cases is lower (both  $< 6\%$ ), the effect of fiber bundle breakage in particular on the mechanical properties cannot be neglected.

This doctoral thesis covers several aspects regarding the material science investigations on SMC. The introduced methods and results of the microstructural analysis, experimental damage investigation and damage characterization are all brought together in order to evaluate and quantify the occurring damage mechanisms. As a result, methods to comprehensively characterize various aspects of fiber-reinforced polymers on the microscopic and mesoscopic scale based on  $\mu$ CT technique are introduced. Finally, all those methods are applied to evaluate the relationship between microstructure and damage behavior of the examined SMC material system.



# Author's Publications

In addition to the Bibliography, contributions published by the author Ludwig Schöttl as first or co-author are listed below. First the publications as first author and then those as co-author are listed in order of occurrence. In this doctoral thesis these own publications are marked by a \*-symbol. The publications are additionally listed in the bibliography.

- [131] L. Schöttl, D. Dörr, P. Pinter, K. A. Weidenmann, P. Elsner, and L. Kärger, “A novel approach for segmenting and mapping of local fiber orientation of continuous fiber-reinforced composite laminates based on volumetric images,” *NDT & E International*, vol. 110, p. 102194, 2020.
- [240] L. Schöttl, W. V. Liebig, K. A. Weidenmann, K. Inal, and P. Elsner, “Microstructure characterization of discontinuous fiber reinforced polymers based on volumetric images: Fiber bundle tracking and weld line investigation,” in *4th International Conference Hybrid 2020 Materials and Structures*, Web-Conference, 2020, pp. 97 – 101.
- [241] L. Schöttl, P. Kolb, W. V. Liebig, K. A. Weidenmann, K. Inal, and P. Elsner, “Crack characterization of discontinuous fiber-reinforced composites by using micro-computed tomography: Cyclic in-situ testing, crack segmentation and crack volume fraction,” *Composites Communications*, vol. 21, p. 100384, 2020.

- [242] L. Schöttl, K. A. Weidenmann, T. Sabiston, K. Inal, and P. Elsner, “Fiber bundle tracking method to analyze sheet molding compound microstructure based on computed tomography images,” *NDT & E International*, vol. 117, p. 102370, 2021.
- [243] L. Schöttl, W. V. Liebig, K. A. Weidenmann, K. Inal, and P. Elsner, “The use of the empirical crack orientation tensor to characterize the damage anisotropy,” *Composites Communications*, vol. 25, p. 100613, 2021.
- [9] J. Görthofer, N. Meyer, T. D. Pallicity, L. Schöttl, A. Trauth, M. Schemmann, M. Hohberg, P. Pinter, P. Elsner, F. Henning, A. Hrymak, T. Seelig, K. A. Weidenmann, L. Kärger, and T. Böhlke, “Virtual process chain of sheet molding compound: Development, validation and perspectives,” *Composites Part B: Engineering*, vol. 169, pp. 133 – 147, 2019.
- [10] J. Görthofer, N. Meyer, T. D. Pallicity, L. Schöttl, A. Trauth, M. Schemmann, M. Hohberg, P. Pinter, P. Elsner, F. Henning, A. Hrymak, T. Seelig, K. A. Weidenmann, L. Kärger, and T. Böhlke, “Motivating the development of a virtual process chain for sheet molding compound composites,” in *Proceedings in Applied Mathematics and Mechanics (PAMM)*, vol. 19, no. 1, Vienna, Austria, 2019, p. e201900124.
- [114] R. Maertens, A. Hees, L. Schöttl, W. Liebig, P. Elsner, and K. A. Weidenmann, “Fiber shortening during injection molding of glass fiber-reinforced phenolic molding compounds: fiber length measurement method development and validation,” *Polymer-Plastics Technology and Materials*, vol. 60, no. 8, pp. 872 – 885, 2021.

- [118] N. Meyer, L. Schöttl, L. Bretz, A. N. Hrymak, and L. Kärger, “Direct Bundle Simulation approach for the compression molding process of Sheet Molding Compound,” *Composites Part A: Applied Science and Manufacturing*, vol. 132, p. 105809, 2020.
- [244] R. Maertens, L. Schöttl, V. W. Liebig, P. Elsner, and K. A. Weidenmann, “Evaluating Material Homogeneity in the Long Fiber Thermoset Injection Molding Process by Image Texture Analysis,” submitted to *Composites Communications*.
- [245] J. Görthofer, N. Meyer, L. Schöttl, A. Trauth, M. Schemmann, P. Pinter, B. Fengler, S. Ilinzeer, M. Hohberg, T. D. Pallicity, L. Kärger, K. A. Weidenmann, P. Elsner, F. Henning, A. Hrymak, and T. Böhlke, “Compression Molding of the Demonstrator Structure,” in *Continuous-Discontinuous Fiber-Reinforced Polymers*. Munich, Germany: Hanser Verlag, 2019, pp. 297 – 314.
- [254] M. Bartkowiak, L. Schöttl, P. Elsner, and K. A. Weidenmann, “Combined In Situ X-Ray Computed Tomography and Acoustic Emission Analysis for Composite Characterization - A Feasibility Study,” in *22nd Symposium on Composites*, ser. Key Engineering Materials, vol. 809. Kaiserslautern, Germany: Trans Tech Publications Ltd., 2019, pp. 604 – 609.



# Supervised student thesis

Below the master's thesis is listed, which was supervised by the author Ludwig Schöttl. The results of this work are marked correspondingly in this doctoral thesis. The master's thesis is additionally listed in the bibliography.

- [248] I. Sönmez, "Detection and characterization of cracks in  $\mu$ CT images of sheet molding compounds (GF-SMC) by means of machine learning methods," Master's thesis (unpublished), Karlsruhe Institute of Technology (KIT), Institute for Applied Materials (IAM-WK), 2020.



# Bibliography

- [1] G. W. Dunnington, *Carl Friedrich Gauss: Titan of science*. New York, USA: Exposition Press, 1955.
- [2] European Union. Reducing CO<sub>2</sub> emissions from passenger cars. Visited on 2020-04-23. [Online]. Available: [www.ec.europa.eu/clima/policies/transport/vehicles/cars\\_en](http://www.ec.europa.eu/clima/policies/transport/vehicles/cars_en)
- [3] A. T. Mayyas, A. R. Mayyas, and M. Omar, “Sustainable lightweight vehicle design: A case study in eco-material selection for body-in-white,” in *Lightweight Composite Structures in Transport*, J. Njuguna, Ed. Duxford, United Kingdom: Woodhead Publishing, 2016, pp. 267 – 302.
- [4] European Union. Greenhouse gas emission statistics - emission inventories. Visited on 2020-06-22. [Online]. Available: [www.ec.europa.eu/eurostat/statistics-explained](http://www.ec.europa.eu/eurostat/statistics-explained)
- [5] R. M. Jones, *Mechanics of composite materials*, 2nd ed. Philadelphia, USA: Taylor & Francis, 1999.
- [6] E. Witten and V. Mathes, “The Market for Glass Fibre Reinforced Plastics (GRP) in 2019,” AVK Industrievereinigung verstärkte Kunststoffe, Tech. Rep., 2019, visited on 2020-07-13. [Online]. Available: [www.avk-tv.de/publications.php](http://www.avk-tv.de/publications.php)
- [7] P. Eyerer, T. Hirth, and P. Elsner, *Polymer Engineering*. Springer Berlin, Heidelberg, 2008.

- [8] S. Carmignato, W. Dewulf, and R. Leach, *Industrial X-Ray Computed Tomography*. Cham, Switzerland: Springer, 2018.
- [9] J. Görthofer, N. Meyer, T. D. Pallicity, L. Schöttl, A. Trauth, M. Schemmann, M. Hohberg, P. Pinter, P. Elsner, F. Henning, A. Hrymak, T. Seelig, K. A. Weidenmann, L. Kärger, and T. Böhlke, “Virtual process chain of sheet molding compound: Development, validation and perspectives,” *Composites Part B: Engineering*, vol. 169, pp. 133 – 147, 2019.
- [10] J. Görthofer, N. Meyer, T. D. Pallicity, L. Schöttl, A. Trauth, M. Schemmann, M. Hohberg, P. Pinter, P. Elsner, F. Henning, A. Hrymak, T. Seelig, K. A. Weidenmann, L. Kärger, and T. Böhlke, “Motivating the development of a virtual process chain for sheet molding compound composites,” in *Proceedings in Applied Mathematics and Mechanics (PAMM)*, vol. 19, no. 1, Vienna, Austria, 2019, p. e201900124.
- [11] W. Voigt, “Ueber die Beziehung zwischen den beiden Elasticitätsconstanten isotroper Körper,” *Annalen der Physik*, vol. 274, no. 12, pp. 573 – 587, 1889.
- [12] A. Reuss, “Berechnung der Fließgrenze von Mischkristallen auf Grund der Plastizitätsbedingung für Einkristalle,” *ZAMM - Journal of Applied Mathematics and Mechanics / Zeitschrift für Angewandte Mathematik und Mechanik*, vol. 9, no. 1, pp. 49 – 58, 1929.
- [13] T. Mori and K. Tanaka, “Average stress in matrix and average elastic energy of materials with misfitting inclusions,” *Acta Metallurgica*, vol. 21, no. 5, pp. 571 – 574, 1973.
- [14] J. D. Eshelby and R. E. Peierls, “The determination of the elastic field of an ellipsoidal inclusion, and related problems,” *Proceedings of the*



- Royal Society of London. Series A. Mathematical and Physical Sciences*, vol. 241, no. 1226, pp. 376 – 396, 1957.
- [15] J. D. Eshelby and R. E. Peierls, “The elastic field outside an ellipsoidal inclusion,” *Proceedings of the Royal Society of London. Series A. Mathematical and Physical Sciences*, vol. 252, no. 1271, pp. 561 – 569, 1959.
- [16] A. Zaoui, “Continuum Micromechanics: Survey,” *Journal of Engineering Mechanics*, vol. 128, no. 8, pp. 808 – 816, 2002.
- [17] R. Hill, “Elastic properties of reinforced solids: Some theoretical principles,” *Journal of the Mechanics and Physics of Solids*, vol. 11, no. 5, pp. 357 – 372, 1963.
- [18] R. Hill, “A self-consistent mechanics of composite materials,” *Journal of the Mechanics and Physics of Solids*, vol. 13, no. 4, pp. 213 – 222, 1965.
- [19] Z. Hashin and S. Shtrikman, “On some variational principles in anisotropic and nonhomogeneous elasticity,” *Journal of the Mechanics and Physics of Solids*, vol. 10, no. 4, pp. 335 – 342, 1962.
- [20] P. Kanouté, D. P. Boso, J. L. Chaboche, and B. A. Schrefler, “Multiscale Methods for Composites: A Review,” *Archives of Computational Methods in Engineering*, vol. 16, pp. 31 – 75, 2009.
- [21] M. Schemmann, J. Görthofer, T. Seelig, A. Hrymak, and T. Böhlke, “Anisotropic meanfield modeling of debonding and matrix damage in SMC composites,” *Composites Science and Technology*, vol. 161, pp. 143 – 158, 2018.
- [22] M. Schemmann, “Biaxial Characterization and Mean-field Based Damage Modeling of Sheet Molding Compound Composites,”

- Dissertation, Karlsruhe Institute of Technology (KIT), Karlsruhe, Germany, 2018.
- [23] L. Kehler, J. T. Wood, and T. Böhlke, “Mean-field homogenization of thermoelastic material properties of a long fiber-reinforced thermoset and experimental investigation,” *Journal of Composite Materials*, vol. 54, no. 25, pp. 3777 – 3799, 2020.
- [24] M. L. Kehler, “Thermomechanical Mean-Field Modeling and Experimental Characterization of Long Fiber-Reinforced Sheet Molding Compound Composites,” Dissertation, Karlsruhe Institute of Technology (KIT), Karlsruhe, Germany, 2019.
- [25] K. L. Goh, *Discontinuous-Fibre Reinforced Composites: Fundamentals of Stress Transfer and Fracture Mechanics*, ser. Engineering Materials and Processes. Springer London, 2017.
- [26] A. Puck and H. Schürmann, “Failure analysis of FRP laminates by means of physically based phenomenological models,” in *Failure Criteria in Fibre-Reinforced-Polymer Composites*, M. J. Hinton, A. S. Kaddour, and P. D. Soden, Eds. Amsterdam, Netherlands: Elsevier, 2004, pp. 264 – 297.
- [27] E. S. Greenhalgh, *Failure analysis and fractography of polymer composites*. Cambridge, United Kingdom: Woodhead Publishing, 2009.
- [28] R. Talreja and C. V. Singh, *Damage and Failure of Composite Materials*. Cambridge, United Kingdom: Cambridge University Press, 2012.
- [29] R. von Mises, “Mechanik der plastischen Formänderung von Kristallen,” *ZAMM - Journal of Applied Mathematics and Mechanics / Zeitschrift für Angewandte Mathematik und Mechanik*, vol. 8, no. 3, pp. 161 – 185, 1928.

- 
- [30] E. K. Ashkenazi, "Problems of the anisotropy of strength," *Mekhanika Polimerov*, vol. 1, no. 2, pp. 79 – 92, 1965.
- [31] V. D. Azzi and S. W. Tsai, "Anisotropic strength of composites," *Experimental Mechanics*, vol. 5, no. 9, pp. 283 – 288, 1965.
- [32] S. W. Tsai and E. M. Wu, "A General Theory of Strength for Anisotropic Materials," *Journal of Composite Materials*, vol. 5, no. 1, pp. 58 – 80, 1971.
- [33] Z. Hashin, "Failure Criteria for Unidirectional Fiber Composites," *Journal of Applied Mechanics*, vol. 47, no. 2, pp. 329 – 334, 1980.
- [34] H. Mughrabi, "Assessment of Fatigue Damage on the Basis of Nonlinear Compliance Effects," in *Handbook of Materials Behavior Models*, J. Lemaitre, Ed. San Diego, USA: Academic Press, 2001, pp. 622 – 632.
- [35] R. Talreja and W. Watt, "Fatigue of composite materials: damage mechanisms and fatigue-life diagrams," *Proceedings of the Royal Society of London. A. Mathematical and Physical Sciences*, vol. 378, no. 1775, pp. 461 – 475, 1981.
- [36] R. Talreja, "Damage and fatigue in composites – A personal account," *Composites Science and Technology*, vol. 68, no. 13, pp. 2585 – 2591, 2008.
- [37] P. T. Curtis, "An investigation of the tensile fatigue behaviour of improved carbon fibre composite materials," in *Proceedings of 6th international conference on composite materials (ICCM-6)*, London, England, 1987, pp. 454 – 464.
- [38] K. L. Reifsnider, K. Schulte, and J. C. Duke, "Long-Term Fatigue Behavior of Composite Materials," in *Long-Term Behavior of*

- Composites*, T. K. O'Brien, Ed. Philadelphia, USA: ASTM International, 1983, pp. 136 – 159.
- [39] H. T. Hahn and R. Y. Kim, "Fatigue Behavior of Composite Laminate," *Journal of Composite Materials*, vol. 10, no. 2, pp. 156 – 180, 1976.
- [40] K. Friedrich, K. Schulte, G. Horstenkamp, and T. W. Chou, "Fatigue behaviour of aligned short carbon-fibre reinforced polyimide and polyethersulphone composites," *Journal of Materials Science*, vol. 20, no. 9, pp. 3353 – 3364, 1985.
- [41] K. Schulte, "Damage Development Under Cyclic Loading," in *Proceedings of the European Symposium on Damage Development and Failure Process in Composites Materials*, Leuven, Belgium, 1987, pp. 39 – 54.
- [42] W. W. Stinchcomb, "Nondestructive evaluation of damage accumulation processes in composite laminates," *Composites Science and Technology*, vol. 25, no. 2, pp. 103 – 118, 1986.
- [43] H. Mao and S. Mahadevan, "Fatigue damage modelling of composite materials," *Composite Structures*, vol. 58, no. 4, pp. 405 – 410, 2002.
- [44] H. L. Cox, "The elasticity and strength of paper and other fibrous materials," *British Journal of Applied Physics*, vol. 3, no. 3, pp. 72 – 79, 1952.
- [45] A. H. Cottrell, J. D. Bernal, C. E. H. Bawn, and F. C. Frank, "Strong solids," *Proceedings of the Royal Society of London. Series A. Mathematical and Physical Sciences*, vol. 282, no. 1388, pp. 2 – 9, 1964.
- [46] A. Kelly and W. R. Tyson, "Tensile properties of fibre-reinforced metals: Copper/tungsten and copper/molybdenum," *Journal of the Mechanics and Physics of Solids*, vol. 13, no. 6, pp. 329 – 350, 1965.

- 
- [47] G. A. Cooper, "The structure and mechanical properties of composite materials," *Reviews of Physics in Technology*, vol. 2, no. 2, pp. 49 – 91, 1971.
- [48] D. Hull and T. W. Clyne, "Fibres and matrices," in *An Introduction to Composite Materials*, 2nd ed., ser. Cambridge Solid State Science Series. Cambridge, United Kingdom: Cambridge University Press, 1996, pp. 9 – 38.
- [49] M. Kachanov, "Continuum Model of Medium with Cracks," *Journal of the Engineering Mechanics Division*, vol. 106, no. 5, pp. 1039 – 1051, 1980.
- [50] M. Kachanov, "Effective Elastic Properties of Cracked Solids: Critical Review of Some Basic Concepts," *Applied Mechanics Reviews*, vol. 45, no. 8, pp. 304 – 335, 1992.
- [51] M. Kachanov, "Elastic Solids with Many Cracks and Related Problems," in *Advances in Applied Mechanics*. Elsevier, 1993, vol. 30, pp. 259 – 445.
- [52] M. Kachanov, *Micromechanics of Materials, with Applications*, ser. Solid Mechanics and Its Applications, I. Sevostianov, Ed. Cham, Switzerland: Springer, 2018.
- [53] V. A. Lubarda and D. Krajcinovic, "Damage tensors and the crack density distribution," *International Journal of Solids and Structures*, vol. 30, no. 20, pp. 2859 – 2877, 1993.
- [54] D. K. Hallbauer, H. Wagner, and N. G. W. Cook, "Some observations concerning the microscopic and mechanical behaviour of quartzite specimens in stiff, triaxial compression tests," *International Journal of Rock Mechanics and Mining Sciences & Geomechanics Abstracts*, vol. 10, no. 6, pp. 713 – 726, 1973.

- [55] G. N. Hounsfield, "Computerized transverse axial scanning (tomography): Part 1. Description of system," *The British Journal of Radiology*, vol. 46, no. 552, pp. 1016 – 1022, 1973.
- [56] Nobelprize.org. The Nobel Prize in Physiology or Medicine 1979. Visited on 2020-09-21. [Online]. Available: [www.nobelprize.org/prizes/medicine/1979/](http://www.nobelprize.org/prizes/medicine/1979/)
- [57] D. F. Swinehart, "The Beer-Lambert Law," *Journal of Chemical Education*, vol. 39, no. 7, pp. 333 – 335, 1996.
- [58] T. M. Buzug, *Computed Tomography: From Photon Statistics to Modern Cone-Beam CT*. Springer Berlin, Heidelberg, 2010.
- [59] I. M. Low, *Polymer Composites and Nanocomposites for X-Rays Shielding*, ser. Composites Science and Technology, N. Z. N. Azman, Ed. Springer Singapore, 2020.
- [60] I. Han, L. Demir, and M. Şahin, "Determination of mass attenuation coefficients, effective atomic and electron numbers for some natural minerals," *Radiation Physics and Chemistry*, vol. 78, no. 9, pp. 760 – 764, 2009.
- [61] J. H. Hubbell and S. M. Seltzer, "Tables of x-ray mass attenuation coefficients and mass energy-absorption coefficients 1 keV to 20 MeV for elements  $z = 1$  to 92 and 48 additional substances of dosimetric interest," *National Institute of Standards and Technology*, 1995.
- [62] G. T. Herman and S. Sameer, Eds., *Fundamentals of Computerized Tomography : Image Reconstruction from Projections*, 2nd ed., ser. Advances in Pattern Recognition. Springer London, 2009.
- [63] L. A. Feldkamp, L. C. Davis, and J. W. Kress, "Practical cone-beam algorithm," *Journal of the Optical Society of America*, vol. 1, no. 6, pp. 612 – 619, 1984.

- 
- [64] L. L. Geyer, U. J. Schoepf, F. G. Meinel, J. W. Nance, G. Bastarrika, J. A. Leipsic, N. S. Paul, M. Rengo, A. Laghi, and C. N. De Cecco, "State of the Art: Iterative CT Reconstruction Techniques," *Radiology*, vol. 276, no. 2, pp. 339 – 357, 2015.
- [65] S. C. Garcea, Y. Wang, and P. J. Withers, "X-ray computed tomography of polymer composites," *Composites Science and Technology*, vol. 156, pp. 305 – 319, 2018.
- [66] C. T. Herakovich, J. Aboudi, S. W. Lee, and E. A. Strauss, "Damage in composite laminates: Effects of transverse cracks," *Mechanics of Materials*, vol. 7, no. 2, pp. 91 – 107, 1988.
- [67] C. T. Sun and K. C. Jen, "On the Effect of Matrix Cracks on Laminate Strength," *Journal of Reinforced Plastics and Composites*, vol. 6, no. 3, pp. 208 – 222, 1987.
- [68] J. A. Nairn, "The Strain Energy Release Rate of Composite Microcracking: A Variational Approach," *Journal of Composite Materials*, vol. 23, no. 11, pp. 1106 – 1129, 1989.
- [69] J.-W. Lee and I. M. Daniel, "Progressive Transverse Cracking of Crossply Composite Laminates," *Journal of Composite Materials*, vol. 24, no. 11, pp. 1225 – 1243, 1990.
- [70] G. C. Sih, E. P. Chen, S. L. Huang, and E. J. Mcquillen, "Material Characterization on the Fracture of Filament-Reinforced Composites," *Journal of Composite Materials*, vol. 9, no. 2, pp. 167 – 186, 1975.
- [71] F. Sket, A. Enfedaque, C. Alton, C. González, J. M. Molina-Aldareguia, and J. Llorca, "Automatic quantification of matrix cracking and fiber rotation by X-ray computed tomography in shear-deformed carbon fiber-reinforced laminates," *Composites Science and Technology*, vol. 90, pp. 129 – 138, 2014.

- [72] B. Yu, R. S. Bradley, C. Soutis, and P. J. Withers, “A comparison of different approaches for imaging cracks in composites by X-ray microtomography,” *Philosophical Transactions of the Royal Society A: Mathematical, Physical and Engineering Sciences*, vol. 374, no. 2071, p. 20160037, 2016.
- [73] P. J. Schilling, B. R. Karedla, A. K. Tatiparthi, M. A. Verges, and P. D. Herrington, “X-ray computed microtomography of internal damage in fiber reinforced polymer matrix composites,” *Composites Science and Technology*, vol. 65, no. 14, pp. 2071 – 2078, 2005.
- [74] W. Hufenbach, R. Böhm, M. Gude, M. Berthel, A. Hornig, S. Rucevskis, and M. Andrich, “A test device for damage characterisation of composites based on in situ computed tomography,” *Composites Science and Technology*, vol. 72, no. 12, pp. 1361 – 1367, 2012.
- [75] B. Yu, R. S. Bradley, C. Soutis, P. J. Hogg, and P. J. Withers, “2D and 3D imaging of fatigue failure mechanisms of 3D woven composites,” *Composites Part A: Applied Science and Manufacturing*, vol. 77, pp. 37 – 49, 2015.
- [76] B. Yu, R. Blanc, C. Soutis, and P. J. Withers, “Evolution of damage during the fatigue of 3D woven glass-fibre reinforced composites subjected to tension-tension loading observed by time-lapse X-ray tomography,” *Composites Part A: Applied Science and Manufacturing*, vol. 82, pp. 279 – 290, 2016.
- [77] R. Böhm, J. Stiller, T. Behnisch, M. Zscheyge, R. Protz, S. Radloff, M. Gude, and W. Hufenbach, “A quantitative comparison of the capabilities of in situ computed tomography and conventional computed tomography for damage analysis of composites,” *Composites Science and Technology*, vol. 110, pp. 62 – 68, 2015.



- 
- [78] P. Wright, X. Fu, I. Sinclair, and S. M. Spearing, “Ultra High Resolution Computed Tomography of Damage in Notched Carbon Fiber-Epoxy Composites,” *Journal of Composite Materials*, vol. 42, no. 19, pp. 1993 – 2002, 2008.
- [79] T. Hirano, K. Usami, Y. Tanaka, and C. Masuda, “In situ x-ray CT under tensile loading using synchrotron radiation,” *Journal of Materials Research*, vol. 10, no. 2, pp. 381 – 386, 1995.
- [80] A. E. Scott, M. Mavrogordato, P. Wright, I. Sinclair, and S. M. Spearing, “In situ fibre fracture measurement in carbon–epoxy laminates using high resolution computed tomography,” *Composites Science and Technology*, vol. 71, no. 12, pp. 1471 – 1477, 2011.
- [81] Z. Li, L. Guo, L. Zhang, and Q. Wang, “In situ experimental investigation on the out-plane damage evolution of 3D woven carbon-fiber reinforced composites,” *Composites Science and Technology*, vol. 162, pp. 101 – 109, 2018.
- [82] K. Wang, S. Pei, Y. Li, J. Li, D. Zeng, X. Su, X. Xiao, and N. Chen, “In-situ 3D fracture propagation of short carbon fiber reinforced polymer composites,” *Composites Science and Technology*, vol. 182, p. 107788, 2019.
- [83] F. Cosmi and A. Bernasconi, “Micro-CT investigation on fatigue damage evolution in short fibre reinforced polymers,” *Composites Science and Technology*, vol. 79, pp. 70 – 76, 2013.
- [84] S. C. Garcea, M. N. Mavrogordato, A. E. Scott, I. Sinclair, and S. M. Spearing, “Fatigue micromechanism characterisation in carbon fibre reinforced polymers using synchrotron radiation computed tomography,” *Composites Science and Technology*, vol. 99, pp. 23 – 30, 2014.

- [85] S. C. Garcea, I. Sinclair, and S. M. Spearing, “In situ synchrotron tomographic evaluation of the effect of toughening strategies on fatigue micromechanisms in carbon fibre reinforced polymers,” *Composites Science and Technology*, vol. 109, pp. 32 – 39, 2015.
- [86] S. C. Garcea, I. Sinclair, and S. M. Spearing, “Fibre failure assessment in carbon fibre reinforced polymers under fatigue loading by synchrotron X-ray computed tomography,” *Composites Science and Technology*, vol. 133, pp. 157 – 164, 2016.
- [87] S. C. Garcea, I. Sinclair, S. M. Spearing, and P. J. Withers, “Mapping fibre failure in situ in carbon fibre reinforced polymers by fast synchrotron X-ray computed tomography,” *Composites Science and Technology*, vol. 149, pp. 81 – 89, 2017.
- [88] N. Otsu, “A threshold selection method from gray-level histograms,” in *IEEE Transactions on Systems, Man, and Cybernetics*, vol. 9, no. 1, 1979, pp. 62 – 66.
- [89] T. Kurita, N. Otsu, and N. Abdelmalek, “Maximum likelihood thresholding based on population mixture models,” *Pattern Recognition*, vol. 25, no. 10, pp. 1231 – 1240, 1992.
- [90] P. Pinter, “Microstructure Characterization of Continuous-Discontinuous Fibre Reinforced Polymers based on Volumetric Images,” Dissertation, Karlsruhe Institute of Technology (KIT), Karlsruhe, Germany, 2018.
- [91] P. Pinter, K. A. Weidenmann, and P. Elsner, “Microstructure Characterization,” in *Continuous-Discontinuous Fiber-Reinforced Polymers*. Munich, Germany: Hanser Verlag, 2019, pp. 119 – 134.
- [92] W.-H. Tsai, “Moment-preserving Thresholding: A New Approach,” *Computer Vision, Graphics and Image Processing*, vol. 29, pp. 377 – 393, 1985.

- 
- [93] A. R. Jac Fredo, R. S. Abilash, and C. Suresh Kumar, "Segmentation and analysis of damages in composite images using multi-level threshold methods and geometrical features," *Measurement*, vol. 100, pp. 270 – 278, 2017.
- [94] J. D. Nielsen, K. H. Madsen, O. Puonti, H. R. Siebner, C. Bauer, C. G. Madsen, G. B. Saturnino, and A. Thielscher, "Automatic skull segmentation from MR images for realistic volume conductor models of the head: Assessment of the state-of-the-art," *NeuroImage*, vol. 174, pp. 587 – 598, 2018.
- [95] J. Huo, J. Wu, J. Cao, and G. Wang, "Supervoxel based method for multi-atlas segmentation of brain MR images," *NeuroImage*, vol. 175, pp. 201 – 214, 2018.
- [96] R. Adams and L. Bischof, "Seeded region growing," *IEEE Transactions on Pattern Analysis and Machine Intelligence*, vol. 16, no. 6, pp. 641 – 647, 1994.
- [97] R. M. Haralick, S. R. Sternberg, and X. Zhuang, "Image Analysis Using Mathematical Morphology," *IEEE Transactions on Pattern Analysis and Machine Intelligence*, vol. 9, no. 4, pp. 532 – 550, 1987.
- [98] S. Chen and R. M. Haralick, "Recursive erosion, dilation, opening, and closing transforms," *IEEE Transactions on Image Processing*, vol. 4, no. 3, pp. 335 – 345, 1995.
- [99] S. G. Advani and C. L. Tucker, "The Use of Tensors to Describe and Predict Fiber Orientation in Short Fiber Composites," *Journal of Rheology*, vol. 31, no. 8, pp. 751 – 784, 1987.
- [100] M. Gupta and K. K. Wang, "Fiber orientation and mechanical properties of short-fiber-reinforced injection-molded composites: Simulated and experimental results," *Polymer Composites*, vol. 14, no. 5, pp. 367 – 382, 1993.

- [101] K. Ken-Ichi, "Distribution of directional Data and fabric Tensor," *International Journal of Engineering Science*, vol. 22, no. 2, pp. 149 – 164, 1984.
- [102] H.-T. Kau, "Determination of the orientation of short glass fibers in sheet molding compound (SMC)," *Polymer Composites*, vol. 8, no. 2, pp. 82 – 93, 1987.
- [103] W. C. Jackson, S. G. Advani, and C. L. Tucker, "Predicting the Orientation of Short Fibers in Thin Compression Moldings," *Journal of Composite Materials*, vol. 20, no. 6, pp. 539 – 557, 1986.
- [104] F. Folgar and C. L. Tucker, "Orientation Behavior of Fibers in Concentrated Suspensions," *Journal of Reinforced Plastics and Composites*, vol. 3, no. 2, pp. 98 – 119, 1984.
- [105] R. C. Givler, M. J. Crochet, and R. B. Pipes, "Numerical Prediction of Fiber Orientation in Dilute Suspensions," *Journal of Composite Materials*, vol. 17, no. 4, pp. 330 – 343, 1983.
- [106] K. Schladitz, A. Bueter, M. Godehardt, O. Wirjadi, J. Fleckenstein, T. Gerster, U. Hassler, K. Jaschek, M. Maisl, U. Maisl, S. Mohr, U. Netzelmann, T. Potyra, and M. O. Steinhauser, "Non-destructive characterization of fiber orientation in reinforced SMC as input for simulation based design," *Composite Structures*, vol. 160, pp. 195 – 203, 2017.
- [107] P. Pinter, S. Dietrich, B. Bertram, L. Kehler, P. Elsner, and K. A. Weidenmann, "Comparison and error estimation of 3D fibre orientation analysis of computed tomography image data for fibre reinforced composites," *NDT & E International*, vol. 95, pp. 26 – 35, 2018.
- [108] M. Krause, J. M. Hausherr, B. Burgeth, C. Herrmann, and W. Krenkel, "Determination of the fibre orientation in composites using the

- structure tensor and local X-ray transform,” *Journal of Materials Science*, vol. 45, no. 4, pp. 888 – 896, 2009.
- [109] C. Hanneschläger, V. Revol, B. Plank, D. Salaberger, and J. Kastner, “Fibre structure characterisation of injection moulded short fibre-reinforced polymers by X-ray scatter dark field tomography,” *Case Studies in Nondestructive Testing and Evaluation*, vol. 3, pp. 34 – 41, 2015.
- [110] P. Pinter, B. Bertram, and K. A. Weidenmann, “A Novel Method for the Determination of Fibre Length Distributions from  $\mu$ CT-data,” in *6th Conference on Industrial Computed Tomography*, Wels, Austria, 2016, pp. 1 – 8.
- [111] P. A. Hessman, T. Riedel, F. Welschinger, K. Hornberger, and T. Böhlke, “Microstructural analysis of short glass fiber reinforced thermoplastics based on x-ray micro-computed tomography,” *Composites Science and Technology*, vol. 183, p. 107752, 2019.
- [112] J. Kastner, C. Heinzl, B. Plank, D. Salaberger, C. Gusenbauer, and S. Senck, “New X-ray computed tomography methods for research and industry,” in *7th Conference on Industrial Computed Tomography*, Leuven, Belgium, 2017, pp. 1 – 10.
- [113] D. Salaberger, M. Jerabek, T. Koch, and J. Kastner, “Consideration of Accuracy of Quantitative X-Ray CT Analyses for Short-Glass-Fibre-Reinforced Polymers,” in *20th Symposium on Composites*, ser. Materials Science Forum, vol. 825. Vienna, Austria: Trans Tech Publications Ltd., 2015, pp. 907 – 913.
- [114] R. Maertens, A. Hees, L. Schöttl, W. Liebig, P. Elsner, and K. A. Weidenmann, “Fiber shortening during injection molding of glass fiber-reinforced phenolic molding compounds: fiber length

- measurement method development and validation,” *Polymer-Plastics Technology and Materials*, vol. 60, no. 8, pp. 872 – 885, 2021.
- [115] R. Gloeckner, S. Kolling, and C. Heiliger, “A Monte-Carlo Algorithm for 3D Fibre Detection from Microcomputer Tomography,” *Journal of Computational Engineering*, vol. 2016, pp. 1 – 9, 2016.
- [116] M. Teßmann, S. Mohr, S. Gayetskyy, U. Haßler, R. Hanke, and G. Greiner, “Automatic Determination of Fiber-Length Distribution in Composite Material Using 3D CT Data,” *EURASIP Journal on Advances in Signal Processing*, vol. 2010, no. 1, p. 545030, 2010.
- [117] D. Salaberger, K. A. Kannappan, J. Kastner, J. Reussner, and T. Auinger, “Evaluation of computed tomography data from fibre reinforced polymers to determine fibre length distribution,” *International Polymer Processing*, vol. 26, pp. 283 – 291, 2011.
- [118] N. Meyer, L. Schöttl, L. Bretz, A. N. Hrymak, and L. Kärger, “Direct Bundle Simulation approach for the compression molding process of Sheet Molding Compound,” *Composites Part A: Applied Science and Manufacturing*, vol. 132, p. 105809, 2020.
- [119] O. Guiraud, L. Orgéas, P. J. J. Dumont, and S. Rolland du Roscoat, “Microstructure and deformation micromechanisms of concentrated fiber bundle suspensions: An analysis combining x-ray microtomography and pull-out tests,” *Journal of Rheology*, vol. 56, no. 3, pp. 593 – 623, 2012.
- [120] T. H. Le, P. J. J. Dumont, L. Orgéas, D. Favier, L. Salvo, and E. Boller, “X-ray phase contrast microtomography for the analysis of the fibrous microstructure of SMC composites,” *Composites Part A: Applied Science and Manufacturing*, vol. 39, no. 1, pp. 91 – 103, 2008.
- [121] P. J. J. Dumont, J. P. V. L. Orgéas, V. Michaud, D. Favier, and J. A. E. Manson, “Processing, characterisation and rheology of transparent

- concentrated fibre-bundle suspensions,” *Rheologica Acta*, vol. 46, no. 5, pp. 639 – 651, 2007.
- [122] S. Mori and P. C. M. van Zijl, “Fiber tracking: principles and strategies – a technical review,” *NMR in Biomedicine*, vol. 15, pp. 468 – 480, 2002.
- [123] J.-D. Tournier, F. Calamante, and A. Connelly, “Improved probabilistic streamlines tractography by 2nd order integration over fibre orientation distributions,” in *Proceeding of the International Society for Magnetic Resonance in Medicine 18*, Stockholm, Sweden, 2010, p. 1670.
- [124] J.-D. Tournier, F. Calamante, and A. Connelly, “MRtrix: Diffusion tractography in crossing fiber regions,” *International Journal of Imaging Systems and Technology*, vol. 22, no. 1, pp. 53 – 66, 2012.
- [125] Y. Song, U. Gandhi, C. Pérez, T. Osswald, S. Vallury, and A. Yang, “Method to account for the fiber orientation of the initial charge on the fiber orientation of finished part in compression molding simulation,” *Composites Part A: Applied Science and Manufacturing*, vol. 100, pp. 244 – 254, 2017.
- [126] P. J. Basser, S. Pajevic, C. Pierpaoli, J. Duda, and A. Aldroubi, “In vivo fiber tractography using DT-MRI data,” *Magnetic Resonance in Medicine*, vol. 44, no. 4, pp. 625 – 632, 2000.
- [127] S. Mori, B. J. Crain, V. P. Chacko, and P. C. M. Van Zijl, “Three-dimensional tracking of axonal projections in the brain by magnetic resonance imaging,” *Annals of Neurology*, vol. 45, no. 2, pp. 265 – 269, 1999.
- [128] A. Bhattacharya, C. Heinzl, A. Amirkhanov, J. Kastner, and R. Wenger, “MetaTracts - A method for robust extraction and visualization of carbon fiber bundles in fiber reinforced composites,” in *IEEE Pacific*

- Visualization Symposium (PacificVis)*, Hangzhou, China, 2015, pp. 191 – 198.
- [129] I. Straumit, S. V. Lomov, and M. Wevers, “Quantification of the internal structure and automatic generation of voxel models of textile composites from X-ray computed tomography data,” *Composites Part A: Applied Science and Manufacturing*, vol. 69, pp. 150 – 158, 2015.
- [130] Fraunhofer SCAI. MpCCI – Multiphysics Interfaces. Visited on 2021-04-21. [Online]. Available: [www.mpcci.de](http://www.mpcci.de)
- [131] L. Schöttl, D. Dörr, P. Pinter, K. A. Weidenmann, P. Elsner, and L. Kärger, “A novel approach for segmenting and mapping of local fiber orientation of continuous fiber-reinforced composite laminates based on volumetric images,” *NDT & E International*, vol. 110, p. 102194, 2020.
- [132] D. Dörr, “Simulation of the thermoforming process of UD fiber-reinforced thermoplastic tape laminates,” Dissertation, Karlsruher Institut für Technologie (KIT), Karlsruhe, Germany, 2019.
- [133] B. K. Bay, T. S. Smith, D. P. Fyhrie, and M. Saad, “Digital volume correlation: Three-dimensional strain mapping using X-ray tomography,” *Experimental Mechanics*, vol. 39, no. 3, pp. 217 – 226, 1999.
- [134] B. K. Bay, “Methods and applications of digital volume correlation,” *The Journal of Strain Analysis for Engineering Design*, vol. 43, no. 8, pp. 745 – 760, 2008.
- [135] A. Moussawi, J. Xu, H. Nouri, S. Guessasma, and G. Lubineau, “Volume digital image correlation to assess displacement field in compression loaded bread crumb under X-ray microtomography,” *Innovative Food Science & Emerging Technologies*, vol. 25, pp. 78 – 87, 2014.



- 
- [136] E. Verhulp, B. Rietbergen, and R. Huiskes, “A three-dimensional digital image correlation technique for strain measurements in microstructures,” *Journal of Biomechanics*, vol. 37, no. 9, pp. 1313 – 1320, 2004.
- [137] N. Lenoir, M. Bornert, J. Desrues, P. Bésuelle, and G. Viggiani, “Volumetric Digital Image Correlation Applied to X-ray Microtomography Images from Triaxial Compression Tests on Argillaceous Rock,” *Strain*, vol. 43, no. 3, pp. 193 – 205, 2007.
- [138] A. Germaneau, P. Doumalin, and J.-C. Dupré, “Comparison between X-ray micro-computed tomography and optical scanning tomography for full 3D strain measurement by digital volume correlation,” *NDT & E International*, vol. 41, no. 6, pp. 407 – 415, 2008.
- [139] M. A. Sutton, W. J. Wolters, W. H. Peters, W. F. Ranson, and S. R. McNeill, “Determination of displacements using an improved digital correlation method,” *Image and Vision Computing*, vol. 1, no. 3, pp. 133 – 139, 1983.
- [140] M. A. Sutton, M. Cheng, W. H. Peters, Y. J. Chao, and S. R. McNeill, “Application of an optimized digital correlation method to planar deformation analysis,” *Image and Vision Computing*, vol. 4, no. 3, pp. 143 – 150, 1986.
- [141] M. A. Sutton, J.-J. Orteu, and H. W. Schreier, *Image Correlation for Shape, Motion and Deformation Measurements: Basic Concepts, Theory and Applications*. Springer New York, 2009.
- [142] M. A. Sutton, “Computer Vision-Based, Noncontacting Deformation Measurements in Mechanics: A Generational Transformation,” *Applied Mechanics Reviews*, vol. 65, no. 5, pp. 050 802 01 – 050 802 23, 2013.
- [143] E. Maire and P. J. Withers, “Quantitative X-ray tomography,” *International Materials Reviews*, vol. 59, no. 1, pp. 1 – 43, 2014.

- [144] S. Klein, M. Staring, K. Murphy, M. A. Viergever, and J. P. W. Pluim, “elastix: A Toolbox for Intensity-Based Medical Image Registration,” in *IEEE Transactions on Medical Imaging*, vol. 29, no. 1, 2010, pp. 196 – 205.
- [145] D. Shamonin, E. Bron, B. Lelieveldt, M. Smits, S. Klein, and M. Staring, “Fast Parallel Image Registration on CPU and GPU for Diagnostic Classification of Alzheimer’s Disease,” *Frontiers in Neuroinformatics*, vol. 7, p. 50, 2014.
- [146] Amira-Avizo. Digital Volume Correlation (DVC). Visited on 2021-04-21. [Online]. Available: [www.thermofisher.com/de/de/home/electron-microscopy/products/software-em-3d-vis/3d-visualization-analysis-software/digital-volume-correlation](http://www.thermofisher.com/de/de/home/electron-microscopy/products/software-em-3d-vis/3d-visualization-analysis-software/digital-volume-correlation)
- [147] LaVision. Digital Volume Correlation (DVC). Visited on 2021-04-21. [Online]. Available: [www.lavision.de/en/techniques/dic-dvc](http://www.lavision.de/en/techniques/dic-dvc)
- [148] Volume Graphics. VGSTUDIO MAX Add-on Modules for Material Analyses. Visited on 2021-04-21. [Online]. Available: [www.volumegraphics.com](http://www.volumegraphics.com)
- [149] S. Roux, F. Hild, P. Viot, and D. Bernard, “Three-dimensional image correlation from X-ray computed tomography of solid foam,” *Composites Part A: Applied Science and Manufacturing*, vol. 39, no. 8, pp. 1253 – 1265, 2008.
- [150] J. Réthoré, J.-P. Tinnes, S. Roux, J.-Y. Buffière, and F. Hild, “Extended three-dimensional digital image correlation (X3D-DIC),” *Comptes Rendus Mécanique*, vol. 336, no. 8, pp. 643 – 649, 2008.
- [151] N. Limodin, J. Réthoré, J.-Y. Buffière, F. Hild, S. Roux, W. Ludwig, J. Rannou, and A. Gravouil, “Influence of closure on the 3D

- propagation of fatigue cracks in a nodular cast iron investigated by X-ray tomography and 3D volume correlation,” *Acta Materialia*, vol. 58, no. 8, pp. 2957 – 2967, 2010.
- [152] J. Réthoré, N. Limodin, J.-Y. Buffière, F. Hild, W. Ludwig, and S. Roux, “Digital volume correlation analyses of synchrotron tomographic images,” *The Journal of Strain Analysis for Engineering Design*, vol. 46, no. 7, pp. 683 – 695, 2011.
- [153] A. M. Turing, “Computing Machinery and Intelligence,” *Mind*, vol. 59, no. 236, pp. 433 – 460, 1950.
- [154] W. S. McCulloch and W. Pitts, “A logical calculus of the ideas immanent in nervous activity,” *The bulletin of mathematical biophysics*, vol. 5, no. 4, pp. 115 – 133, 1943.
- [155] D. O. Hebb, *The Organization of Behavior: A Neuropsychological Theory*. New York, USA: John Wiley Ed., 1949.
- [156] J. McCarthy, M. L. Minsky, N. Rochester, and C. E. Shannon, “A Proposal for the Dartmouth Summer Research Project on Artificial Intelligence, August 31, 1955,” *AI Magazine*, vol. 27, no. 4, pp. 12 – 14, 2006.
- [157] P. Hamet and J. Tremblay, “Artificial intelligence in medicine,” *Metabolism*, vol. 69, pp. 36 – 40, 2017.
- [158] R. Abduljabbar, H. Dia, S. Liyanage, and S. A. Bagloee, “Applications of Artificial Intelligence in Transport: An Overview,” *Sustainability*, vol. 11, no. 189, pp. 1 – 24, 2019.
- [159] M. Chui, J. Manyika, M. Miremadi, N. Henke, R. Chung, P. Nel, and S. Malhotra, “Notes from the AI Frontier. Insights from Hundreds of Use Cases,” McKinsey Global Institute, Tech. Rep., 2018, visited on 2020-07-01. [Online]. Available: [www.mckinsey.com/~/media/mckins](http://www.mckinsey.com/~/media/mckins)

ey/featuredinsights/artificialintelligence/notesfromtheaifrontierapplicationsandvalueofdeeplearning/notes-from-the-ai-frontier-insights-from-hundreds-of-use-cases-discussion-paper.ashx

- [160] F. Chollet, *Deep Learning with Python*. Manning Publications, 2018.
- [161] S. Samarasinghe, *Neural networks for applied sciences and engineering: from fundamentals to complex pattern recognition*. Boca Raton, USA: Auerbach Publ., 2007.
- [162] J. Moolayil, *Learn Keras for Deep Neural Networks : A Fast-Track Approach to Modern Deep Learning with Python*. Berkeley, USA: Apress, 2019.
- [163] G. E. Hinton, N. Srivastava, A. Krizhevsky, I. Sutskever, and R. Salakhutdinov, “Improving neural networks by preventing co-adaptation of feature detectors,” *Computing Research Repository*, vol. abs/1207.0580, 2012.
- [164] N. Srivastava, G. Hinton, A. Krizhevsky, I. Sutskever, and R. Salakhutdinov, “Dropout: A Simple Way to Prevent Neural Networks from Overfitting,” *Journal of Machine Learning Research*, vol. 15, pp. 1929 – 1958, 2014.
- [165] G. E. Dahl, T. N. Sainath, and G. E. Hinton, “Improving deep neural networks for LVCSR using rectified linear units and dropout,” in *IEEE International Conference on Acoustics, Speech and Signal Processing (ICASSP)*, Vancouver, Canada, 2013, pp. 8609 – 8613.
- [166] Y. Lecun, B. Boser, J. S. Denker, D. Henderson, and R. E. Howard, “Handwritten digit recognition with a back-propagation network,” *Advances in Neural Information Processing Systems*, vol. 2, pp. 396 – 404, 1990.

- 
- [167] Y. Lecun, L. Bottou, Y. Bengio, and P. Haffner, "Gradient-based learning applied to document recognition," *Proceedings of the IEEE*, vol. 86, no. 11, pp. 2278 – 2324, 1998.
- [168] A. Krizhevsky, I. Sutskever, and G. E. Hinton, "ImageNet Classification with Deep Convolutional Neural Networks," in *Advances in Neural Information Processing Systems 25*, F. Pereira, C. J. C. Burges, L. Bottou, and K. Q. Weinberger, Eds. Lake Tahoe, USA: Curran Associates, Inc., 2012, pp. 1097 – 1105.
- [169] K. Simonyan and A. Zisserman, "Very Deep Convolutional Networks for Large-Scale Image Recognition," in *International Conference on Learning Representations (ICLR)*, San Diego, USA, 2015, pp. 1 – 14.
- [170] K. He, X. Zhang, S. Ren, and J. Sun, "Deep Residual Learning for Image Recognition," in *The IEEE Conference on Computer Vision and Pattern Recognition (CVPR)*, Las Vegas, USA, 2016, pp. 770 – 778.
- [171] C. V. Dung and L. D. Anh, "Autonomous concrete crack detection using deep fully convolutional neural network," *Automation in Construction*, vol. 99, pp. 52 – 58, 2019.
- [172] O. Ronneberger, P. Fischer, and T. Brox, "U-Net: Convolutional Networks for Biomedical Image Segmentation," in *Medical Image Computing and Computer-Assisted Intervention – MICCAI 2015*, N. Navab, J. Hornegger, W. M. Wells, and A. F. Frangi, Eds. Munich, Germany: Springer International Publishing, 2015, pp. 234 – 241.
- [173] D. Ciresan, A. Giusti, L. M. Gambardella, and J. Schmidhuber, "Deep Neural Networks Segment Neuronal Membranes in Electron Microscopy Images," in *Advances in Neural Information Processing Systems 25*, F. Pereira, C. J. C. Burges, L. Bottou, and K. Q. Weinberger, Eds. Lake Tahoe, USA: Curran Associates, Inc., 2012, pp. 2843 – 2851.

- [174] C. J. Van Rijsbergen, “Information Retrieval,” in *Proceedings of the Joint IBM/University of Newcastle upon Tyne Seminar on Data Base Systems*. London, United Kingdom: Butterworth-Heinemann, 1979, pp. 1 – 14.
- [175] C. Feng, H. Zhang, H. Wang, S. Wang, and Y. Li, “Automatic Pixel-Level Crack Detection on Dam Surface Using Deep Convolutional Network,” *Sensors*, vol. 20, no. 2069, 2020.
- [176] N. Chinchor, “Evaluation Metrics,” in *Proceedings of the 4th Conference on Message Understanding*, ser. MUC4 ’92. Stroudsburg, USA: Association for Computational Linguistics, 1992, pp. 22 — 29.
- [177] D. Gross and T. Seelig, *Fracture Mechanics: With an Introduction to Micromechanics*, 3rd ed. Cham, Switzerland: Springer, 2018.
- [178] P. Paris and F. Erdogan, “A Critical Analysis of Crack Propagation Laws,” *Journal of Fluids Engineering*, vol. 85, no. 4, pp. 528 – 533, 1963.
- [179] M. J. Owen and P. T. Bishop, “Crack-growth relationships for glass-reinforced plastics and their application to design,” *Journal of Physics D: Applied Physics*, vol. 7, no. 9, pp. 1214 – 1224, 1974.
- [180] M. J. Owen and P. T. Bishop, “The significance of microdamage in glass-reinforced plastics at macroscopic stress concentrators,” *Journal of Physics D: Applied Physics*, vol. 5, no. 9, pp. 1621 – 1636, 1972.
- [181] V. La Saponara and R. Elhajjar, “Experimental Methods to Quantify Microdamage and Microstructure Anomalies in Fiber-Reinforced Polymer Composites: Overview,” in *Handbook of Damage Mechanics: Nano to Macro Scale for Materials and Structures*. Springer New York, 2013, pp. 1 – 22.

- 
- [182] S. Gholizadeh, “A review of non-destructive testing methods of composite materials,” in *XV Portuguese Conference on Fracture (PCF)*, vol. 1, Lisbon, Portugal, 2016, pp. 50 – 57.
- [183] N. M. Zaitoun and M. J. Aqel, “Survey on Image Segmentation Techniques,” in *International Conference on Communications, management, and Information technology (ICCMIT 2015)*, vol. 65, Prague, Czech Republic, 2015, pp. 797 – 806.
- [184] B. Yu, R. S. Bradley, C. Soutis, P. J. Hogg, and P. J. Withers, “2D and 3D imaging of fatigue failure mechanisms of 3D woven composites,” *Composites Part A: Applied Science and Manufacturing*, vol. 77, pp. 37 – 49, 2015.
- [185] X. P. Zhou, Y. X. Zhang, and Q. L. Ha, “Real-time computerized tomography (CT) experiments on limestone damage evolution during unloading,” *Theoretical and Applied Fracture Mechanics*, vol. 50, no. 1, pp. 49 – 56, 2008.
- [186] S.-Q. Yang, Z. Yang, H.-W. Jing, and T. Xu, “Fracture evolution mechanism of hollow sandstone under conventional triaxial compression by X-ray micro-CT observations and three-dimensional numerical simulations,” *International Journal of Solids and Structures*, vol. 190, pp. 156 – 180, 2020.
- [187] L. Wang, N. Limodin, A. E. Bartali, J.-F. Witz, R. Seghir, J.-Y. Buffiere, and E. Charkaluk, “Influence of pores on crack initiation in monotonic tensile and cyclic loadings in lost foam casting A319 alloy by using 3D in-situ analysis,” *Materials Science and Engineering: A*, vol. 673, pp. 362 – 372, 2016.
- [188] R. F. Agyei, I. Hanhan, and M. D. Sangid, “Detecting damage initiation in short fiber composites via in-situ X-ray tomography and digital

- volume correlation,” *Composites Communications*, vol. 22, p. 100524, 2020.
- [189] J. Rannou, N. Limodin, J. Réthoré, A. Gravouil, W. Ludwig, M.-C. Baïetto-Dubourg, J.-Y. Buffière, A. Combescure, F. Hild, and S. Roux, “Three dimensional experimental and numerical multiscale analysis of a fatigue crack,” *Computer Methods in Applied Mechanics and Engineering*, vol. 199, no. 21, pp. 1307 – 1325, 2010.
- [190] S. Jiang and J. Zhang, “Real-time crack assessment using deep neural networks with wall-climbing unmanned aerial system,” *Computer-Aided Civil and Infrastructure Engineering*, vol. 35, no. 6, pp. 549 – 564, 2020.
- [191] Y.-J. Cha, W. Choi, and O. Büyüköztürk, “Deep Learning-Based Crack Damage Detection Using Convolutional Neural Networks,” *Computer-Aided Civil and Infrastructure Engineering*, vol. 32, no. 5, pp. 361 – 378, 2017.
- [192] X. Yang, H. Li, Y. Yu, X. Luo, T. Huang, and X. Yang, “Automatic Pixel-Level Crack Detection and Measurement Using Fully Convolutional Network,” *Computer-Aided Civil and Infrastructure Engineering*, vol. 33, no. 12, pp. 1090 – 1109, 2018.
- [193] L. Pauly, D. Hogg, R. Fuentes, and H. Peel, “Deeper Networks for Pavement Crack Detection,” in *Proceedings of the 34th International Symposium in Automation and Robotics in Construction (ISARC)*. Taipei, Taiwan: The International Association for Automation and Robotics in Construction, 2017, pp. 479 – 485.
- [194] R. Fan, M. J. Bocus, Y. Zhu, J. Jiao, L. Wang, F. Ma, S. Cheng, and M. Liu, “Road crack detection using deep convolutional neural network and adaptive thresholding,” in *IEEE Intelligent Vehicles Symposium (IV)*, Paris, France, 2019, pp. 474 – 479.



- 
- [195] A. Zhang, K. C. P. Wang, B. Li, E. Yang, X. Dai, Y. Peng, Y. Fei, Y. Liu, J. Q. Li, and C. Chen, “Automated Pixel-Level Pavement Crack Detection on 3D Asphalt Surfaces Using a Deep-Learning Network,” *Computer-Aided Civil and Infrastructure Engineering*, vol. 32, no. 10, pp. 805 – 819, 2017.
- [196] A. Zhang, K. C. P. Wang, Y. Fei, Y. Liu, S. Tao, C. Chen, J. Q. Li, and B. Li, “Deep Learning-Based Fully Automated Pavement Crack Detection on 3D Asphalt Surfaces with an Improved CrackNet,” *Journal of Computing in Civil Engineering*, vol. 32, no. 5, pp. 1 – 14, 2018.
- [197] F. Chen and M. R. Jahanshahi, “NB-CNN: Deep Learning-Based Crack Detection Using Convolutional Neural Network and Naive Bayes Data Fusion,” *IEEE Transactions on Industrial Electronics*, vol. 65, no. 5, pp. 4392 – 4400, 2018.
- [198] H.-T. Bang, S. Park, and H. Jeon, “Defect identification of composites via thermography and deep learning techniques,” *Composite Structures*, vol. 246, p. 112405, 2020.
- [199] M. Kouzehgar, Y. K. Tamilselvam, M. V. Heredia, and M. R. Elara, “Self-reconfigurable façade-cleaning robot equipped with deep-learning-based crack detection based on convolutional neural networks,” *Automation in Construction*, vol. 108, p. 102959, 2019.
- [200] Q. Zou, Z. Zhang, Q. Li, X. Qi, Q. Wang, and S. Wang, “DeepCrack: Learning Hierarchical Convolutional Features for Crack Detection,” *IEEE Transactions on Image Processing*, vol. 28, no. 3, pp. 1498 – 1512, 2019.
- [201] L. Orgéas and P. J. J. Dumont, “Sheet Molding Compounds,” in *Wiley Encyclopedia of Composites*. New Jersey, USA: John Wiley & Sons, Inc., 2012, pp. 1 – 36.

- [202] D. Bücheler, “Locally Continuous-fiber Reinforced Sheet Molding Compound,” Dissertation, Karlsruhe Institute of Technology (KIT), Karlsruhe, Germany, 2018.
- [203] A. Motaghi and A. N. Hrymak, “Microstructure characterization in direct sheet molding compound,” *Polymer Composites*, vol. 40, no. S1, pp. E69 – E77, 2019.
- [204] C. Y. Chen and C. L. Tucker, “Mechanical Property Predictions for Short Fiber/Brittle Matrix Composites,” *Journal of Reinforced Plastics and Composites*, vol. 3, no. 2, pp. 120 – 129, 1984.
- [205] U. N. Gandhi, S. Goris, T. A. Osswald, , and Y.-Y. Song, *Discontinuous Fiber-Reinforced Composites: Fundamentals and Applications*. Munich, Germany: Hanser Verlag, 2020.
- [206] T. Sabiston, K. Inal, and P. Lee-Sullivan, “Method to determine the required microstructure size to be represented by a second order fibre orientation tensor using X-ray micro computed tomography to evaluate compression moulded composites,” *Composites Science and Technology*, vol. 182, p. 107777, 2019.
- [207] Z. Jendli, F. Meraghni, J. Fitoussi, and D. Baptiste, “Micromechanical analysis of strain rate effect on damage evolution in sheet molding compound composites,” *Composites Part A: Applied Science and Manufacturing*, vol. 35, no. 7, pp. 779 – 785, 2004.
- [208] S. K. Chaturvedi, C. T. Sun, and R. L. Sierakowski, “Mechanical characterization of sheet molding compound composites,” *Polymer Composites*, vol. 4, no. 3, pp. 167 – 171, 1983.
- [209] A. Trauth, “Characterisation and Modelling of Continuous-Discontinuous Sheet Moulding Compound Composites for Structural Applications,” Dissertation, Karlsruhe Institute of Technology (KIT), Karlsruhe, Germany, 2019.

- [210] F. K. Schwab, “Curing Simulations of a Fibre-Reinforced Thermoset on a Micro-and Nano-Scale,” Dissertation, Karlsruhe Institute of Technology (KIT), Karlsruhe, Germany, 2019.
- [211] J. Huether, P. Rupp, I. Kohlschreiber, and K. A. Weidenmann, “An enhanced method to determine the Young’s modulus of technical single fibres by means of high resolution digital image correlation,” *Measurement Science and Technology*, vol. 29, no. 4, p. 045601, 2018.
- [212] “MultiStar 272 Data Sheet,” visited on 2021-05-16. [Online]. Available: [www.jm.com/content/dam/jm/global/en/engineered-products/EP-documents/Product\\_Data\\_Sheets/Fibers/Assembled\\_Rovings/Europe/MultiStar272.pdf](http://www.jm.com/content/dam/jm/global/en/engineered-products/EP-documents/Product_Data_Sheets/Fibers/Assembled_Rovings/Europe/MultiStar272.pdf)
- [213] B. Rohrmüller, P. Gumbsch, and J. Hohe, “Microstructural characterization of glass fiber reinforced SMC by nanoindentation and single-fiber push-out test,” in *4th International Conference Hybrid 2020 Materials and Structures*, Web-Conference, 2020, pp. 78 – 83.
- [214] B. Rohrmüller, P. Gumbsch, and J. Hohe, “Calibrating a fiber–matrix interface failure model to single fiber push-out tests and numerical simulations,” *Composites Part A: Applied Science and Manufacturing*, vol. 150, p. 106607, 2021.
- [215] B. von Bernstorff and G. W. Ehrenstein, “Failure mechanism in SMC subjected to alternating stresses,” *Journal of Materials Science*, vol. 25, no. 9, pp. 4087 – 4097, 1990.
- [216] J. Kabelka, L. Hoffmann, and G. W. Ehrenstein, “Damage process modeling on SMC,” *Journal of Applied Polymer Science*, vol. 62, no. 1, pp. 181 – 198, 1996.
- [217] S. S. Wang, E. S.-M. Chim, and N. M. Zahlan, “Fatigue Crack Propagation in Random Short-Fiber SMC Composite,” *Journal of Composite Materials*, vol. 17, no. 3, pp. 250 – 266, 1983.

- [218] S. S. Wang and E. S.-M. Chim, "Fatigue Damage and Degradation in Random Short-Fiber SMC Composite," *Journal of Composite Materials*, vol. 17, no. 2, pp. 114 – 134, 1983.
- [219] S. S. Wang, E. S.-M. Chim, and H. Suemasu, "Mechanics of Fatigue Damage and Degradation in Random Short-Fiber Composites, Part I - Damage Evolution and Accumulation," *Journal of Applied Mechanics*, vol. 53, no. 2, pp. 339 – 346, 1986.
- [220] S. S. Wang, E. S.-M. Chim, and H. Suemasu, "Mechanics of Fatigue Damage and Degradation in Random Short-Fiber Composites, Part II - Analysis of Anisotropic Property Degradation," *Journal of Applied Mechanics*, vol. 53, no. 2, pp. 347 – 353, 1986.
- [221] J. F. Mandell, "Fatigue Behavior of Short Fiber Composite Materials," in *Fatigue of Composite Materials*, ser. Composite Materials Series, K. L. Reifsnider, Ed. Amsterdam, Netherlands: Elsevier, 1991, vol. 4, pp. 231 – 337.
- [222] F. Meraghni and M. L. Benzeggagh, "Micromechanical modelling of matrix degradation in randomly oriented discontinuous-fibre composites," *Composites Science and Technology*, vol. 55, no. 2, pp. 171 – 186, 1995.
- [223] F. Meraghni, C. J. Blakeman, and M. L. Benzeggagh, "Effect of interfacial decohesion on stiffness reduction in a random discontinuous-fibre composite containing matrix microcracks," *Composites Science and Technology*, vol. 56, no. 5, pp. 541 – 555, 1996.
- [224] A. Ben Cheikh Larbi, K. Sai, H. Sidhom, and D. Baptiste, "Constitutive model of micromechanical damage to predict reduction in stiffness of a fatigued SMC composite," *Journal of Materials Engineering and Performance*, vol. 15, no. 5, pp. 575 – 580, 2006.

- [225] J. Fitoussi, M. Bocquet, and F. Meraghni, "Effect of the matrix behavior on the damage of ethylene–propylene glass fiber reinforced composite subjected to high strain rate tension," *Composites Part B: Engineering*, vol. 45, no. 1, pp. 1181 – 1191, 2013.
- [226] M. Shirinbayan, J. Fitoussi, F. Meraghni, B. Surowiec, M. Bocquet, and A. Tcharkhtchi, "High strain rate visco-damageable behavior of Advanced Sheet Molding Compound (A-SMC) under tension," *Composites Part B: Engineering*, vol. 82, pp. 30 – 41, 2015.
- [227] M. Shirinbayan, J. Fitoussi, M. Bocquet, F. Meraghni, B. Surowiec, and A. Tcharkhtchi, "Multi-scale experimental investigation of the viscous nature of damage in Advanced Sheet Molding Compound (A-SMC) submitted to high strain rates," *Composites Part B: Engineering*, vol. 115, pp. 3 – 13, 2017.
- [228] M. Shirinbayan, J. Fitoussi, F. Meraghni, B. Surowiec, M. Laribi, and A. Tcharkhtchi, "Coupled effect of loading frequency and amplitude on the fatigue behavior of advanced sheet molding compound (A-SMC)," *Journal of Reinforced Plastics and Composites*, vol. 36, no. 4, pp. 271 – 282, 2017.
- [229] M. Shirinbayan, J. Fitoussi, N. Abbasnezhad, F. Meraghni, B. Surowiec, and A. Tcharkhtchi, "Mechanical characterization of a Low Density Sheet Molding Compound (LD-SMC): Multi-scale damage analysis and strain rate effect," *Composites Part B: Engineering*, vol. 131, pp. 8 – 20, 2017.
- [230] Z. Jendli, J. Fitoussi, F. Meraghni, and D. Baptiste, "Anisotropic strain rate effects on the fibre–matrix interface decohesion in sheet moulding compound composites," *Composites Science and Technology*, vol. 65, no. 3, pp. 387 – 393, 2005.

- [231] J. F. Mandell and B. L. Lee, “Matrix Cracking in Short Fiber Reinforced Composites under Static and Fatigue Loading,” in *Composite Materials: Testing and Design (6th Conference)*, I. M. Daniel, Ed. Phoenix, USA: ASTM International, 1982, pp. 200 – 222.
- [232] D. R. Atodaria, S. K. Putatunda, and P. K. Mallick, “Fatigue crack growth model and mechanism of a random fiber SMC composite,” *Polymer Composites*, vol. 20, no. 2, pp. 240 – 249, 1999.
- [233] T. Sabiston, P. Pinter, J. Lévesque, K. A. Weidenmann, and K. Inal, “Evaluating the number of fibre orientations required in homogenization schemes to predict the elastic response of long fibre sheet moulding compound composites from X-ray computed tomography measured fibre orientation distributions,” *Composites Part A: Applied Science and Manufacturing*, vol. 114, pp. 278 – 294, 2018.
- [234] J. Fitoussi, G. Guo, and D. Baptiste, “A statistical micromechanical model of anisotropic damage for S.M.C. composites,” *Composites Science and Technology*, vol. 58, no. 5, pp. 759 – 763, 1998.
- [235] L. Kehrér, P. Pinter, and T. Böhlke, “Mean and full field homogenization of artificial long fiber reinforced thermoset polymers,” in *Proceedings in Applied Mathematics and Mechanics (PAMM)*, vol. 17, no. 1, Weimar, Germany, 2017, pp. 603 – 604.
- [236] L. Kehrér, D. Wicht, J. T. Wood, and T. Böhlke, “Dynamic mechanical analysis of pure and fiber-reinforced thermoset- and thermoplastic-based polymers and free volume-based viscoelastic modeling,” in *GAMM-Mitteilungen*, vol. 41, no. 1, 2018, p. e201800007.
- [237] J. Görthofer, M. Schneider, F. Ospald, A. Hrymak, and T. Böhlke, “Computational homogenization of sheet molding compound

- composites based on high fidelity representative volume elements,” *Computational Materials Science*, vol. 174, p. 109456, 2020.
- [238] Z. Chen, T. Huang, Y. Shao, Y. Li, H. Xu, K. Avery, D. Zeng, W. Chen, and X. Su, “Multiscale finite element modeling of sheet molding compound (SMC) composite structure based on stochastic mesostructure reconstruction,” *Composite Structures*, vol. 188, pp. 25 – 38, 2018.
- [239] M. Schemmann, S. Gajek, and T. Böhlke, “Biaxial Tensile Tests and Microstructure-Based Inverse Parameter Identification of Inhomogeneous SMC Composites,” in *Advances in Mechanics of Materials and Structural Analysis*, H. Altenbach, F. Jablonski, W. H. Müller, K. Naumenko, and P. Schneider, Eds. Cham, Switzerland: Springer, 2018, pp. 329 – 342.
- [240] L. Schöttl, W. V. Liebig, K. A. Weidenmann, K. Inal, and P. Elsner, “Microstructure characterization of discontinuous fiber reinforced polymers based on volumetric images: Fiber bundle tracking and weld line investigation,” in *4th International Conference Hybrid 2020 Materials and Structures*, Web-Conference, 2020, pp. 97 – 101.
- [241] L. Schöttl, P. Kolb, W. V. Liebig, K. A. Weidenmann, K. Inal, and P. Elsner, “Crack characterization of discontinuous fiber-reinforced composites by using micro-computed tomography: Cyclic in-situ testing, crack segmentation and crack volume fraction,” *Composites Communications*, vol. 21, p. 100384, 2020.
- [242] L. Schöttl, K. A. Weidenmann, T. Sabiston, K. Inal, and P. Elsner, “Fiber bundle tracking method to analyze sheet molding compound microstructure based on computed tomography images,” *NDT & E International*, vol. 117, p. 102370, 2021.

- [243] L. Schöttl, W. V. Liebig, K. A. Weidenmann, K. Inal, and P. Elsner, “The use of the empirical crack orientation tensor to characterize the damage anisotropy,” *Composites Communications*, vol. 25, p. 100613, 2021.
- [244] R. Maertens, L. Schöttl, V. W. Liebig, P. Elsner, and K. A. Weidenmann, “Evaluating Material Homogeneity in the Long Fiber Thermoset Injection Molding Process by Image Texture Analysis,” submitted to *Composites Communications*.
- [245] J. Görthofer, N. Meyer, L. Schöttl, A. Trauth, M. Schemmann, P. Pinter, B. Fengler, S. Ilinzeer, M. Hohberg, T. D. Pallicity, L. Kärger, K. A. Weidenmann, P. Elsner, F. Henning, A. Hrymak, and T. Böhlke, “Compression Molding of the Demonstrator Structure,” in *Continuous-Discontinuous Fiber-Reinforced Polymers*. Munich, Germany: Hanser Verlag, 2019, pp. 297 – 314.
- [246] C. Ding and X. He, “Cluster merging and splitting in hierarchical clustering algorithms,” in *IEEE International Conference on Data Mining*, Washington DC, USA, 2002, pp. 139 – 146.
- [247] S. T. Wierzchon and M. A. Klopotek, *Modern Algorithms of Cluster Analysis*. Cham, Switzerland: Springer, 2018.
- [248] I. Sönmez, “Detection and characterization of cracks in  $\mu$ CT images of sheet molding compounds (GF-SMC) by means of machine learning methods,” Master’s thesis (unpublished), Karlsruhe Institute of Technology (KIT), Institute for Applied Materials (IAM-WK), 2020.
- [249] D. P. Kingma and J. Ba, “Adam: A Method for Stochastic Optimization,” in *International Conference on Learning Representations 2015*, San Diego, USA, 2015, pp. 1 – 15.
- [250] XYLON International GmbH, [www.yxlon.de](http://www.yxlon.de), visited on 2020-07-13. [Online]. Available: [www.yxlon.de/Yxlon/media/Content/Products/X-](http://www.yxlon.de/Yxlon/media/Content/Products/X-)



rayandCTinspectionsystems/YXLONCTPrecision/YXLON-CT-Precision-Product-brochure-DE.pdf

- [251] A. Heni, “Construction and development of an in-situ testing setup for computed tomography,” Bachelor’s thesis (unpublished), Karlsruhe Institute of Technology (KIT), Institute for Applied Materials (IAM-WK), 2012.
- [252] S. Dietrich, K. A. Weidenmann, and P. Elsner, “3D tomographic characterization of sandwich structures,” *NDT & E International*, vol. 62, pp. 77 – 84, 2014.
- [253] S. Dietrich, M. Koch, P. Elsner, and K. Weidenmann, “Measurement of Sub-Surface Core Damage in Sandwich Structures Using In-situ Hertzian Indentation During X-ray Computed Tomography,” *Experimental Mechanics*, vol. 54, no. 8, pp. 1385 – 1393, 2014.
- [254] M. Bartkowiak, L. Schöttl, P. Elsner, and K. A. Weidenmann, “Combined In Situ X-Ray Computed Tomography and Acoustic Emission Analysis for Composite Characterization - A Feasibility Study,” in *22nd Symposium on Composites*, ser. Key Engineering Materials, vol. 809. Kaiserslautern, Germany: Trans Tech Publications Ltd., 2019, pp. 604 – 609.
- [255] A. Amirkhanov, A. Amirkhanov, D. Salaberger, J. Kastner, M. E. Gröller, and C. Heinzl, “Visual Analysis of Defects in Glass Fiber Reinforced Polymers for 4DCT Interrupted In situ Tests,” *Computer Graphics Forum*, vol. 35, no. 3, pp. 201 – 210, 2016.
- [256] J. S. Cintra and C. L. Tucker, “Orthotropic closure approximations for flow-induced fiber orientation,” *Journal of Rheology*, vol. 39, no. 6, pp. 1095 – 1122, 1995.
- [257] B. Jähne, *Digitale Bildverarbeitung und Bildgewinnung*, 7th ed. Berlin, Germany: Springer Vieweg, 2012.

- [258] P. Yayla, “Fracture Surface Morphology of Delamination Failure of Polymer Fiber Composites Under Different Failure Modes,” *Journal of Failure Analysis and Prevention*, vol. 16, no. 2, pp. 264 – 270, 2016.
- [259] J. Cook, J. E. Gordon, C. C. Evans, D. M. Marsh, and F. P. Bowden, “A mechanism for the control of crack propagation in all-brittle systems,” *Proceedings of the Royal Society of London. Series A. Mathematical and Physical Sciences*, vol. 282, no. 1391, pp. 508 – 520, 1964.
- [260] S. Tamboura, H. Ayari, M. Shirinbayan, M. A. Laribi, H. Bendaly, H. Sidhom, A. Tcharkhtchi, and J. Fitoussi, “Experimental and numerical multi-scale approach for Sheet-Molding-Compound composites fatigue prediction based on fiber-matrix interface cyclic damage,” *International Journal of Fatigue*, vol. 135, p. 105526, 2020.
- [261] M. Naebe, M. M. Abolhasani, H. Khayyam, A. Amini, and B. Fox, “Crack Damage in Polymers and Composites: A Review,” *Polymer Reviews*, vol. 56, no. 1, pp. 31 – 69, 2016.
- [262] M. R. Piggott, *Load bearing fibre composites*, 2nd ed. Boston, USA: Kluwer Academic Publ., 2002.
- [263] A. Trauth, M. Bondy, K. A. Weidenmann, and W. Altenhof, “Mechanical properties and damage evolution of a structural sheet molding compound based on a novel two step curing resin system,” *Materials & Design*, vol. 143, pp. 224 – 237, 2018.

# List of Figures

1.1	Greenhouse gas emission breakdown by the source sectors in the EU-27 2018 (data by European Environment Agency [4]). 25 % of greenhouse gases are emitted by the transport sector including international aviation. . . . .	2
1.2	GFRP shares of the European market by application area in 2019 (data by Witten and Mathes [6]). The two main application areas for GFRP are infrastructure and transport. . . . .	3
1.3	GFRP production volumes in Europe according to the manufacturing processes and semi-finished components in 2019 (data by Witten and Mathes [6]). The production fraction of SMC in 2019 is 18 %. Long fiber-reinforced thermoplastics (LFT), glass-mat reinforced thermoplastics (GMT), resin transfer molding (RTM) and bulk molding compounds (BMC). . . . .	4
1.4	Schematic interaction between manufacturing, microstructure and properties. Consideration of the three aspects for fiber-reinforced polymers from a materials science perspective. . . . .	5
1.5	Illustration of the virtual process chain and the cooperations between the research areas within the IRTG (figure by Görthofer et al. [9, 10]*). . . . .	7
2.1	Fundamentals of continuum kinematics. . . . .	11
2.2	The Voigt and Reuss homogenization approaches and the effect of the fiber volume fraction $\phi_F$ on the effective Young's modulus $\bar{E}$ . . . . .	14

2.3	Typical failure modes of (short) fiber-reinforced composites. In (a) failing of the fiber-matrix interface and resulting fiber debonding, (b) fracture of fibers under tensile stress and (c) crack propagation through matrix material. . . . .	16
2.4	Schematic fatigue-life diagram for unidirectional fiber-reinforced composites with tensile load parallel to the fiber orientation, where $\epsilon_c$ is the composite fracture strain and $\epsilon_M$ the fatigue limit of the matrix (re-illustration, original figure by Talreja and Watt [35]).	17
2.5	Classification of fatigue life by three stages in which different damage mechanisms occur for fiber-reinforced composites. In I) multiple crack formation, II) transition to single macroscopic crack propagation and III) final fracture (re-illustrations, original figures by Schulte [41], Mao and Mahadevan [43]). . . . .	18
2.6	Effective composite strength $\bar{\sigma}_{\max}$ with respect to the fiber volume content $\phi_F$ . Impact of the fiber volume content $\phi_F$ on the damage mechanism and the critical fiber volume content $\phi_{\text{crit}}$ . . . . .	21
2.7	Schematic illustration of the stress-strain curve for composites with fiber volume content above and below the critical one, according to Cooper [47]. Impact of the fiber volume content on the formation of single or multiple cracks (re-illustration, original figure by Cooper [47]). . . . .	22
2.8	Introducing the crack orientation based on the crack normal vector $\mathbf{g}$ .	23
2.9	Illustration of the Lambert-Beer-Law of decreasing beam intensity and the linear attenuation coefficient $\mu$ . . . . .	25
2.10	General cone-beam computed tomography setup. . . . .	27
2.11	Conflict between voxel size and scanned volume of the cone-beam computed tomography setup. . . . .	28
2.12	The filtered backprojection reconstruction process (figures by Carmignato et al. [8]). . . . .	29
2.13	Properties of volumetric images, like gray-values $g$ (scalar), fiber orientations $\mathbf{n}$ (vector) and two-dimensional cross section image. .	30

2.14	Classification of different ex-situ and in-situ imaging strategies. Schematic illustration of the test protocols and stress curves, where the load is applied displacement controlled (re-illustration, original figures by Garcea et al. [65]). . . . .	31
2.15	Illustrating the application of convolutional filters on two-dimensional images. Filter mask $f_{(x',y')}$ according to Equation 2.35. By applying the filter mask with a mask size of three, the input image size is reduced by two in both dimensions, since the filter mask cannot applied to the image edges (no image extension). . . . .	34
2.16	Illustration of the simple gray-value thresholding principles for segmenting two objects (Schematic gray-value histogram). . . . .	35
2.17	Illustrating the segmentation process of the Seed-Region-Growing (SRG) method. (a) shows an exemplary input image and in (b) the seed voxels are defined by a strict threshold $k_{seed}$ . Subsequently, the region is expanded iteratively by using the second threshold $k_{growth}$ in (c). . . . .	37
2.18	Eliminating binary errors by using morphological closing operation. Two binary images with a grid and a circle are shown in (a). In (b) salt-and-pepper-noise is added to the original images (33 %-noise) and (c) shows the closing operator result (background in black and segmented object in white). . . . .	38
2.19	Digital volume correlation principles illustrated schematically on artificial data. . . . .	46
2.20	Incremental value from artificial intelligence usage in selected sectors 2018 (data by Chui et al. [158, 159]). . . . .	49
2.21	Contrast between classical programming and artificial neural network paradigm (re-illustration, original image by Chollet [160]). . . . .	49
2.22	Connection and communication between (a) biological and (b) artificial neural networks (figures by Samarasinghe [161]). . . . .	50

2.23	Interaction of the input data, neurons, connections, the layer-wise structure and the predicted results of artificial neural network. . . .	50
2.24	Data processing and activation function $f$ of a single neuron $j$ within an artificial neural network. . . . .	51
2.25	Determination of weight factors by using the training data set and iterative optimization (re-illustration, original figures by Chollet [160]). . . . .	52
2.26	Schematic illustration of the principle approach for pattern recognition based in convolution neural networks (new-illustration, original illustration by Chollet [160]). . . . .	54
2.27	The VGG16 architecture for pattern detection and classification by Simonyan and Zisserman [169] (illustration by Dung and Anh [171]). . . . .	55
2.28	The difference between the classification, detection and segmentation tasks of CNN. For classification in (a) the output is a single class label. In (b) the detected object is located by bounding boxes (red) and (c) the object is segmented pixel-wise (white pixels). . . . .	56
2.29	The U-Net architecture for object segmentation tasks by Ronneberger et al. [172]. . . . .	57
2.30	Monitoring and quantifying over- and underestimation of the segmented objects by means of precision and recall metrics. . . .	58
2.31	Segmentation and classification of different type of cracks within woven glass fiber reinforced composite (figure by Yu et al. [76]). . .	61
2.32	Synchrotron tomography in-situ testing on nodular graphite cast iron. (a) Tomo-graphy image of the occurred crack, (b) $u$ -displacement field vertical to the crack surface by DVC and (c) the determined crack surface by correlation residual field thresholding (figures by Rannou et al. [189]). . . . .	63

2.33	Comparing the results and output of crack classification, detection and segmentation by using CNN for safety and inspection tasks. In (a) crack classification by Kouzehgar et al. [199], in (b) crack detection by Jiang and Zhang [190] and in (c) crack segmentation by Yang et al. [192]. . . . .	64
3.1	Manufacturing process of semi-finished SMC. . . . .	69
3.2	The SMC compression molding process of generic geometries. In (a) placing the semi-finished SMC initial charge, (b) compression molding and (c) finally, curing of the resin. . . . .	69
3.3	Different initial charge configurations and flow paths. In (a) long flow path, (b) medium flow path and (c) no significant flow path due to full charge coverage . . . . .	71
3.4	The fiber orientation distribution histogram of SMC plate with an initial mold coverage of 33 %. Fiber volume fraction of the most dominate fiber orientation is approximately 21 vol.% (figure by Gandhi et al. [205]). . . . .	72
3.5	The SMC compression molding process. In (a) placing two semi-finished SMC initial charges, (b) compression molding and (c) weld line formation. . . . .	73
3.6	Principle microstructure of unidirectional laminates, SMC with random oriented chopped fiber bundles and short-fiber reinforced polymer injection molding. . . . .	74
3.7	The SMC characteristic fiber bundle arrangement on the microstructural level. Fiber bundles in white and the surrounding matrix in black. $\mu$ CT cross section acquired at different scale levels. . . . .	75
3.8	Classifying the SMC microstructure by different scale levels. Illustrating the conflict between voxel size and scanned volume with respect to laboratory $\mu$ CT scanning based on three exemplary SMC specimens. Using different characterization methods on respective scale levels. Referenced glass fiber diameter of 13.5 $\mu$ m. . . . .	76

3.9	Illustrating the effect of the fiber content on the mechanical behavior. Typical stress-strain curves of SMC with different fiber volume content between 30 wt.% and 65 wt.% (figure by Chaturvedi et al. [208]). . . . .	77
3.10	Typical stress-strain curves of SMC regarding the charge coverage between 33 % and 100 %, along and perpendicular to the MFD. The stress-strain curves illustrate the increasing anisotropic mechanical behavior as a result of decreasing charge coverage. Fiber weight content of the examined SMC is 65 wt.% (figure by Gandhi et al. [205]). . . . .	78
3.11	Effective composite strength $\bar{\sigma}_{\max}$ , the effect of the fiber volume content $\phi_F$ and the critical fiber volume content $\phi_{\text{crit}}$ of the examined SMC material according to von Bernstorff and Ehrenstein [215]. The curves are generated based on the data in Table 3.4 and Table 3.3. . . . .	80
3.12	Schematic stress-strain curves of fiber-reinforced composites where (a) single crack formation and (b) multiple matrix cracking occurs with respect to the fiber volume content $\phi_F$ [47, 207, 215].	81
3.13	Typical failure modes of SMC. In (a) cracking of the matrix, (b) crack propagation along the fiber bundle and (c) fiber bundle breakage under tensile stress. . . . .	83
3.14	$\mu$ CT image cross sections of typical SMC failure modes. In (a) Cracking of the matrix, (b) crack propagation along the fiber bundle and (c) fiber bundle breakage under tensile stress (voxel size of $6.8\text{ }\mu\text{m}$ ). . . . .	83
3.15	3D illustration of the characteristic failure modes of SMC. At a) fiber bundle fracture perpendicular to the bundle orientation, b) horizontal intra-bundle pseudo-delamination, c) inter-bundle fracture of the matrix and d) vertical intra-bundle pseudo-delamination. . . . .	84



4.1	Illustration of the planar fiber orientation $\mathbf{n}$ with respect to the symmetry ( $\mathbf{n} \hat{=} -\mathbf{n}$ ). . . . .	92
4.2	In (a) the alignment of the cylindrical reference volumes $\mathcal{B}$ and (b) the shape of the weighting function $c(r)$ (Gaussian function, $\sigma = 1/3R$ ) (re-illustration, original figures by Schöttl et al. [131]*). . . . .	94
4.3	$\mu$ CT cross section of a typical SMC sample. Classification of the SMC microstructure by mesoscopic and microscopic bundles. In (a) an exemplary SMC microstructure, (b) the mesoscopic bundles and (c) the microscopic bundles are marked, respectively. Voxel size is $9.1\ \mu\text{m}$ and glass-fiber diameter $13.5\ \mu\text{m}$ (re-illustration, original figures by Schöttl et al. [242]*). . . . .	96
4.4	Iterative tracking along the path with the highest probability to the experimental fiber orientation data $\mathbf{n}$ (figure by Schöttl et al. [242]*). . . . .	97
4.5	The distance between the two trajectories $\mathcal{S}_A$ and $\mathcal{S}_B$ (figure by Schöttl et al. [242]*). . . . .	99
4.6	The orientation difference $\phi_\alpha$ of section pair $\alpha$ (figure by Schöttl et al. [242]*). . . . .	99
4.7	Illustration of the hierarchical agglomerative clustering scheme to identify mesoscopic bundles (figure by Schöttl et al. [242]*). . . . .	101
4.8	Iterative tracking along a circular arc. Linking the tracking radii $R_1$ , $R_2$ and the aperture angle $\theta$ (figure adapted from Tournier et al. [124]). . . . .	102
4.9	Parallelization of the fiber bundle tracking process and dividing the volumetric data into sub-volumes by means of cut off radius $r_{\text{cut}}$ . . . . .	104
4.10	Introducing the curvature $\kappa$ of a space curve $\mathbf{r}(s)$ . . . . .	105
4.11	In (a) an exemplary gray-scale image and in (b) to (d) the crack segmentation process by means of the SRG method. For comparison the single thresholding result is shown in (e). Background in black and segmented crack in white. . . . .	107
4.12	Eliminating incorrect segmented voxels by using the closing operation (background in black and segmented crack in white). . . . .	108

4.13	Ambiguity and singularity in continuum kinematics due to crack formation. . . . .	109
4.14	Schematic illustration of the process for generating the training data. Acquisition of input images and corresponding ground truth from volumetric images for training of the CNN model. The dimension bars were not part of the input data or ground truth and were added for display only. . . . .	110
4.15	In the upper row representative input images and the corresponding ground truth below (background in black and labeled cracks in white). On the left side original images and on the right images, which were modified by using image augmentation. The image size is 96 pixels $\times$ 96 pixels and the voxel size 6.2 – 7.0 $\mu\text{m}$ . The dimension bars were not part of the input data or ground truth and were added for display only. . . . .	111
4.16	Segmenting cracks within volumetric images with variable size by using a trained U-Net model. Extracting image section, crack segmentation by applying the trained U-Net and reassembling of the volumetric prediction data. . . . .	113
4.17	Procedure to segment cracks within volumetric images with variable size by using the trained U-Net model. Minimizing discretization effects of the patches by initiating, evaluating and reassembling using multiple slightly shifted grids. . . . .	114
4.18	Illustration of cracks within a solid and the crack normal unit vectors $\mathbf{g}$ (figure by Schöttl et al. [243].) . . . . .	115
4.19	Image processing to determine the crack normal orientations. In (a) the voxel-wise segmented crack, (b) the Gaussian blurring result ( $\sigma = 1.5$ voxel) and (c) the gradient in vertical direction (background in black and the crack in white, voxel size of 6.8 $\mu\text{m}$ , re-illustration original figures by Schöttl et al. [243]*). . . . .	116
4.20	Illustration of the accumulated crack volume $V_{\text{Crack}}$ and the reference volume $V_{\text{ref}}$ . . . . .	119

4.21	Identification of damage mechanisms by taking the surrounding microstructure into account. Classification approach for the damage mechanisms based on the control volume $\mathcal{B}$ around the crack. The proportions of radius $R$ , fiber diameter and bundle width are not illustrated realistically. . . . .	121
4.22	Introducing mathematical criteria $\rho_{I,j}$ , $\rho_{II,j}$ and $\rho_{III,j}$ to quantify the damage mechanisms in SMC that are associated with crack formation. The damage mechanisms are classified for each crack voxel $j$ individually. . . . .	122
5.1	XYLON CT Precision $\mu$ CT System [250]. . . . .	126
5.2	Illustrating the principle in-situ $\mu$ CT testing setup. Combining $\mu$ CT scanning and in-situ tensile testing in order to acquire volumetric images of damaged microstructures. . . . .	127
5.3	The $\mu$ CT system including detector, rotation table and X-ray tube. Furthermore, the mechanical setup to conducted in-situ tensile tests, which consists of a CFRP load frame where the specimen is clamped inside (figure by Schöttl et al. [241]*). . . . .	128
5.4	Illustration of the $\mu$ CT system and the in-situ testing setup. In (a) the cross section of the in-situ setup and (b) the clamped SMC specimen without the load frame (figures by Schöttl et al. [241]*). . . . .	128
5.5	Illustration of the (a) displacement and (b) nominal stress along the interrupted in-situ $\mu$ CT test applying cyclic tensile load which is increased by each load step. . . . .	129
5.6	Plate orientation of the extracted SMC samples in $0^\circ$ , $45^\circ$ and $90^\circ$ to the MFD. Illustration of the initial charge coverage, flow region and MFD. . . . .	130
5.7	Illustration of the double semi-circle notched sample geometry, which is used for in-situ $\mu$ CT tests. Sample thickness $t = 1.5 - 2.0$ mm (figure by Schöttl et al. [241]*). . . . .	131

6.1	Characterizing the microstructure of the HO-0° specimen. In (a) a gray-value $\mu$ CT cross section and (b) the fiber orientation visualized by HSV color map. . . . .	135
6.2	In (a) the fiber orientation histogram of the entire specimen and (b) the empirical second-order orientation tensor $\mathbf{N}$ of the HO-0° specimen. Load direction $\hat{=}$ 0°. . . . .	135
6.3	Characterizing the microstructure of the HO-45° specimen. In (a) a gray-value $\mu$ CT cross section and (b) the fiber orientation visualized by HSV color map. . . . .	136
6.4	In (a) the fiber orientation histogram of the entire specimen and (b) the empirical second-order orientation tensor $\mathbf{N}$ of the HO-45° specimen. Load direction $\hat{=}$ 0°. . . . .	136
6.5	Characterizing the microstructure of the HO-90° specimen. In (a) a gray-value $\mu$ CT cross section and (b) the fiber orientation visualized by HSV color map. . . . .	137
6.6	In (a) the fiber orientation histogram of the entire specimen and (b) the empirical second-order orientation tensor $\mathbf{N}$ of the HO-90° specimen. Load direction $\hat{=}$ 0°. . . . .	137
6.7	Characterizing the microstructure of the RO specimen. In (a) a gray-value $\mu$ CT cross section and (b) the fiber orientation visualized by HSV color map. . . . .	138
6.8	In (a) the fiber orientation histogram of the entire specimen and (b) the empirical second-order orientation tensor $\mathbf{N}$ of the RO specimen. Load direction $\hat{=}$ 0°. . . . .	138
6.9	Illustrating the fiber orientation state of the four examined SMC specimens for in-situ $\mu$ CT testing according to the scheme by Cintra and Tucker [256]. . . . .	139
6.10	The (a) gray-value volumetric image acquired by $\mu$ CT scanning and (b) the visualized tracked and clustered fiber bundles (figures by Schöttl et al. [242]*). Sample No. 1 in Table 4.1. . . . .	141

6.11	Tracked and clustered fiber bundles within the in-situ $\mu$ CT specimen HO-0°. In (a) the gray-value $\mu$ CT volumetric image and (b) the visualized fiber bundles (figures by Schöttl et al. [242]*). Sample No. 2 in Table 4.1. . . . .	142
6.12	Close-up of the tracked and clustered fiber bundles within the marked region in Figure 6.11 (b) (figure by Schöttl et al. [242]*). .	142
6.13	Analyzing the SMC fiber bundle within a weld line region. In (a) the $\mu$ CT cross section, (b) the tracked fiber bundles and (c) the fiber bundle curvature (figures by Schöttl et al. [240]*). Sample No. 3 in Table 4.1. . . . .	143
6.14	The mean and maximum curvature distribution orthogonal to the examined SMC weld line (data by Schöttl et al. [240]*). . . . .	143
6.15	Four cyclic load steps are carried out. Initially and after each load step the specimen is screened by means of $\mu$ CT scanning. In (a) the displacement $u$ and (b) the nominal stress $\sigma_N$ curves along the in-situ test process are plotted (figure by Schöttl et al. [241]*). . .	145
6.16	The SMC damage evolution within the $\mu$ CT cross section. In (b) the initial and (c) to (f) the enlarged SMC microstructure after the respective load steps (figures by Schöttl et al. [241]*). . . . .	146
6.17	Five cyclic load steps are carried out. Initially and after each load step the specimen is screened by means of $\mu$ CT scanning. In (a) the displacement $u$ and (b) the nominal stress $\sigma_N$ curves along the in-situ test process are plotted. . . . .	147
6.18	$\mu$ CT cross sections of the damaged SMC microstructure with highly diagonally oriented fiber bundles. The crack in (a) is initiated during the fourth load step close to the surface. During the fifth load step the crack propagates in length (b) and width (c). In (d) the fractured microstructure. . . . .	148

6.19	Three cyclic load steps are carried out. Initially and after each load step the specimen is screened by means of $\mu$ CT scanning. In (a) the displacement $u$ and (b) the nominal stress $\sigma_N$ curves along the in-situ test process are plotted. . . . .	150
6.20	In (a) to (d) representative $\mu$ CT cross sections. No cracks are observed during the three load steps. The HO-90° specimen fractures right after the third load step. . . . .	150
6.21	Five load steps are carried out. Initially and after each load step the specimen is screened by means of $\mu$ CT scanning. In (a) the displacement $u$ and (b) the nominal stress $\sigma_N$ curves through the in-situ test process are plotted. . . . .	152
6.22	The damage propagation within the RO specimen. In (a) to (d) the SMC microstructure after the respective load steps. The $\mu$ CT cross section reveal the crack initiation and propagation within the microstructure, in particular at the tip of a cavity. . . . .	153
6.23	$\mu$ CT cross section of the (a) initial and (b) fractured RO sample, in which fiber bundle breakage, pull-out and matrix fragmentation occurred. . . . .	153
6.24	Crack segmentation by means of the SRG method. In the upper row gray-scale $\mu$ CT cross sections of the HO-0° specimen and below the corresponding binary images, in which the cracks are segmented (white) (data by Schöttl et al. [241]*). . . . .	156
6.25	3D-visualization of the segmented cracks together with the microstructure (transparent) for all four load steps of the HO-0° specimen (figures by Schöttl et al. [243]*). . . . .	156
6.26	Required input data for DVC including volumetric images of the initial and deformed specimen. Corresponding gray-scale $\mu$ CT cross section of the (a) initial and (b) deformed microstructure. Formation of a crack with a large crack opening. . . . .	157

6.27	Illustration of the DVC results inside the marked region in Figure 6.26 (b). Identifying the crack by means of the difference volume in (b) and illustrating the von Mises strain field around the crack in (c). . . . .	158
6.28	Examining a single crack inside a fiber bundle. In (a) the $\mu$ CT cross section, (b) difference volume and (c) von Mises strain field determined by means of DVC. . . . .	159
6.29	Illustration of a matrix crack in (a) and the corresponding DVC results regarding the difference volume in (b) and von Mises strain field around the crack in (c). . . . .	160
6.30	3D-visualization of the indicated cracks within the HO-45° specimen after the fifth load step by using the DVC method. Cracks are segmented by selecting an absolute difference volume threshold of 0.9. . . . .	160
6.31	Monitoring the training progress of the U-Net architecture by means of the loss value. Loss value distribution of the training and validation data set. . . . .	161
6.32	Testing the trained U-Net Model. Exemplary input images, ground truth, prediction and binary prediction (background in black and labeled cracks in white). The image size is 96 pixels $\times$ 96 pixels and the voxel size 6.1 – 7.0 $\mu\text{m}$ . . . . .	162
6.33	Segmenting cracks within a large-scale volumetric image by means of the trained U-Net model. In (a) an exemplary $\mu$ CT cross section and in (b) the crack prediction result by the U-Net model, where cracks are indicated by white and background in black. The volumetric image was obtained after the fourth load step of the RO specimen, presented in Figure 6.22. . . . .	163
6.34	3D-visualization of the segmented cracks within the RO specimen after the fourth load step by means of the U-Net model. . . . .	163

6.35	Measuring the crack and damage accumulation. In (a) the crack volume and (b) the normalized crack volume fraction distribution $\rho_{\text{Crack}}$ initial and after all respective load steps. . . . .	167
6.36	Crack volume fraction $\rho_{\text{Crack}}$ over maximum nominal stress $\sigma_{N,\text{max}}$ of the respective load steps. Comparison between SMC specimens with different microstructures. . . . .	168
6.37	Propagation and development of the damage mechanisms during the in-situ $\mu\text{CT}$ test. Examining the proportion of matrix cracking, pseudo-delamination and fiber breakage within the SMC sample with HO-0° microstructure. . . . .	170
6.38	Overview of the both fracture surfaces of the HO-0° specimen. Two locations are marked were at 1) fiber bundle breakage and at 2) fiber bundle pull-out is observed. . . . .	172
6.39	Close-up of the region 1) in Figure 6.38 (a) and (b) of the HO-0° specimen. The SEM images in (a) and (b) show broken and partially pulled-out fibers. . . . .	172
6.40	Fracture surface A of the HO-0° specimen. Close-up of the marked region in Figure 6.39 (a). The SEM image shows broken and slightly pulled-out fiber filaments. . . . .	172
6.41	Detailed SEM images of the pulled-out fiber bundle at location 2) in Figure 6.40. The SEM image (a) shows the remaining matrix material and (b) the pulled-out fiber bundle on the fracture surface of the HO-0° specimen. . . . .	173
6.42	Overview of both fracture surfaces A and B. Two highlighted regions of the RO specimen are examined in detail. . . . .	174
6.43	Pulled out fiber bundle and remaining matrix gap. Close-up SEM images of the marked regions in Figure 6.42 at location 1) of the RO specimen. . . . .	174
6.44	Close-up SEM images of fiber bundle breakage and matrix fragments within the regions marked in Figure 6.42 at location 2) of the RO specimen. . . . .	174



6.45	Fiber bundle breakage and matrix fragments. Close-up SEM images of the marked regions in Figure 6.44 of the RO specimen. .	175
6.46	Overview of both fracture surfaces A and B. The HO-90° specimen was extracted with a plate orientation of 90°. . . . .	176
6.47	Close-up SEM images of a pulled out fiber bundle in Figure 6.46 at location 1), which is aligned along the fracture surface. Furthermore, the SEM image shows matching matrix fracture contours in both fracture surfaces of the HO-90° specimen. . . . .	176
6.48	Close-up SEM images of partial pulled out and broken fibers. The fibers are embedded by a matrix region with a smooth fracture surface. The region of the close-up SEM images is illustrated in Figure 6.46 at location 2) of the HO-90° specimen. . . . .	177
6.49	Close-up SEM images of the HO-90° specimen at marked regions in Figure 6.46 at location 3) show the matrix fracture surfaces with periodic grooves. . . . .	177
6.50	Detailed SEM images of the marked regions in Figure 6.49. The SEM images show periodic the groove pattern in detail. On the left side, the SEM images reveal matching matrix fragments on both fracture surfaces of the HO-90° specimen. . . . .	177
7.1	Comparing the DVC performance with those of the SRG method regarding the crack segmentation results. In (a) the gray-value image, (b) SRG and (c) DVC the crack segmentation results of an exemplary $\mu$ CT cross section. In contrast to SRG, cracks are segmented rather smoothed by using the DVC method. . . . .	188
7.2	Illustrating the (a) initial and (b) deformed microstructure together with the (c) difference volume determined by DVC. Comparison between initial and deformed microstructure demonstrates the capability of the DVC method to identify even the formation of pseudo-delamination crack with marginal crack opening. . . . .	189

7.3	Visualizing the von Mises strain field determined by DVC around a matrix crack formation. The crack is segmented according to Figure 6.30 and visualized by a uniform color. . . . .	190
7.4	Comparing the capability of the trained U-Net model and the SRG method to segment cracks. First row shows gray-scale image sections, second and third row show the corresponding the CNN and SRG results, respectively (crack in white and background in black). . . . .	193
7.5	Crack orientation distribution with respect to the crack density. Comparing the crack orientation results (a) studied by Wang et al. [219] and (b) characterized in this doctoral thesis (figure in (a) by Wang et al. [219]). . . . .	195
7.6	Comparing macroscopic damage variable and norm. crack volume fraction. Development of the (a) damage variable and (b) crack volume fraction with respect to the applied stress and the fiber architecture (figure in (a) by Shirinbayan et al. [229]). . . . .	197
7.7	The Cook-Gordon mechanism of longitudinal splitting. Introducing shear stress parallel to the interface by means of tension crack propagation towards a longitudinal fiber (re-illustration, original figures by Greenhalgh [27] and Cook et al. [259]). . . . .	201
7.8	Difference between (a) extensive fiber debonding and (b) dominate fiber breakage of GFRP laminate (original figures by Greenhalgh [27]). . . . .	202
7.9	Classification of the analyzed damage mechanisms. Visualization of the damage mechanism fractions by a ternary plot and a detailed view of the relevant region. All the SMC specimens investigated exhibit predominant matrix cracking. . . . .	204

---

7.10	Damage mechanisms in SMC with planar randomly oriented fiber bundles (RO) under cyclic load. In (a) an exemplary $\mu$ CT cross section of the RO sample and (b) illustration of the observed damage phenomena. At (I) crack initiation at a pore tip, (II) crack propagation through the UPPH matrix and (III) bypassing fiber bundles. . . . .	206
7.11	Illustration of the observed damage mechanisms in HO-90° SMC. In (a) $\mu$ CT cross section and in (b) schematic illustration of the crack formation, where predominately matrix cracking and pseudo-delamination occurs. . . . .	208



# List of Tables

2.1	Mass attenuation coefficients $\mu_m$ of elements and compounds (data on quartz by Han et al. [60] and the other data by Hubbell and Seltzer [61]) . . . . .	26
2.2	Detailed categorization of the pixel-wise object segmentation results.	57
2.3	Summary of presented crack classification, detection and segmentation models in civil engineering. Image size, number of training data and achieved accuracy. . . . .	65
2.4	Additional information of the achieved performance precision, recall and F-measure metrics of different crack segmentation models in civil engineering. . . . .	65
3.1	Components of the examined glass fiber-reinforced UPPH SMC. . .	70
3.2	Effect of the charge coverage on the fiber orientation distribution of glass fiber-reinforced polyester SMC. The data are manually extracted from the contribution of Chen and Tucker [204]. . . . .	72
3.3	Mechanical properties of the UPPH matrix. Tensile strength and failure strain of the UPPH matrix were characterized by Miriam Bartkowiak at the IAM-WK. . . . .	79
3.4	Mechanical properties of the glass fibers. . . . .	79
3.5	Mechanical properties of the UPPH glass fiber reinforced SMC. . . .	79

3.6	Summary of the predominant damage mechanisms in SMC considering the load case and fiber content, which have been studied by several authors. The examined SMC composites consist of diverse matrix systems, which are reinforced by chopped glass fiber bundles. Matrix Cracking = MC, Pseudo-Delamination = PD, Fiber Pull-Out = PO and Fiber Breakage = FB. Damage mechanisms indicated by parentheses (×) are not explicitly identified by the authors as predominant mechanisms but are relevant nonetheless. . . . .	87
4.1	Selected parameters of the fiber bundle tracking and clustering method [118, 240, 242]*. . . . .	103
4.2	Selected parameters of the digital image correlation analysis. . . .	109
4.3	Parameters and options of the convolutional neural network and the training process. . . . .	112
4.4	Schematic cases of different types, shapes and orientations of cracks and the resulting second-order crack orientation tensors $D$ . .	118
6.1	Summary of microstructure properties. Charge coverage, coherence, plate orientation and principal fiber orientation of the examined SMC specimens. . . . .	140
6.2	Selected load step parameters of the respective in-situ $\mu$ CT test examining the HO-0° specimen. Furthermore, the measured nominal stress maximum $\sigma_{N,\max}$ and drop $\Delta\sigma_N$ of each load step (data by Schöttl et al. [241]*). . . . .	144
6.3	Selected load step parameters of the respective in-situ $\mu$ CT test examining the HO-45° specimen. Furthermore, the measured nominal stress maximum $\sigma_{N,\max}$ and drop $\Delta\sigma_N$ of each load step. .	147
6.4	Selected load step parameters of the respective in-situ $\mu$ CT test examining the HO-90° specimen. Furthermore, the measured nominal stress maximum $\sigma_{N,\max}$ and drop $\Delta\sigma_N$ of each load step. .	149

6.5	Selected load step parameters of the respective in-situ $\mu$ CT test examining the RO specimen. Furthermore, the measured nominal stress maximum $\sigma_{N,\max}$ and drop $\Delta\sigma_N$ of each load step. . . . .	151
6.6	Evaluating the trained U-Net performance by different metrics and data sets. . . . .	162
6.7	Characterizing the spatial damage anisotropy of the in-situ $\mu$ CT tested HO-0° specimen in Figure 6.16. Crack orientation histogram and crack orientation tensor $\mathbf{D}$ of the respective load steps (data by Schöttl et al. [243]*). . . . .	165
6.8	Analyzing the spatial damage anisotropy of the HO-45° and RO specimens during the final load step of in-situ $\mu$ CT test. Crack orientation histogram and crack orientation tensor $\mathbf{D}$ , respectively. . . . .	166
6.9	Quantifying the damage mechanisms for three SMC samples with HO-0°, HO-45° and RO microstructures. The damage mechanism fractions are quantified for the respective samples during the final in-situ $\mu$ CT load step. . . . .	169
7.1	Comparing the maximum nominal stress of the in-situ $\mu$ CT tested specimens with the quasi-static tensile test results by Trauth [209] on the same SMC material system with an initial charge coverage of 33 %. . . . .	185
A.1	Selected parameter and details of the performed $\mu$ CT, which are used for the fiber bundle analysis. . . . .	285
A.2	Selected parameter and details of the performed in-situ $\mu$ CT scans. . . . .	286
A.3	Microstructure properties of the SMC samples examined by means of interrupted in-situ $\mu$ CT testing. . . . .	286
A.4	Detailed structure of the U-Net architecture. . . . .	287





# Symbols and Abbreviations

## Abbreviations

vol.%	Volume Fraction in Percent
wt.%	Weight Fraction in Percent
μCT	Micro-Computed Tomography
ANN	Artificial Neural Networks
CFRP	Carbon Fiber-Reinforced Polymer
CNN	Convolutional Neural Networks
DicoFRP	Discontinuous Fiber-Reinforced Polymers
DVC	Digital Volume Correlation
GFRP	Glass Fiber-Reinforced Polymer
HO	Highly Oriented
IAM	Institute for Applied Materials
IRTG	International Research Training Group
KIT	Karlsruhe Institute of Technology
MFD	Mold Filling Direction
RO	Randomly Oriented
RVE	Representative Volume Element
SEM	Scanning Electron Microscopy
SMC	Sheet Molding Compounds
SRCT	Synchrotron Radiation Computed Tomography
SRG	Seed-Region-Growing
UPPH	Unsaturated Polyester-Polyurethane Hybrid

**Scalar**

$\delta(\cdot)$	Dirac Delta Function
$\epsilon$	Tensile Strain
$\epsilon_{vM}$	von Mises equivalent strain
$\kappa$	Curvature
$\lambda$	Eigenvalues
$\mu$	Linear Attenuation Coefficient
$\mu_m$	Mass Attenuation Coefficient
$\nu$	Poisson's Ratio/Transverse Contraction
$\phi$	Volume Fraction Content
$\psi$	Orientation Distribution Function
$\rho$	Density
$\rho_0$	Total Crack Density
$\rho_{Crack}$	Crack Volume Fraction
$\sigma$	Tensile Stress
$\theta, \tau$	Angle
$\{x, y, z\}$	Coordinates
$d$	Diameter
$E$	Young's Modulus
$G$	Shear Modulus
$g$	Gray-value
$I$	Intensity
$k$	Threshold
$L$	Length
$R$	Radius
$t$	Time
$V$	Volume
$V_{Crack}$	Accumulated Crack Volume
$V_{ref}$	Reference Volume
$w$	Weight Fraction Content

**Vectors**

$g$	Crack Normal Unit Vector
$n$	Fiber Orientation Unit Vector
$p$	Unit Vector
$u$	Displacement Vector
$v$	Eigenvector
$X$	Reference Position Vector
$x$	Position Vector
$\{e_x, e_y, e_z\}$	Coordinate System Axis Vectors

**Tensors**

$D$	Second-order Crack Orientation Tensor
$\varepsilon$	Infinitesimal Strain Tensor
$C$	Stiffness Tensor
$\mathbb{I}^S$	Fourth-order Symmetric Identity Tensor
$L$	Localization Tensor
$S$	Compliance Tensor
$H$	Displacement Gradient Tensor
$I$	Second-order Identity Tensor
$N$	Second-order Fiber Orientation Tensor
$P$	Second-order Crack Density Tensor
$\sigma$	Cauchy Stress Tensor

**Operators**

$(\cdot)^T$	Transpose
$(\cdot)^{-1}$	Inverse
$\cdot$	Scalar Product
$d$	Derivative
$\  \cdot \ $	Euclidean Norm
$\otimes$	Dyadic Product
$\partial$	Partial Derivative

$\text{sym}(\cdot)$	Symmetry
$\text{tr}(\cdot)$	Trace

### Indices

$(\bar{\cdot})$	Effective Value
$(\cdot)_0$	Initial
$(\cdot)_F$	Fiber
$(\cdot)_M$	Matrix
$(\cdot)_{\text{Crack}}$	Crack
$(\cdot)_{\text{crit}}$	Critical
$(\cdot)_{\text{max}}$	Maximum
$(\cdot)_{\text{nom}}$	Nominal
$(\cdot)_{\text{ref}}$	Reference
$(\cdot)_{FM}$	Fiber-Matrix Interface
$(\cdot)_{i,j}$	Summation or Iteration Index
$\langle \cdot \rangle$	Arithmetic Volume Average Value

### Volume and Trajectory

$\mathcal{B}$	Control Volume
$\mathcal{R}$	Mesosopic bundle
$\mathcal{S}$	Microscopic bundle

# A Appendix

Detailed operation parameters of the  $\mu$ CT scans, which were presented and analyzed in this work are listed in Table A.1 and Table A.2. Table A.1 lists the scanning parameters regarding the microstructure characterization and Table A.2 those of the in-situ  $\mu$ CT measurements, respectively.

In addition to the  $\mu$ CT parameters in Table A.2, the characterized microstructure properties of the respective SMC specimens are listed in Table A.3. The table includes the charge coverage, plate orientation, principal fiber orientation and coherence.

Table A.1: Selected parameter and details of the performed  $\mu$ CT, which are used for the fiber bundle analysis.

Property	Unit	Sample No. 1	Sample No. 2	Sample No. 3
Voxel size	$\mu\text{m}$	9.1	6.8	17.2
Exposure time	ms	1000	500	1000
Current	mA	0.03	0.20	0.05
Voltage	kV	130	150	150
Frame binning	-	2	2	2
X-ray tube head	-	Transmission	Reflection	Reflection

Table A.2: Selected parameter and details of the performed in-situ  $\mu$ CT scans.

Label	Voxel size	Exposure time	Current	Voltage	Frame binning	X-ray tube head
HO-0°	6.8 $\mu$ m	500 ms	0.20 mA	150 kV	2	Reflection
HO-45°	6.1 $\mu$ m	500 ms	0.24 mA	150 kV	2	Reflection
HO-90°	6.2 $\mu$ m	500 ms	0.25 mA	140 kV	2	Reflection
RO	6.5 $\mu$ m	500 ms	0.20 mA	150 kV	2	Reflection

Table A.3: Microstructure properties of the SMC samples examined by means of interrupted in-situ  $\mu$ CT testing.

Label	Specimen name	Geometry	Charge coverage	Plate orientation	Principal fiber orientation	Coherence of $N$
HO-0°	23-0-1	see Fig. 5.7	50 %	0°	4.0°	0.25
HO-45°	C25-01-45-07	see Fig. 5.7	25 %	45°	45.4°	0.47
HO-90°	18-90-2	see Fig. 5.7	50 %	90°	78.5°	0.40
RO	C25-01-45-14	see Fig. 5.7	25 %	45°	isotropic	0.13

Details of the U-Net architecture by Ronneberger et al. [172], including layer type, depth, output size and number of parameters are provided in Table A.4. The CNN architecture is trained and applied as part of this doctoral thesis and is implemented by using Tensorflow 2.3.1, Keras 2.4.3 and Jupyter Notebook 2.2.8.

Table A.4: Detailed structure of the U-Net architecture.

Layer	Layer type	Depth	Output size	Parameter
0	Input		96	0
1	Convolutional	32	96	320
2	Dropout		96	0
3	Convolutional	32	96	9248
4	Max pooling		48	0
5	Convolutional	64	48	18496
6	Dropout		48	0
7	Convolutional	64	48	36928
8	Max pooling		24	0
9	Convolutional	128	24	73856
10	Dropout		24	0
11	Convolutional	128	24	147584
12	Convolutional Up-Sampling	64	48	32832
13	Concatenation (Layer No. 7)		48	0
14	Convolutional	64	48	73792
15	Dropout		48	0
16	Convolutional	64	48	36928
17	Convolutional Up-Sampling	32	96	8224
18	Concatenation (Layer No. 3)		96	0
19	Convolutional	32	96	18464
20	Dropout		96	0
21	Convolutional	32	96	9248
22	Output		96	66

